Design, synthesis, characterization, and catalytic evaluation of unsymmetric Schiff-Base calixpyrrole transition metal complexes for hydrogen evolution

by

Sachithra Somachandra Manamalage

B.S., University of Colombo, 2018

AN ABSTRACT OF A DISSERTATION

submitted in partial fulfillment of the requirements for the degree

DOCTOR OF PHILOSOPHY

Department of Chemistry
College of Arts and Sciences

KANSAS STATE UNIVERSITY
Manhattan, Kansas

2025

Abstract

Recently, considerable advancements have been achieved in developing new molecular electrocatalysts for the production of hydrogen, such as understanding their mechanisms, factors that affect the catalytic reaction, etc. Hydrogen presents itself as a potential fuel substitute due to being a renewable energy source with zero carbon emissions, having a maximum gravimetric energy density to replace petroleum and other petroleum products.

This work demonstrates the successful design, formulation, and electrochemical H_2 evaluation of a novel mono- and bimetallic Schiff-base complexes bearing unsymmetric ligands derived from a calixpyrrole framework, developed as electrocatalysts for the hydrogen evolution reaction (HER). The introduction of chemically distinct coordination binding pockets, such as salen or imidazole (termed salixpyrrole and imixpyrrole, respectively), has enabled a straightforward pathway to coordinate various transition metals into the secondary coordination sphere, leading to the construction of tunable metal complexes with enhanced catalytic properties.

Both monometallic (2) and bimetallic (3) salixpyrrole complexes were found to be catalytically active in the presence of *p*-toluenesulfonic acid (*p*TSA). Mechanistic investigations indicated that 2 follows a second-order dependence on acid and first-order dependence on catalyst, whereas 3 operates via a distinct pathway. The bimetallic species exhibits exceptional catalytic performance with a TOF of 4640 s^{-1} and significantly lower overpotential of 0.39 V, emphasizing the benefit of incorporating a second metal center into the catalyst framework.

The imixpyrrole system (4), on the other hand, was developed by including an imidazole pendant group into the ligand scaffold and shown to be catalytically active for HER in the presence of various acids. Three different acid sources (anilinium.BF_4, imidazolium.BF_4,

triethylammonium.BF_4) with varying pK_a were selected, and HER activity was systematically evaluated in THF. Complex 4 displayed PCET behavior with a KIE value of 6.45 in the presence of weak acid and a more classical pathway (KIE =1.06) with stronger acid anilinium. The highest TOF of 33040 s^{-1} with a lower overpotential value of 0.53 V and a faradaic efficiency of 99.3% was achieved with anilinium. Although complex 4 behaves homogeneously in the presence of both anilinium and triethylammonium acid, it displayed heterogeneous behavior with imidazolium, demonstrating the profound impact of proton source on catalytic efficiency and mechanism.

A stepwise metalation strategy to synthesize heterobimetallic Schiff-base complexes was investigated next. A successful incorporation of redox-inactive Zn (II) and redox-active Cu(I) ions into the secondary coordination sphere of the imixpyrrole system resulted in two diamagnetic heterobimetallic complexes (5 and 6). The electrochemical features provide insight into metal-metal synergism, pointing to enhanced HER potential.

Collectively, this work provides a new blueprint for the rational design of electronically tunable, unsymmetric Schiff-base complexes capable of efficient proton reduction. It highlights the essential roles of ligand asymmetry, proton source, and multimetallic cooperativity in governing catalytic performance, laying the foundation for the future development of next generation HER catalysts.

Design, synthesis, characterization, and catalytic evaluation of unsymmetric Schiff-Base calixpyrrole transition metal complexes for hydrogen evolution

by

Sachithra Somachandra Manamalage

B.S., University of Colombo, 2018

A DISSERTATION

submitted in partial fulfillment of the requirements for the degree

DOCTOR OF PHILOSOPHY

Department of Chemistry
College of Arts and Sciences

KANSAS STATE UNIVERSITY
Manhattan, Kansas

2025

Approved by:

Major Professor
Ryan J. Rafferty

Copyright

Abstract

Recently, considerable advancements have been achieved in developing new molecular electrocatalysts for the production of hydrogen, such as understanding their mechanisms, factors that affect the catalytic reaction, etc. Hydrogen presents itself as a potential fuel substitute due to being a renewable energy source with zero carbon emissions, having a maximum gravimetric energy density to replace petroleum and other petroleum products.

This work demonstrates the successful design, formulation, and electrochemical H_2 evaluation of a novel mono- and bimetallic Schiff-base complexes bearing unsymmetric ligands derived from a calixpyrrole framework, developed as electrocatalysts for the hydrogen evolution reaction (HER). The introduction of chemically distinct coordination binding pockets, such as salen or imidazole (termed salixpyrrole and imixpyrrole, respectively), has enabled a straightforward pathway to coordinate various transition metals into the secondary coordination sphere, leading to the construction of tunable metal complexes with enhanced catalytic properties.

Both monometallic (2) and bimetallic (3) salixpyrrole complexes were found to be catalytically active in the presence of *p*-toluenesulfonic acid (*p*TSA). Mechanistic investigations indicated that 2 follows a second-order dependence on acid and first-order dependence on catalyst, whereas 3 operates via a distinct pathway. The bimetallic species exhibits exceptional catalytic performance with a TOF of 4640 s^{-1} and significantly lower overpotential of 0.39 V, emphasizing the benefit of incorporating a second metal center into the catalyst framework.

The imixpyrrole system (4), on the other hand, was developed by including an imidazole pendant group into the ligand scaffold and shown to be catalytically active for HER in the presence of various acids. Three different acid sources (anilinium.BF_4, imidazolium.BF_4,

triethylammonium.BF_4) with varying pK_a were selected, and HER activity was systematically evaluated in THF. Complex 4 displayed PCET behavior with a KIE value of 6.45 in the presence of weak acid and a more classical pathway (KIE =1.06) with stronger acid anilinium. The highest TOF of 33040 s^{-1} with a lower overpotential value of 0.53 V and a faradaic efficiency of 99.3% was achieved with anilinium. Although complex 4 behaves homogeneously in the presence of both anilinium and triethylammonium acid, it displayed heterogeneous behavior with imidazolium, demonstrating the profound impact of proton source on catalytic efficiency and mechanism.

A stepwise metalation strategy to synthesize heterobimetallic Schiff-base complexes was investigated next. A successful incorporation of redox-inactive Zn (II) and redox-active Cu(I) ions into the secondary coordination sphere of the imixpyrrole system resulted in two diamagnetic heterobimetallic complexes (5 and 6). The electrochemical features provide insight into metal-metal synergism, pointing to enhanced HER potential.

Collectively, this work provides a new blueprint for the rational design of electronically tunable, unsymmetric Schiff-base complexes capable of efficient proton reduction. It highlights the essential roles of ligand asymmetry, proton source, and multimetallic cooperativity in governing catalytic performance, laying the foundation for the future development of next generation HER catalysts.

Table of Contents

List of Figures

List of Tables

List of Schemes

Acknowledgements

With an extreme sense of gratitude and excitement, I take this opportunity to thank all the individuals who have helped and encouraged me during my Ph. D. journey.

I would first like to sincerely thank Prof. Peter E. Sues for his guidance and support throughout my doctoral studies. It was an inestimable privilege for me to have the opportunity to work under his supervision. I thank him for supporting me during the hardest time of my life and for encouraging and trusting me, which gave me the strength to continue my work. I would also like to extend my sincere and immense gratitude to Prof. Ryan Rafferty. He has been an outstanding advisor who always encouraged the students and remains dedicated to their success. I will always be grateful for their guidance, patience, scientific ideas, support, encouragement, and motivation throughout my journey at Kansas State University. Their mentorship has played a pivotal role in my accomplishments here, and I couldn't have wished for better Ph.D. advisors. I would also like to express my heartfelt gratitude to the Sues group members, both past and present, for their unwavering support, insightful conversations, and the strong sense of community they have fostered throughout my time here.

I would like to express my deepest gratitude to my doctoral committee members, Dr. Christer Aakeroy, Dr. Jun Li, Dr. Tendai Gadzikwa, Dr. Placidus Amama, and Dr. Chuancheng Duan for their continuous guidance in every step of my Ph. D. work. It is my pleasure to thank them for their valuable suggestions, which contributed towards the improvement of my thesis.

I would also like to express my special and profound thanks to the Department of Chemistry, Kansas State University for the instrumental facilities without which the work included in this thesis would not have been possible. I would like to thank Dr. Boris Averkiev for helping

me with single-crystal XRD studies and Mr. Jim Hodgson for with glassware support. Together with this, I would also like to thank all the instrumental operators, including my colleagues, for their carefulness and patience, which led to swift and correct analysis of the samples. Special thanks go to Michael Hinton for sharing all your teaching skills and making teaching CHM1 and CHM2 labs easy. I would also like to thank all the other staff members of the Chemistry Department and K-State for their help whenever I was in need.

I have indeed been fortunate enough to have good friends around me throughout this journey. I would like to thank Ishara, Nishadhi, Kushan, Dishan, Tuhin, Dola, Pricilla, Mrs. Surangi, and others for their helping hand. I express my gratitude to all my friends at K-state for making the journey memorable.

A very special thanks to my close persons/ best friends, Piumi and Madhu. During my hard times, they stood with me and became a supportive system to eliminate the negativity, which helped me a lot to fight my battle. Without their continuous encouragement and motivation, I probably would not have achieved this.

Finally, my Ph. D. endeavor could not have been completed without endless love, unending support, tolerance, and blessings from my family. My deepest gratitude, especially to my "THATHTHA" thank you for being my steady source of strength and quiet resilience, your presence has been a source of comfort and confidence throughout this journey, and for that, I am deeply grateful, my late "AMMA", and "LOKU AMMA" who always believed in me and supported me. I would also like to thank my sister "Vindula" and brother-in-law "Dileepa" as well as all my family for being there for me throughout this process and offering me comfort through challenging times. They are the pillars of my achievements. Their enormous sacrifices and unconditional love in every stage of my life motivated me to overcome all the challenges.

Dedication

To my beloved mother,

This thesis is dedicated to you, whose dreams for me have become my reality. Your unwavering belief in my potential and your countless sacrifices have guided me to this moment.

Though you are not here to witness this milestone, I know you are with me in spirit, celebrating this achievement as a realization of your hopes and dreams.

Everything I have accomplished is a testament to your love, strength, and vision.

This is for you, Amma, with all my love.

Chapter 1 - Introduction

One of the most pressing global challenges facing the 21st century is developing a clean and renewable energy source as an alternative to fossil fuel.[1–3] With the increasing world population along with rising living standards, global energy consumption tends to increase rapidly over the next half-century. It is predicted that global energy consumption will grow by at least 2-folds, from our current burn rate of 12.8 TW to 28-35 TW by 2050.[1,2,4,5]. Even though it is possible to meet this energy requirement with existing natural energy reserves (coal, oil, and dry natural gases[6]), this will come with rising economic and environmental impacts, such as increased carbon emission.[7,8] All together demands the necessity of developing new renewable and sustainable energy sources.[9–11] Coming up with new energy sources will require increased energy efficiency, new methods to reuse existing carbon-based fuels, and an intimidating amount of new carbon-neural energy. Therefore, the challenge for science, specifically for the discipline of chemistry, is to develop a secure, sustainable, and carbon-neutral energy system on a larger scale in a cost-effective manner

In contrast to fossil fuels, that have finite sources in the world, energy sources such as solar, wind, geothermal, hydropower, and biomass are renewable and each of these categories are evenly distributed. These sources also have the potential to generate energy with almost zero emission of both air pollution and greenhouse gases, such as CO_2. However, the economic potential is limited by environmental factors such as the availability of solar irradiation, wind patterns, weather concerns like the availability of rain, and competing land uses. Currently, renewable energy sources provide about 14% of global energy demand, mainly dominated by traditional biomass used for cooking and heating.[12] Meanwhile, 15% (4.6 thousand TWh out of 30.6 thousand TWh) of global electricity demand is supplied by large-scale hydropower plants where it has almost

reached its capacity due to availability (**Figure 1.1**). Therefore, the necessity of discovering a new renewable energy source, one that is not limited by environmental factors, has become the top priority of the scientific community.

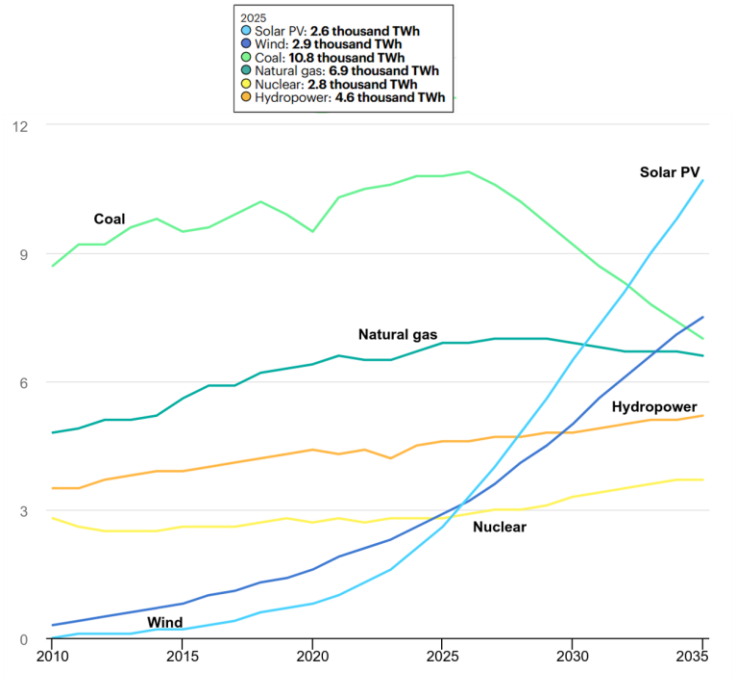

Figure 1.1. World electricity generation in the stated policies scenario 2010-2035. Adopted from REF[12].

Hydrogen stands out as one of the most fascinating alternatives to non-renewable energy sources like fossil fuels. Consequently, the transition of the global energy system from fossil fuels to hydrogen is an essential task. Hydrogen is considered a clean fuel for the next generation because it does not produce harmful gases, such as NOx, SOx, or greenhouse gases when burned; it merely transforms from water to hydrogen and back to water during use. However, the primary method of hydrogen production, steam reforming, relies on fossil fuels like natural gas as a starting material. This means that hydrogen production again depends on non-renewable resources, resulting in greenhouse gas emissions during its creation. Therefore, there is a global demand for new hydrogen production technologies sourced from carbon-free materials.

1.1. Molecular hydrogen (H_2) importance

During the State of the Union address in 20##, U.S. President Bush proposed "$1.2 billion in research funding so that America can lead the world in developing clean, hydrogen-powered automobiles" emphasizing the necessity of developing an H_2 economy.[13] This is not a new idea, world renowned author Jules Verne was the first one to recognize the possibility of hydrogen derived from water electrolysis and stated that "I believe that water will one day be the coal of the future" in 1874[14]. Then Rudolf suggested the usage of hydrogen produced from water electrolysis as a transportation fuel in the 1930s[15] as well as the importance of using hydrogen as an energy storage was suggested by Francis Bacon[16]. Therefore, the vision of using hydrogen as an alternative energy source has been a very compelling yet unrealized discussion for over an extended period.

Hydrogen is considered an attractive alternative for the energy crisis due to having the largest gravimetric energy density which makes it a frontline candidate, as well as the only by-product of water electrolysis, making it environmentally friendly. The estimated requirement of a hydrogen-based economy is around 150 million tons annually which indicates the demand for efficient electrolytic and/or photochemical hydrogen evolution reaction (HER) catalysts.[13] Therefore, the development of both homogeneous and heterogeneous catalysts for HER from water/proton sources has received significant attention.

Hydrogen is not only an attractive alternative energy carrier but also has great demand in other industrial sectors. It is an essential starting material for ammonia production via the Haber-Bosch process, which accounts for 54% of global hydrogen use, also an important chemical in the chemical industry/refineries which accounts for around 35% of its usage (**Figure 1.2**).

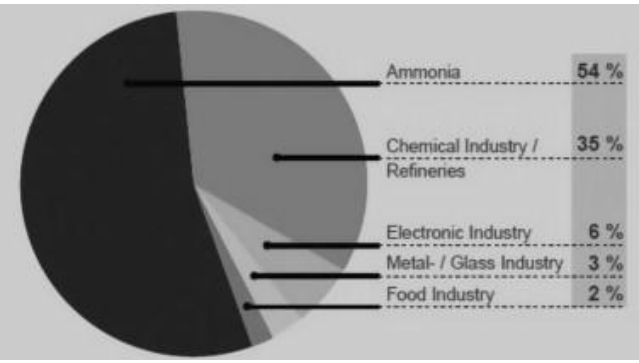

Figure 1.2. Percent of global hydrogen use by industry. Reproduced with permission from REF[17].

1.2. Hydrogenase

A major challenge related to developing homogeneous and heterogeneous catalysts to activate small molecules like H_2 is the necessity of transferring multiple protons and electrons to a substrate. Nature has provided the best inspiration for synthetic catalyst design known as enzymes. Hydrogenases are one of the most well-studied groups of metalloenzymes that catalyze one of the simplest molecular reactions HER and molecular hydrogen oxidation reactions (HOR) to protons and electrons.[18,19] The hydrogenase term was first proposed by Stephenson and Strickland while observing the activity in anaerobically grown *Escherichia Coli* cells for reversible dye reduction which was inhibited by CO suggesting that a transition metal was involved in H_2 activation in 1931.[20,21]

The hydrogenases can be divided into three main groups such as nickel-iron [NiFe], di-iron [FeFe], and iron [Fe] hydrogenase. This categorization is mainly based on the metal composition in the active site. Among the hydrogenases [FeFe] favors the H_2 evolution and it is the most studied enzyme while [NiFe] prefers the H_2 oxidation. Some characteristic features observed for hydrogenases were the involvement of one or both metals in catalysis and the unique ligand environment around each metal. It also observed a bridged bimetallic center with open access is one of the key features for [NiFe] and [FeFe] hydrogenase while the third class [Fe] hydrogenase

only contains one metal center with cofactors which has phenol moieties and CO ligands.[22] The protein environment provides distinct gas channels, electron-transfer chains, and proton pathways to facilitate the HER also regulates the uptake of H_2. The most promising enzyme for H_2 evolution is considered to be [FeFe]-hydrogenase which has turnover frequencies of 10^2-10^4 s^{-1} and produces hydrogen at 10^4 molecule H_2 s^{-1} rate.

The [FeFe]-hydrogenase enzyme contains S-bridged proximal and distal Fe metal with an intermetallic distance of 2.6 Å (**Figure 1.3**).[23] Each metal center can be seen coordinated to a unique ligand environment, where one Fe coordinated with active cubane [4Fe4s] through a cysteine bridge while other Fe ions contain a free coordination site resulting in two Fe metals with chemically distinguished environment.[24–27] Also, the pendent amine group on the dithiol bridge seems to participate in the HER mechanism facilitating a proton shuttle between substrates. When it comes to [FeNi]-Hydrogenase, the complex is now heterobimetallic with a unique ligand environment around each metal. The Fe center is coordinated by two thiolate ligands between the Ni and Fe, one CO ligan and two CN^- ligands while the Ni center is tetracoordinated with two terminal cysteine thiolates besides the bridging thiolates.[27,28] Interestingly, some of the O_2-sensitive [NiFe]-hydrogenases were reported to be showing a distorted proximal [4Fe4S] cubane where one of the Fe atoms in the cubane is located close enough to bind to a hydroxyl group of an aspartate.[27,29,30] Moreover, it was observed that the active state of hydrogenase contains low-spin Fe^{II} and Ni^{II} centers emphasizing the necessity of having low-spin metal centers in the active site of the catalyst.[27,28]

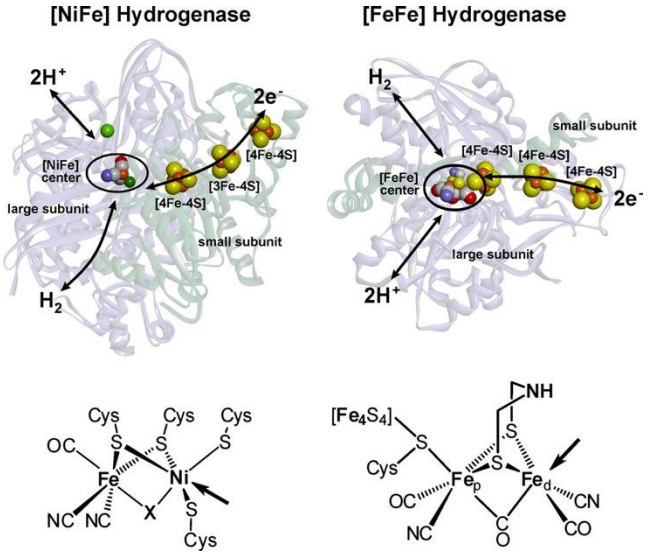

Figure 1.3. Structures of the [NiFe] hydrogenase and the [FeFe] hydrogenase. Reproduced with permission from REF[23].

Schematically indicated are the ET chain (via iron-sulfur centers) and pathways for the dihydrogen and the H^+ transfer. At the bottom, the chemical structures of the active sites of the two types of hydrogenases are given; the arrows indicate the open metal coordination site.[31]

In summary, the structural features that should be considered when developing synthetic mimics to achieve high HER reactivity are, 1) the availability of law-valent metals. 2) homo or hetero metallic structure with a unique coordination environment around each metal, 3) structural flexibility for H_2 to access the active site of the catalyst, 4) the availability of "in-built" functional groups that can participate in proton shuttle or the groups that are rich in electrons to supply electrons rapidly during HER.

1.3. Homogenous catalysts

When designing an enzyme mimic, inorganic chemists often consider homogenous catalysts, which are dissolved in the same phase as the reactants.[32–36] Some key advantages of homogeneous catalysts are the high degree of interaction between the catalyst and reactant molecules, which means catalysis is not limited to catalytically active surface area like in the heterogenous system

increasing the catalytic activity, high selectivity, avoids mass transfer limitations, and high level of rational manipulation where you have a higher degree of control over catalyst structure and mechanism.[37,38] Therefore, numerous homogenous synthetic models have been developed to provide further insight into reaction mechanisms.[23,34–36] The majority of synthetic models are made up of transition metal complexes due to their fascinating characteristics such as 1) the ability to form stable interactions with substances that have π-electron systems at various oxidation states; this feature is especially important for low-valent metal complexes as it enables them to participate in redox cycles, 2) the ability to coordinate with a variety of ligands with a flexibility in their coordination number, and 3) the ability to alter the electronic and/or steric conditions in active site with various combinations of participatory and non-participative ligands.[32]

Homogeneous catalyst systems have several disadvantages, including low thermal stability and the complexity of separation processes during synthesis. Additionally, these catalysts are often irrecoverable after the reaction, which limits their use in industry. As a result, homogeneous systems are still not as efficient or economically viable for industrial-scale production processes.[39]

1.3.1. Hydrogenase mimics

Over the past years, several biomimetic hydrogenase models have been developed for electrocatalytic hydrogen evolution reaction (HER). Interestingly, Reihlen et al. reported that the preparation of analogous dithiolate-bridged hexacarbonyl di-iron complexes, $[(\mu\text{-SEt})_2Fe(CO)_6]$ in 1929, even before the structural elements of [FeFe]-hydrogenases active site being discovered (**Figure 1.4**).[40] The structural characterization of the H-cluster in 1998-1999 by Peters et al.[41,42] paved the way for many groups such as Pickett, Rauchfuss, Darensbourg, and many others to create synthetic hydrogenase models.[43–45] These first-generation [FeFe]-hydrogenase mimics were synthesized by replacing two CO groups with two CN^- ligands to produce [(μ-

pdt)$Fe_2(CO)_4(CN)_2]^{2-}$ dianion (**Figure 1.4**), which inspired further synthetic advances in inorganic chemistry research. Currently, over 300 synthetic models can be found.[28,46]

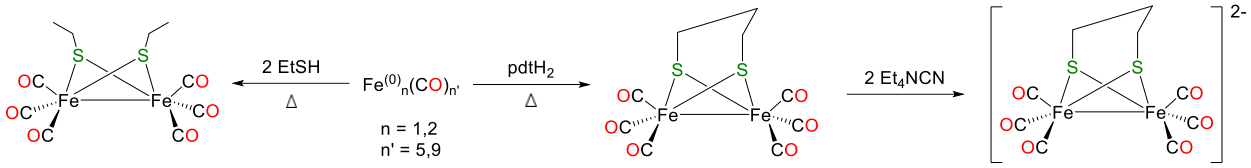

Figure 1.4. Synthesis scheme for the preparation of [(μ-$SEt)_2Fe(CO)_6$] (left), and precursor diiron hexacarbonyl complex (middle) used in route to the first true [FeFe] hydrogenase model [(μ-pdt)$Fe_2(CO)_4(CN)_2]^{2-}$ (right).

Interestingly, even to date, the research on synthesizing better catalytic models for HER has been highly debated, with nearly 100 new papers published in the last five years.[47–52] Much of the second-generation work has been done to develop the ligand architecture in the active site, to overcome limitations like large overpotential requirements, to increase turnover frequencies (TOF), and to make it more efficient and cost-effective.

All of the model complexes that exist for the [FeFe]-hydrogenases do not display enzyme-like bifunctional activity. Thus, this complex only allows for H_2 formation at higher overpotentials, with low turnover frequencies, and usually require strong acids.[53–56] Even after many changes in the complex structure, such as bearing a terminal hydride having an adjacent amine in the periphery of the Fe atom, fine-tuning the electronic properties of Fe by replacing CO ligands in the initial structure with CN and phosphines failed to allow efficient H_2 generation.[35,57–59] Finally, it was discovered that the presence of an internal base enables efficient proton-shuffling to a basic iron site, formation of a metal hydride, or having easy access to law valent Fe^IFe^I, Fe^0Fe^I, and Fe^0Fe^0 oxidation states are considered as the main criteria towards high activity of synthetic hydroganage enzyme mimics. Based on that, [(*terminal*-H)$Fe_2(Hadt^H)(CO)_2(dppv)_2]^{+2}$ (dppv = *cis*-$C_2H_2(PPh_2)_2$) and $[Ni(P^{Ph}{}_2N^{c6H4X})_2](BF_4)_2$ (x = OMe, H, CF_3) complexes were developed and displayed a fast formation of a metal hydride along with slow isomerization rate for the bridging hydride formation

which would hamper H_2 formation. The Ni monometallic complex was reported to have a turnover frequency of 100 000 s^{-1} which clearly emphasizes the importance of an internal proton relay. [23,34–36,60]

Initially, researchers focused on the metal and the surrounding ligands, such as CO and CN, in hydrogenase to evaluate the synthetic models. However, the perspective shifted from the idea that "reactivity occurs at the metal center," leading them to focus on the more reactive ligands (actor) as key players when synthesizing catalysts.[61,62] The basic idea was that the metal can cooperate with the ligands in a synergistic manner, where it facilitates chemical processes like bond activation steps in the catalytic cycle. Based on this concept, complexes based on “redox non-innocent ligands gained more attraction in HER world.

1.3.2. Porphyrin systems

Researchers have investigated various ligand structures to develop better catalytic models. Computational studies revealed more information into minima and transition state structures of catalytically relevant intermediates which improved the ligand structures towards more efficient HRE.[63] Recently, it has been reported that synergy between metal and ligand-based redox activities could improve the catalytic performance of metal complexes.[64–66] This combination enables electron transfer between hybrid ligands π-orbitals and metal d orbitals, facilitating multi-step electron transfer processes in metal complexes.

One of the notable series of complexes that utilize redox non-innocent ligands is porphyrin-based macrocycles which are known to undergo H_2 evolution from H_2O or organic acids.[67,68] Porphyrins can be considered as interesting ligands mainly due to their tetrapyrrolic structure with four nitrogen atoms in the porphyrin core which enables the coordination of a variety of metal cations. The physical and chemical properties of the ligand system can be easily altered by

introducing different functional groups on meso- or β-positions[69,70] or by coordinating an axial ligand to the metal center.[71,72] The transition and post-transition metal complexes of porphyrins are known for their acid-resistance characteristics which is a key property of acid-catalyzed HER catalysis.[73,74] Additionally, the extended 18 π-electron conjugated system in macrocyclic porphyrins facilitates the multi-electron and proton transfer reactions allowing HER to occur either on the metal ion or in the porphyrin ligand system.[75] Moreover, porphyrin ligands can provide low-valent metal ions with strong reducing powers which is also important in HER catalyst development.[76]

Most importantly, metalloporphyrins can be found in active sites of enzymes facilitating light harvesting, energy conversion, electron transfer, O_2 activation, and peroxide degradation. Heme unit is one of the vastly investigated biological porphyrin units which can be seen in catalyzing O_2 activation in cytochrome P450, O_2 binding in hemoglobin and myoglobin, peroxide degradation in peroxidase and catalases.[77,78] In all these applications, the central heme unit is the same, while the axial ligand varies which seems to be the prominent feature to change their activities (**Figure 1.5**). Therefore, researchers have been investigating porphyrin units and their activities for small molecule activation by installing various substituents to the ligand backbone to study the effects of electronics, axial ligands, proton relays, charged groups, and sterically bulky groups for the secondary coordination sphere.[78]

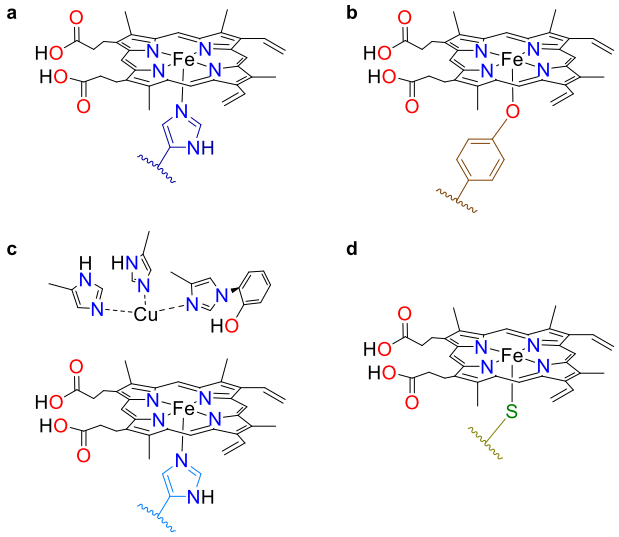

Figure 1.5. Heme active sites of (a) hemoglobin, (b) peroxidase, (c) CcO, and (d) cytochrome P450.

The first ever porphyrin-based homogeneous catalyst was reported by Kellett and Spiro in 1985.[79] They reported three cobalt(II) complexes with water-soluble porphyrins, *meso*-tetrapyrid-4ylporphine, *meso*-tetrakis(*N*-methylpyridinium-4-yl)porphin chloride, and *meso*-tetrakis(*N*,*N*,*N*-trimethylanilinium-4-yl)porphin chloride which seems to activate H_2 in DMSO upon addition of 0.5-20% water. The Co complex with *meso*-tetrakis(*N*,*N*,*N*-trimethylanilinium-4-yl)porphin chloride in the presence of water reacted surprisingly fast and the reported rate constant for HER was $>10^4$ $M^{-1}s^{-1}$ which was larger than some of the Co complexes at that time for HER. They also noted the complex reaction 8 orders of magnitude faster with H_3O^+ than with H_2O. These factors supported the establishment of cobalt complexes based on porphyrins can be excellent molecular catalysts for HER. Then factors like controlling the pK_a and steric parameters and electronic properties of the secondary coordination sphere on porphyrin systems were vastly investigated.

In 2011, Nocera and co-workers reported electrocatalytic H_2 evolution with hangman cobalt(II) porphyrins (**Figure 1.6**) in acetonitrile. Benzoic acid and p-toluene sulfonic acid were used as the proton sources at an overpotential of 800 mV.[80] They reported one cobalt porphyrin

complex with a xanthene backbone and a carboxylic acid moiety in the secondary coordination sphere positioned over the catalytic center and another with bromine instead of a carboxylic acid group. The carboxylic-contained complex showed a reversible one-electron Co(II)/Co(I) reduction at -1.10 V vs Fc/Fc^+ whereas the bromine-contained complex showed catalytic proton reduction at a potential 120 mV more negative for HER from benzoic acid. This implies a possible intramolecular proton transfer from the carboxylic hanging group to the metal center which facilitates efficient hydrogen generation and significantly reduces overpotential. Surprisingly, with strong acids, both complexes displayed catalytic waves at similar potentials which indicates in the presence of strong acids the hangman effect was not observed as it was able to directly protonate Co^I.[81,82] These results also emphasize the effect of the proton source when determining the catalytic activity of complexes for small molecular activation. The catalysts contain a carboxylic acid hanging group in the secondary coordination sphere in porphyrin complexes reported to undergo reduction catalysts such as hydrogen evolution, oxygen reduction, and carbon dioxide reduction.[80,83–87]

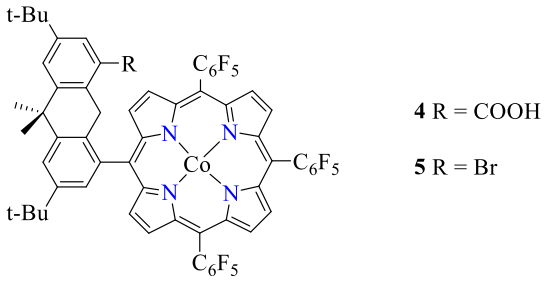

Figure 1.6. Molecular structures of hangman porphyrins (4 and 5) for H_2 evolution.

After extensive research on monometallic metalloporphyrins with various metals such as Co, Fe, Pd, Ni, and Cu for HER, a doubly fused binuclear Cu(II) porphyrin, CuF_2P was reported by Moore and coworkers in 2018, to be active for electrocatalytic HER in comparison with the

non-fused Cu porphyrin monomeric complex (**Figure 1.7**).[88] The fused bimetallic complex gained attraction due to the favorable properties for catalytic applications such as 1) availability of multiple coordination sites for metals, 2) delocalized electrons across an extended scaffold, ability to be reduced as well as oxidized at significantly less applied potentials than to those potentials required for analogous non-fused porphyrins, and 4) provide alternative strategy to adjust redox properties of molecular catalyst besides synthesizing catalysts with electron-withdrawing, electron-donating or acidic functional groups.[89,90] Kinetic investigation of fused porphyrin complex in dichloromethane by using TFA as a proton source resulted in an observed rate constant above 2,000,000 s^{-1} which is considered the highest reported in the literature for HER. Compared to the analogous non-fused copper porphyrin it also showed lower overpotential demonstrating the capacity to modify macrocycles towards binuclear complexes for preparing efficient electrocatalysts.

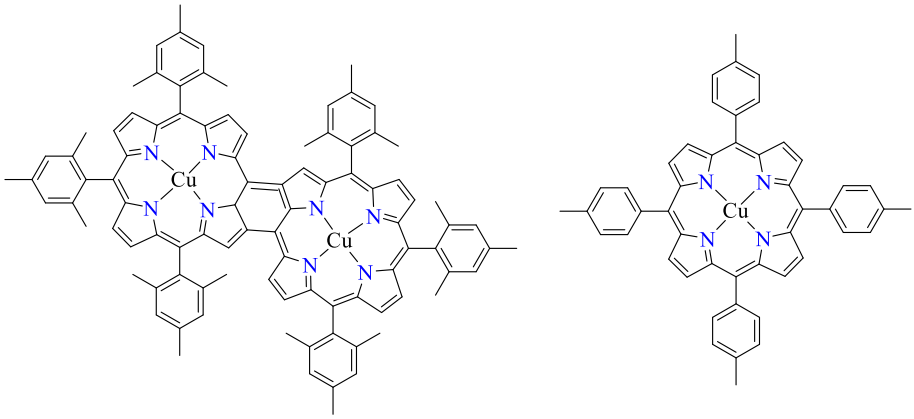

37 **38**

Figure 1.7. Molecular structures of a di-Cu complex (37) and a monometallic Cu-complex (38).

Although cofacial metalloporphyrins are not widely investigated for HER, it is one of the popular ligand systems for O_2 activation, CO_2 activation, and water oxidation.[91–95] The flexibility of changing metal-metal separation and the electronics in the ligand system makes it very

interesting to investigate any catalytic reaction. The presence of binuclear Ni and Fe centers in the hydrogenase active site inspired the investigation of molecular inorganic catalysts containing binuclear centers for HER, where an appropriate metal separation between two planes allows them to interact. Naruta's Pacman porphyrins (**Figure 1.8**) were studied for CO_2 reduction where they studied overpotential and kinetic parameter changes with secondary coordinated spheres.[91] They reported the synthesis of a few porphyrin dimers and their corresponding monomers; it was found that although the overpotential is unfavorable, the k_{cat} was significantly higher for the dimer compared to its monomer. (η = 1.06 V, k_{cat} = 2.36 × 10^8 s^{-1} for dimer whereas η = 0.75-0.85 V, k_{cat} = 871.4 s^{-1} for monomers). They also synthesized asymmetrical dimers (Fe_2TPFPP-TMP) where the two Fe atoms have quite different electronic environments. In contrast, the dimer mentioned above (Fe_2DTMP) is symmetrical with two Fe centers that have similar electronic environments. Surprisingly, the asymmetrical dimer showed favorable overpotentials compared to the symmetrical dimer and its corresponding monomer. (η = 0.71 V). These results increase interest in investigating asymmetrical cofacial systems for small molecule activation.

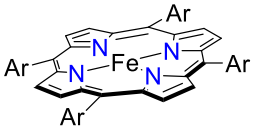

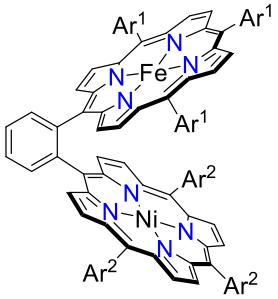

FeTPFPP, Ar = C_6F_5
$FeTF_2PP$, Ar = 2,6-$F_2C_6H_3$
$FeTCl_2PP$, Ar = 2,6-$Cl_2C_6H_3$
FeTPP, Ar = C_6H_5
FeTMP, Ar = 2,4,6-$Me_3C_6H_2$

Fe_2DTPFPP, Ar^1,Ar^2 = C_6F_5
Fe_2DTF_2PP, Ar^1,Ar^2 = 2,6-$F_2C_6H_3$
Fe_2DTCl_2PP, Ar^1,Ar^2 = 2,6-$Cl_2C_6H_3$
Fe_2DTPP, Ar^1,Ar^2 = C_6H_5
Fe_2DTMP, Ar^1,Ar^2 = 2,4,6-$Me_3C_6H_2$
Fe_2TPFPP-TMP, Ar^1 = 2,4,6-$Me_3C_6H_2$, Ar^2 = C_6F_5

Figure 1.8. Chemical structures of the six Fe porphyrin dimers and their corresponding monomers.

Recently, a bimetallic macrocycle featuring a relatively flexible arrangement of two cofacially linked Ni-porphyrins was synthesized by Apfel and coworkers as a catalyst for HER, which seems to achieve higher faradaic efficiency of up to 95% confirming the possibility of dinuclear cofacial systems for HER (**Figure 1.9**).[96] The report showed the dimer displayed the same photophysical and electrochemical properties as its corresponding monomer. Interestingly, the dimer showed faster kinetics with 49,421 ppm hydrogen generation after 5 h electrolysis and a turnover frequency of 1.4 $mmolg^{-1}h^{-1}$ whereas the monomer analogue displayed only 7,032 ppm H_2 with 0.64 $mmolg^{-1}h^{-1}$. They attributed this higher catalytic activity of the dimer to the electron-mediating function of the linker molecule which should enhance the intramolecular electron transfer within the macrocycle or the synergistic effects between the two nickel centers. These results highlight the necessity of cofacial macrocyclic arrangement for electrocatalytic HER.

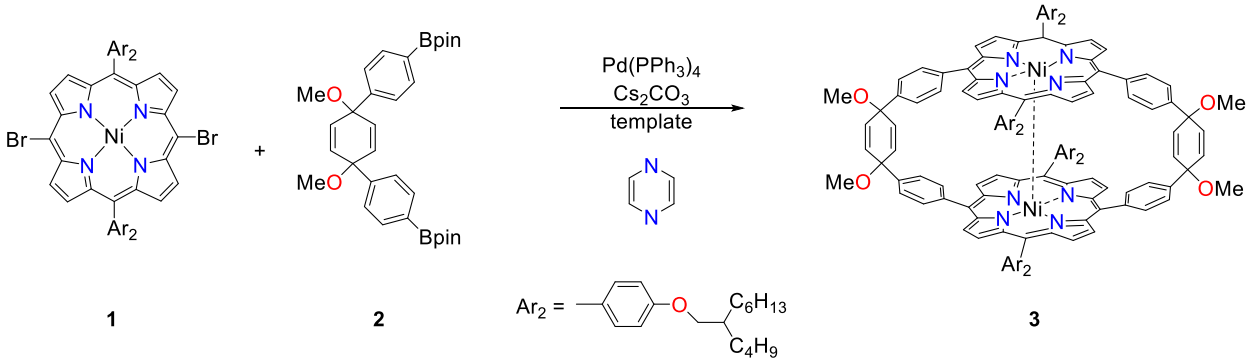

Figure 1.9. Synthesis of 3, Ni–Ni distance obtained by DFT (B3LYP/6-31G(d)).

1.3.3. Schiff-base systems

Aside from porphyrin porphyrin-containing complexes discussed above, other commonly used redox active non-innocent chelating ligands for catalytic activities are Schiff-base ligands in transition metal complexes. The term derived from the name of the German chemist Hugo Schiff in 1864 who described the product resulting from the reaction between primary amines with carbonyl compound for the first time, in 1864.[97] A Schiff-base can be considered as an analog of

an aldehyde or ketone where oxygen is substituted with a primary amine through condensation. The double bond between C and N is identified as an imine bond and is considered by many to be synonymous with azomethines.[98] Due to their simplicity of synthesis over porphyrins and phosphine systems which facilitate simple modification using a variety of functionalized amines such as aryl, alkyl, heteroaryl, or cycloalkyl, etc. as well as the ability to easily coordinate with various metals, they have captured scientific community's interest. Additionally, they are known to show similar catalytic activity as porphyrins.

One of the leading classes of Schiff-base ligands in homogeneous catalysis is salens or salophen systems which are derived from the condensation between salicylaldehyde and diamine. In addition to exhibiting structural diversity and selectivity in coordinating with various metals[99,100], these have a high tolerance against moisture due to their increased stability upon metal coordination.[101] The salen and salen-like Schiff base complexes are known to be catalytically active for a variety of organic synthesis such as alkene epoxidation, epoxide ring opening, cyclopropanations, aziridination, selective hydrogenations, carbonyl cyanosilylation, polymerization, and imine additions.[102–109] one of the promising homogenous Schiff-base-based catalyst is Jacobsen's catalysts (**Figure 1.10**), which features a Mn(III) metal coordination to chiral ligand system and reported as efficient catalysts for asymmetric epoxidation of cis-alkenes.[110] They noted that Schiff base systems are better at enantioselectivity than chiral porphyrin systems due to bearing chirotopic carbons in the vicinity of the metal which results in better stereochemical communication in the epoxidation step. Additionally, salen and salen-like systems have been studied for small molecule activation and reported as catalytically active for oxygen activation and reduction, hydrolysis and water splitting, hydrogenation and hydrogen evolution CO_2 activation and reduction, etc.[99,111–115]

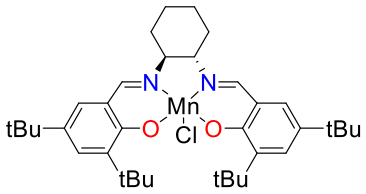

Figure 1.10. Structure of Jacobsen's catalyst.

Another class of ligands that is important in developing catalysts is Schiff base containing diazole and phenol rings due to its wide range of biological applications such as antifungal[116], antioxidant[117], antibacterial[118], antitumor[119], anti-inflammatory[120], and antipyretic.[121] More importantly, imidazole, an azole subsidiary that contains two nitrogen atoms, is the center substance in different natural products and biological frameworks including enzymes.[122–124] Imidazole-based Schiff base catalysts attract significant attention in small molecule activation due to their metal coordination capability which enables the imidazole to act as a secondary ligand to enhance the electron density at the metal center, as well as the basic nitrogen at the N3 position, facilitates the coordination with various transition metals such as Cu, Fe, Ni, and Pd[125], the ability to tune electronic properties by contributing to ligand field effect and facilitating π-electron delocalization between the imidazole and Schiff base framework[126], the ability to engage in hydrogen bonding interactions[127], the ability to act as a proton shuttle in catalytic cycles,[128] the capability to enhance radical stability and electron delocalization in catalytic oxidation and reduction processes.[129] However, to this date, very little attention has been paid to imidazole-based Schiff base systems as molecular catalysts, in terms of small molecule activation.

Another extensively studied Schiff base system is binuclear macrocyclic Co(II) calixpyrrole complexes (**Figure 1.11**).[130–132] The ligand system adopted a wedged “pacman”-like structure resembling cofacial diporphyrin complexes.[133–135] This ligand architecture was extensively studied by Love[136] and Sessler[137] separately and reported higher reaction yields than “pacman” porphyrins while retaining a similar binuclear structure. Moreover, these complexes

were found to be catalytically active for dioxygen reduction at similar potentials as cofacial porphyrins as well as a formation of superoxo intermediate as a minor species during catalysis leading lower selectivity towards the four-electron reduction of oxygen to water.[132] That phenomenon was attributed to faster electron transfer compared to proton transfer resulting in the generation of a peroxo intermediate emphasizing the importance of proton shuttling or faster proton transfer mechanisms like PCET.[132] Later studies of the Love group investigated the effect of changing bite angle and metal-metal distance which was revealed by substituting anthracenyl backbone instead of *o*-phenylenediamine spacer favors the formation of the desired superoxo complex over peroxo intermediate through reversible oxygen binding.[138] The authors reported that using stronger acids inhibits the catalyst, unlike porphyrin analogues, and they reasoned that usage of too strong acid might protonate the pyrrolide donors causing metal ion dissociation.[138]

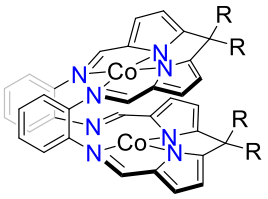

Figure 1.11. Structure of a bimetallic Co macrocyclic Schiff-base calixpyrrole complex.

The development of asymmetric catalysts can be considered a somewhat novel approach in molecular catalyst synthesis because they exhibit high catalytic activity, stereoselectivity, and broad substrate generality. Shibasaki and coworkers have focused on synthesizing heterobimetallic Lewis acid/Brønsted base bifunctional catalysts using chiral Schiff base ligands for catalyzing organic reactions.[139] They focused on constructing unique and flexible ligand environments around each meant center to achieve high catalytic activity resembling most enzyme active sites like cytochrome C oxidase. They have developed multiple bifunctional hereto-dinuclear and homodinuclear Schiff base catalysts for various asymmetric transformations. They have reported increased catalytic activity and selectivity due to the new metal combinations and unique

environments. Although this approach has not been tested with small molecule activation, it is expected to yield promising results due to the rapid expansion of the field.

1.4. Performance evaluation factors for electrocatalysts

Electrocatalytic hydrogen evolution is an uphill, energy-requiring reaction as reflected by positive Gibbs free energy value (ΔG). The reaction also needs to overcome a significant kinetic barrier for it to be a successful reaction. The role of catalysts is very crucial in that aspect as it supports lowering the kinetic barrier for the specific reaction, in this case, HER (**Figure 1.12a**). The evaluation of the catalytic performance for hydrogen evolution reaction can be done based on several key factors demonstrating the activity of the catalyst, catalyst stability, and catalyst efficiency (**Figure 1.12b**). The activity of the catalyst is characterized by overpotential, Tafel slope, and exchange current density depending on the catalyst's nature (**Figure 1.12b**). The stability of the catalyst is indicated by changes in overpotential or current over time (**Figure 1.12c**), while its efficiency is defined by the faradaic efficiency and turnover frequency parameters (**Figure 1.12.d**).[140]

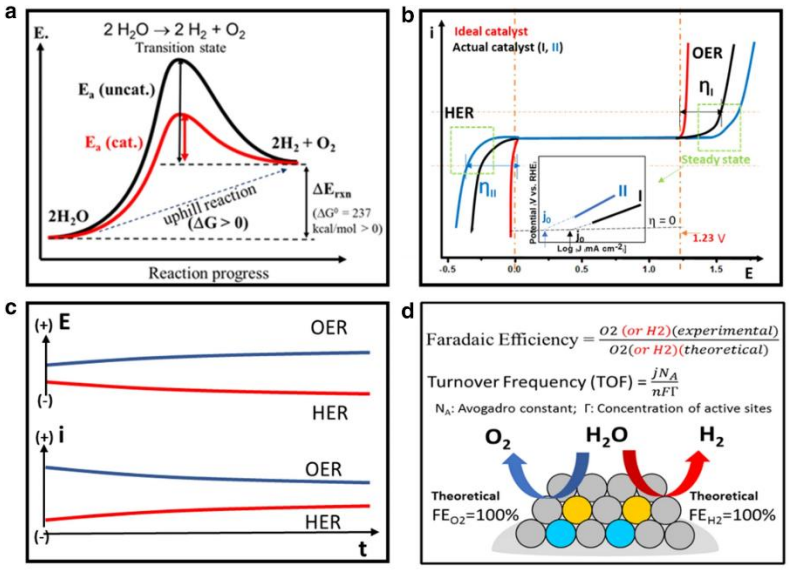

Figure 1.12. A Schematic illustration of the catalyst's role in lowering the activation energy barrier; b–d schematic illustrations of the performance evaluation parameters of electrocatalyst,

including, b activity in terms of overpotential, Tafel slope, and exchange current density, c stability in terms of current- and potential-time curves, and d efficiency in terms of faradaic efficiency and turnover frequency. Reproduced with permission from REF[140].

1.4.1. Evaluating the activity of the catalyst.

Overpotential (η) refers to the difference between the practical potential needed to be applied to the system to make it function and the standard potential of the redox couple of the H^+/H_2 under the operating conditions or the difference between the actual voltage needed for the reaction due to the higher kinetic barrier and thermodynamic potential (1.23 V).[141] The applied potential highly depends on the reaction conditions such as choice of solvent, proton source, acid concentration, and temperature and the standard potential of the H^+/H_2 couple strongly depends on both the solvent and the pK_a value of the proton source used.[142] This parameter is a very crucial descriptor in evaluating the activity of the electrocatalysts because it represents the energy requirement of the catalyst in other words the extra voltage requirement beyond the thermodynamic potential. A good electrocatalyst is a catalyst that can facilitate the reaction with minimal energy loss. Therefore, a lower η value for a targeted reaction means that it requires less additional energy to drive the reaction efficiently hence, considered a good catalyst.

Another important feature used to indicate the activity of the catalyst is the Tafel slope which is closely linked to the rate of HER specifically for heterogenous catalysts. The Tafel plot graphing the overpotential (η) as a function of log j which is the current density that is expressed by the equation: $\eta = a + b \log j$ results in two important kinetic parameters. One is the Tafel slope b which is related to the catalytic reaction mechanism in terms of electron transfer kinetics, and the other is the exchange current density j_o which can be extracted by obtaining the current at zero overpotential representing the intrinsic charge transfer under equilibrium conditions.[140] By definition, a smaller Tafel slope means faster reaction kinetics and vice versa. A higher exchange current density means a greater charge transfer rate and a lower reaction barrier therefore to be

identified as a better catalyst, a lower Tafel slope and higher exchange current density values are expected.

1.4.2. Evaluating the stability of the catalyst

Thermodynamic and kinetic stability is an important parameter to consider in evaluating the catalyst potential for use in real-world applications such as fuel cells. There are two main methods to evaluate the stability of an electrocatalyst. One is by chronoamperometry (I-t curve) or Chronopotentiometry (E-t curve) and the other method is cyclic voltammetry (CV). The first method evaluates the current variations with time under fixed potential (I-t curve) or the potential variation with time under fixed current (E-t curve). The longer the resulting current or potential remains constant, the catalyst is considered more stable and better. The CV method measures the current by cycling the potential through a potential range. Usually, this experiment requires more than 5000 cycles of run at a decided scan rate.[140] The steadier the current value is, the more cycles, the more stable the catalyst is. Both of those methods are very common methods to evaluate catalyst stability in homogenous catalysis. Linear sweep voltammetry (LSV) is another method that can be applied to both homogenous and heterogeneous systems but is more popular with solid catalyst systems. This method measures the overpotential shift before and after CV at a specific current density. The smaller the change of overpotential is, the better the catalyst's stability. [143]

1.4.3. Evaluating the efficiency of the catalyst.

Faradaic efficiency is a quantitative parameter obtained during bulk electrolysis experiments and defined as moles of H_2 quantified/mol of H_2 theoretical based on charge transferred through the cell × 100%.[144] The experimental value of hydrogen can be determined by analyzing the gas production from the cell using the gas displacement method, gas chromatography, or by using a hydrogen gas detector. This parameter quantifies the selectivity of the catalyst toward H_2 gas

production, values closer to 100% indicate the highly efficient catalyst meaning most of the charge is used to produce hydrogen gas.

Turnover frequency (TOF) is another useful parameter to evaluate the efficiency of the catalyst which describes the reaction rate in terms of the catalytic site. By definition, it indicates the amount of reactants that can be converted to the desired products (the number of electrons exchanged) per catalytic site of the redox-active compound in the solution per second.[140] Calculating TOF values precisely for homogenous systems is much easier compared to heterogenous systems due to the necessity of estimating a precise number of active sites per electrode area. Despite that fact, the TOF parameter is still considered a generous way to compare catalytic activity among different catalysts.

1.5. Sues group chemistry

Love and Sessler both independently developed macrocyclic Schiff base calixpyrrole systems[130–132,137,138,145,146] based on years of studies on cofacial "pacman" porphyrins.[147–150] Interestingly, compared to porphyrins, Schiff base synthesis is much more straightforward and simpler while displaying similar catalytic reactivities. Moreover, similar to "pacman" porphyrins, macrocycles are also known to adopt cofacial geometries. As discussed above, the promising catalytic activity of Naruta's Pacman asymmetric porphyrins and Shibasaki's unsymmetric calixpyrroles catalysts for organic reaction catalysis inspired the creation of multiple coordination sites and synthesizing bimetallic complexes. Their modification of the secondary coordination sphere favors catalytic activities, and some of the modifications even favored the formation of heterobimetallic structures. Furthermore, the Love group macrocycle system was shown to be catalytically active towards small molecules. Given the promising results generated by Naruta's group, shibasaki's group, and Love's group, the Sues group has decided to apply a similar approach

to synthesize unsymmetric complexes. That is, targeting a system like the Love group macrocycle where the complex adopts a cofacial arrangement with two chemically distinct coordination spheres.

1.6. Thesis goals

The goal of this thesis is the development and characterization of novel unsymmetric Schiff base complexes for use as small molecule activation electrocatalysts. The synthesis and characterization of salixpyrrole and imixpyrrole complexes are discussed, as well as their electrochemical properties and electrochemical activity towards hydrogen evaluation are evaluated. Additionally, the factors affecting catalytic activity such as metal type and number of metals, acid strength, etc. are discussed. Mechanisms are tested by electrochemical methods.

Chapter 2 discusses the development of novel monometallic and bimetallic unsymmetric cofacial palladium complexes supported by ligands featuring calixpyrrole and salen coordination motifs, characterization of those complexes, and preliminary catalytic activity towards hydrogen evolution reaction. The results of this work were published in the *Inorganic Chemistry* Journal of the American Chemical Society.[49] Both complexes were isolated in a good yield and coordinated with palladium to obtain mono-and bimetallic complexes. The electrocatalytic activity was evaluated using *para*-toluenesulfonic acid monohydrate as the proton source, which revealed the catalytic activity of both complexes towards HER and the generation of homogenous catalysts. The catalytic activity of two complexes towards HER was compared to each other to study the effect of several metals in the unsymmetric cofacial system for catalytic activity.

Chapter 3 focuses on devoloping unsymmetric cofacial palladium complexes supported by ligands featuring calixpyrrole and imadzole coordination motifs. The characterization of those complexes, and the tunability of the complex in the presence of different proton sources towards

hydrogen evolution reaction were discussed. The complexes were isolated in a good yield and coordinated with palladium to obtain monometallic complex. The electrocatalytic activity was evaluated using anilinium.BF_4, Imidazolium.BF_4, and triethylammonium.BF_4, which revealed the catalytic activity of imixpyrrole complexes towards HER in the presence of all three acids and the mechanistic differences. The catalytic activity of the complex in the presence of each acid towards HER was compared to each other to study the profound impact of external conditions on the unsymmetric cofacial system for catalytic activity.

Building on this farmwork, Chapter 4 explores a novel synthetic strategy for constructing heterobimetallic Schiff-base complexes. Through a stepwise metalation approach, incorporation of various transition metal ions into the secondary coordination sphere of the imixpyrrole system was studied. Electrochemical characterization was carried out to understand the redox features of the synthesized complexes. Although crystallographic characterization remains elusive due to challenges in crystalizing charged multimetallic complexes, spectroscopic and analytical evidence was used to confirm the formation of the expected complexes.

Chapter 5 postulated future opportunities with these unique ligand architectures. Specifically, different ways to modify the ligand scaffold to become more accessible by shifting to more positive potentials. This may be achieved by changing metel-metal separation of the cofacial system, introducing different hetero atoms, and incorperating cataions into the ligand scaffold are a few suggestions that are being discussed.

1.7. References

(1) Nocera, D. G. On the Future of Global Energy. *Daedalus* **2006**, *135* (4), 112–115. https://doi.org/10.1162/daed.2006.135.4.112.

(2) Lewis, N. S.; Nocera, D. G. Powering the Planet: Chemical Challenges in Solar Energy Utilization. *Proceedings of the National Academy of Sciences* **2006**, *103* (43), 15729–15735. https://doi.org/10.1073/pnas.0603395103.

(3) Eisenberg, R.; Nocera, D. G. Preface: Overview of the Forum on Solar and Renewable Energy. *Inorg. Chem.* **2005**, *44* (20), 6799–6801. https://doi.org/10.1021/ic058006i.

(4) Hoffert, M. I.; Caldeira, K.; Jain, A. K.; Haites, E. F.; Harvey, L. D. D.; Potter, S. D.; Schlesinger, M. E.; Schneider, S. H.; Watts, R. G.; Wigley, T. M. L.; Wuebbles, D. J. Energy Implications of Future Stabilization of Atmospheric CO2 Content. *Nature* **1998**, *395* (6705), 881–884. https://doi.org/10.1038/27638.

(5) *Energy and Transportation: Challenges for the Chemical Sciences in the 21st Century*; National Academies Press: Washington, D.C., 2003. https://doi.org/10.17226/10814.

(6) United Nations Department of Economic and Social Affairs. *Energy Statistics Pocketbook 2025*; Energy Statistics Pocketbook; United Nations, 2025. https://doi.org/10.18356/9789211069280.

(7) Petit, J. R.; Jouzel, J.; Raynaud, D.; Barkov, N. I.; Barnola, J.-M.; Basile, I.; Bender, M.; Chappellaz, J.; Davis, M.; Delaygue, G.; Delmotte, M.; Kotlyakov, V. M.; Legrand, M.; Lipenkov, V. Y.; Lorius, C.; PÉpin, L.; Ritz, C.; Saltzman, E.; Stievenard, M. Climate and Atmospheric History of the Past 420,000 Years from the Vostok Ice Core, Antarctica. *Nature* **1999**, *399* (6735), 429–436. https://doi.org/10.1038/20859.

(8) *Stable Carbon Cycle–Climate Relationship During the Late Pleistocene*. https://doi.org/10.1126/science.1120130.

(9) *Basic Research Needs to Assure a Secure Energy Future. A Report from the Basic Energy Sciences Advisory Committee*; Oak Ridge National Lab. (ORNL), Oak Ridge, TN (United States), 2003. https://doi.org/10.2172/811872.

(10) Karas, T. H. Energy and National Security.

(11) File.Pdf. https://www.bis.doc.gov/index.php/documents/section-232-investigations/87-the-effect-of-imports-of-crude-oil-on-national-security-1999/file (accessed 2025-03-03).

(12) Alšauskas, O. World Energy Outlook 2024.

(13) *Sustainable Hydrogen Production | Science*. https://www.science.org/doi/10.1126/science.1103197 (accessed 2025-03-05).

(14) The Mysterious Island.Pdf. https://freeclassicebooks.com/2019%20New%20Free%20Classic%20ebooks/S-Z/Verne%20Jules/English/pdfs/The%20Mysterious%20Island.pdf (accessed 2025-03-05).

(15) *The Forever Fuel: The Story of Hydrogen. (1981).*

(16) Glazier, W. H. The Task of Medicine. *Sci Am* **1973**, *228* (4), 13–17. https://doi.org/10.1038/scientificamerican0473-13.

(17) Chaubey, R.; Sahu, S.; James, O. O.; Maity, S. A Review on Development of Industrial Processes and Emerging Techniques for Production of Hydrogen from Renewable and Sustainable Sources. *Renewable and Sustainable Energy Reviews* **2013**, *23* (C), 443–462.

(18) Vignais, P. M.; Billoud, B.; Meyer, J. Classification and Phylogeny of Hydrogenases. *FEMS Microbiol Rev* **2001**, *25* (4), 455–501. https://doi.org/10.1111/j.1574-6976.2001.tb00587.x.

(19) *Occurrence, Classification, and Biological Function of Hydrogenases: An Overview | Chemical Reviews*. https://pubs.acs.org/doi/10.1021/cr050196r (accessed 2025-03-05).
(20) Stephenson, M.; Stickland, L. H. Hydrogenase: A Bacterial Enzyme Activating Molecular Hydrogen: The Properties of the Enzyme. *Biochem J* **1931**, *25* (1), 205–214. https://doi.org/10.1042/bj0250205.
(21) Green, D. E.; Stickland, L. H. Studies on Reversible Dehydrogenase Systems. *Biochemical Journal* **1934**, *28* (3), 898–900. https://doi.org/10.1042/bj0280898.
(22) Wang, C.; Lai, Z.; Huang, G.; Pan, H.-J. Current State of [Fe]-Hydrogenase and Its Biomimetic Models. *Chemistry – A European Journal* **2022**, *28* (57), e202201499. https://doi.org/10.1002/chem.202201499.
(23) *From Enzymes to Functional Materials—Towards Activation of Small Molecules - Möller - 2018 - Chemistry – A European Journal - Wiley Online Library*. https://chemistry-europe.onlinelibrary.wiley.com/doi/10.1002/chem.201703451 (accessed 2025-03-05).
(24) Happe, R. P.; Roseboom, W.; Pierik, A. J.; Albracht, S. P. J.; Bagley, K. A. Biological Activition of Hydrogen. *Nature* **1997**, *385* (6612), 126–126. https://doi.org/10.1038/385126a0.
(25) *A low-spin iron with CN and CO as intrinsic ligands forms the core of the active site in [Fe]-hydrogenases - Pierik - 1998 - European Journal of Biochemistry - Wiley Online Library*. https://febs.onlinelibrary.wiley.com/doi/10.1046/j.1432-1327.1998.2580572.x (accessed 2025-03-05).
(26) Pandey, A. S.; Harris, T. V.; Giles, L. J.; Peters, J. W.; Szilagyi, R. K. Dithiomethylether as a Ligand in the Hydrogenase H-Cluster. *J. Am. Chem. Soc.* **2008**, *130* (13), 4533–4540. https://doi.org/10.1021/ja711187e.
(27) Fontecilla-Camps, J. C.; Volbeda, A.; Cavazza, C.; Nicolet, Y. Structure/Function Relationships of [NiFe]- and [FeFe]-Hydrogenases. *Chem. Rev.* **2007**, *107* (10), 4273–4303. https://doi.org/10.1021/cr050195z.
(28) Ogata, H.; Lubitz, W.; Higuchi, Y. Structure and Function of [NiFe] Hydrogenases. *The Journal of Biochemistry* **2016**, *160* (5), 251–258. https://doi.org/10.1093/jb/mvw048.
(29) Ogata, H.; Kellers, P.; Lubitz, W. The Crystal Structure of the [NiFe] Hydrogenase from the Photosynthetic Bacterium *Allochromatium Vinosum*: Characterization of the Oxidized Enzyme (Ni-A State). *Journal of Molecular Biology* **2010**, *402* (2), 428–444. https://doi.org/10.1016/j.jmb.2010.07.041.
(30) Matias, P. M.; Soares, C. M.; Saraiva, L. M.; Coelho, R.; Morais, J.; Le Gall, J.; Carrondo, M. A. [NiFe] Hydrogenase from Desulfovibrio Desulfuricans ATCC 27774: Gene Sequencing, Three-Dimensional Structure Determination and Refinement at 1.8 Å and Modelling Studies of Its Interaction with the Tetrahaem Cytochrome C3. *J. Biol. Inorg. Chem.* **2001**, *6* (1), 63–81. https://doi.org/10.1007/s007750000167.
(31) Lubitz, W.; Ogata, H.; Rüdiger, O.; Reijerse, E. Hydrogenases. *Chem. Rev.* **2014**, *114* (8), 4081–4148. https://doi.org/10.1021/cr4005814.
(32) *A general overview on hydrogenation catalytic systems - ScienceDirect*. https://www.sciencedirect.com/science/article/pii/B9780443156564000033#bib1 (accessed 2025-03-07).
(33) Bediako, D. K.; Solis, B. H.; Dogutan, D. K.; Roubelakis, M. M.; Maher, A. G.; Lee, C. H.; Chambers, M. B.; Hammes-Schiffer, S.; Nocera, D. G. Role of Pendant Proton Relays and Proton-Coupled Electron Transfer on the Hydrogen Evolution Reaction by Nickel Hangman

Porphyrins. *Proceedings of the National Academy of Sciences* **2014**, *111* (42), 15001–15006. https://doi.org/10.1073/pnas.1414908111.
(34) Stewart, M. P.; Ho, M.-H.; Wiese, S.; Lindstrom, M. L.; Thogerson, C. E.; Raugei, S.; Bullock, R. M.; Helm, M. L. High Catalytic Rates for Hydrogen Production Using Nickel Electrocatalysts with Seven-Membered Cyclic Diphosphine Ligands Containing One Pendant Amine. *J. Am. Chem. Soc.* **2013**, *135* (16), 6033–6046. https://doi.org/10.1021/ja400181a.
(35) Rauchfuss, T. B. Diiron Azadithiolates as Models for the [FeFe]-Hydrogenase Active Site and Paradigm for the Role of the Second Coordination Sphere. *Acc Chem Res* **2015**, *48* (7), 2107–2116. https://doi.org/10.1021/acs.accounts.5b00177.
(36) Helm, M. L.; Stewart, M. P.; Bullock, R. M.; DuBois, M. R.; DuBois, D. L. A Synthetic Nickel Electrocatalyst with a Turnover Frequency Above 100,000 S−1 for H2 Production. *Science* **2011**, *333* (6044), 863–866. https://doi.org/10.1126/science.1205864.
(37) *Combining the Benefits of Homogeneous and Heterogeneous Catalysis with Tunable Solvents and Nearcritical Water - PMC*. https://pmc.ncbi.nlm.nih.gov/articles/PMC6259171/ (accessed 2025-03-07).
(38) *Control of Selectivity in Homogeneous Catalysis through Noncovalent Interactions - Mahmudov - 2023 - Chemistry – A European Journal - Wiley Online Library*. https://chemistry-europe.onlinelibrary.wiley.com/doi/full/10.1002/chem.202203861 (accessed 2025-03-07).
(39) *Synthesis Strategies towards Tagged Homogeneous Catalysts To Improve Their Separation - Diekamp - 2023 - Angewandte Chemie International Edition - Wiley Online Library*. https://onlinelibrary.wiley.com/doi/10.1002/anie.202304223 (accessed 2025-03-07).
(40) Reihlen, H.; Gruhl, A.; V. Hessling, G. Über Den Photochemischen Und Oxydativen Abbau von Carbonylen. *Justus Liebigs Ann. Chem.* **1929**, *472* (1), 268–287. https://doi.org/10.1002/jlac.19294720113.
(41) Nicolet, Y.; Piras, C.; Legrand, P.; Hatchikian, C. E.; Fontecilla-Camps, J. C. Desulfovibrio Desulfuricans Iron Hydrogenase: The Structure Shows Unusual Coordination to an Active Site Fe Binuclear Center. *Structure* **1999**, *7* (1), 13–23. https://doi.org/10.1016/s0969-2126(99)80005-7.
(42) Peters, J. W.; Lanzilotta, W. N.; Lemon, B. J.; Seefeldt, L. C. X-Ray Crystal Structure of the Fe-Only Hydrogenase (CpI) from Clostridium Pasteurianum to 1.8 Angstrom Resolution. *Science* **1998**, *282* (5395), 1853–1858. https://doi.org/10.1126/science.282.5395.1853.
(43) Capon, J.-F.; Gloaguen, F.; Pétillon, F. Y.; Schollhammer, P.; Talarmin, J. Organometallic Diiron Complex Chemistry Related to the [2Fe]H Subsite of [FeFe]H2ase. *European Journal of Inorganic Chemistry* **2008**, *2008* (30), 4671–4681. https://doi.org/10.1002/ejic.200800717.
(44) Gloaguen, F.; Lawrence, J. D.; Schmidt, M.; Wilson, S. R.; Rauchfuss, T. B. Synthetic and Structural Studies on [Fe2(SR)2(CN)x(CO)6-x]x- as Active Site Models for Fe-Only Hydrogenases. *J. Am. Chem. Soc.* **2001**, *123* (50), 12518–12527. https://doi.org/10.1021/ja016071v.
(45) Lyon, E. J.; Georgakaki, I. P.; Reibenspies, J. H.; Darensbourg, M. Y. Carbon Monoxide and Cyanide Ligands in a Classical Organometallic Complex Model for Fe-Only Hydrogenase. *Angew Chem Int Ed Engl* **1999**, *38* (21), 3178–3180.
(46) Capon, J.-F.; Gloaguen, F.; Pétillon, F. Y.; Schollhammer, P.; Talarmin, J. Electron and Proton Transfers at Diiron Dithiolate Sites Relevant to the Catalysis of Proton Reduction by

the [FeFe]-Hydrogenases. *Coordination Chemistry Reviews* **2009**, *253* (9), 1476–1494. https://doi.org/10.1016/j.ccr.2008.10.020.
(47) Beyene, B. B.; Das, K.; Kerayu, B. A.; Datta, A.; Hung, C.-H. Electrocatalytic H2 Evolution of a Schiff-Base Assisted Cu(II) Derivative as Catalyst on Homogeneous and Heterogeneous Phase. *Catalysis Communications* **2019**, *119*, 111–114. https://doi.org/10.1016/j.catcom.2018.10.027.
(48) *Electrocatalytic Hydrogen Evolution using a Nickel-based Calixpyrrole Complex: Controlling the Secondary Coordination Sphere on an Electrode Surface - Trowbridge - 2023 - Chemistry – A European Journal - Wiley Online Library*. https://chemistry-europe.onlinelibrary.wiley.com/doi/full/10.1002/chem.202301920 (accessed 2025-03-08).
(49) Somachandra, M. S.; Averkiev, B.; Sues, P. E. Unsymmetric Co-Facial "Salixpyrrole" Hydrogen Evolution Catalysts: Two Metals Are Better than One. *Inorg. Chem.* **2024**, *63* (29), 13346–13357. https://doi.org/10.1021/acs.inorgchem.4c01101.
(50) Tanase, T.; Nakamae, K.; Miyano, H.; Fujisawa, Y.; Ura, Y.; Nakajima, T. Electrochemical Hydrogen Formation Catalysed by a Pd8 String. *Chem. Commun.* **2021**, *57* (85), 11264–11267. https://doi.org/10.1039/D1CC04788D.
(51) Ologunagba, D.; Kattel, S. Pt- and Pd-Modified Transition Metal Nitride Catalysts for the Hydrogen Evolution Reaction. *Phys. Chem. Chem. Phys.* **2022**, *24* (20), 12149–12157. https://doi.org/10.1039/D2CP00792D.
(52) Hardy, M.; Lützen, A. Better Together: Functional Heterobimetallic Macrocyclic and Cage-like Assemblies. *Chemistry – A European Journal* **2020**, *26* (59), 13332–13346. https://doi.org/10.1002/chem.202001602.
(53) McKone, J. R.; Marinescu, S. C.; Brunschwig, B. S.; Winkler, J. R.; Gray, H. B. Earth-Abundant Hydrogen Evolution Electrocatalysts. *Chem. Sci.* **2014**, *5* (3), 865–878. https://doi.org/10.1039/C3SC51711J.
(54) Apfel, U.; Pétillon, F. Y.; Schollhammer, P.; Talarmin, J.; Weigand, W. [FeFe] Hydrogenase Models: An Overview. In *Bioinspired Catalysis*; Weigand, W., Schollhammer, P., Eds.; Wiley, 2014; pp 79–104. https://doi.org/10.1002/9783527664160.ch4.
(55) Chambers, G. M.; Huynh, M. T.; Li, Y.; Hammes-Schiffer, S.; Rauchfuss, T. B.; Reijerse, E.; Lubitz, W. Models of the Ni-L and Ni-SI_a States of the [NiFe]-Hydrogenase Active Site. *Inorg. Chem.* **2016**, *55* (2), 419–431. https://doi.org/10.1021/acs.inorgchem.5b01662.
(56) Dawson, J.; Perotto, C.; McMaster, J.; Schröder, M. [NiFe] Hydrogenases. In *Bioinspired Catalysis*; John Wiley & Sons, Ltd, 2014; pp 49–78. https://doi.org/10.1002/9783527664160.ch3.
(57) *An iron-iron hydrogenase mimic with appended electron reservoir for efficient proton reduction in aqueous media*. https://doi.org/10.1126/sciadv.1501014.
(58) Esmieu, C.; Berggren, G. Characterization of a Monocyanide Model of FeFe Hydrogenases – Highlighting the Importance of the Bridgehead Nitrogen for Catalysis. *Dalton Trans.* **2016**, *45* (48), 19242–19248. https://doi.org/10.1039/C6DT02061E.
(59) Erdem, Ö. F.; Stein, M.; Kaur-Ghumaan, S.; Reijerse, E. J.; Ott, S.; Lubitz, W. Effect of Cyanide Ligands on the Electronic Structure of [FeFe] Hydrogenase Active-Site Model Complexes with an Azadithiolate Cofactor. *Chemistry – A European Journal* **2013**, *19* (43), 14566–14572. https://doi.org/10.1002/chem.201302467.
(60) Vincent, K. A.; Parkin, A.; Armstrong, F. A. Investigating and Exploiting the Electrocatalytic Properties of Hydrogenases. *Chem. Rev.* **2007**, *107* (10), 4366–4413. https://doi.org/10.1021/cr050191u.

(61) van der Vlugt, J. I.; Reek, J. N. H. Neutral Tridentate PNP Ligands and Their Hybrid Analogues: Versatile Non-Innocent Scaffolds for Homogeneous Catalysis. *Angew Chem Int Ed Engl* **2009**, *48* (47), 8832–8846. https://doi.org/10.1002/anie.200903193.
(62) Grützmacher, H. Cooperating Ligands in Catalysis. *Angewandte Chemie International Edition* **2008**, *47* (10), 1814–1818. https://doi.org/10.1002/anie.200704654.
(63) Muckerman, J. T.; Fujita, E. Theoretical Studies of the Mechanism of Catalytic Hydrogen Production by a Cobaloxime. *Chem. Commun.* **2011**, *47* (46), 12456–12458. https://doi.org/10.1039/C1CC15330G.
(64) Jurss, J. W.; Khnayzer, R. S.; Panetier, J. A.; Roz, K. A. E.; Nichols, E. M.; Head-Gordon, M.; Long, J. R.; Castellano, F. N.; Chang, C. J. Bioinspired Design of Redox-Active Ligands for Multielectron Catalysis: Effects of Positioning Pyrazine Reservoirs on Cobalt for Electro- and Photocatalytic Generation of Hydrogen from Water. *Chem. Sci.* **2015**, *6* (8), 4954–4972. https://doi.org/10.1039/C5SC01414J.
(65) Lyaskovskyy, V.; de Bruin, B. Redox Non-Innocent Ligands: Versatile New Tools to Control Catalytic Reactions. *ACS Catal.* **2012**, *2* (2), 270–279. https://doi.org/10.1021/cs200660v.
(66) Luca, O. R.; Crabtree, R. H. Redox-Active Ligands in Catalysis. *Chem. Soc. Rev.* **2013**, *42* (4), 1440–1459. https://doi.org/10.1039/C2CS35228A.
(67) Liao, M.-S.; Scheiner, S. Comparative Study of Metal-Porphyrins, -Porphyrazines, and -Phthalocyanines. *Journal of Computational Chemistry* **2002**, *23* (15), 1391–1403. https://doi.org/10.1002/jcc.10142.
(68) Qi, Z.-L.; Cheng, Y.-H.; Xu, Z.; Chen, M.-L. Recent Advances in Porphyrin-Based Materials for Metal Ions Detection. *International Journal of Molecular Sciences* **2020**, *21* (16), 5839. https://doi.org/10.3390/ijms21165839.
(69) *Solvent and substituent effects on the redox reactions of para-substituted tetraphenylporphyrin | Journal of the American Chemical Society*. https://pubs.acs.org/doi/10.1021/ja00427a046?src=getftr&utm_source=sciencedirect_contenthosting&getft_integrator=sciencedirect_contenthosting (accessed 2025-03-09).
(70) *A study of solvent and substituent effects on the redox potentials and electron-transfer rate constants of substituted iron meso-tetraphenylporphyrins | Journal of the American Chemical Society*. https://pubs.acs.org/doi/10.1021/ja00442a013?src=getftr&utm_source=sciencedirect_contenthosting&getft_integrator=sciencedirect_contenthosting (accessed 2025-03-09).
(71) Lexa, D.; Momenteau, M.; Mispelter, J.; Lhoste, J. M. Electrochemical Study of the Effect of Axial Coordination upon the Redox Behavior of Iron Porphyrins in Dimethylformamide. *Bioelectrochemistry and Bioenergetics* **1974**, *1* (1–2), 108–117. https://doi.org/10.1016/0302-4598(74)85012-9.
(72) Brown, G. M.; Hopf, F. R.; Meyer, T. J.; Whitten, D. G. Effect of Extraplanar Ligands on the Redox Properties and the Site of Oxidation in Iron, Ruthenium, and Osmium Porphyrin Complexes. *J. Am. Chem. Soc.* **1975**, *97* (19), 5385–5390. https://doi.org/10.1021/ja00852a011.
(73) Caughey, W. S.; Corwin, A. H. The Stability of Metalloetioporphyrins toward Acids1. *J. Am. Chem. Soc.* **1955**, *77* (6), 1509–1513. https://doi.org/10.1021/ja01611a034.
(74) Lavallee, D. K. Complexation and Demetalation Reactions of Porphyrins. *Comments on Inorganic Chemistry* **1986**, *5* (3), 155–174. https://doi.org/10.1080/02603598608072281.
(75) *Porphyrin-catalyzed electrochemical hydrogen evolution reaction. Metal-centered and ligand-centered mechanisms - ScienceDirect*.

https://www.sciencedirect.com/science/article/pii/S001085452200025X#b0130 (accessed 2025-03-09).
(76) Lei, H.; Wang, Y.; Zhang, Q.; Cao, R. First-Row Transition Metal Porphyrins for Electrocatalytic Hydrogen Evolution — a SPP/JPP Young Investigator Award Paper. *J. Porphyrins Phthalocyanines* **2020**, *24* (11n12), 1361–1371. https://doi.org/10.1142/S1088424620500157.
(77) *Energy-Related Small Molecule Activation Reactions: Oxygen Reduction and Hydrogen and Oxygen Evolution Reactions Catalyzed by Porphyrin- and Corrole-Based Systems | Chemical Reviews*. https://pubs.acs.org/doi/10.1021/acs.chemrev.6b00299 (accessed 2025-03-10).
(78) *Metalloporphyrins as Catalytic Models for Studying Hydrogen and Oxygen Evolution and Oxygen Reduction Reactions | Accounts of Chemical Research*. https://pubs.acs.org/doi/10.1021/acs.accounts.1c00753 (accessed 2025-03-10).
(79) Kellett, R. M.; Spiro, T. G. Cobalt(I) Porphyrin Catalysts of Hydrogen Production from Water. *Inorg. Chem.* **1985**, *24* (15), 2373–2377. https://doi.org/10.1021/ic00209a011.
(80) Lee, C. H.; Dogutan, D. K.; Nocera, D. G. Hydrogen Generation by Hangman Metalloporphyrins. *J. Am. Chem. Soc.* **2011**, *133* (23), 8775–8777. https://doi.org/10.1021/ja202136y.
(81) M. Roubelakis, M.; Kwabena Bediako, D.; K. Dogutan, D.; G. Nocera, D. Proton -Coupled Electron Transfer Kinetics for the Hydrogen Evolution Reaction of Hangman Porphyrins. *Energy & Environmental Science* **2012**, *5* (7), 7737–7740. https://doi.org/10.1039/C2EE21123H.
(82) Solis, B. H.; Maher, A. G.; Honda, T.; Powers, D. C.; Nocera, D. G.; Hammes-Schiffer, S. Theoretical Analysis of Cobalt Hangman Porphyrins: Ligand Dearomatization and Mechanistic Implications for Hydrogen Evolution. *ACS Catal.* **2014**, *4* (12), 4516–4526. https://doi.org/10.1021/cs501454y.
(83) Bediako, D. K.; Solis, B. H.; Dogutan, D. K.; Roubelakis, M. M.; Maher, A. G.; Lee, C. H.; Chambers, M. B.; Hammes-Schiffer, S.; Nocera, D. G. Role of Pendant Proton Relays and Proton-Coupled Electron Transfer on the Hydrogen Evolution Reaction by Nickel Hangman Porphyrins. *Proceedings of the National Academy of Sciences* **2014**, *111* (42), 15001–15006. https://doi.org/10.1073/pnas.1414908111.
(84) Graham, D. J.; Nocera, D. G. Electrocatalytic H2 Evolution by Proton-Gated Hangman Iron Porphyrins. *Organometallics* **2014**, *33* (18), 4994–5001. https://doi.org/10.1021/om500300e.
(85) Margarit, C. G.; Asimow, N. G.; Gonzalez, M. I.; Nocera, D. G. Double Hangman Iron Porphyrin and the Effect of Electrostatic Nonbonding Interactions on Carbon Dioxide Reduction. *J Phys Chem Lett* **2020**, *11* (5), 1890–1895. https://doi.org/10.1021/acs.jpclett.9b03897.
(86) *Recent progress on metalloporphyrin-based hydrogen evolution catalysis - ScienceDirect*. https://www.sciencedirect.com/science/article/pii/S0010854519306472#b0480 (accessed 2025-03-10).
(87) Jr, R. M.; Dogutan, D. K.; Teets, T. S.; Suntivich, J.; Shao-Horn, Y.; Nocera, D. G. Oxygen Reduction Reactivity of Cobalt(II) Hangman Porphyrins. *Chem. Sci.* **2010**, *1* (3), 411–414. https://doi.org/10.1039/C0SC00281J.
(88) *Electrocatalytic Properties of Binuclear Cu(II) Fused Porphyrins for Hydrogen Evolution | ACS Catalysis*. https://pubs.acs.org/doi/10.1021/acscatal.8b01776 (accessed 2025-03-10).
(89) Costentin, C.; Savéant, J.-M. Towards an Intelligent Design of Molecular Electrocatalysts. *Nat Rev Chem* **2017**, *1* (11), 1–8. https://doi.org/10.1038/s41570-017-0087.

(90) Pegis, M. L.; McKeown, B. A.; Kumar, N.; Lang, K.; Wasylenko, D. J.; Zhang, X. P.; Raugei, S.; Mayer, J. M. Homogenous Electrocatalytic Oxygen Reduction Rates Correlate with Reaction Overpotential in Acidic Organic Solutions. *ACS Cent. Sci.* **2016**, *2* (11), 850–856. https://doi.org/10.1021/acscentsci.6b00261.
(91) *Bio-inspired cofacial Fe porphyrin dimers for efficient electrocatalytic CO2 to CO conversion: Overpotential tuning by substituents at the porphyrin rings | Scientific Reports*. https://www.nature.com/articles/srep24533 (accessed 2025-03-10).
(92) Kadish, K. M.; Frémond, L.; Burdet, F.; Barbe, J.-M.; Gros, C. P.; Guilard, R. Cobalt(IV) Corroles as Catalysts for the Electroreduction of O2: Reactions of Heterobimetallic Dyads Containing a Face-to-Face Linked Fe(III) or Mn(III) Porphyrin. *Journal of Inorganic Biochemistry* **2006**, *100* (4), 858–868. https://doi.org/10.1016/j.jinorgbio.2006.01.010.
(93) *Oxygen Evolution by Oxidation of Water with Manganese Porphyrin Dimers - Naruta - 1994 - Angewandte Chemie International Edition in English - Wiley Online Library*. https://onlinelibrary.wiley.com/doi/abs/10.1002/anie.199418391 (accessed 2025-03-10).
(94) *Characterization of a Dinuclear MnV□O Complex and Its Efficient Evolution of O2 in the Presence of Water - Shimazaki - 2004 - Angewandte Chemie International Edition - Wiley Online Library*. https://onlinelibrary.wiley.com/doi/10.1002/anie.200352564 (accessed 2025-03-10).
(95) *Sci-Hub | Importance of Mn–Mn separation and their relative arrangement on the development of high catalase activity in manganese porphyrin dimer catalysts. J. Chem. Soc., Chem. Commun., (23), 2667–2668 | 10.1039/c39940002667*. https://sci-hub.se/10.1039/c39940002667 (accessed 2025-03-10).
(96) Jökel, J.; Schwer, F.; Von Delius, M.; Apfel, U.-P. A Dinuclear Porphyrin-Macrocycle as Efficient Catalyst for the Hydrogen Evolution Reaction. *Chem. Commun.* **2020**, *56* (91), 14179–14182. https://doi.org/10.1039/D0CC05229A.
(97) *Sci-Hub | Reports from the University Laboratory in Pisa: A new series of organic bases. Annalen Der Chemie und Pharmacie, 131(1), 118–119 | 10.1002/jlac.18641310113*. https://sci-hub.ru/10.1002/jlac.18641310113 (accessed 2025-03-13).
(98) Moss, G. P.; Smith, P. a. S.; Tavernier, D. Glossary of class names of organic compounds and reactivity intermediates based on structure (IUPAC Recommendations 1995). *Pure and Applied Chemistry* **1995**, *67* (8–9), 1307–1375. https://doi.org/10.1351/pac199567081307.
(99) Pessoa, J. C.; Correia, I. Salan vs. Salen Metal Complexes in Catalysis and Medicinal Applications: Virtues and Pitfalls. *Coordination Chemistry Reviews* **2019**, *388*, 227–247. https://doi.org/10.1016/j.ccr.2019.02.035.
(100) Boulechfar, C.; Ferkous, H.; Delimi, A.; Djedouani, A.; Kahlouche, A.; Boublia, A.; Darwish, A. S.; Lemaoui, T.; Verma, R.; Benguerba, Y. Schiff Bases and Their Metal Complexes: A Review on the History, Synthesis, and Applications. *Inorganic Chemistry Communications* **2023**, *150*, 110451. https://doi.org/10.1016/j.inoche.2023.110451.
(101) Baleizão, C.; Garcia, H. Chiral Salen Complexes: An Overview to Recoverable and Reusable Homogeneous and Heterogeneous Catalysts. *Chem Rev* **2006**, *106* (9), 3987–4043. https://doi.org/10.1021/cr050973n.
(102) Baleizão, C.; Garcia, H. Chiral Salen Complexes: An Overview to Recoverable and Reusable Homogeneous and Heterogeneous Catalysts. *Chem. Rev.* **2006**, *106* (9), 3987–4043. https://doi.org/10.1021/cr050973n.

(103) Gogoi, A.; Dewan, A.; Borah, G.; Bora, U. A Palladium Salen Complex: An Efficient Catalyst for the Sonogashira Reaction at Room Temperature. *New J. Chem.* **2015**, *39* (5), 3341–3344. https://doi.org/10.1039/C4NJ01822B.
(104) Dewan, A.; Bora, U.; Borah, G. A Simple and Efficient Tetradentate Schiff Base Derived Palladium Complex for Suzuki–Miyaura Reaction in Water. *Tetrahedron Letters* **2014**, *55* (10), 1689–1692. https://doi.org/10.1016/j.tetlet.2014.01.041.
(105) Duan, R.; Hu, C.; Li, X.; Pang, X.; Sun, Z.; Chen, X.; Wang, X. Air-Stable Salen–Iron Complexes: Stereoselective Catalysts for Lactide and ε-Caprolactone Polymerization through in Situ Initiation. *Macromolecules* **2017**, *50* (23), 9188–9195. https://doi.org/10.1021/acs.macromol.7b01766.
(106) Wang, Z.; Mu, Y. Chiral SalenCo(III) Complexes with Bulky Substituents as Catalysts for Stereoselective Alternating Copolymerization of Racemic Propylene Oxide with Carbon Dioxide and Succinic Anhydride. *Polym. Chem.* **2021**, *12* (12), 1776–1786. https://doi.org/10.1039/D0PY01562H.
(107) Praban, S.; Piromjitpong, P.; Balasanthiran, V.; Jayaraj, S.; Chisholm, M. H.; Tantirungrotechai, J.; Phomphrai, K. Highly Efficient Metal(III) Porphyrin and Salen Complexes for the Polymerization of Rac-Lactide under Ambient Conditions. *Dalton Trans.* **2019**, *48* (10), 3223–3230. https://doi.org/10.1039/C8DT04699A.
(108) Chen, X.-L.; Wang, B.; Pan, L.; Li, Y.-S. Homoleptic, Bis-Ligated Magnesium Complexes for Ring-Opening Polymerization of Lactide and Lactones: Synthesis, Structure, Polymerization Behavior and Mechanism Studies. *Applied Organometallic Chemistry* **2019**, *33* (3), e4770. https://doi.org/10.1002/aoc.4770.
(109) Borhade, S. R.; Waghmode, S. B. Phosphine-Free Pd–Salen Complexes as Efficient and Inexpensive Catalysts for Heck and Suzuki Reactions under Aerobic Conditions. *Tetrahedron Letters* **2008**, *49* (21), 3423–3429. https://doi.org/10.1016/j.tetlet.2008.03.109.
(110) Zhang, W.; Loebach, J. L.; Wilson, S. R.; Jacobsen, E. N. Enantioselective Epoxidation of Unfunctionalized Olefins Catalyzed by Salen Manganese Complexes. *J. Am. Chem. Soc.* **1990**, *112* (7), 2801–2803. https://doi.org/10.1021/ja00163a052.
(111) Bertini, S.; Coletti, A.; Floris, B.; Conte, V.; Galloni, P. Investigation of VO–Salophen Complexes Electronic Structure. *Journal of Inorganic Biochemistry* **2015**, *147*, 44–53. https://doi.org/10.1016/j.jinorgbio.2015.03.003.
(112) Hood, T. M.; Lau, S.; Diefenbach, M.; Firmstone, L.; Mahon, M.; Krewald, V.; Webster, R. L. The Complex Reactivity of [(Salen)Fe]2(μ-O) with HBpin and Its Implications in Catalysis. *ACS Catal.* **2023**, *13* (17), 11841–11850. https://doi.org/10.1021/acscatal.3c02898.
(113) Cozzolino, M.; Leo, V.; Tedesco, C.; Mazzeo, M.; Lamberti, M. Salen, Salan and Salalen Iron(III) Complexes as Catalysts for CO2/Epoxide Reactions and ROP of Cyclic Esters. *Dalton Trans.* **2018**, *47* (37), 13229–13238. https://doi.org/10.1039/C8DT03169J.
(114) Layek, S.; Anuradha; Agrahari, B.; Pathak, D. D. Synthesis and Characterization of a New Pd(II)-Schiff Base Complex [Pd(APD)2]: An Efficient and Recyclable Catalyst for Heck-Mizoroki and Suzuki-Miyaura Reactions. *Journal of Organometallic Chemistry* **2017**, *846*, 105–112. https://doi.org/10.1016/j.jorganchem.2017.05.049.
(115) Cabral, B. N.; Milani, J. L. S.; da Mata, Á. F. A.; Andrade, G. F. S.; da Silva, H. B.; das Chagas, R. P. Facile Synthesis of InIII-Salen Complexes from Indium Metal and Their Use as Catalysts for the Chemical Fixation of Carbon Dioxide in Mild Conditions. *Inorganic*

Chemistry Communications **2023**, *156*, 111315. https://doi.org/10.1016/j.inoche.2023.111315.
(116) Alisir, S. H.; Demir, S.; Sariboga, B.; Buyukgungor, O. A Disparate 3-D Silver(I) Coordination Polymer of Pyridine-3,5-Dicarboxylate and Pyrimidine with Strong Intermetallic Interactions: X-Ray Crystallography, Photoluminescence and Antimicrobial Activity. *Journal of Coordination Chemistry* **2015**, *68* (1), 155–168. https://doi.org/10.1080/00958972.2014.978307.
(117) Kargar, H.; Aghaei-Meybodi, F.; Behjatmanesh-Ardakani, R.; Elahifard, M. R.; Torabi, V.; Fallah-Mehrjardi, M.; Tahir, M. N.; Ashfaq, M.; Munawar, K. S. Synthesis, Crystal Structure, Theoretical Calculation, Spectroscopic and Antibacterial Activity Studies of Copper(II) Complexes Bearing Bidentate Schiff Base Ligands Derived from 4-Aminoantipyrine: Influence of Substitutions on Antibacterial Activity. *Journal of Molecular Structure* **2021**, *1230*, 129908. https://doi.org/10.1016/j.molstruc.2021.129908.
(118) Patra, M.; Gasser, G.; Metzler-Nolte, N. Small Organometallic Compounds as Antibacterial Agents. *Dalton Transactions* **2012**, *41* (21), 6350–6358. https://doi.org/10.1039/C2DT12460B.
(119) Haque, R. A.; Choo, S. Y.; Budagumpi, S.; Iqbal, M. A.; Al-Ashraf Abdullah, A. Silver(I) Complexes of Mono- and Bidentate *N*-Heterocyclic Carbene Ligands: Synthesis, Crystal Structures, and *in Vitro* Antibacterial and Anticancer Studies. *European Journal of Medicinal Chemistry* **2015**, *90*, 82–92. https://doi.org/10.1016/j.ejmech.2014.11.005.
(120) Henkin, R. I. Metal-Albumin-Amino Acid Interactions: Chemical and Physiological Interrelationships. In *Protein-Metal Interactions*; Friedman, M., Ed.; Advances in Experimental Medicine and Biology; Springer New York: Boston, MA, 1974; Vol. 48, pp 299–328. https://doi.org/10.1007/978-1-4684-0943-7_15.
(121) Murtaza, S.; Akhtar, M. S.; Kanwal, F.; Abbas, A.; Ashiq, S.; Shamim, S. Synthesis and Biological Evaluation of Schiff Bases of 4-Aminophenazone as an Anti-Inflammatory, Analgesic and Antipyretic Agent. *Journal of Saudi Chemical Society* **2017**, *21*, S359–S372. https://doi.org/10.1016/j.jscs.2014.04.003.
(122) Krishna, G. A.; Dhanya, T. M.; Shanty, A. A.; Raghu, K. G.; Mohanan, P. V. Transition Metal Complexes of Imidazole Derived Schiff Bases: Antioxidant/Anti-Inflammatory/Antimicrobial/Enzyme Inhibition and Cytotoxicity Properties. *Journal of Molecular Structure* **2023**, *1274*, 134384. https://doi.org/10.1016/j.molstruc.2022.134384.
(123) Shallal, M. A. H. A Literature Review on the Imidazole. *aijmsr* **2019**, *5* (1), 1–11. https://doi.org/10.46281/aijmsr.v5i1.231.
(124) Mandal, S.; Poria, D. K.; Seth, D. K.; Ray, P. S.; Gupta, P. Cyclometalated Rhodium and Iridium Complexes with Imidazole Containing Schiff Bases: Synthesis, Structure and Cellular Imaging. *Polyhedron* **2019**, *73*, 12–21. https://doi.org/10.1016/j.poly.2014.01.033.
(125) Bocian, A.; Skrodzki, M.; Kubicki, M.; Gorczyński, A.; Pawluć, P.; Patroniak, V. The Effect of Schiff Base Ligands on the Structure and Catalytic Activity of Cobalt Complexes in Hydrosilylation of Olefins. *Applied Catalysis A: General* **2020**, *602*, 117665. https://doi.org/10.1016/j.apcata.2020.117665.
(126) Barry, K.-L.; Grimmer, C. D.; Munro, O. Q.; Akerman, M. P. Self-Assembled Supramolecular Structures of *O* , *N* , *N ′* Tridentate Imidazole–Phenol Schiff Base Compounds. *RSC Adv.* **2020**, *10* (13), 7867–7878. https://doi.org/10.1039/C9RA10488G.
(127) Kang, N.; Fan, Y.; Li, D.; Jia, X.; Zhao, S. Preparation of Magnetic Nano-Catalyst Containing Schiff Base Unit and Its Application in the Chemical Fixation of CO2 into Cyclic

Carbonates. *Magnetochemistry* **2024**, *10* (5), 33. https://doi.org/10.3390/magnetochemistry10050033.
(128) McGinley, J.; McCann, M.; Ni, K.; Tallon, T.; Kavanagh, K.; Devereux, M.; Ma, X.; McKee, V. Imidazole Schiff Base Ligands: Synthesis, Coordination Complexes and Biological Activities. *Polyhedron* **2013**, *55*, 169–178. https://doi.org/10.1016/j.poly.2013.03.023.
(129) Slassi, S.; Fix-Tailler, A.; Larcher, G.; Amine, A.; El-Ghayoury, A. Imidazole and Azo-Based Schiff Bases Ligands as Highly Active Antifungal and Antioxidant Components. *Heteroatom Chemistry* **2019**, *2019* (1), 6862170. https://doi.org/10.1155/2019/6862170.
(130) Givaja, G.; Volpe, M.; Leeland, J. W.; Edwards, M. A.; Young, T. K.; Darby, S. B.; Reid, S. D.; Blake, A. J.; Wilson, C.; Wolowska, J.; McInnes, E. J. L.; Schröder, M.; Love, J. B. Design and Synthesis of Binucleating Macrocyclic Clefts Derived from Schiff-Base Calixpyrroles. *Chemistry – A European Journal* **2007**, *13* (13), 3707–3723. https://doi.org/10.1002/chem.200600989.
(131) Givaja, G.; Volpe, M.; Edwards, M. A.; Blake, A. J.; Wilson, C.; Schröder, M.; Love, J. B. Dioxygen Reduction at Dicobalt Complexes of a Schiff Base Calixpyrrole Ligand. *Angewandte Chemie International Edition* **2007**, *46* (4), 584–586. https://doi.org/10.1002/anie.200603201.
(132) - *CORE Reader*. https://core.ac.uk/reader/28962302?utm_source=linkout (accessed 2025-03-23).
(133) Fukuzumi, S.; Okamoto, K.; Gros, C. P.; Guilard, R. Mechanism of Four-Electron Reduction of Dioxygen to Water by Ferrocene Derivatives in the Presence of Perchloric Acid in Benzonitrile, Catalyzed by Cofacial Dicobalt Porphyrins. *J. Am. Chem. Soc.* **2004**, *126* (33), 10441–10449. https://doi.org/10.1021/ja048403c.
(134) Chang, C. J.; Deng, Y.; Shi, C.; Chang, C. K.; Anson, F. C.; Nocera, D. G. Electrocatalytic Four-Electron Reduction of Oxygen to Water by a Highly Flexible Cofacial Cobalt Bisporphyrin. *Chem. Commun.* **2000**, No. 15, 1355–1356. https://doi.org/10.1039/B001620I.
(135) Collman, J. P.; Wagenknecht, P. S.; Hutchison, J. E. Molecular Catalysts for Multielectron Redox Reactions of Small Molecules: The "Cofacial Metallodiporphyrin" Approach. *Angew. Chem. Int. Ed. Engl.* **1994**, *33* (15–16), 1537–1554. https://doi.org/10.1002/anie.199415371.
(136) Givaja, G.; Blake, A. J.; Wilson, C.; Schröder, M.; Love, J. B. Macrocyclic Diiminodipyrromethane Complexes: Structural Analogues of Pac-Man Porphyrins. *Chem. Commun.* **2003**, No. 19, 2508–2509. https://doi.org/10.1039/B308443D.
(137) Veauthier, J. M.; Tomat, E.; Lynch, V. M.; Sessler, J. L.; Mirsaidov, U.; Markert, J. T. Calix[4]Pyrrole Schiff Base Macrocycles: Novel Binucleating Ligands for Cu(I) and Cu(II). *Inorg. Chem.* **2005**, *44* (19), 6736–6743. https://doi.org/10.1021/ic050690d.
(138) Devoille, A. M. J.; Love, J. B. Double-Pillared Cobalt Pacman Complexes: Synthesis, Structures and Oxygen Reduction Catalysis. *Dalton Trans.* **2011**, *41* (1), 65–72. https://doi.org/10.1039/C1DT11424G.
(139) Shibasaki, M.; Matsunaga, S. Bifunctional Asymmetric Catalysis Based on Dinuclear Schiff Base Complexes. *J. Synth. Org. Chem. Jpn.* **2010**, *68* (11), 1142–1149. https://doi.org/10.5059/yukigoseikyokaishi.68.1142.
(140) Wang, S.; Lu, A.; Zhong, C.-J. Hydrogen Production from Water Electrolysis: Role of Catalysts. *Nano Convergence* **2021**, *8* (1), 4. https://doi.org/10.1186/s40580-021-00254-x.

(141) Niu, S.; Li, S.; Du, Y.; Han, X.; Xu, P. How to Reliably Report the Overpotential of an Electrocatalyst. *ACS Energy Lett.* **2020**, *5* (4), 1083–1087. https://doi.org/10.1021/acsenergylett.0c00321.
(142) Artero, V.; Chavarot-Kerlidou, M.; Fontecave, M. Splitting Water with Cobalt. *Angewandte Chemie International Edition* **2011**, *50* (32), 7238–7266. https://doi.org/10.1002/anie.201007987.
(143) Qadeer, M. A.; Zhang, X.; Farid, M. A.; Tanveer, M.; Yan, Y.; Du, S.; Huang, Z.-F.; Tahir, M.; Zou, J.-J. A Review on Fundamentals for Designing Hydrogen Evolution Electrocatalyst. *Journal of Power Sources* **2024**, *613*, 234856. https://doi.org/10.1016/j.jpowsour.2024.234856.
(144) Haddad, A. Z.; Cronin, S. P.; Mashuta, M. S.; Buchanan, R. M.; Grapperhaus, C. A. Metal-Assisted Ligand-Centered Electrocatalytic Hydrogen Evolution upon Reduction of a Bis(Thiosemicarbazonato)Cu(II) Complex. *Inorg. Chem.* **2017**, *56* (18), 11254–11265. https://doi.org/10.1021/acs.inorgchem.7b01608.
(145) Askarizadeh, E.; Yaghoob, S. B.; Boghaei, D. M.; Slawin, A. M. Z.; Love, J. B. Tailoring Dicobalt Pacman Complexes of Schiff-Base Calixpyrroles towards Dioxygen Reduction Catalysis. *Chem. Commun.* **2010**, *46* (5), 710–712. https://doi.org/10.1039/B923189G.
(146) Askarizadeh, E.; Devoille, A. M. J.; Boghaei, D. M.; Slawin, A. M. Z.; Love, Jason. B. Ligand Modifications for Tailoring the Binuclear Microenvironments in Schiff-Base Calixpyrrole Pacman Complexes. *Inorg. Chem.* **2009**, *48* (15), 7491–7500. https://doi.org/10.1021/ic900871g.
(147) Collman, J. P.; Bencosme, C. S.; Durand, R. R. Jr.; Kreh, R. P.; Anson, F. C. Mixed-Metal Face-to-Face Porphyrin Dimers. *J. Am. Chem. Soc.* **1983**, *105* (9), 2699–2703. https://doi.org/10.1021/ja00347a030.
(148) Le Mest, Y.; L'Her, M.; Hendricks, N. H.; Kim, K.; Collman, J. P. Electrochemical and Spectroscopic Properties of Dimeric Cofacial Porphyrins with Nonelectroactive Metal Centers. Delocalization Processes in the Porphyrin .Pi.-Cation-Radical Systems. *Inorg. Chem.* **1992**, *31* (5), 835–847. https://doi.org/10.1021/ic00031a028.
(149) Liu, Y.; Zhou, G.; Zhang, Z.; Lei, H.; Yao, Z.; Li, J.; Lin, J.; Cao, R. Significantly Improved Electrocatalytic Oxygen Reduction by an Asymmetrical Pacman Dinuclear Cobalt(II) Porphyrin–Porphyrin Dyad. *Chem. Sci.* **2019**, *11* (1), 87–96. https://doi.org/10.1039/C9SC05041H.
(150) *Pacman Compounds: From Energy Transfer to Cooperative Catalysis - Lang - 2017 - Chemistry – A European Journal - Wiley Online Library*. https://chemistry-europe.onlinelibrary.wiley.com/doi/10.1002/chem.201703675 (accessed 2025-03-26

Chapter 2 - Unsymmetric co-facial “Salixpyrrole” hydrogen evolution catalysis: two metals are better than one

Portions of this chapter appear in the following manuscript:

Somachandra, M. S.; Averkiev, B.; Sues, P. E. Unsymmetric Co-Facial “Salixpyrrole” Hydrogen Evolution Catalysts: Two Metals Are Better than One. *Inorg. Chem.* **2024**, *63* (29), 13346–13357. https://doi.org/10.1021/acs.inorgchem.4c01101.

2.1. Abstract

Developing ligand architectures that emulate enzyme active sites offers a promising strategy for creating efficient catalysts aimed at activating small molecules for sustainable energy applications. Essential design elements include chemically distinct binding pockets for multiple metal centers and a three-dimensional framework to control the spatial arrangement of catalytic sites. Based on these principles, this study presents mono- and bimetallic unsymmetric cofacial palladium complexes (2 and 3, respectively) supported by ligands featuring calixpyrrole and salen coordination motifs, referred to as "salixpyrrole" ligands. These complexes were synthesized via a straightforward Schiff-base reaction, yielding the desired products in appreciable amounts.

Both complexes (2 and 3) demonstrated activity as hydrogen evolution electrocatalysts, utilizing para-toluenesulfonic acid monohydrate as the proton source. Notably, the two salixpyrrole catalysts exhibited distinct mechanistic behaviors: complex 2 displayed a second-order dependence on acid concentration, while complex 3 followed a first-order dependence. Furthermore, the bimetallic catalyst (3) outperformed its monometallic counterpart (2), achieving significantly higher turnover frequencies (4640 s^{-1} compared to 1680 s^{-1} for 2) and operating at lower overpotentials (0.39 V versus 0.69 V for 2).

These findings establish proof-of-concept that bimetallic catalysts with chemically distinct coordination sites exhibit superior catalytic performance compared to their monometallic or symmetric counterparts, highlighting their potential for advancing sustainable energy solutions.

2.2. Introduction

The development of a secure, clean, and renewable energy source has become a significant technological challenge shaping our global future. Technologies based on the reduction and oxidation of abundant small molecules play an important role in this matter because those technologies can be categorized as clean energy sources. Fuel cells are a promising technology for use as a source of heat and electricity, and hydrogen fuel cells have attracted increasing attention as a potential alternative to carboniferous fossil fuels. Effective hydrogen production from water/proton sources by using a catalyst composed of transition metals plays a vital role in this process. Therefore, researchers have been paying much attention towards designing catalysts for H_2 evolution either in organic solvents in the presence of a proton source or aqueous solutions.[2–4]

Biological systems, on the other hand, use metal clusters, redox-active ligands, and amino acids as enzymes to break down challenging catalytic transformations into sequences of elementary steps to avoid high activation energy barriers. In nature, the hydrogenase enzymes ([Fe], [FeFe], and [NiFe]) use transition metals to catalyze HER and this is achieved through the construction of uniquely shaped microenvironments in enzyme active sites with amino acid side chains and/or cofactors that carefully control the positioning of catalytically active metal centers.[5–7] Moreover, another common theme in natural systems is the use of multiple metal centers in chemically distinct binding sites to facilitate multielectron transfer processes. (**Figure 2.1**).[5–7] Although these enzymes are very capable of catalyzing small molecule activation, their translation to industrial applications has proven difficult.

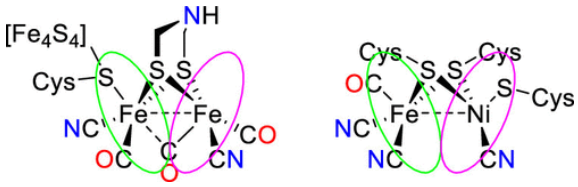

Figure 2.1. Structures of the [FeFe]-hydrogenase (left) and [NiFe]-hydrogenase active sites with the different metal binding sites highlighted. Reproduced with the permission from REF[7].

The chemistry of enzyme active sites has inspired a lot of structural and fundamental synthetic mimics to probe bioinspired multi-electron transfer processes and spectroscopic properties. Rauchfuss *et al*. have created a diiron catalyst to mimic the active site of [FeFe]-Hydrogenase enzyme[8] and Bullock *et al.* have created a series of monometallic nickel diphosphacycloheptane complexes to mimic the natural hydrogenases (**Figure 2.2**).[2,9–11] Most of these complexes exhibit exceptional catalytic activity for H_2 evolution and oxidation. While some of these complexes achieve turnover frequencies of approximately 100,000 s^{-1}, their catalytic performance is hindered by overpotentials of 625 mV. In contrast, some natural hydrogenases are believed to operate with an overpotential <100 mV.[9]

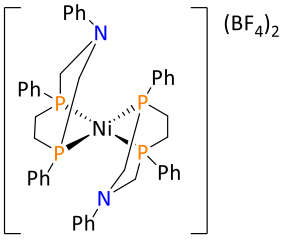

Figure 2.2. General structure of the nickel diphosphacycloheptane complex.

Another synthetic route to design bi- and multimetallic complexes for small molecule activation are cofacial or Pacman diporphyrin complexes, because of the known characteristics of metalloporphyrins in nature for light harvesting, energy conversion, multi-electron transfer, O_2 activation, and peroxide degradation (**Figure 2.3**, left). The synthetic mimics are known to have

exceptional control over the intrametallic separation as well as a well-known coordinative environment of the porphyrin,[12–15], which makes metalloporphyrin competent candidates for HER, OER, and ORR catalysis. Some of these complexes are also known to show fascinating stoichiometric and catalytic small molecule chemistry, like hydrogen activation, OER, and ORR.[16–20] Although initial "Pacman" porphyrin ligands contained two identical binding pockets for metals, a novel approach to better mimic enzyme active sites involves designing a ligand system with a chemically distinct coordination environment.[21–26] However, the synthesis of "Pacman" diporphyrin complexes is significantly difficult and complicated, and known to produce poor yields. These synthetic challenges have slowed the research progress in sustainable energy technologies and represent a significant barrier to further implementation of these exquisite ligand systems.

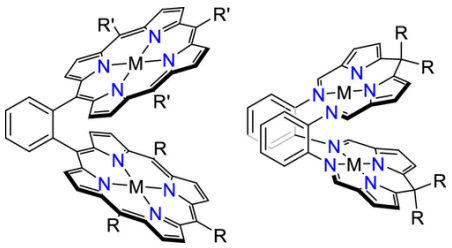

Figure 2.3. General structures of bimetallic cofacial porphyrin (left) and calixpyrrole (right) "pacman" complexes.

Cofacial calixpyrroles are a similar class of ligands developed by Love, Sessler, and their co-workers that can be readily prepared in three high-yielding steps from pyrroles (**Figure 2.3**, right). These ligand systems are known to show similar characteristics to pacman diporphyrin complexes upon metal complexation.[27–36] The structural similarities have drawn the attention of the small molecule activation chemical industry to explore these ligands as building blocks for

more complex ligand architecture. For example, dicobalt complexes of Schiff base calixpyrroles were found to participate in oxygen reduction.[37–40]

Still, platinum (Pt) and Pt-based compounds are considered the best choice among the other electrocatalysts for HER, because of their outstanding activity and high current density. According to the Sabatier principle, to be an ideal HER catalyst, it should have optimum hydrogen adsorption and desorption energies.[41–43] A volcano plot representing calculated hydrogen adsorption energies on different metal surfaces by Nørskov *et al.*[41] relative to exchange current densities indicates the peak position at zero, where Pt is the closest among other metals, and the next closest being Pd (**Figure 2.4**). A large amount of work has gone into the development of non-Pt-based catalysts due to Pt being expensive and scarcity to overcome limitations like low durability and less CO poisoning. Since Pd is one of the Pt group metals with high adsorption energy immediately after Pt, as well as due to the generation of diamagnetic complexes, which would aid with spectroscopic characterization, the usability of Pd as a substitute for Pt has been widely investigated.[44–46]

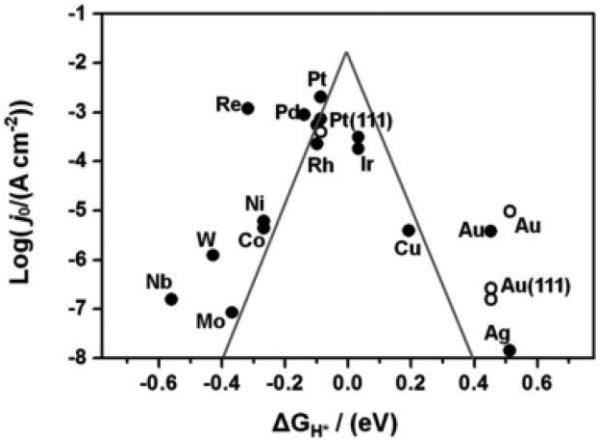

Figure 2.4. Volcano plot of exchange current density (j_0) as a function of the DFT-calculated Gibb's free energy (ΔG_{H^*}) of the adsorbed atomic hydrogen on a pure metal. Reproduced with the permission from REF[43].

In this work, we report on the synthesis of unsymmetric co-facial "Salixpyrrole" and its catalytic activity towards HER. These species are expected to be like co-facial porphyrins with

chemically distinct environments but more flexible and easier synthesis. Recently, our group reported the synthesis of a palladium calixpyrrole complex with pendant amines and its catalytic activity for the HER,[47] which provides a great opportunity to modify the ligand system to have a unique chemically distinguished environment compared to its first coordination sphere. At the same time, this novel synthesis route provides an interesting pathway to synthesize heterobimetallic complexes with targeted chemical environments. Herein, we outline the synthesis of "salixpyrrole" from a previously reported palladium calixpyrrole complex (1) as the starting material. The new ligand structure contained not only calixpyrrole but also salen binding pockets in the second coordination sphere. Both mono- and bimetallic palladium complexes, 2 and 3, respectively, were synthesized and characterized. This work will compare their coordination geometry, electrochemical properties, and catalytic activity toward HER.

2.3. Results and discussion

2.3.1. A novel method to synthesize complex 1

Recently, our group reported the synthesis of palladium calixpyrrole complex (1) by deprotonating the pyrrole species with two equivalents of KH, followed by a salt metathesis reaction with one equivalent of $Pd(OAc)_2$ in THF to produce a four-coordinated square planar complex. The yield of the reaction was reported as 57.4 %, which can be considered a moderate yield.[47] During this study, we were able to develop a synthesis procedure to increase the reaction yield of this product to 70%, which is beneficial in future synthesis. The pyrrole ligand was reacted with one equivalent of $Pd(OAc)_2$ in DCM, resulting in a red color powder with ^1H NMR peaks comparable to those published in the paper. Similar to the published results, the imine C-H signals were shifted upfield from 5.3 ppm to 7.75 ppm, and the pyrrole NH signals between 11 and 12 ppm have disappeared, confirming the coordination of Pd to the calixpyrrole core. The increase in

yield upon changing solvent can be attributed to the higher polarity of THF compared to DCM, leading to lower product purity. THF can act as a ligand and compete with Schiff base for coordination with Pd(II), forming solvated Pd(II) species.[48] The absence of KH base also could be a factor in resulting in higher yields, since KH is a very strong base, it may over-deprotonate pyrrole groups, leading to side reactions.[49]

2.3.2. Synthesis and characterization of complexes 2 and 3

The monometallic palladium salixpyrrole complex (2) was synthesized by following an extremely straightforward pyrrolidine-catalyzed Schiff-base reaction developed by Garcia Ruano and Cid *et al.*[50] The synthesis was done by using complex 1 and 4-tert-butyl-salicylaldehyde (Scheme 2.3.1) as starting materials, and the product was isolated in moderate yields (51%). A simple condensation reaction between one equivalent of complex 1 with excess 4-*tert*-butyl-salicylaldehyde in THF resulted in the expected monometallic pd complex (**Scheme 2.1**). In this procedure, pyrrolidine was used as a catalyst to prevent the usage of highly concentrated acidic media during transamination, as well as molecular sieves were used as a water scavenger to increase the reaction rate. The ^{1}H NMR spectra show characteristic peaks for salicylaldehyde incorporation compared to complex 1. The appearance of the 2nd imine peak at 8.19 ppm and the upfeild shift of the previous imine peak from 7.75 ppm to 7.49 ppm confirms the salicylaldehyde substitution. Also, the appearance of the peak at 1.27 ppm, which can be attributed to the *tert*-butyl, supports that conclusion.

Our initial attempts to synthesize the free salixpyrrole ligand were unsuccessful according to the ^{1}H NMR spectra of the crude reaction mixture, which shows multiple imine and aldehyde groups. We attributed these results to the hydrolysis of the existing imine bond in the free ligand of complex 1. It is believed that the conditions that are applied to form the new imine bond with

4-*tert*-butyl-salicylaldehyde lead to the hydrolysis of the existing imine bond, hence multiple unwanted side reactions. Therefore, complex 1 was utilized as the starting material, with Pd employed to lock the imine bond within calixpyrrole functionalities.

Scheme 2.1. General Synthetic Procedure for Salixpyrrole Complexes **2** and **3**.

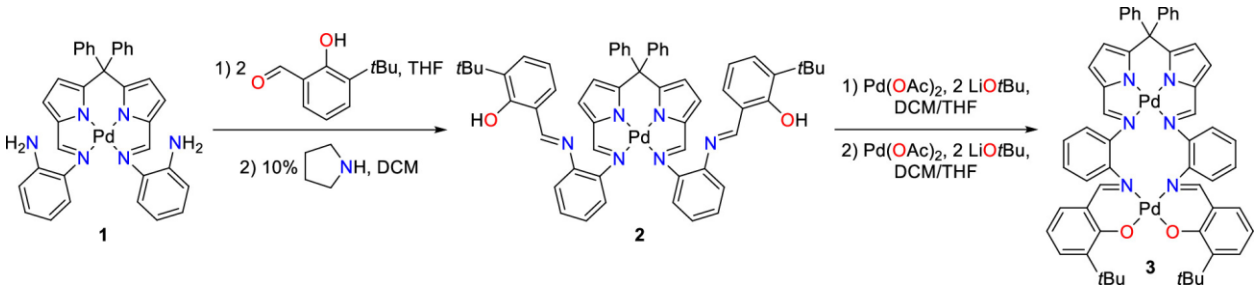

The bimetallic palladium complex (3) was synthesized using 2 as a starting material. The monometallic complex reacted with an excess of $Pd(OAc)_2$, which was used as the metal source, and Li*O*tBu, which was used as the base to deprotonate the phenols (**Scheme 2.1**). The reaction was done in two steps to provide the lost palladium during Pd-black formation under the reaction conditions. The product was isolated in moderate yields (47%), and the ^{1}H NMR spectrum confirms the metal coordination with the characteristic salen imine peak shift upfield from 8.19 ppm to 7.21 ppm. The pyrrole imine also shifted to upfield from 7.49 ppm to the range between 7.23 – 7.16 ppm, which is understandable considering it is further away from metal coordination.

In addition to NMR spectroscopy, both 2 and 3 complexes were characterized in the solid state utilizing single-crystal X-ray diffractometry (**Figure 2.5**). The monometallic complex (2) adopted a square planar coordination geometry, which resembles the configuration of complex 1. An exception, however, was that the metal was bound completely in the plane of the calixpyrrole ligand nitrogen donors, whereas, in complex 1, the palladium center adopted a distorted square planar configuration with the metal bound slightly out of the calixpyrrole ligand nitrogen donors.[47] Moreover, the palladium center was more tightly bound to the pyrrolidine nitrogen with shorter

bond lengths of 1.937 Å between Pd(1)-N(17), whereas to the imine donors (Pd(1)-N(12) bond lengths of 2.118 Å) (**Table 2.1**). These results are consistent with complex 1[47] and the results reported by Love *et al*.[51] for bimetallic palladium "pacman" complexes. It was also observed that the angle between N(17)-Pd(1)-N(17) bond for pyrrolidine donors was compressed just below 90° (86.3°), compared to the bond angle between N(17)-Pd(1)-N(12) which is more compressed being almost 80° (80.4°) (**Table 2.1**). This can be attributed to the formation of the five-membered ring between imine and pyrrolidine donors and the palladium metal center upon coordination. To compensate for the compressed angles, the bond angle between N(12)-Pd(1)-N(12) for the imine bond donors was expanded beyond 90° (112.1°) (**Table 2.1**). The calixpyrrole C=N imine bond length for complex 2 (N(12)-C(13) bond length of 1.32 Å) was slightly longer than the imine bond seen in the free ligand (N(3)-C(6) and N(4)-C(11) bond lengths of 1.28 Å and 1.29 Å, respectively). These results were comparable to those imine bond lengths seen in the analogous palladium complexes.[47,51] It could be due to π back-bonding from the palladium center, which weakens the imine bond. On the other hand, the 2nd imine bond, salen C=N in complex 2, was much similar in length to the free ligand imine bond length.

Table 2.1. Selected bond lengths and bond angles for 2.

Bond Lengths (Å)		**Bond angles (Deg)**	
Pd(1)-N(17)	1.937(3)	N(17)-Pd(1)-N(17)	86.3(5)
Pd(1)-N(12)	2.118(3)	N(17)-Pd(1)-N(12)	80.4(4)
N(12)-C(13)	1.325(4)	N(12)-Pd(1)-N(12)	112.1(5)
N(9)-C(8)	1.281(4)	N(12)-C(13)-C(14)	119.2(3)
H(20)-N(9)	1.58		
O(20)-N(9)	2.57		

Interestingly, complex 2 displayed C_2-symmetry with the pendent groups on opposite sides of the calixpyrrole plane. The phenol moieties in salicylaldehyde can be seen hydrogen bonded to

the salen imine nitrogens with H(20)-N(9) and O(20)-N(9) distances of 1.58 and 2.57 Å, respectively (**Table 2.1**).

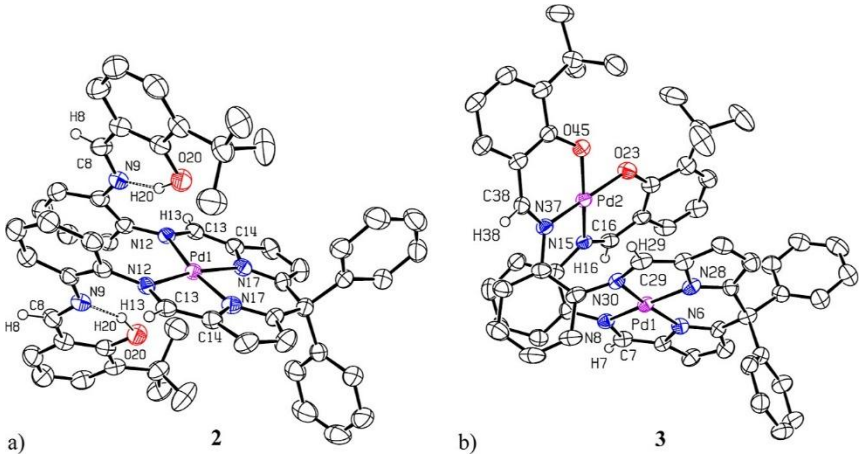

Figure 2.5. ORTEP3 representation (thermal ellipsoids at 50% probability) and atom numbering for: (a) 2, most of the hydrogens have been omitted for clarity. (b) 3, most of the hydrogens have been omitted for clarity.

On the other hand, the bimetallic complex (3) adopted a distorted cofacial conformation with two square planar palladium centers (**Figure 2.5**). The coordination geometry of the calixpyrrole core was very similar to the reported palladium complexes.[47,51] Interestingly, with the second metal coordination, the palladium was bound slightly out of the plane of the four nitrogen donors in the calixpyrrole center (0.011 Å). Additionally, compared to the monometallic complex, the palladium center was found to be more tightly bound to the pyrrolide nitrogens. It was reflected by having shorter bond lengths between the pyrrolide nitrogen Pd(1)-N(6) and Pd(1)-N((8) (1.92 Å compared to 1.937 Å between Pd(1)-N(17) in 2) as well as bond lengths between imine donors Pd(1)-N(8) and Pd(1)-N(30) (2.07 and 2.04 Å, respectively compared to Pd(1)-N(12) bond lengths of 2.118 Å of 2) (**Table 2.2**). It was also observed that the angle between N(6)-Pd(1)-N(28) bonds for pyrrolide donors was compressed just below 90° (89.4°), compared to the bond angle between N(6)-Pd(1)-N(8) and N(28)-Pd(1)-N(30) which were more compressed being almost 80° (80.7° and 80.0°, respectively) (**Table 2.2**). This can be attributed to the formation of the five-membered

ring between imine and pyrrolidine donors and the palladium metal center upon coordination. In contrast, the bond angle between N(8)-Pd(1)-N(30) for imine donors was expanded beyond 90° (110.3°) to compensate for the compressed angles. Lastly, the calixpyrrole C=N imine bond length for complex 3 (N(8)-C(7) and N(30)-C(29) bond lengths of 1.32 and 1.32 Å, respectively) was slightly longer than the imine bonds seen in the free ligand (N(3)-C(6) and N(4)-C(11) bond lengths of 1.28 Å and 1.29 Å, respectively) but similar to the imine bonds in complex 2 (**Table 2.2**). As discussed earlier, it is believed that this weakening could be due to π back-bonding from the palladium center. Even though the calixpyrrole binding pocket displayed parameters similar to the reported palladium complexes (5), the salen binding pocket exhibited some moderate differences compared to some known monometallic palladium salophen systems (4) (**Figure 2.6**).[52–54]

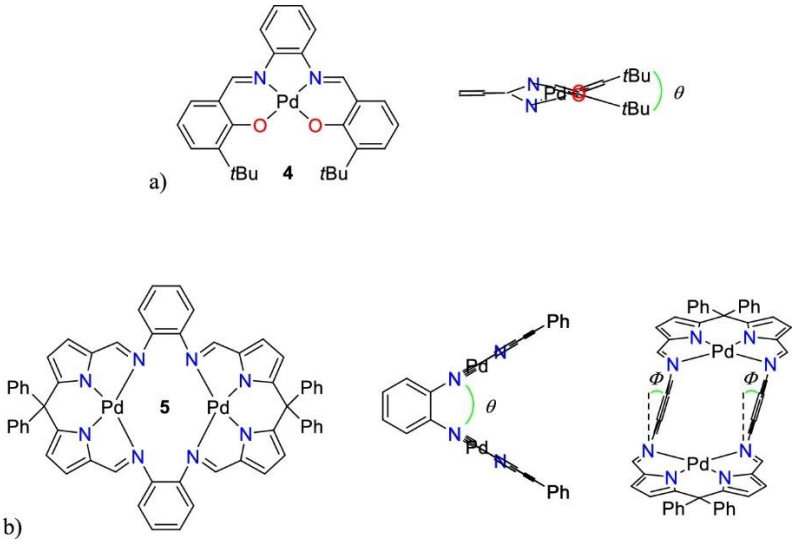

Figure 2.6. (a) Structure of the monometallic *tert*-butyl substituted palladium salophen complex 4 (left) and a side-on view of the tetradentate plane showing the dihedral angle (right); and (b) Structure of the bimetallic palladium "pacman" calixpyrrole complex 5 (left), a side-on view showing the dihedral angle between the cofacial planes (middle), and a front-on view showing the torsional twist (right).

The palladium center in the salen portion of 3 adopted a square planar configuration with the metal bound slightly out of the plane of the two nitrogen and two oxygen donors (0.005 Å). The Pd(II) center is coordinated in a cis-planar fashion by the two phenolic oxygen atoms and two imine nitrogen atoms. Surprisingly, the palladium center was found slightly closer to the oxygen donors rather than the imine nitrogens, whereas in most of the known monometallic salophen complexes, it was found to be closer to the imine nitrogens[53,54] (Pd(2)-O(45), Pd(2)-O(23), Pd(2)-N(15, and Pd(2)-N(37) bond lengths of 2.01, 2.00, 2.04, and 2.03 Å). Additionally, all of the bond lengths for complex 3 were lengthened by 0.02 to 0.05 Å in contrast to the reported monometallic complexes.[53,54] These changes can be attributed to the more strained/twisted binding mode forced by the co-facial arrangement compared to the monometallic ligand architecture. It is also observed that the bond angle between the phenolate donors O(45)-Pd(2)-O(23) for 3 was significantly compressed below 90°(82.1°), whereas the bond angles for the two six-membered ring systems O(45)-Pd(2)-N(37) and O(23)-Pd(2)-N(15) were close to 90° (91.6 and 89.4°) (**Table 2.2**). Lastly, the bond angle between the imine donors N(15)-Pd(2)-N(37) was well expanded beyond 90° (98.4°). These results were consistent with the previous findings for palladium-based monometallic salophen complexes.[53,54] The salen C=N imine bond lengths for the coordinated salen core for 3 (N(37)-C(38) and N(15)-C(16) bond lengths of 1.30 and 1.32 Å, respectively) were longer than those seen in the uncoordinated portion of the Salen core in 2 (N(9)-C(8) bond lengths of 1.28 Å)which was attributed to the π back-bonding from the palladium center (**Table 2.2**).

Additionally, the metal-metal distance and dihedral angle between the calixpyrrole plane (PdN_4) and salen plane (PdN_2O_2) were found to be larger in comparison to the reported palladium calixpyrrole “pacman” complex 5 by Love *et al.* [52] (Pd(1)-Pd(2) distance 4.09 Å and dihedral angle

of 3, 52.3° compared to 3.83 Å and 44.7° seen for 5). It is hypothesized that this increased separation between the cofacial planes is caused by the bulky *tert*-butyl groups. This hypothesis can be supported by the following: 1) the two metal centers in 3 were more offset than the metal centers in 5 (average torsional twist $\Phi = 27.9°$ as opposed to $\Phi = 25.0$),[52] likely to minimize steric clash between the meso-phenyl moieties of the calixpyrrole unit and the *tert*-butyl groups; and 2) the more distorted square planer salen palladium metal center which further twists the entire structure (dihedral angle of 13.1° for 3 as opposed to 5.8° seen for 4),[53] likely due to the steric bulk of the *tert*-butyl functionalities (**Figure 2.5**).

Table 2.2. Selected bond lengths and bond angles for 3.

Bond Lengths (Å)		**Bond angles (Deg)**	
Pd(1)-Pd(2)	4.09		
		For calixpyrrole core	
Pd(1)-N(6)	1.921(4)	N(6)-Pd(1)-N(8)	80.67(16)
Pd(1)-N(28)	1.917(4)	N(28)-Pd(1)-N(6)	89.41(16)
Pd(1)-N(8)	2.067(4)	N(28)-Pd(1)-N(30)	80.04(16)
Pd(1)-N(30)	2.044(4)	N(30)-Pd(1)-N(8)	110.26(16)
N(8)-C(7)	1.320(6)		
N(30)-C(29)	1.316(7)		
		For salen core	
Pd(2)-N(15)	2.043(4)	O(23)-Pd(2)-N(15)	91.57(15)
Pd(2)-N(37)	2.029(4)	O(45)-Pd(2)-N(37)	89.42(15)
Pd(2)-O(23)	1.998(4)	O(23)-Pd(2)-O(45)	82.13(14)
Pd(2)-O(45)	2.011(4)	N(37)-Pd(2)-N(15)	98.36(16)
N(15)-C(16)	1.315(6)		
N(37)-C(38)	1.296(6)		

The straightforward and modular nature of this synthetic route makes it attractive for the synthesis of novel cofacial systems. In this synthesis, different functionalities were incorporated

such as hydroxide functionality on the salicylaldehyde starting material were incorporated ortho into the imine bond as well as the transition metal complex incorporated adjacent to the pendent amines on 1. These modifications suggest that this synthetic route for Schiff-base formation was relatively insensitive to steric encumbrance in these positions. However, systems that place too much bulk close to the aldehyde or imine groups may make the imine-bond formation sluggish. Therefore, it is hypothesized that various aldehydes with acidic protic groups like phenols and calixpyrrole starting materials with various donor groups and meso-substituents can be utilized. These types of modifications will be extremely useful in future studies for tuning the binding pockets of the cofacial systems or even with the synthesis advancements of heterobimetallic unsymmetric complexes.

2.3.3. Electrochemical characterization

The electrochemical properties of the salixpyrrole complexes 2 and 3 were evaluated using cyclic voltammetry (CV) in THF due to the limited solubility in more polar solvents like acetonitrile. Tetrabutylammonium hexafluorophosphate (TBAP) was used as the supporting electrolyte. The monometallic complex showed similar electrochemical characteristics to complex 1 and its free ligand in THF (**Figure 2.7a**) The voltammogram for 2 displayed a quasi-reversible redox couple around -0.25 V vs ferrocene/ferrocenium (Fc/Fc^+) couple, which can be attributed to the calixpyrrole ligand-based oxidation according to the previous computational studies on complex 1.[47] This hypothesis is further supported by the reducing open circuit potential (OCP) of 2, which was measured to be -1.97 V vs $Ag/AgNO_3$ suggesting the redox couple corresponded to an oxidative process. The appearance of the more anodic shoulder on the reduction peak around -0.35 V vs Fc/Fc^+ suggested the occurrence of the two overlapping electron transfer processes. The cyclic voltammograms of salophen complex 4 and its free ligand also displayed reduction peaks

around -0.33 V and -0.20 V vs Fc/Fc^+, respectively in THF (**Figure 2.7 d** and **e**). Therefore, it is possible to assume that the shoulder around -0.35 V in 2 corresponds to the "salen" portion of the salixpyrrole ligand. Additionally, there were two irreversible oxidation peaks around 0.43 V and 0.72 V vs Fc/Fc^+ in the CV for complex 2. When comparing 2 to the 4 and its free ligand in THF, which displayed similar irreversible oxidations around 0.55 V, 0.74 V vs Fc/Fc^+ and 0.33 V, 0.7 V vs Fc/Fc^+, respectively (**Figure 2.7**), it is possible to attribute these irreversible oxidations to the salen portion of the ligand in 2.

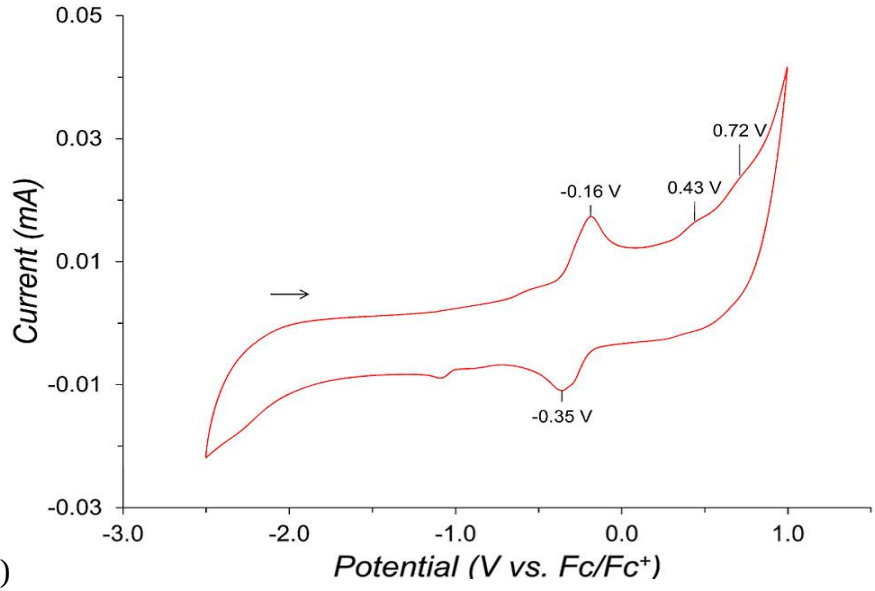

(a)

(b)

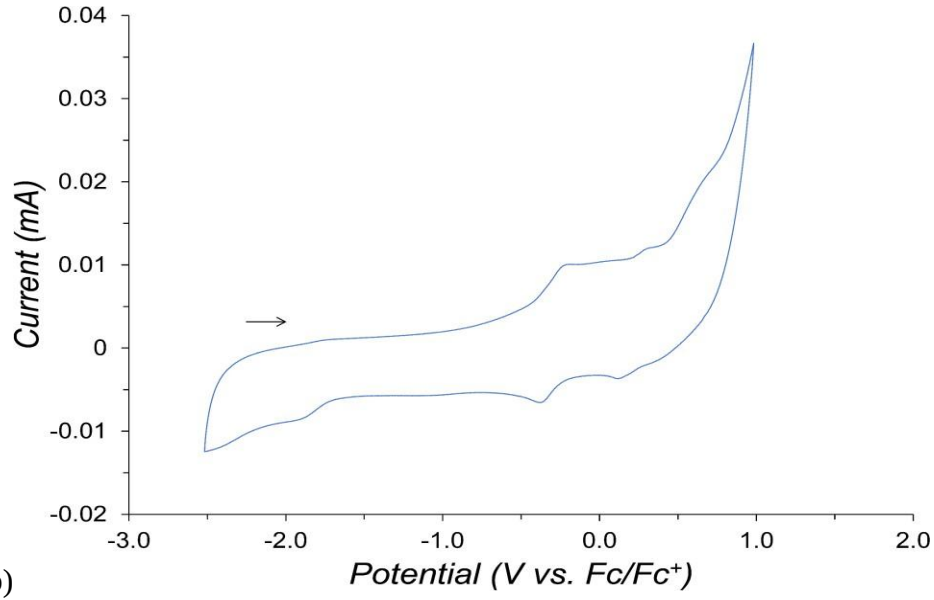
0.04
0.03
0.02
0.01
0
-0.01
-0.02
Current (mA)
-3.0
-2.0
-1.0
0.0
1.0
2.0
Potential (V vs. Fc/Fc+)

(c)

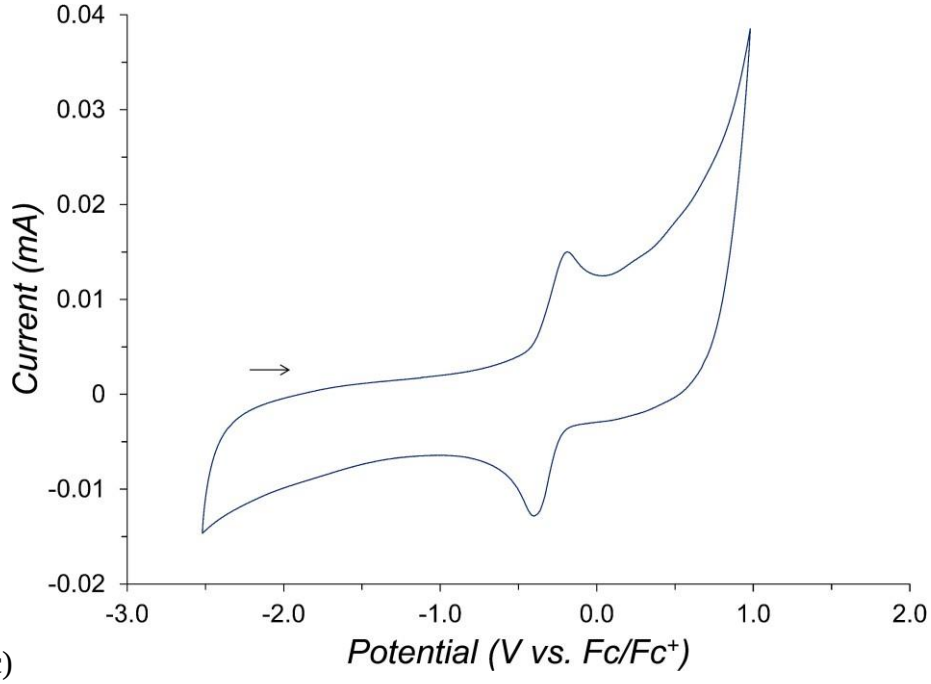
0.04
0.03
0.02
0.01
0
-0.01
-0.02
Current (mA)
-3.0
-2.0
-1.0
0.0
1.0
2.0
Potential (V vs. Fc/Fc+)

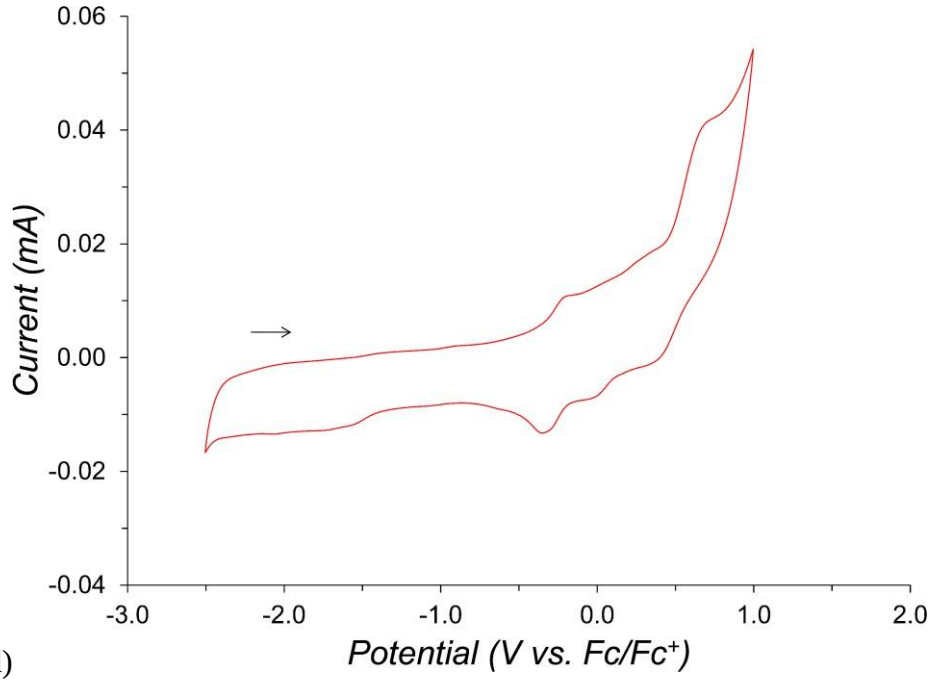
0.06
0.04
0.02
0.00
-0.02
-0.04
Current (mA)
-3.0
-2.0
-1.0
0.0
1.0
2.0
Potential (V vs. Fc/Fc+)

(d)

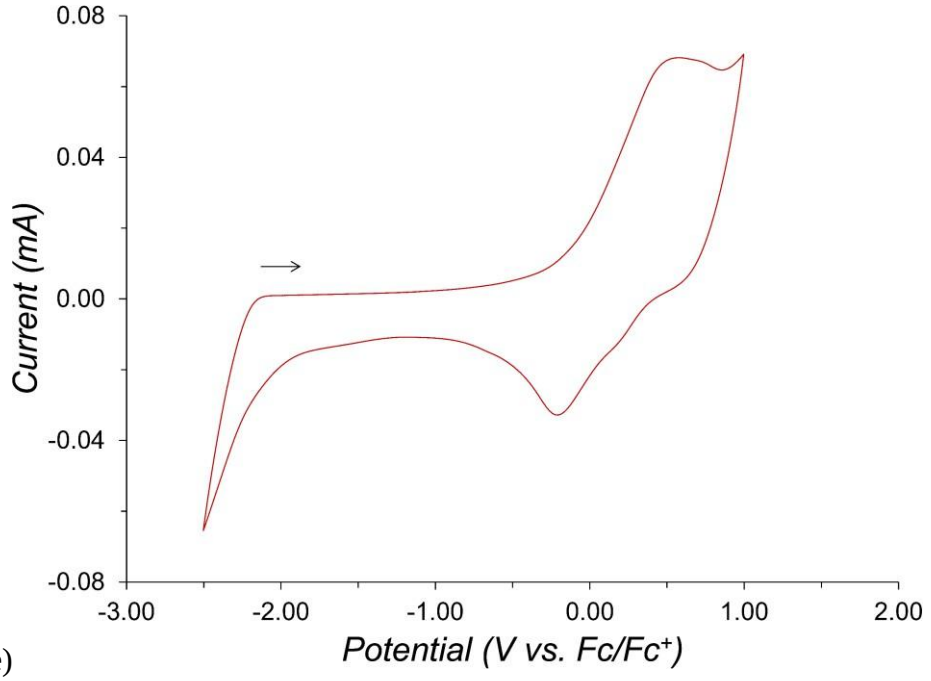
0.08
0.04
0.00
-0.04
-0.08
Current (mA)
-3.00
-2.00
-1.00
0.00
1.00
2.00
Potential (V vs. Fc/Fc+)

(e)

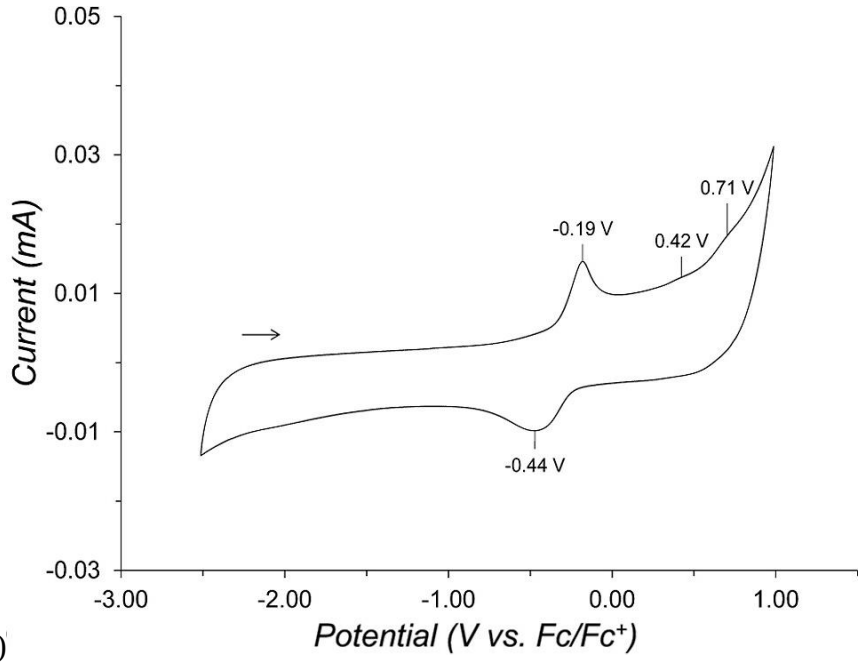

(f)

Figure 2.7. Representative CVs (0.1 M TBAP in THF, 0.25 mM ligand or complex, glassy carbon working electrode, platinum wire counter electrode, 0.01 M Ag/AgNO3 reference electrode, scan rate = 800 mV/s) of: a) complex 2; b) the free ligand of 1; c) complex 1; d) the free ligand of 4; (e) complex 4; and (f) complex 3.

Bimetallic complex 3 also had similar electrochemical characteristics as 2 (**Figure 2.7f**). The evident quasi-reversible couple around -0.32 V vs Fc/Fc^+ was attributed to the calixpyrrole ligand-based oxidation, which was further supported by the measured OCP of -1.52 V vs $Ag/AgNO_3$, suggesting an oxidative process. The two irreversible oxidation peaks around 0.42 V and 0.71 V vs Fc/Fc^+ were attributed to the palladium salen portion of 3 after comparing it with the cyclic voltammograms of salophen complex 4 and its free ligand. Moreover, the reduction peak around -0.44 was quite broad compared to the reduction peak in 2, which suggests the occurrence of two overlapping electron transfer processes.

Interestingly, further examination of the redox couple of 2 and 3 around -0.25 V and -0.32 V vs Fc/Fc^+, respectively (**Figure 2.8** and **Figure 2.9**), revealed that this feature's reversibility depended on the scanning window utilized. If irreversible oxidations at more

positive potentials were excluded, a more linear correlation between peak potential and scan rate was seen. Furthermore, the peak current ratio (anodic (i_a)/cathodic (i_c)) became much closer to unity, and the peak current was increasing as a function of the square root of the scan rate, confirming the redox couple's reversibility.[55] In particular, for 2, the reduction peak no longer displayed the shoulder, which was seen with the larger scanning window as well as for 3, the broad peak around -0.44 V vs Fc/Fc^+ became less broad with a narrower scanning window (**Figure 2.9**). According to these results, the shoulder feature in the reduction peak of the voltammogram of 2 and the broadening of the reduction peak in 3 can be attributed to one of the oxidations in the positive region discussed above.

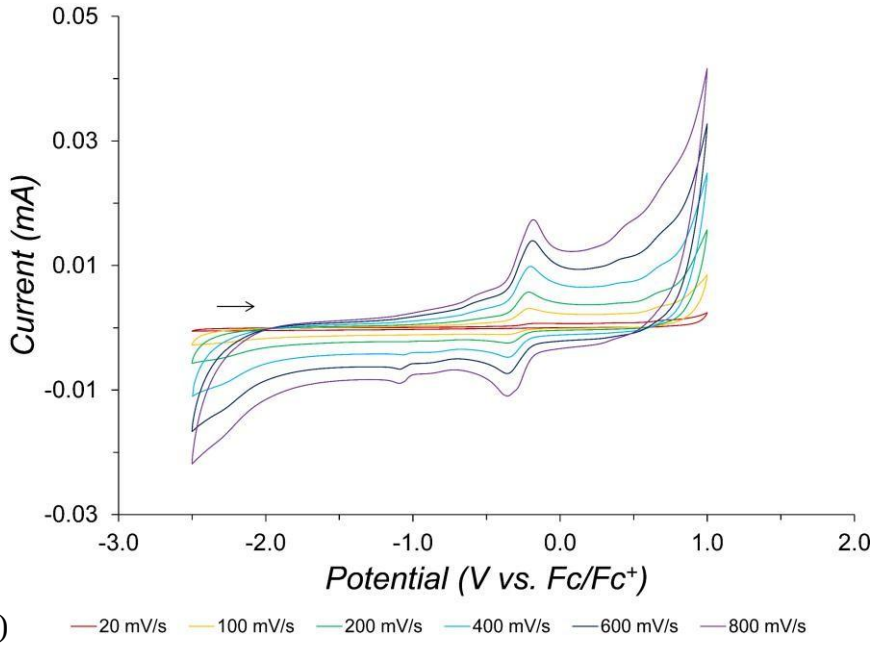

(a)

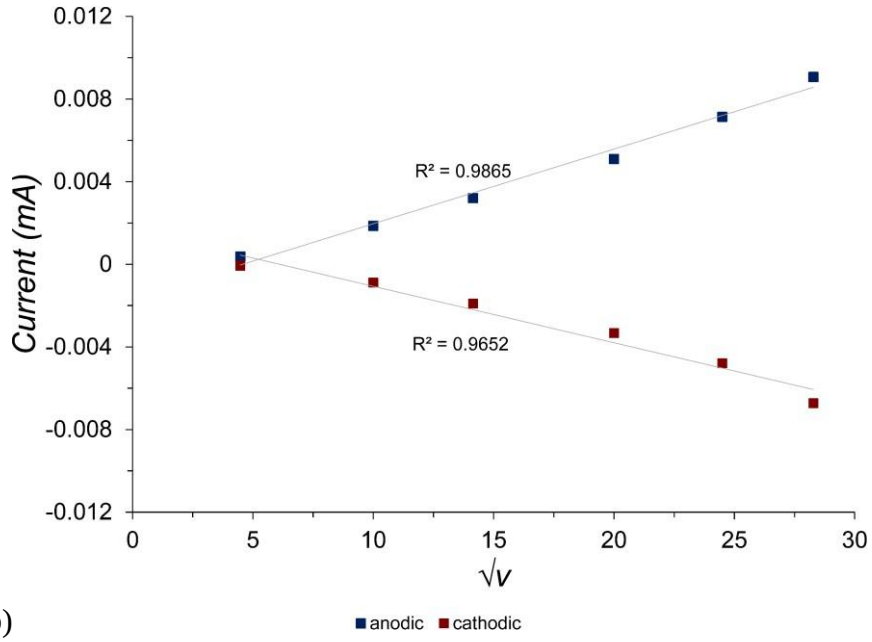
0.012
0.008
0.004
0
-0.004
-0.008
-0.012
Current (mA)
R² = 0.9865
R² = 0.9652
0
5
10
15
20
25
30
√v
anodic
cathodic

(b)

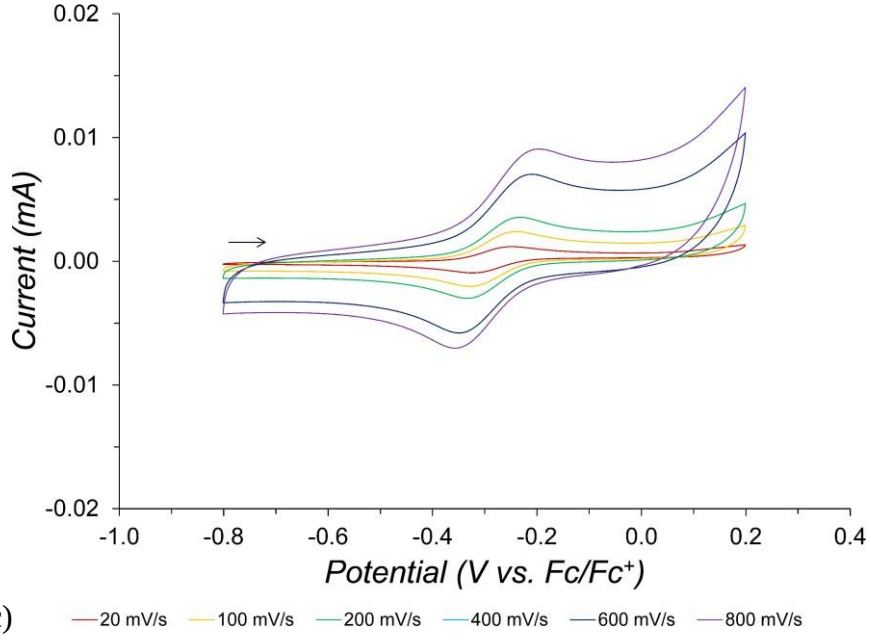
0.02
0.01
0.00
-0.01
-0.02
Current (mA)
-1.0
-0.8
-0.6
-0.4
-0.2
0.0
0.2
0.4
Potential (V vs. Fc/Fc⁺)
20 mV/s
100 mV/s
200 mV/s
400 mV/s
600 mV/s
800 mV/s

(c)

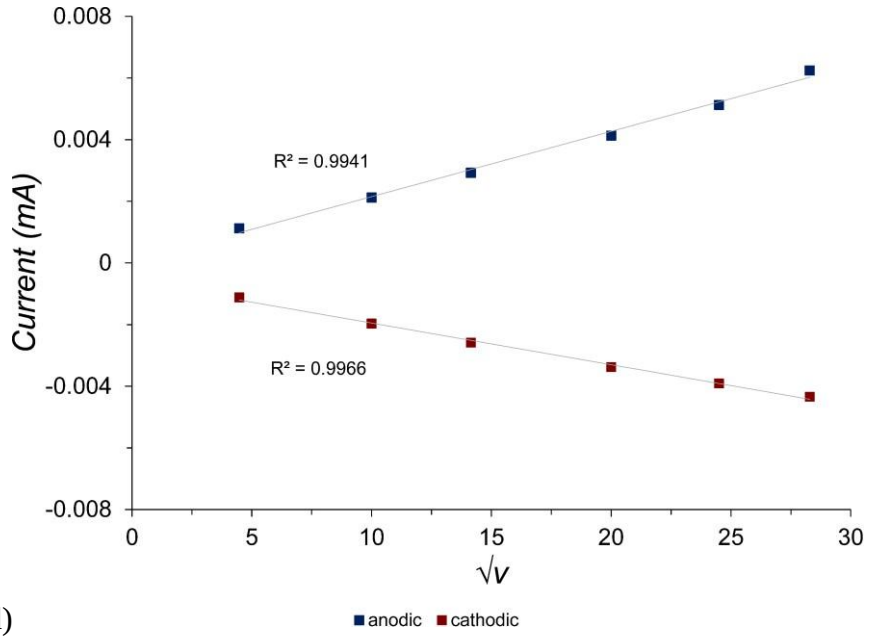

(d)

Figure 2.8. a) CVs of the quasi-reversible redox couple of **2** with a wide scanning window at different scan rates (0.1 M TBAP in THF, 0.25 mM **2**, glassy carbon working electrode, platinum wire counter electrode, 0.01 M Ag/AgNO3 reference electrode, scan rate = 20 to 800 mV/s); b) plot of anodic and cathodic current vs. the square-root of scan rate; c) CVs of the quasi-reversible redox couple of **2** with a narrow scanning window at different scan rates; and d) plot of anodic and cathodic current vs. the square-root of scan rate.

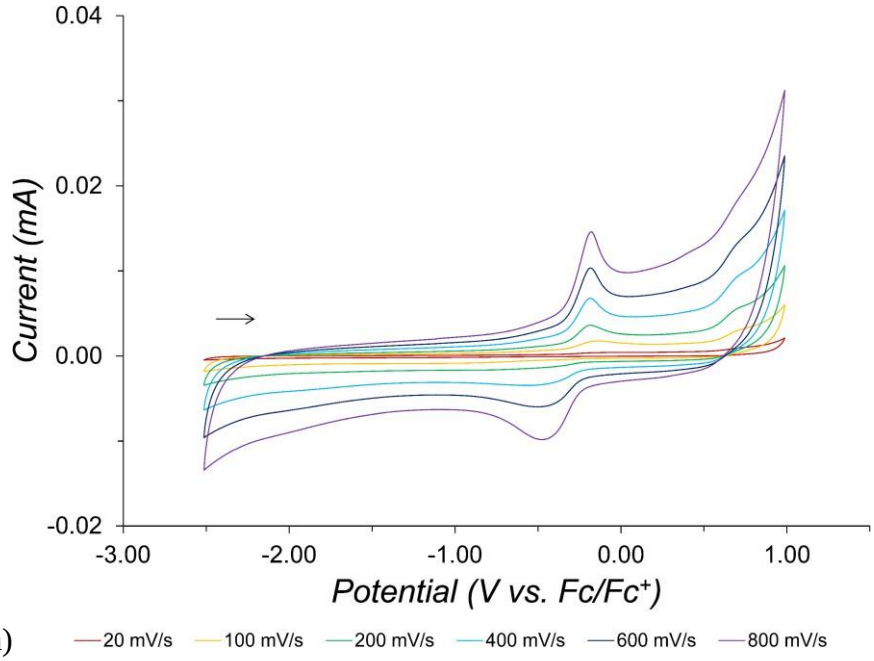

(a)

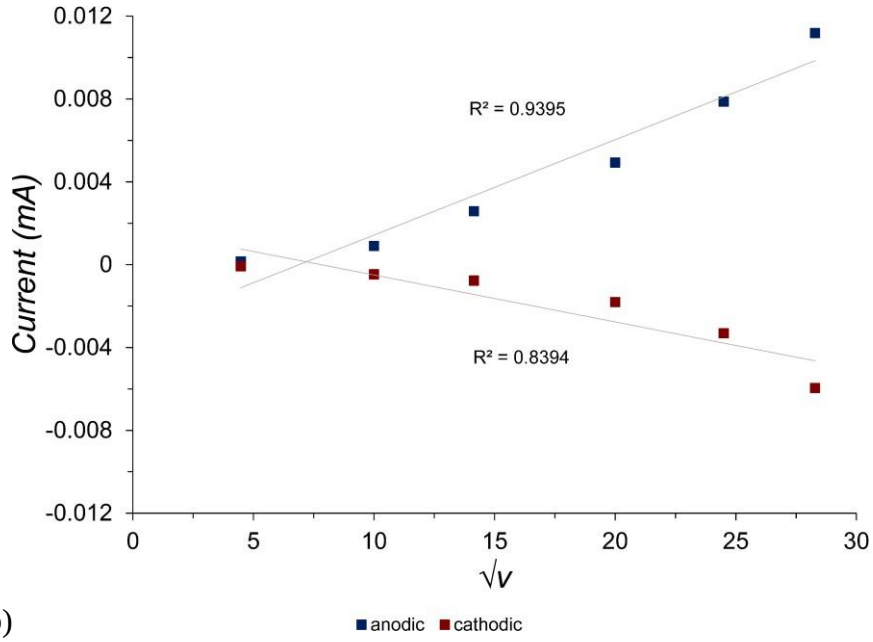
0.012
0.008
0.004
0
-0.004
-0.008
-0.012
Current (mA)
R² = 0.9395
R² = 0.8394
0
5
10
15
20
25
30
√v
anodic
cathodic

(b)

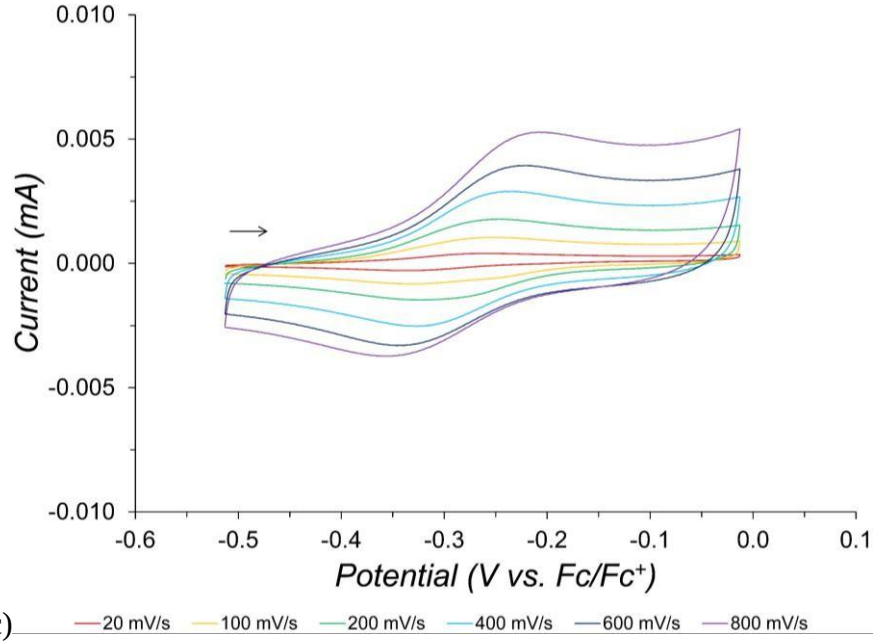
0.010
0.005
0.000
-0.005
-0.010
Current (mA)
-0.6
-0.5
-0.4
-0.3
-0.2
-0.1
0.0
0.1
Potential (V vs. Fc/Fc⁺)
20 mV/s
100 mV/s
200 mV/s
400 mV/s
600 mV/s
800 mV/s

(c)

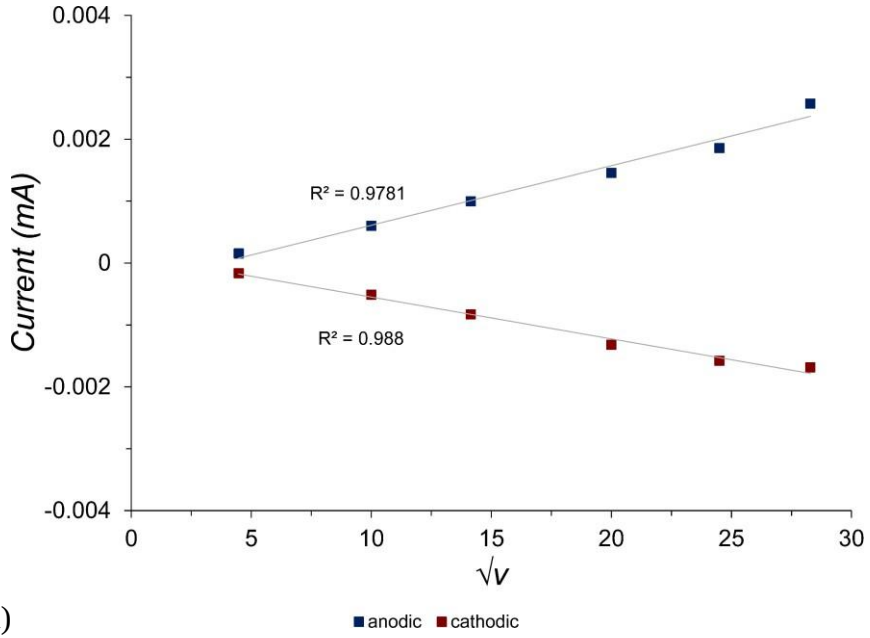

(d)

Figure 2.9. a) CVs of the quasi-reversible redox couple of 3 with a wide scanning window at different scan rates (0.1 M TBAP in THF, 0.25 mM 3, glassy carbon working electrode, platinum wire counter electrode, 0.01 M Ag/AgNO3 reference electrode, scan rate = 20 to 800 mV/s); b) plot of anodic and cathodic current vs. the square-root of scan rate; c) CVs of the quasi-reversible redox couple of 3 with a narrow scanning window at different scan rates; and d) plot of anodic and cathodic current vs. the square-root of scan rate.

2.3.4. Electrocatalytic hydrogen evolution reaction (HER)

Para-toluenesulfonic acid monohydrate was used as the proton source to examine the electrochemical behavior of complexes 2 and 3. Irreversible reductions accompanied by increased peak currents were indicative of catalytic HER at -2.2 V and -2.35 V vs Fc/Fc^{+} for 2 and 3, respectively, under unoptimized conditions (**Figure 2.10**). Surprisingly, the onset of catalysis did not correlate with any of the electrochemical features observed in **Figure 2.7** for both complexes. The differential pulse voltammetry (DPV) technique was used to further analyze the complexes. Unfortunately, no additional irreversible features were observed in both voltammograms at negative potentials but the characteristic irreversible oxidation peaks discussed above were visible during DPV at positive potentials with the expected enhancement in the current. Furthermore, ^{1}H

NMR spectroscopy results confirmed that the direct protonation of complexes 2 and 3 did not occur upon the addition of *p*TSA under non-reducing conditions. Even though there was no visible direct protonation in the presence of strong acids like *p*TSA, it is possible that there is a weak interaction between complexes and *p*TSA based on literature precedent.[52] The authors reported hydrogen bonding interaction between TsO^- groups and the tetraprotonated macrocyclic free ligand of complex 5. They used *p*TSA as an acid catalyst to facilitate the imine formation during the ligand synthesis. The initial crystal structure presented had three TsO^- units hydrogen-bonded to iminopyrrole units. Treatment with triethylamine was needed to remove the *p*TSA and isolate the free ligand of 5. Therefore, it is possible to hypothesize such interaction occurring with 2 and 3, which would facilitate HER.

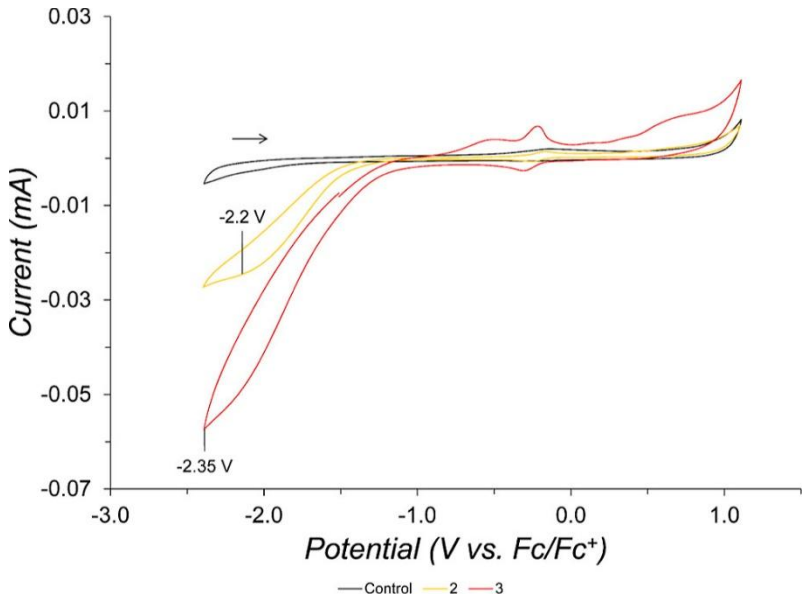

Figure 2.10. Representative CVs of 2 and 3 showing electrocatalytic HER in THF (0.1 M TBAP, no complex or 0.25 mM complex, 25 mM *p*TSA, glassy carbon working electrode, platinum wire counter electrode, 0.01 M $Ag/AgNO_3$ reference electrode, scan rate = 50 mV/s).

However, if the scanning window for CVs of 2 and 3 narrowed down to negative potentials, an irreversible reduction was seen around -2.8 V and -2.9 V vs Fc/Fc^+, respectively, in the absence of acid (**Figure 2.11**). These irreversible reductions appeared to be very unstable and disappeared

after multiple cycles. Therefore, for this work, i_p was obtained from the peak current of the second scan in **Figure 2.11** for 2 and 3, respectively. This approach was taken to estimate catalytic rates conservatively. Catalytic onset for HER was anodic compared to these reductions; therefore, it can be hypothesized that in the presence of *p*TSA, the reduced forms of 2 and 3 are stabilized such that catalytic turnover can occur. This phenomenon can be supported by Dempsey and co-workers' article, where they reported a Co(dmg) complex as HER catalyst.[56] The emergence of a new catalytic wave indicated the oxidation of Co species, which is stabilized by the acids present in the medium. It is anticipated that a similar behavior could be observed with compounds 2 and 3.

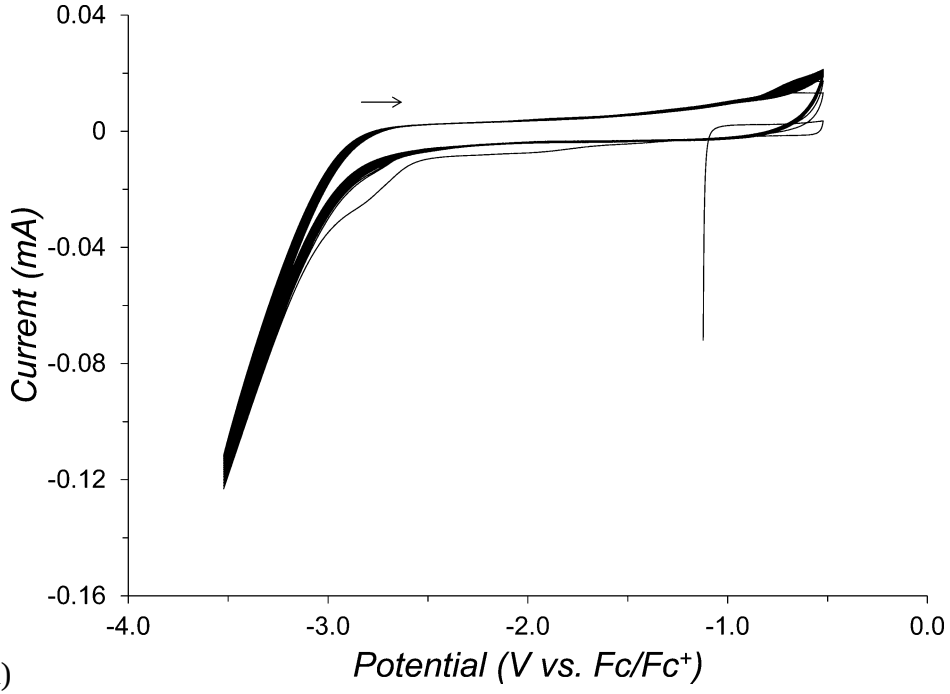

(a)

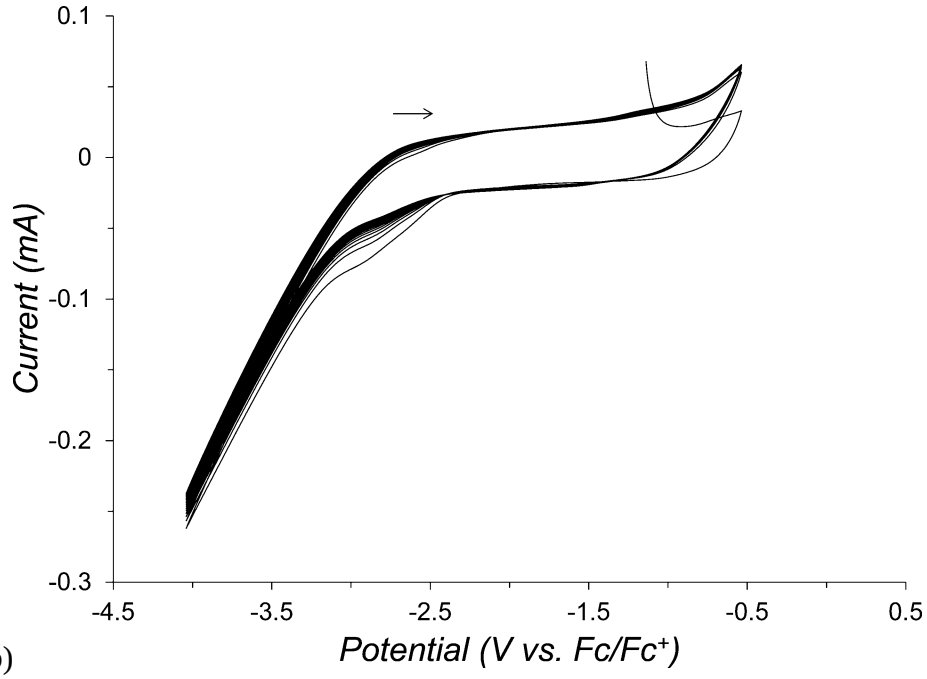

(b)

Figure 2.11. CVs of the salixpyrrole complexes in the absence of acid (0.1 M TBAP in THF, glassy carbon working electrode, 0.25 mM 2 or 3, platinum wire counter electrode, 0.01 M Ag/AgNO3 reference electrode) for: a) 2 (scan rate = 1 V/s); and b) 3 (scan rate = 8 V/s).

Next, the studies were carried out to figure out the current dependence on the scan rate (**Figure 2.12** and **Figure 2.13**). At the higher scan rates, the peak position shifted cathodically and became less well-defined. Therefore, the catalytic current $i_{cat,}$ was measured at the point where it begins to plateau the most. The scan rate independence point was achieved around 1 V/s for 2 and 8 V/s for 3, suggesting that the bimetallic system displayed faster reaction kinetics compared to the monometallic system. Additionally, the current response for both 2 and 3 was varied linearly with the square root of the scan rate, suggesting a homogeneous process for salixpyrrole systems.[57] These results contradict the results seen for complex 1, which generated a heterogeneous catalyst in the presence of *p*TSA.[47] Therefore, several controls were carried out to confirm the homogeneity of the catalytic process for salixpyrrole systems.[58] A simple "rinse" test indicated that the catalytically active species were not adsorbed on the glassy carbon electrode surface (**Figure 2.14**). Then, a mercury pool test was carried out to rule out

nanoparticle formation for 2 or residual Pd-black affecting HER for 3 (**Figure 2.15**). Lastly, it was confirmed that platinum was not leaching from the counter electrode (**Figure 2.16**).

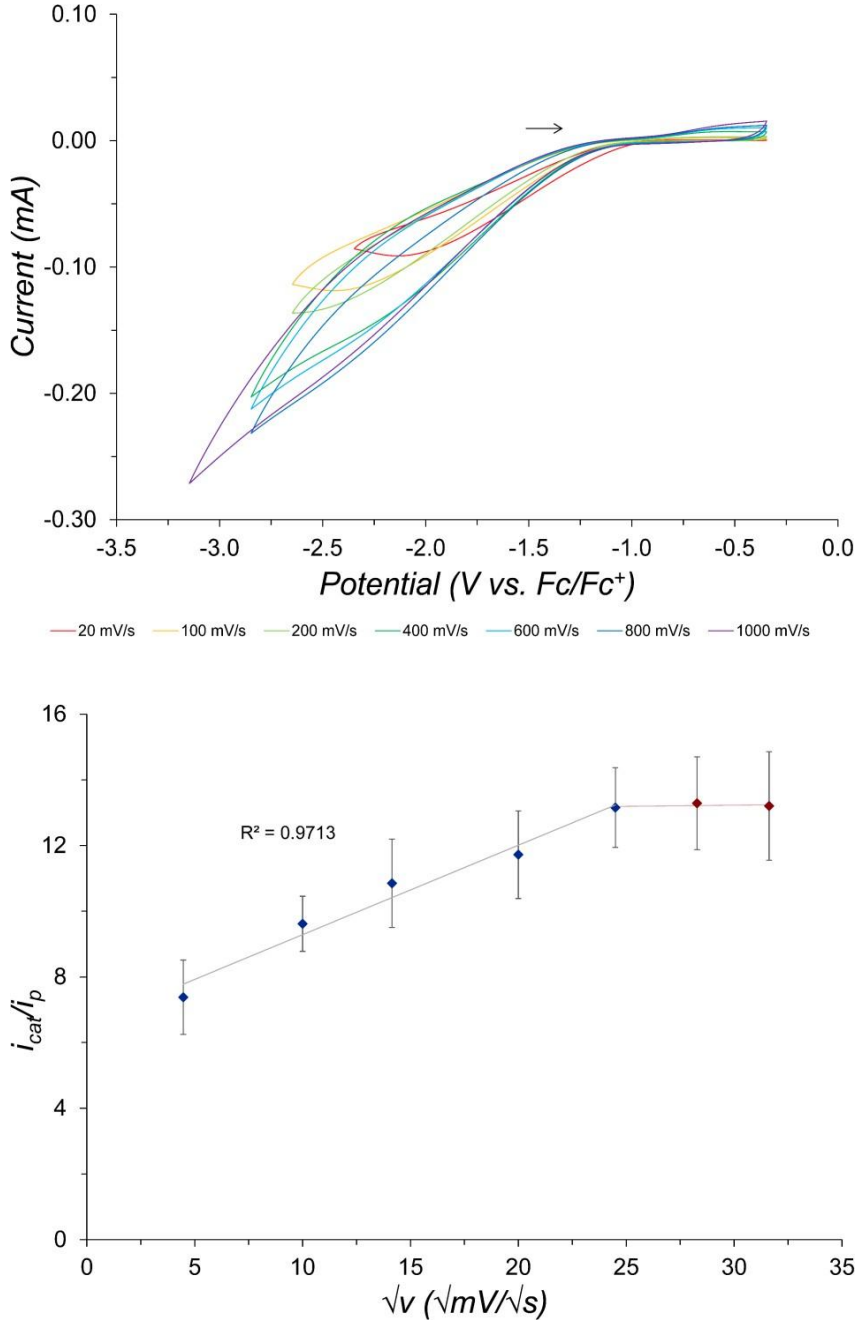

Figure 2.12. a) Catalytic CVs at different scan rates (0.1 M TBAP in THF, 0.25 mM 2, 25 mM *p*TSA, glassy carbon working electrode, platinum wire counter electrode, 0.01 M AgNO3 reference electrode, scan rate = 20 to 1000 mV/s); b) plot of normalized catalytic current vs. scan rate.

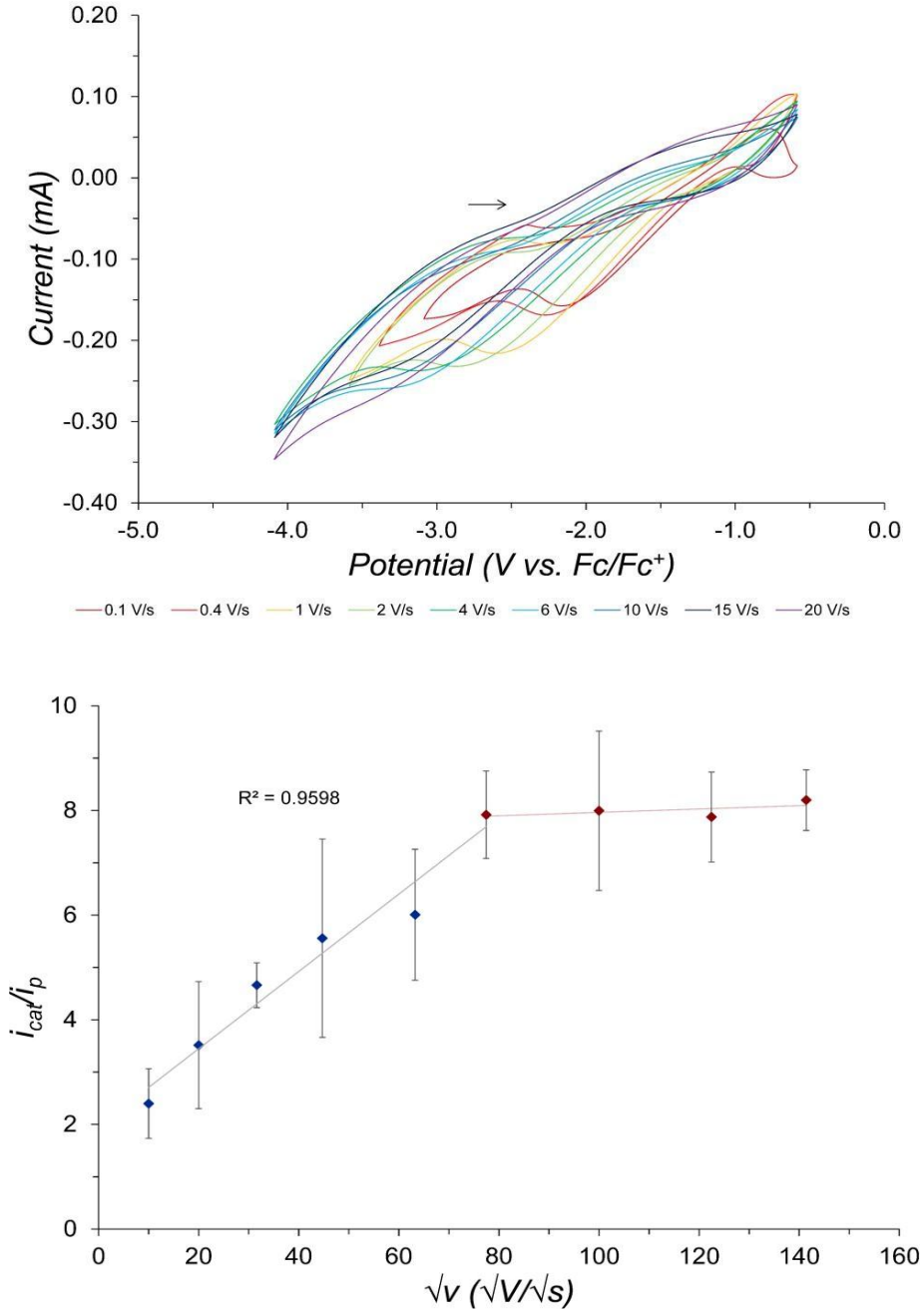

Figure 2.13. a) Catalytic CVs at different scan rates (0.1 M TBAP in THF, 0.25 mM 3, 25 mM *p*TSA, glassy carbon working electrode, platinum wire counter electrode, 0.01 M AgNO3 reference electrode, scan rate = 100 mV/s to 20 V/s); b) plot of normalized catalytic current vs. scan rate.

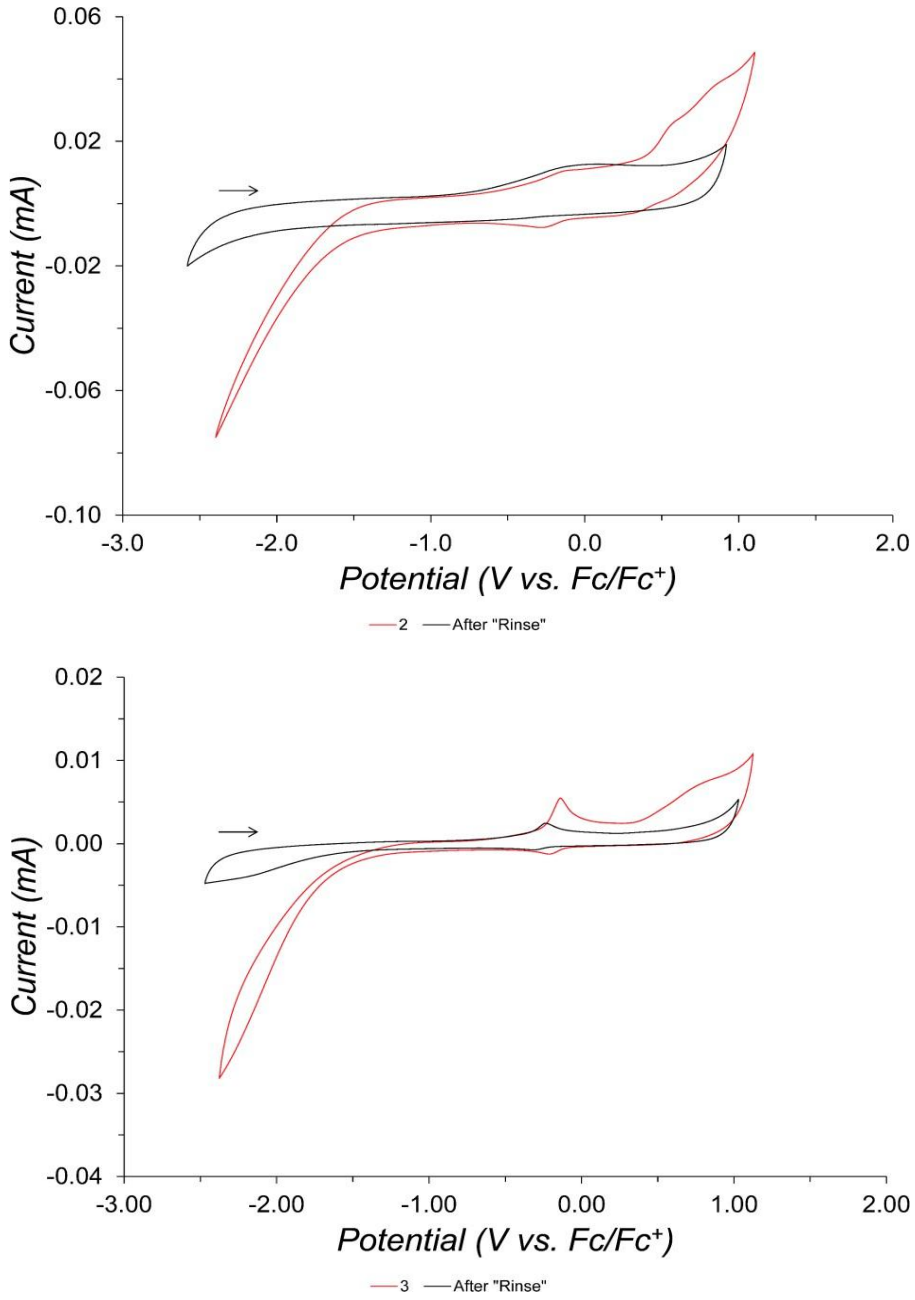

Figure 2.14. CVs of rinse test results using THF as the rinsing solvent (0.1 M TBAP in THF, 0.25 to 0 mM 2 or 3, 25 mM *p*TSA, glassy carbon working electrode, platinum wire counter electrode, 0.01 M Ag/AgNO3 reference electrode, scan rate = 800 V/s) for: a) 2; and b) 3.

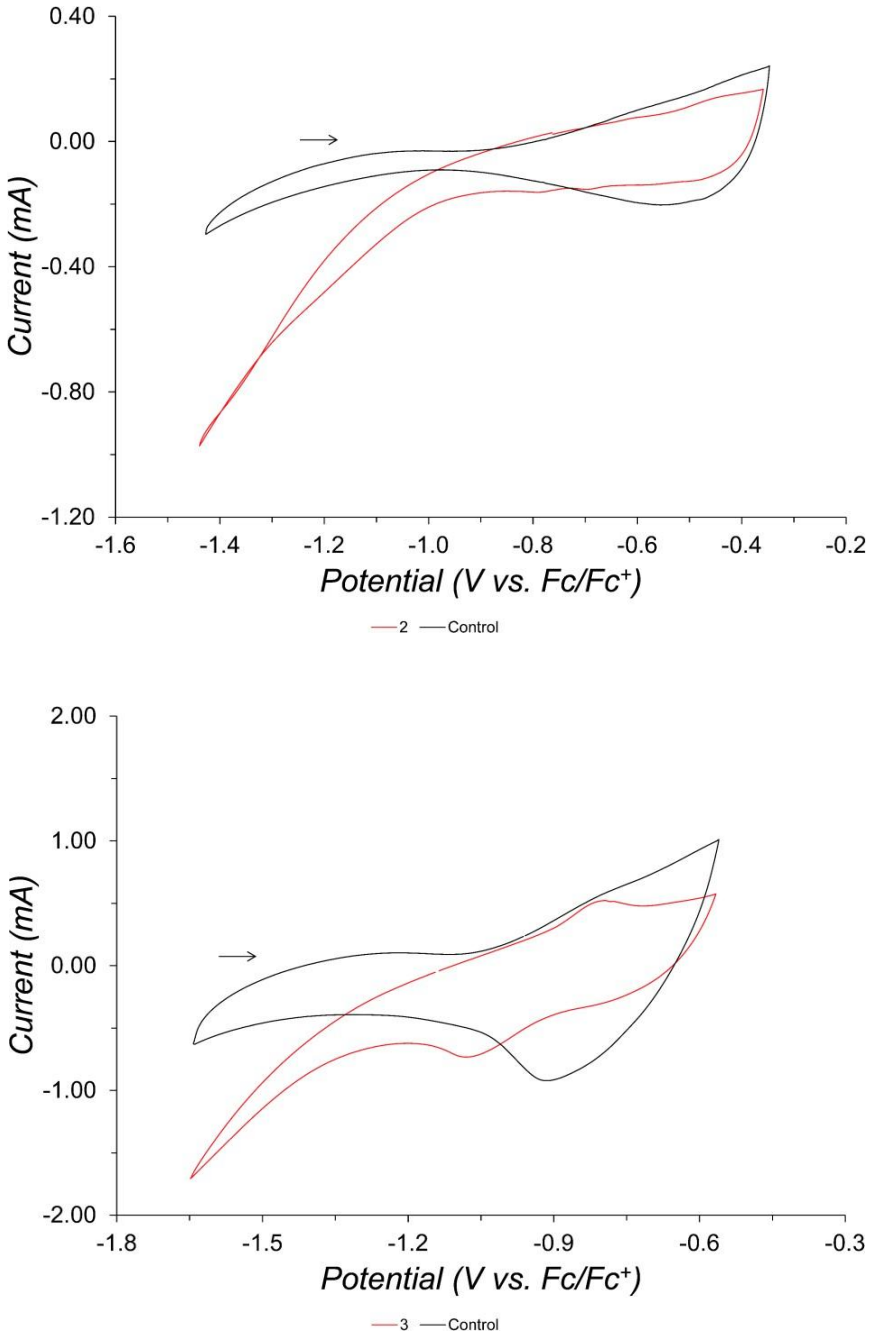

Figure 2.15. CVs of mercury pool tests for hydrogen evolution (0.1 M TBAP in THF, 0.25 mM 2 or 3, 45 mM *p*TSA, mercury pool working electrode, platinum wire counter electrode, 0.01 M $Ag/AgNO_3$ reference electrode) for: a) 2 (scan rate = 1 V/s); and b) 3 (scan rate = 8 V/s).

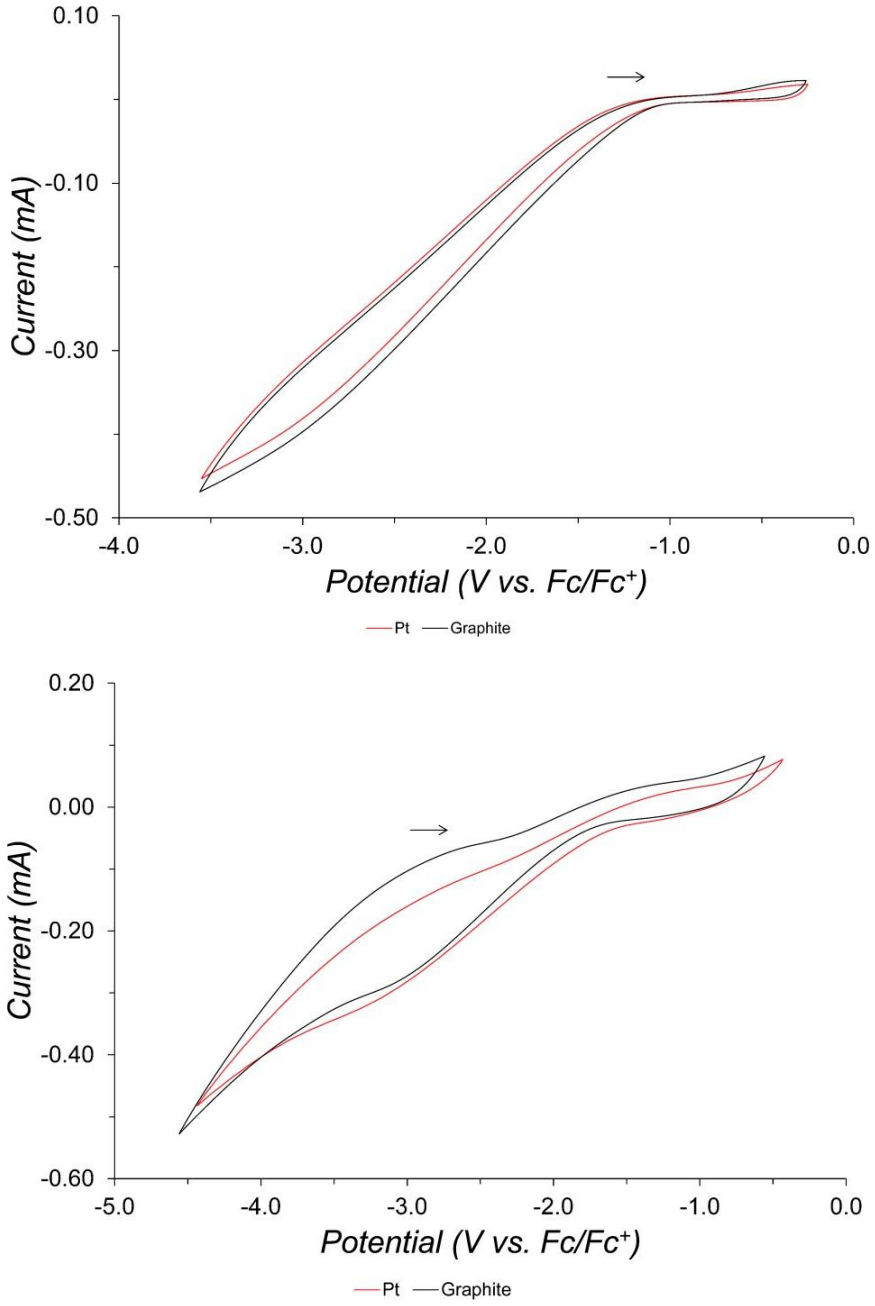

Figure 2.16. CVs of hydrogen evolution with a graphite rod counter electrode (0.1 M TBAP in THF, 0.25 mM 2 or 3, 45 mM *p*TSA, glassy carbon working electrode, 0.01 M Ag/AgNO3 reference electrode) for: a) 2 (scan rate = 1 V/s); and b) 3 (scan rate = 8 V/s).

2.3.5. Kinetic investigation

The catalyst dependence of the salixpyrrole system for HER was investigated, and the i_{cat} was measured at 3.0 V to limit overlap with direct reduction of *p*TSA at the glassy carbon electrode due to the absence of distinct peaks or plateaus in both voltammograms for 2 and 3 (**Figure 2.17**). For both systems catalytic current was found to increase linearly with catalyst concentration (**Figure 2.18** and **Figure 2.19**). This relationship indicated a first-order dependence on the catalyst according to Eq. 1[59], where n is the number of electrons transferred in the redox event (2 for HER), *F* is Faraday's constant (96,485 C/mol), A is the electrode surface area in cm^2 (although the electrochemical surface area is preferred it is usually treated as the geometric surface area), D is the diffusion coefficient in cm^2s^{-1}, and x is the order with respect to acid.

$$i_{cat} = nFA[cat]\sqrt{Dk[H^+]^x} \qquad (1)$$

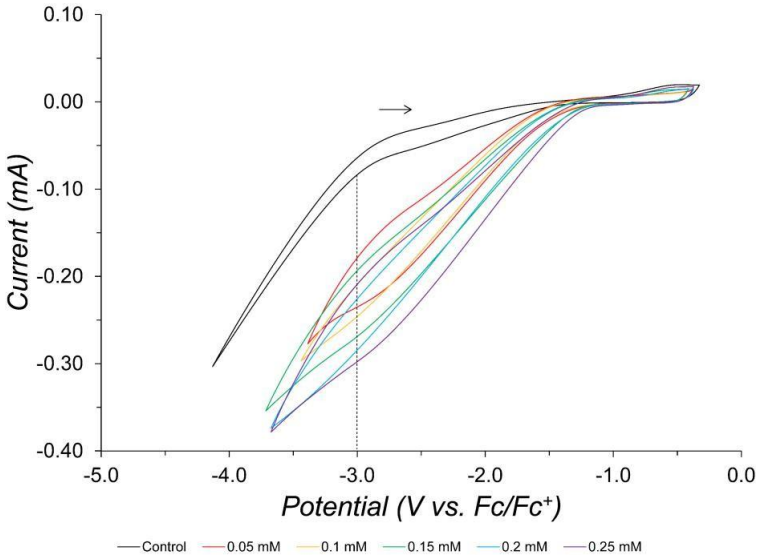

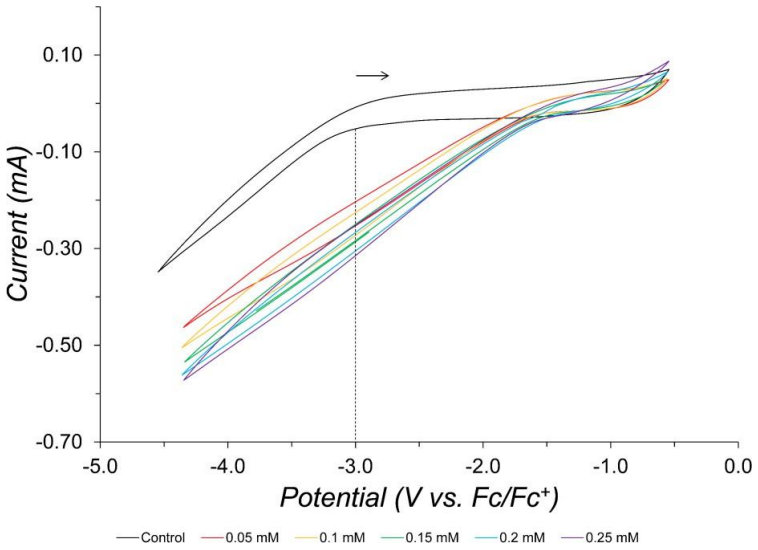

Figure 2.17. Catalytic CVs with increasing catalyst concentration (0.1 M TBAP in THF, 0.05 to 0.25 mM 2 or 3, 45 mM *p*TSA, glassy carbon working electrode, platinum wire counter electrode, 0.01 M AgNO3 reference electrode) for: a) 2 (scan rate = 1 V/s, current for 0.1 to 0.25 mM 2 picked at 3.0 V to limit overlap with background); and b) 3 (scan rate = 8 V/s, current for 0.05 to 0.25 mM 3 picked at 3.0 V to limit overlap with background).

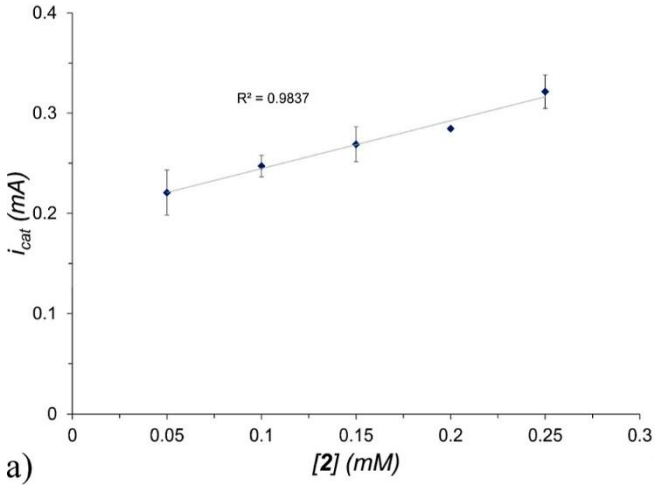

Figure 2.18. Plot of i_{cat} vs. catalyst concentration for 2 (0.1 M TBAP in THF, 0.05 to 0.25 mM 2, 45 mM *p*TSA, glassy carbon working electrode, platinum wire counter electrode, 0.01 M $AgNO_3$ reference electrode, scan rate = 1 V/s).

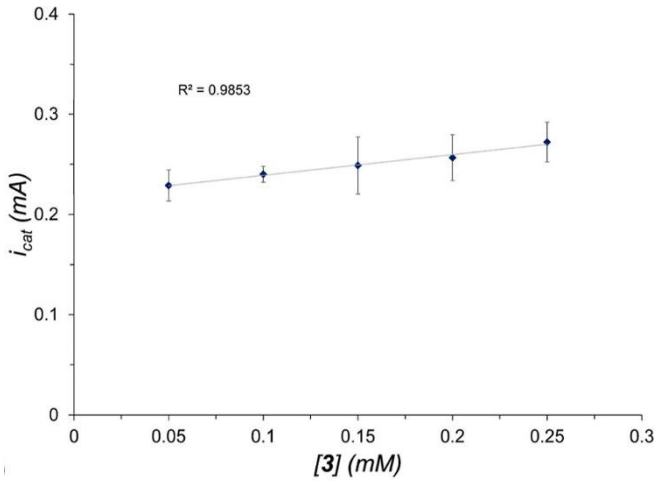

Figure 2.19. Plot of i_{cat} vs. catalyst concentration for 3 (0.1 M TBAP in THF, 0.05 to 0.25 mM 3, 45 mM *p*TSA, glassy carbon working electrode, platinum wire counter electrode, 0.01 M $AgNO_3$ reference electrode, scan rate = 8 V/s).

The effect of water on HER was also explored due to the usage of monohydrated *p*TSA as the proton source, and both 2 and 3 exhibited an increased catalytic current response with the addition of more water equivalents. The monometallic complex displayed the highest current response with *p*TSA.$3H_2O$, while the bimetallic complex displayed the highest response with *p*TSA.H_2O (**Figure 2.20**). Bullock *et al*. reported similar results for nickel diphosphacycloheptane and diphosphacyclooctane complexes bearing pendant amine groups.[60–64] The authors reported a catalytic rate enhancement with the addition of water, and it was attributed to more facile proton delivery through water, which acts as an intermolecular proton relay between the acid substrate and the catalyst that contains bulky substituents.[63,64] Therefore, it is believed that water plays a similar role with respect to the salixpyrrole systems. As we discussed above in 2, the palladium center is sterically hindered by the pendant salen functionalities, which sit above and below the plane of the metal. In 3, cofacial arrangement and bulky *tert*-butyl groups partially restricted the access to the space between the two coordination planes. So, it could be envisioned that water acts as a cocatalyst and enhances the proton transfer from bulky *p*TSA in solution for both 2 and 3.

Interestingly, for 2, there was a slight anodic shift in i_{cat} with the addition of three and four equivalents of water, which was not visible with 3 (**Figure 2.20**). Based on the literature precedent, this suggests that a water-assisted proton transfer was preceding an electron transfer in the rate-determining step for 2. According to Artero *et al*., the cobalt polypyridyl HER electrocatalyst displayed an anodic shift for the Co^{II}/Co^{I} couple upon acid addition, suggesting a coupled chemical reaction like protonation. The catalyst was found to proceed through an ECEC mechanism, where E represents an electron transfer followed by a protonation-like chemical transfer (C). For 2, in particular for three or four equivalents of water with respect to *p*TSA, i_{cat} was measured at the peak current, but for all other cases, including all concentrations of water for 3, i_{cat} was measured at 3.0 V as mentioned before (**Figure 2.21**).

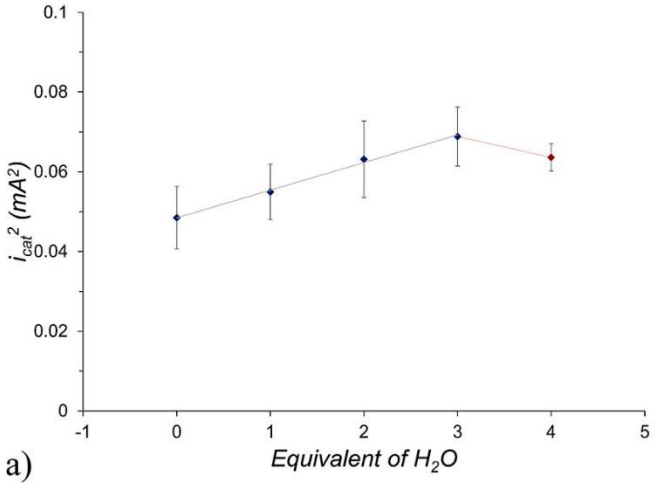

a)

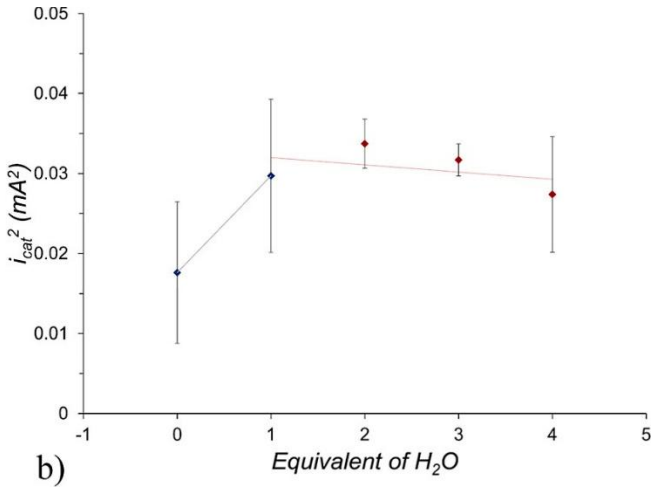

Figure 2.20. Plot of i_{cat}^2 vs equivalents of water with respect to *p*TSA for: a) 2 (0.1 M TBAP in THF, 0.25 mM 2, 45 mM *p*TSA, 0 to 180 mM H_2O, glassy carbon working electrode, platinum wire counter electrode, 0.01 M $AgNO_3$ reference electrode, scan rate = 1 V/s). b) 3 (0.1 M TBAP in THF, 0.25 mM 3, 45 mM *p*TSA, 0 to 180 mM H_2O, glassy carbon working electrode, platinum wire counter electrode, 0.01 M $AgNO_3$ reference electrode, scan rate = 8 V/s).

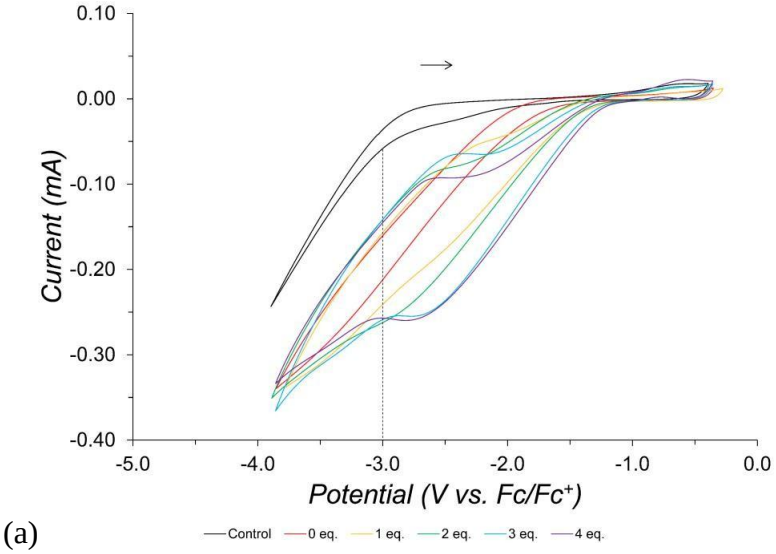

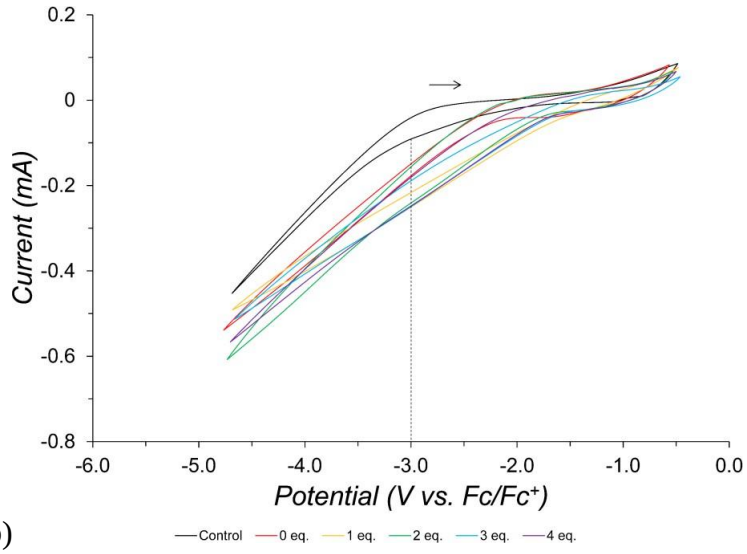

(b)

Figure 2.21. Catalytic CVs with increasing water equivalents with respect to *p*TSA (0.1 M TBAP in THF, 0.25 mM 2 or 3, 45 mM *p*TSA, 0 to 180 mM H2O, glassy carbon working electrode, platinum wire counter electrode, 0.01 M AgNO3 reference electrode) for: a) 2 (scan rate = 1 V/s, current for 0 to 90 mM H2O picked at 3.0 V to limit overlap with background); and b) 3 (scan rate = 8 V/s, current for 0 to 180 mM H2O picked at 3.0 V to limit overlap with background).

Lastly, the acid dependence for salixpyrrole systems was investigated (**Figure 2.22**). Interestingly, for this scenario, the two systems behaved significantly differently from one another. The monometallic system displayed a linear correlation between i_{cat} and acid concentration, while the bimetallic system displayed a linear correlation between i_{cat} and the square root of acid concentration (**Figure 2.23**). According to Eq. 1, 2 indicated a second-order dependence with an acid independence point around 60 mM of *p*TSA, while 3 indicated a first-order dependence with an acid independence point around 40 mM of *p*TSA.

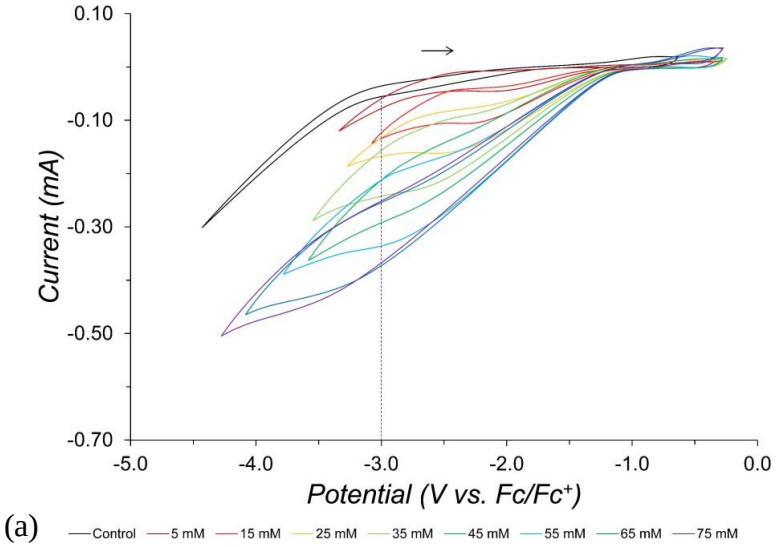

(a)

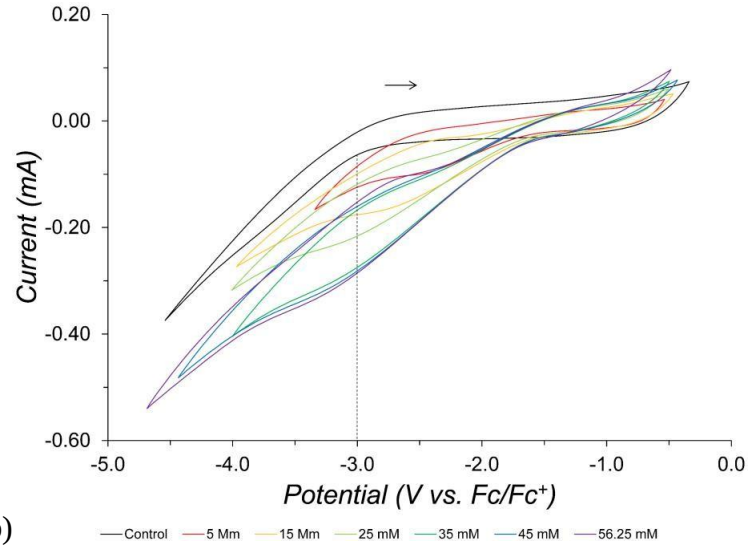

(b)

Figure 2.22. Catalytic CVs with increasing acid concentration (0.1 M TBAP in THF, 0.25 mM 2 or 3, glassy carbon working electrode, platinum wire counter electrode, 0.01 M AgNO3 reference electrode) for: a) 2 (5 to 75 mM *p*TSA, scan rate = 1 V/s, current for 55 mM *p*TSA and above picked at 3.0 V to limit overlap with background); and b) 3 (5 to 56.25 mM *p*TSA, scan rate = 8 V/s, current for 25 mM *p*TSA and above picked at 3.0 V to limit overlap with background).

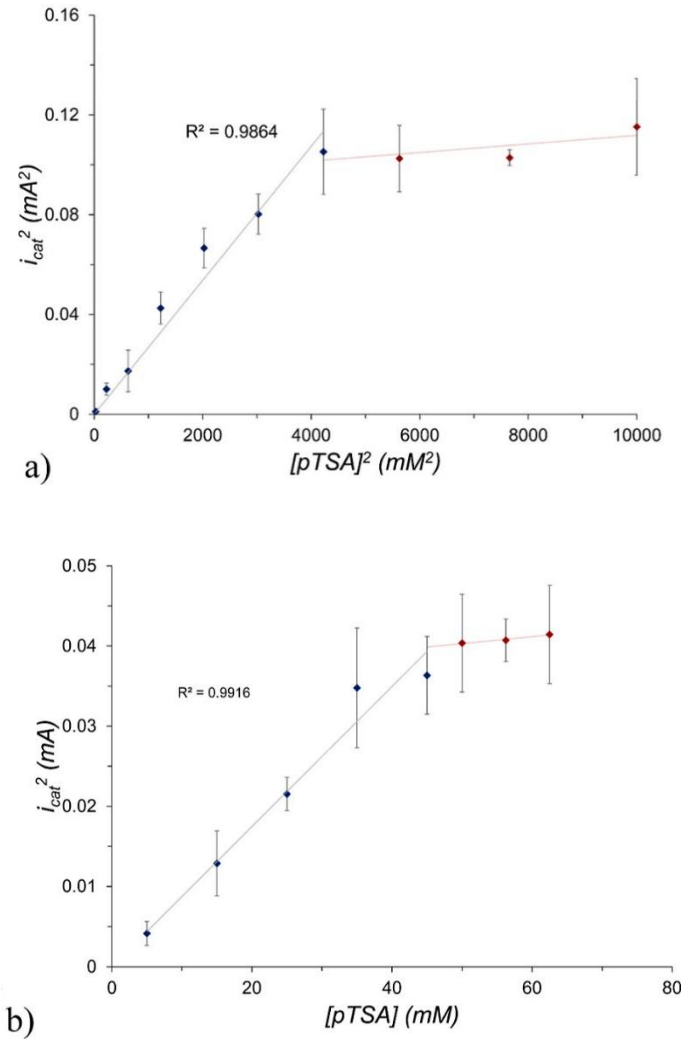

Figure 2.23. Plot of i_{cat}^2 vs acid concentration for: (a) 2 (0.1 M TBAP in THF, 0.25 mM 2, 5 to 87.5 mM *p*TSA, glassy carbon working electrode, platinum wire counter electrode, 0.01 M $AgNO_3$ reference electrode, scan rate = 1 V/s). (b) 3, 5 to 62.5 mM *p*TSA, glassy carbon working electrode, platinum wire counter electrode, 0.01 M $AgNO_3$ reference electrode, scan rate = 8 V/s).

Once the optimized conditions were achieved, other important parameters like turnover frequency (TOF), overpotential, and faradaic efficiency were calculated. The TOF for homogeneous catalysts like salixpyrrole was calculated using eq 5 (v = scan rate), which is a simplified version of the equations below.[65] The Randle-Sevcik equation (eq 2)provides the relationship between the peak current i_p and catalytic concentration, where v is the scan rate in

the absence of acid, R is the ideal gas constant, T is the temperature in K (298 K), n is the number of electrons transferred in HER (2), the factor of 0.4463 is related to the diffusion equations.[66]

$$i_p = 0.4463FA[cat]\sqrt{\frac{F\nu D}{RT}} \quad \textbf{(2)}$$

Thus, the ratio between catalytic and peak current (i_{cat}/i_p) can be obtained from the quotient eq 1 and eq 2.

$$\frac{i_{\text{cat}}}{i_{\text{p}}} = \frac{n}{0.4463}\sqrt{\frac{RTk[H^+]^x}{F\nu}} \quad \textbf{(3)}$$

Under pseudo-first-order conditions, $k_{obs} = k[H^+]^2$ equation simplifies to eq 4.[67]

$$\frac{i_{\text{cat}}}{i_{\text{p}}} = \frac{n}{0.4463}\sqrt{\frac{RTk_{obs}}{F\nu}} \quad \textbf{(4)}$$

Then, eq 4 can be simplified to eq 5 under optimized conditions.

$$k_{\text{obs}} = TOF_{\text{max}} = \left(1.94\ V^{-1}\right)\nu\left(\frac{i_{\text{cat}}}{i_{\text{p}}}\right)^2 \quad \textbf{(5)}$$

All the above equations that can be used to calculate TOF, are best suited for electrocatalysts under "pure kinetic conditions" where an S-shaped catalytic wave that is scan rate independent is easily observed. Although the CVs reported for this project show plateau current at low acid concentrations at optimized conditions, data collected at higher acid concentrations no longer displayed S-shaped waves. This can be attributed to the proximity of the catalytic wave to the edge of the solvent window and the overlap with the direct reduction of *p*TSA at the glassy carbon electrode. One of the alternative methods developed to determine

TOF for electrocatalysts that do not operate under pure kinetic conditions is the foot of the wave analysis (FOWA) method, which requires an accurate measurement of $E_{1/2}$ for the catalyst in the absence of substrate. As discussed above, according to our data, it is not possible for 2 and 3 to FOWA to calculate TOF.[65,68–71] Therefore, despite the absence of S-shaped waves, the TOF was calculated by using Eq. 5 according to Dempsey and co-workers' recent review.[72,72,73] The authors have reported that this method is still applicable to TOF calculations as an initial assessment of catalytic performance. Moreover, they also reported that calculating TOFs in this way for nonideal systems was inherently conservative, as it underestimated rate constants. The calculated TOFs for 2 and 3 were found to be 1680 ± 120 and 4640 ± 840 s^{-1}, respectively. Despite the resulting higher current response with *p*TSA.3H_2O, the *p*TSA.H_2O was used to calculate these measurements due to increased background overlapping at optimized conditions (**Figure 2.24**). Although these values are not as large as the many reported HER catalysts such as the fastest HRE catalyst reported by Bullock and co-workers which had TOF of 100,000 s^{-1},[60–64] the salixpyrrole system can be considered quite active, and comparatively favorable for HER, like many known HER electrocatalysts from Artero,[74,75] Grapperhaus,[65,76,77] and many others.[78–85] It was also quite impressive that the bimetallic system was almost three times faster than the monometallic system, or 40% faster on a per Pd atom basis.

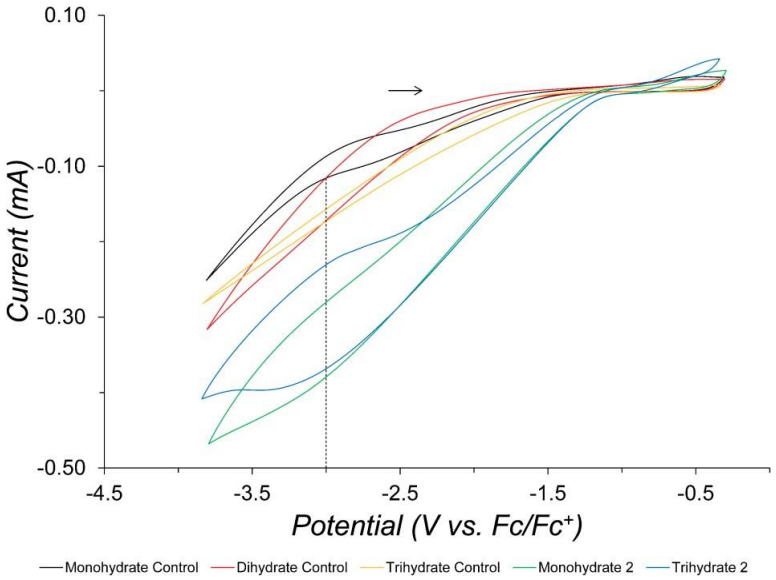

Figure 2.24. Catalytic CVs showing the increase in background overlap with increasing water concentrations using 65 mM *p*TSA (0.1 M TBAP in THF, 0.25 mM 2, 0 to 130 mM additional H2O added, glassy carbon working electrode, platinum wire counter electrode, 0.01 M $AgNO_3$ reference electrode, scan rate = 1 V/s). Therefore, the values used to calculate TOF for 2 were picked at 3.0 V using 65 mM *p*TSA without additional H_2O to limit overlap with the background.

At optimized conditions, the homogenous catalysts 2 and 3 operate at an overpotential of 0.39 ± 0.2 and 0.69 ± 0.4 V, respectively, moreover, 3 displayed a much lower overpotential than 2. These overpotentials were calculated using established procedures from Appel and Helm (see experimental section for calculations).[86] The experimentally determined pK_a for monohydrate *p*TSA in THF was found to be 11.8.[87] Interestingly, the overpotential for 3 was significantly smaller compared to many known HER catalysts, including the diphosphacycloheptane systems developed by Bullock *et al*. which had overpotentials of 0.7 V.[63,64] These results confirmed that complex 3 was not only much faster and more active than 2 but also much more efficient and required less energy input.

Controlled potential electrolysis (CPE) studies were carried out to figure out the stability and faradaic efficiency of salixpyrrole systems. For 2, the calculated faradaic efficiency was 90.5

± 5.8% while for 3 it was 91.7 ± 2.5% (see experimental section for calculations). Both systems displayed a linear increase in charge transfer versus time, resulting in a stable current response for CPE over time, indicating the catalysts were relatively stable under the reaction conditions. They did not undergo large structural changes during the catalytic cycle (**Figure 2.25** and **Figure 2.26**). Once again, the bimetallic catalyst was proven to be more desirable compared to its monometallic analog, with a larger proportion of the charge productivity generating the desired product.

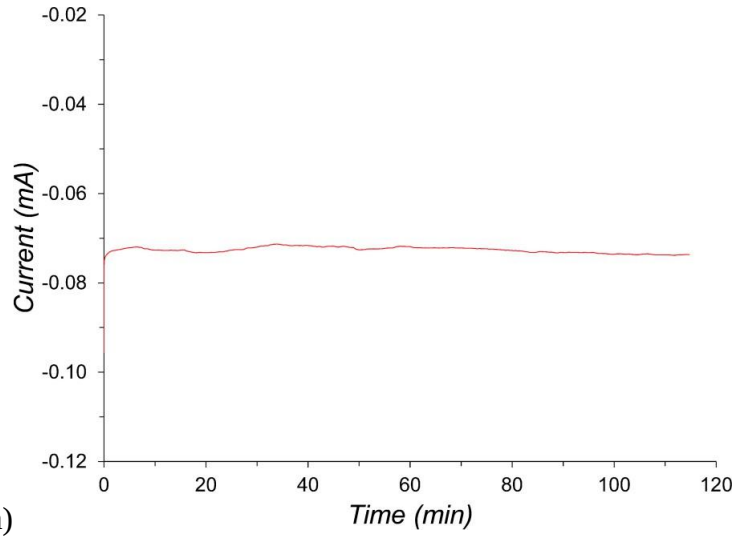

(a)

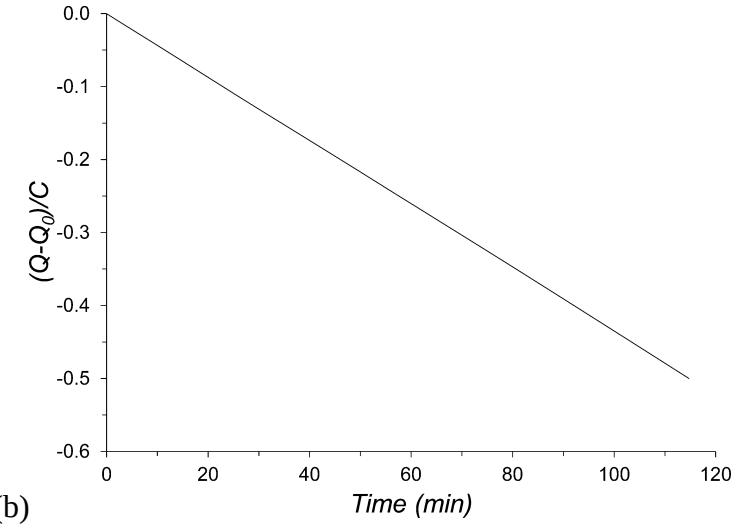

(b)

Figure 2.25. A representative controlled potential electrolysis experiment in THF (0.2 M TBAP, 0.25 mM 2, and 65 mM *p*TSA with a 6 mm glassy carbon rod working electrode, 0.01 M $Ag/AgNO_3$ reference electrode; 0.1M TBAP, 65 mM ferrocene with a 6 mm graphite counter electrode; 0.5 C of charge passed, potential held at -3.00 V vs. Fc/Fc^+) showing: a) current vs time; b) normalized charge transferred vs. time.

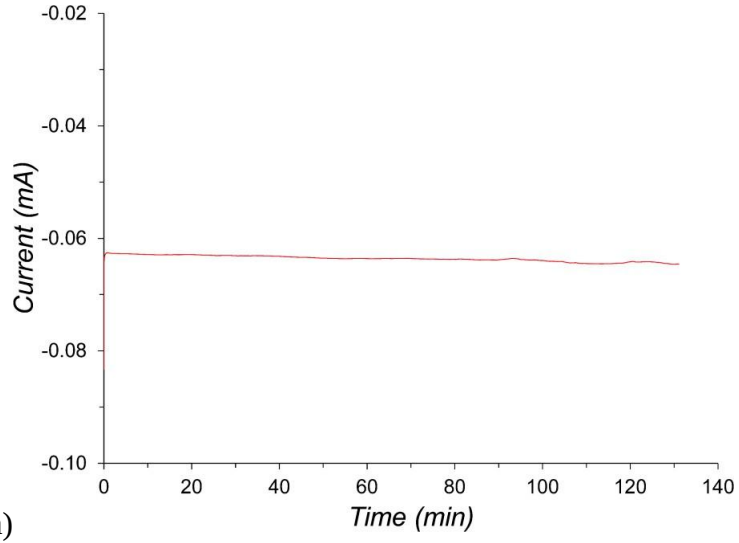

(a)

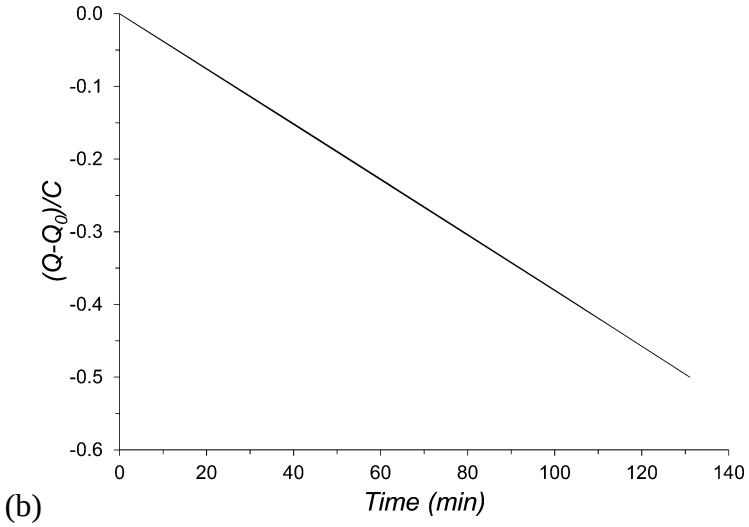

(b)

Figure 2.26. A representative controlled potential electrolysis experiment in THF (0.2 M TBAP, 0.25 mM 3, and 45 mM *p*TSA with a 6 mm glassy carbon rod working electrode, 0.01 M $Ag/AgNO_3$ reference electrode; 0.1M TBAP, 45 mM ferrocene with a 6 mm graphite counter electrode; 0.5 C of charge passed, potential held at -3.00 V vs. Fc/Fc^+) showing: a) current vs. time; b) normalized charge transferred vs. time.

2.3.6. Mechanistic implications

To further understand the mechanism of hydrogen evolution using salixpyrrole systems, kinetic isotope effect (KIE) studies were carried out in the presence of *p*TSA-d_1.D_2O or *p*TSA-d_3 (**Figure 2.27**). The rate constants derived from Eq. 3 were used to obtain KIE values. For 2, the obtained H/D KIE value was 1.33 ± 0.08, whereas for 3 it was 1.13 ± 0.13. Both complexes displayed smaller KIE values, which were distinct from inverse KIEs that were reported for some metal-hydrides HER catalysts as well as from larger KIEs associated with electrocatalysts thought to be proceeding through proton shuttling.[88,89] Therefore, it is believed that the salixpyrroles systems were displaying secondary KIE values, indicating that H/D bond breaking was not involved in the rate-determining step.[90] A similar H/D KIE value was observed for zinc-based thiosemicarbazone electrocatalysts that affected both HER and hydrogen oxidation in methanol in the presence of acetic acid and triethylamine, respectively.[77] It was found that for zinc systems,

the ligand reduction and the coupling of reduced thiosemicarbazone radical intermediates were critical for catalytic activity.

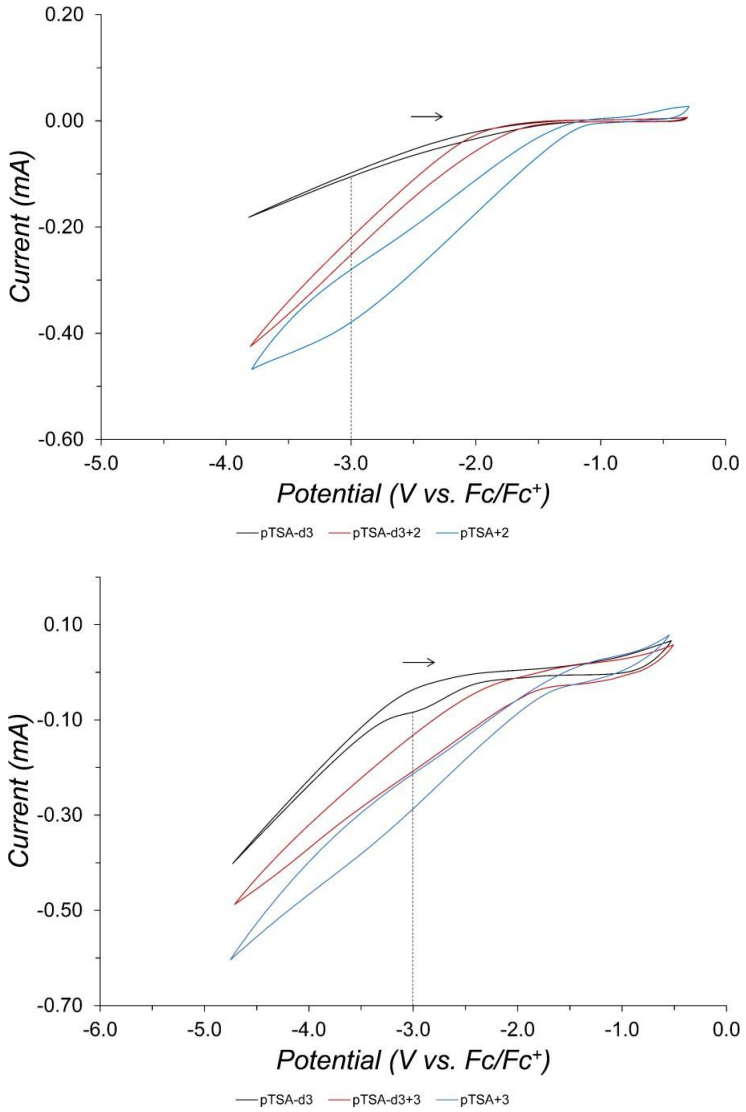

Figure 2.27. CVs of H/D KIE experiments (0.1 M TBAP in THF, 0.25 mM 2 or 3, glassy carbon working electrode, platinum wire counter electrode, 0.01 M $AgNO_3$ reference electrode) for: a) 2 (65 mM *p*TSA or *p*TSA-d_3, scan rate = 1 V/s, current picked at 3.0 V to limit overlap with background); and b) 3 (45 mM *p*TSA or *p*TSA-d_3, scan rate = 8 V/s, current picked at 3.0 V to limit overlap with background).

Initially, it was believed that the pendant salen phenol moieties in 2 could act as proton shuttles and participate in proton-coupled electron transfer (PCET). Although a PCET process

after the rate-determining step would still be possible with experimental results for 2, it is unlikely that it could occur beforehand due to the small KIE value observed. It is possible that the hydrogen bonding that was seen between salen imine and phenol moieties in the crystal structure of 2 is strong enough to prevent the hydroxyl group from participating in proton shuttles. Based on the results obtained from kinetic studies and KIE values, two protonations preceded the rate-determining step, which does not involve bimolecular hydrogen production (first-order dependence with respect to the catalyst was observed for 2). Further mechanistic studies are anticipated to further elucidate the mechanism of action for monometallic system 2 as there is limited literature to support it. Additionally, the hydrolysis of the free imine functionality (salen imine) was an initial concern for 2 due to the reaction conditions that were used for HER. But, based on CPE results and spectroscopic evidence (UV-vis), it was confirmed that complex 2 is stable in the presence of *p*TSA in optimized conditions (**Figure 2.28**). It is also believed that the hydrolysis of 2 is not occurring to any significant extent. In particular, it was confirmed that the hydrolysis of both salen pendant groups to generate starting material 1 seems impossible considering the homogenous nature of 2 for HER, as 1 seems to generate a heterogeneous HER catalyst in the presence of *p*TSA.[47]

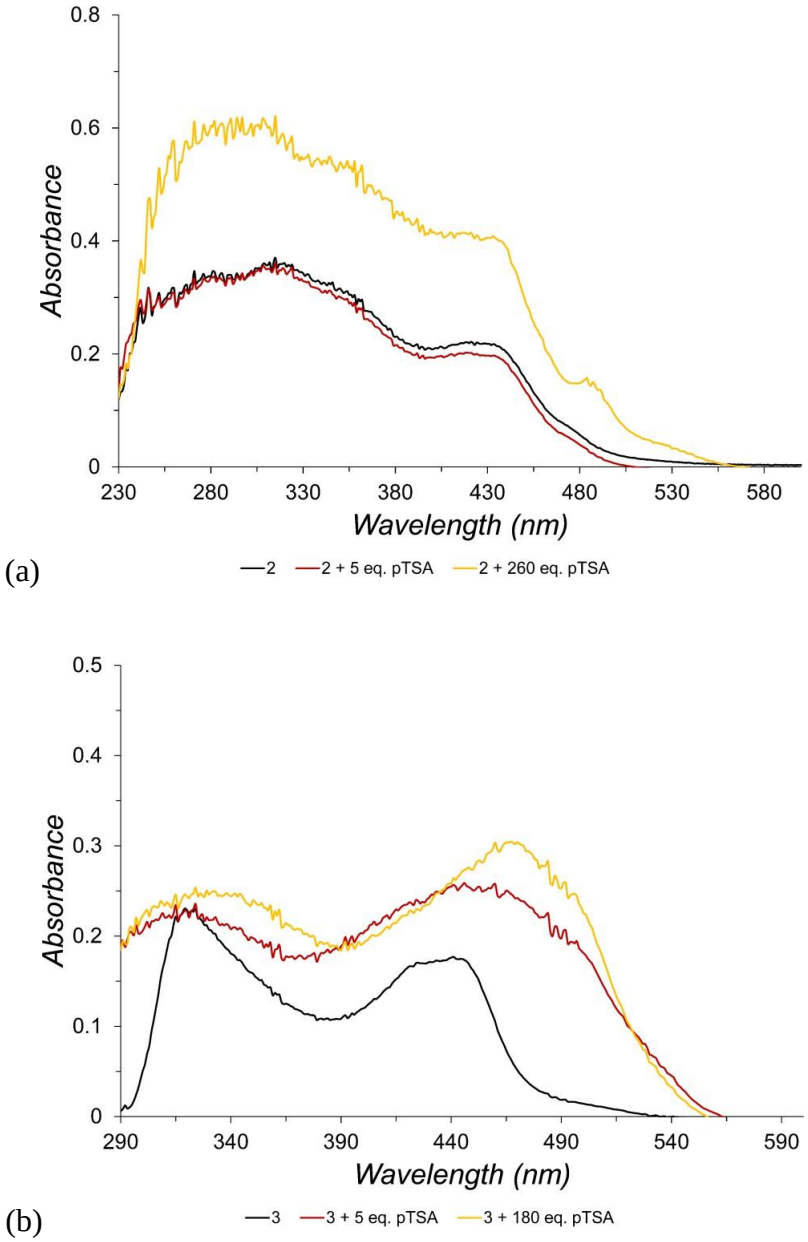

Figure 2.28. UV-vis spectra of: a) 2, 2 with 5 equivalents of *p*TSA, and 2 with 260 equivalents of *p*TSA in THF; and b) 3, 3 with 5 equivalents of *p*TSA, and 3 with 180 equivalents of *p*TSA in THF.

On the other hand, the bimetallic complex 3 displayed first-order dependency with respect to acid, whereas the monometallic complex showed second-order dependency, which indicates that the two complexes follow distinct catalytic pathways from each other. Considering faster kinetics and lower overpotential value upon coordination of extra palladium metal, it can be

hypothesized that having two metal centers is critical for catalytic performance. Due to less literature precedent about palladium-based salen HER electrocatalysts, it is difficult to predict how the two planes of the salixpyrrole system interact with the proton source to produce hydrogen. It can be envisioned that the bimetallic complex would act similarly to the zinc thiosemicarbazone HER electrocatalyst, as it also displayed a first-order dependence on the catalyst and acid.[77] The authors have reported that the Zn complex facilitates the HER through ligand-centered radical coupling compared to the usual metal-hydride formation as the key intermediate. The reaction mechanism involves protonation and reduction to produce a ligand-centered radical, possibly on one or more imine moieties, followed by fast inter- or intramolecular coupling and then hydrogen evolution to complete the catalytic cycle. According to the observed kinetic data for the salixpyrrole system, it is possible to consider other alternative pathways, such as the formation of the most common metal-hydride intermediates or full reduction of one of the ligand arms to generate an amide. According to the literature, the latter is more feasible, which is proved by theoretical calculations using density functional theory for nickel calixpyrrole analogue.[91] Future mechanistic studies are yet to be done to get a clear idea.

The increased activity was seen for 3 compared to 2, widening up whole new possibilities for catalyst design. The activation of the catalyst can be tuned not only by ligand architecture but also with various combinations of metals. Therefore, the scope for modifying the cofacial salixpyrrole system is beyond the monometallic catalyst or the traditional symmetric “pacman” system. The study to examine heterobimetallic unsymmetric analogs of 3 is underway.

2.4. Conclusion

In summary, mono- and bimetallic complexes bearing unsymmetric ligands with calixpyrrole and salen coordination binding pockets, or "salixpyrrole" complexes **2** and **3**, respectively, were synthesized, fully characterized, and their electrochemical properties were studied. Unlike traditional unsymmetric co-facial "pacman" porphyrin systems, the salixpyrrole species could be generated in a straightforward and relatively high-yielding Schiff-base reaction using the previously reported palladium calixpyrrole complex **1** as a starting material.

Both **2** and **3** were found to be active HER electrocatalysts in the presence of *p*TSA, even though the onset of catalysis did not correlate with any electrochemical features in the absence of substrate. The monometallic salixpyrrole species was found to follow a second-order dependence on acid concentration and a first-order dependence on the catalyst, ruling out a bimolecular pathway for hydrogen production. Additionally, TOFs up to 1680 s^{-1} were displayed, with an overpotential of 0.69 V and a faradaic efficiency of 90.5%. Moreover, a H/D KIE value of 1.33 was measured for **2**, indicating that H/D bond-breaking was not involved in the rate-determining step.

For the bimetallic complex **3**, on the other hand, a completely different mechanism of action was uncovered. The bimetallic system was found to be first-order in both acid and catalyst. Furthermore, a H/D KIE value of 1.13 was seen, which was very similar to a zinc thiosemicarbazone HER catalyst that operated through a ligand-based radical and bimolecular hydrogen production.[66] It was thought that **3** could proceed through a similar catalytic mechanism based on the results from the kinetic investigations. A dramatic increase in TOFs (4640 s^{-1}) and a more modest increase in faradaic efficiency (91.7%), as well as a significant decrease in

overpotential (0.39 V), were also seen for **3,** in comparison to **2**. This suggested that coordination of the second palladium center greatly enhanced catalytic efficiency.

These results gave critical insight into ligand/catalyst design in that a bimetallic co-facial catalyst with chemically distinct binding sites generated a superior catalytic system in comparison to its monometallic analogue. Moreover, previously reported palladium-based symmetric calixpyrrole "pacman" complexes were not reported to be catalytically active for any transformation.[46] Therefore, the unsymmetric nature of the salixpyrrole species was also found to impart distinct chemical reactivity to the systems reported herein. Further studies aimed at elucidating the exact mechanisms of action for **2** and **3**, as well as the catalytic activity of heterobimetallic salixpyrrole systems, are currently underway.

2.5. Experimental section

2.5.1. General considerations

All procedures and manipulations were performed under an argon or nitrogen atmosphere using standard Schlenk-line and glove box techniques unless stated otherwise. Solvents were dried and deoxygenated under argon using a LC Technology Solutions Inc. SP-1 stand-alone solvent purification system. All alcohols were dried and distilled over activated magnesium (magnesium turnings and a crystal of iodine) under a nitrogen atmosphere. Deuterated solvents were purchased from Cambridge Isotope Laboratories, Sigma Aldrich, Acros Organics, or Alfa Aesar, degassed, and dried over activated molecular sieves prior to use. **1** was synthesized according to a literature procedure (spectroscopic characterization matched reported data),[43] and anhydrous *para*-toluenesulfonic acid was prepared by treating *para*-toluenesulfonic anhydride with one equivalent of H_2O. All other reagents were purchased from commercial sources and utilized without further purification unless stated otherwise. NMR spectra were recorded at ambient temperature and

pressure using a Bruker 400 MHz spectrometer (400 MHz for ^{1}H and 101 MHz for ^{13}C). The ^{1}H and ^{13}C NMR spectra were measured relative to partially deuterated solvent peaks, but are reported relative to tetramethylsilane (TMS). Elemental analyses were performed at the University of Rochester, Department of Chemistry, on a PerkinElmer 2400 Series II Analyzer. All crystals were mounted in inert oil and transferred to the cold gas stream of a diffractometer. Single crystal X-ray data were collected using a Rigaku XtaLAB Synergy-S diffractometer equipped with a HyPix-6000HE Hybrid Photon Counting (HPC) detector and dual Mo and Cu microfocus sealed X-ray source (Cu Kα λ = 1.54184 Å). The data collection strategy was calculated using CrysAlisPro to ensure desired data redundancy and percent completeness. Unit cell determination, initial indexing, data collection, frame integration, Lorentz-polarization corrections and final cell parameter calculations were carried out using CrysAlisPro. An absorption correction was performed using the SCALE3 ABSPACK scaling algorithm embedded within CrysAlisPro. The structures were solved using the ShelXT structure solution program using Intrinsic Phasing and refined by Least Squares using the ShelXL program. All non-hydrogen atoms were refined anisotropically. Hydrogen atom positions were calculated geometrically and refined using the riding model. Olex2 was used for the preparation of the publication materials. Cyclic voltametric measurements were recorded using a Bio-Logic model SP-50 potentiostat. Tetrabutylammonium hexafluorophosphate (TBAP) was used as the supporting electrolyte and was recrystallized prior to use by slow addition of pentane into a THF solution followed by cooling in a freezer (-30 °C). The working electrode was a glassy carbon electrode or a mercury pool electrode; the reference electrode was a $Ag/AgNO_3$ non-aqueous electrode (0.01 M in CH_3CN with 0.1 M TBAP); and a platinum wire or graphite rod was used as the counter electrode. The glassy carbon electrode was polished with 0.05 μm alumina and washed with distilled water prior to each measurement.

Electrochemical measurements were conducted at room temperature under an argon or nitrogen atmosphere and processed using EC-Lab V11.21. Reported half-wave potentials were referenced to the Fc/Fc^+ redox couple by adding high purity ferrocene to the sample solution. Controlled potential electrolysis experiments were also performed with a Biologic SP-50 model potentiostat and processed using EC-Lab V11.21. The working electrode was a 6 mm glassy carbon rod, the counter electrode was a 6 mm graphite rod, and the reference electrode was a 0.01 M $Ag/AgNO_3$ non-aqueous electrode (0.01 M in CH_3CN with 0.1 M TBAP). The amount of hydrogen produced was quantified using an ATO Inc. model ATO-SKY2000-H2 handheld gas detector (0 to 500 ppm) and a calibration curve derived from known volumes of ultra-high purity hydrogen gas (Airgas).

2.5.2. Synthesis of 2

A solution of 0.200 g (0.313 mmol) of **1** in approximately 2 mL of THF was added to a solution of 0.334 g (1.878 mmol) of 3-*tert*-butylsalicylaldehyde in approximately 1 mL of THF charged with 3Å activated molecular sieves. A catalytic amount of pyrrolidine was added (0.3 mL of 10 mol% pyrrolidine in DCM) and the color of the solution immediately turned from orange to dark red. The reaction mixture was stirred overnight and then approximately 10 mL of pentane was added. After stirring the suspension for an additional 1 h the solvent was decanted. This step was repeated three times, and the precipitation was isolated by filtration. The orange powder was washed with 2 x 10 mL pentane to remove any unreacted 3-*tert*-butylsalicylaldehyde. The product was dissolved in approximately 10 mL of DCM and filtered to remove the 3Å activated molecular sieves. The filtrate was dried under reduced pressure to give **2** as an orange solid. Yield: 0.155 g (51.2%). Crystals suitable for single crystal X-ray diffraction studies were grown from the slow evaporation of a pentane/dichloromethane solution of **2**. **^{1}H NMR** (400 MHZ, $CDCl_3$) δ: 8.19 (s, 2H, imine-CH), 7.49 (s, 2H, imine-CH), 7.32 (d, 2H, aromatic-CH, J = 7.5 Hz), 7.25 – 7.21 (m,

4H, aromatic-CH), 7.19 – 7.14 (m, 6H, aromatic-CH), 7.08 (d, 2H, aromatic-CH, *J* = 7.5 Hz), 7.00 – 6.98 (m, 6H, aromatic-CH), 6.82 – 6.75 (m, 4H, aromatic-CH and pyrrole-CH), 6.45 (dd, 2H, aromatic-CH, *J* = 6.0, 3.2 Hz), 5.91 (d, 2H, pyrrole-CH, *J* = 7.5 Hz), and 1.27 (s, 18H, C-(CH_3)$_3$) ppm. **^{13}C NMR** (101 MHz, $CDCl_3$) δ: 163.02 (imine-CH), 160.44 (aromatic-C), 159.30 (imine-CH), 150.32 (aromatic-C), 146.78 (aromatic-C), 143.06 (aromatic-C), 142.51 (aromatic-C), 137.76 (d, aromatic-C), 137.24 (d, aromatic-C), 130.51 (aromatic-CH), 130.11 (aromatic-CH), 129.36 (aromatic-CH), 127.53 (aromatic-CH), 126.78 (aromatic-CH), 126.14 (aromatic-CH), 126.14 (aromatic-CH), 124.40 (aromatic-CH), 119.00 (aromatic-C), 118.78 (aromatic-CH), 118.41 (aromatic-CH), 117.91 (pyrrole-CH), 112.33 (pyrrole-CH), 62.15 (*C*-Ph_2), 34.72 (*C*-(CH_3)$_3$), and 29.13 (C-(*C*H_3)$_3$) ppm. Elemental analysis calcd for $C_{57}H_{52}N_6O_2Pd$·0.33DCM: C, 69.71, H, 5.37, N, 8.51, found: C, 69.51, H, 5.36, N, 8.36.

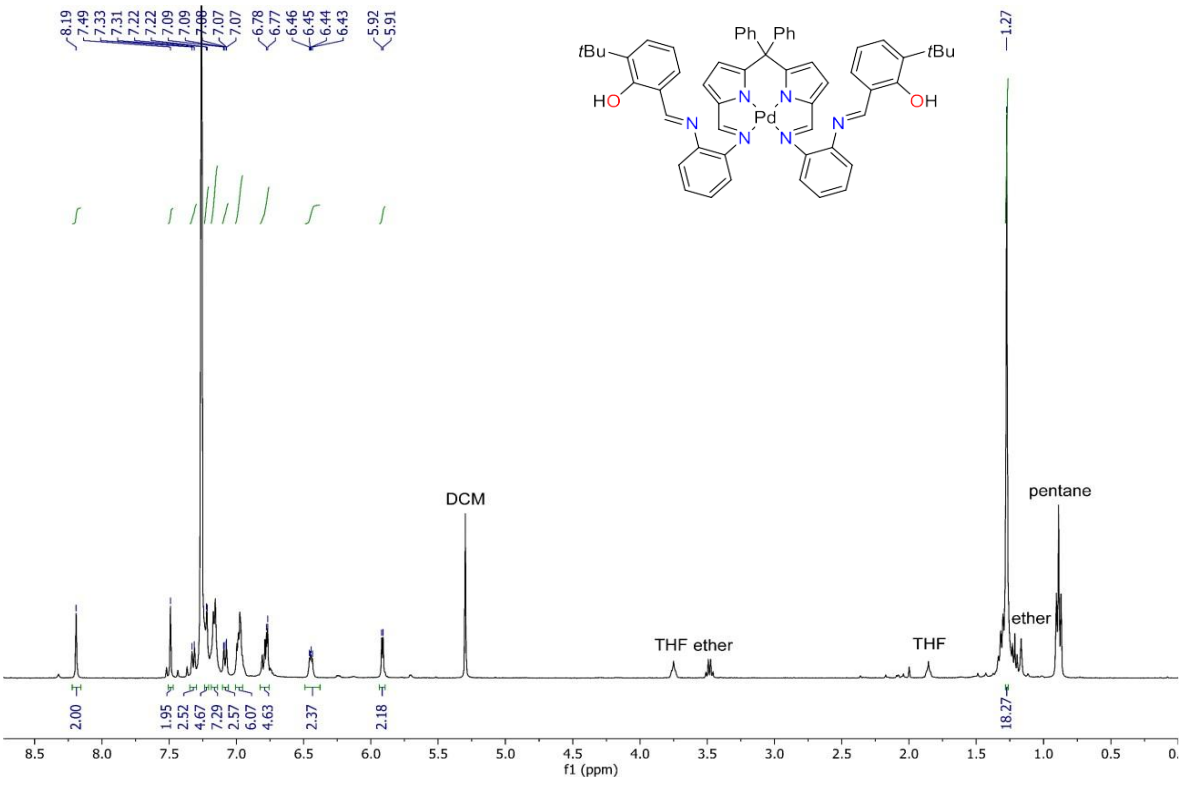

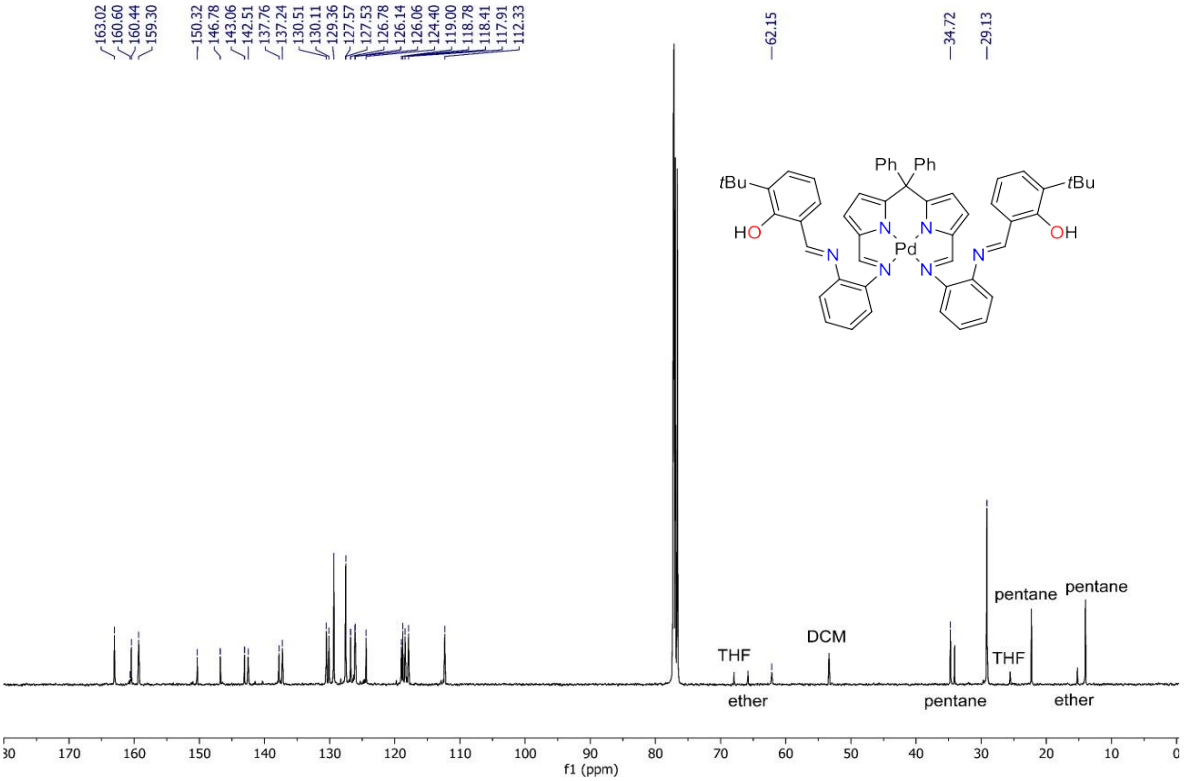

Figure 2.29. ^{1}H NMR spectrum (400 MHz, $CDCl_3$) of 2 (top), ^{13}C NMR spectrum (101 MHz, $CDCl_3$) of 2 (bottom).

2.5.3. Synthesis of 3

A solution of 0.100 g (0.445 mmol) of $Pd(OAc)_2$ in approximately 2 mL of DCM was added to a solution of 0.100 g (0.104 mmol) of **2** in approximately 2 mL of DCM. A solution of 0.017 g (0.210 mmol) of Li*O*t*Bu in approximately 1 mL of THF was then added, followed by another 5 mL of DCM. The reaction mixture was stirred for 2 hours, Celite was added, and then stirred for another 30 min. The solution was filtered to remove Pd-black and Celite. The filtrate was dried under reduced pressure to give a dark red residue. The product was dissolved in approximately 2 mL of DCM, and another portion of $Pd(OAc)_2$ (0.100 g in 2 mL of DCM), Li*O*t*Bu (0.017 g in 1 mL of THF), and 5 ml of DCM were added. The previous steps were then repeated yielding a dark red residue. The product was dissolved in a minimum amount of THF (around 3 mL) and layered with pentane (around 3 mL). A black precipitate formed immediately

after layering, which was removed by filtration through Celite. The clear orange filtrate was then placed in a freezer (-30 °C) overnight. The orange solid was collected by filtration and dried under reduced pressure to give **3**. Yield: 0.052 g (47.2%). Crystals suitable for single crystal X-ray diffraction studies were grown from the slow evaporation of a pentane/tetrahydrofuran solution of **3**. **^{1}H NMR** (400 MHz, $CDCl_3$) δ: 7.54 (s, 2H, imine-CH), 7.31-7.28 (m, 2H, aromatic-CH), 7.23 - 7.16 (m, 8H, aromatic-CH and imine-CH), 7.08 (d, 2H, aromatic-CH, *J* = 8.2 Hz), 7.05 (d, 2H, aromatic-CH, *J* = 5.9 Hz), 6.95 – 6.87 (m, 6H, aromatic-CH), 6.84 – 6.77 (m, 4H, aromatic-CH and pyrrole-CH), 6.64 (d, 2H, aromatic-CH, *J* = 7.8 Hz), 6.32 (t, 2H, aromatic-CH, *J* = 7.5 Hz), 5.84 (d, 2H, pyrrole-CH *J* = 4.0 Hz), and 1.42 (s, 18H, C-$(CH_3)_3$) ppm. **^{13}C NMR** (101 MHz, $CDCl_3$) δ: 169.86 (imine-CH), 164.89 (aromatic-C), 159.22 (imine-CH), 152.39 (aromatic-C), 146.39 (aromatic-C), 145.27 (aromatic-C), 144.00 (aromatic-C), 141.25 (aromatic-C), 140.38 (aromatic-C), 138.12 (aromatic-C), 132.64 (aromatic-CH), 132.43 (aromatic-CH), 129.48 (aromatic-CH), 129.17 (aromatic-CH), 127.65 (aromatic-CH), 127.54 (aromatic-CH), 127.42 (aromatic-CH), 126.57 (aromatic-CH), 126.36 (aromatic-C), 126.32 (aromatic-C), 126.18 (aromatic-CH), 124.65 (aromatic-CH), 121.19 (aromatic-C), 119.29 (pyrrole-CH), 114.75 (aromatic-CH), 113.42 (pyrrole-CH), 62.82 (*C*-Ph_2), 35.68 (*C*-$(CH_3)_3$), and 29.85 (C-(*C*$H_3)_3$) ppm. Elemental analysis calcd for $C_{57}H_{50}N_6O_2Pd_2$·0.33DCM: C, 63.05, H, 4.68, N, 7.69, found: C, 63.01, H, 4.58, N, 7.32.

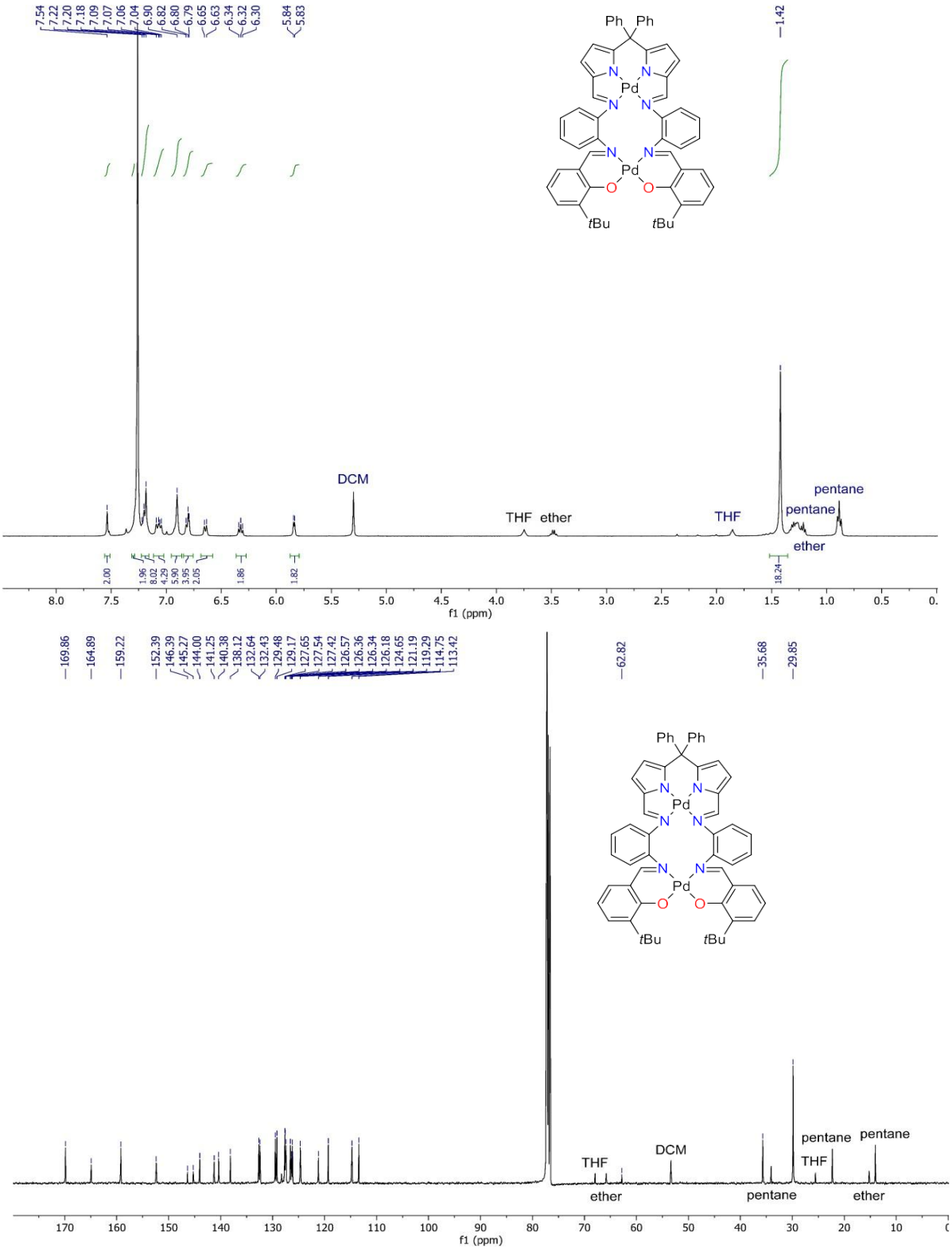

Figure 2.30. ^{1}H NMR spectrum (400 MHz, $CDCl_3$) of 3 (top), ^{13}C NMR spectrum (101 MHz, $CDCl_3$) of 3 (bottom).

Table 2.3. Selected Crystal Data, Data Collection, and Refinement Parameters for 2 and 3.

	2	**3**
Empirical formula	$C_{57}H_{52}N_6O_2Pd$	$C_{57}H_{50}N_6O_2Pd_2$
FW	959.44	1063.83
lattice type	monoclinic	Monoclinic
space group	C2	$P2_1/c$
T, K	200.0(1)	180.0(1)
a, Å	23.1945(2)	13.5236(2)
b, Å	14.65309(13)	16.6893(3)
c, Å	6.73346(6)	20.9406(5)
α, deg	90	90
β, deg	91.9239(8)	95.6763(18)
γ, deg	90	90
V, $Å^3$	2287.22(3)	4703.12(16)
Z	2	4
ρ_{calc}/Mg m^{-3}	1.393	1.502
μ(Cu/Mo, Kα) mm^{-1}	3.673 (Cu)	6.566 (Cu)
F(000)	996.0	2168
cryst size, mm^3	0.07 x 0.042 x 0.018	0.129 x 0.007 x 0.004
range θ collected, deg	7.136 to 155.596	3.284 to 77.372
reflns collected/unique	28657/4897	31843/9236
abs cor	Semi-empirical from equivalents	
Max and min transmn coeff.	1.000 and 0.87625	1.000 and 0.640
goodness of fit	1.063	1.063

R1(I>2σ(I))a	0.0202	0.0435
wR2 (all data)a	0.0499	0.1137
peak and hole, e Å-3	023 and -0.41	0.726 and -1.19

[a] Definition of R indices: $R_1 = \Sigma(F_O - F_C)/\Sigma(F_O)$; $wR_2 = [\Sigma[w(F_O^2 - F_C^2)^2]/[\Sigma[w(F_O^2)^2]]^{1/2}$

2.5.4. Electrocatalytic H_2 evolution

The electrochemical conditions of the catalytic trials included 0.1 M TBAP electrolyte in THF, 0.05 mM to 0.25 mM of **2** or **3**, 5 to 350 equivalents of *para*-toluenesulfonic acid monohydrate (*p*TSA, 5 to 87.5 mM), and scan rates between 20 mV/s to 20 V/s. The three-electrode setup consisted of a glassy carbon working electrode, a platinum wire or graphite rod counter electrode, and a 0.01 M $Ag/AgNO_3$ reference electrode. All CVs were referenced versus the Fc/Fc^+ redox couple. All CVs were recorded under an argon or nitrogen atmosphere in dry THF. For the "rinse" test results, the working electrode was removed from the cell following catalysis, rinsed with THF solvent, and then placed in a fresh acidic electrolyte solution without **2** or **3** present (0.1 M TBAP, 25 mM *p*TSA). To determine the kinetic isotope effect (KIE), *para*-toluenesulfonic acid-$d_1 \cdot D_2O$ (*p*TSA-d_3, 65 mM for **2** and 45 mM for **3**) in THF was utilized.

2.5.5. Sample overpotential calculation[86,87,92]

$$E^{\circ}_{H^+} = E_{H^+} - 0.05916\,V \times \mathrm{p}K_a \quad \text{(S1)}$$

$$E^{\circ}_{H^+} = (-0.343\,V) - 0.05916\,V \times 11.8 = -1.04\,V$$

$$\eta = \left|E_{H^+} - E_{cat/2}\right| \quad \text{(S2)}$$

$$\eta = |(-1.04\,V - (-1.73 \pm 0.04\,V| = 0.69 \pm 0.04\ \text{V}$$

2.5.6. Sample turnover frequency calculation[59]

$$TOF_{\max} = (1.94\,V^{-1})\nu\left(\frac{i_{\mathrm{cat}}}{i_{\mathrm{p}}}\right)^2 \quad \text{(S3)}$$

$$TOF_{\max} = (1.94\ V^{-1}) \times 1\ V/s \times \left(\frac{0.338735\ mA}{0.011499\ mA}\right)^2$$

$$TOF_{\max} = 1{,}680\ \pm 150\ s^{-1}$$

2.5.7. Sample faradaic efficiency calculation

$$Theoretical\ moles\ of\ H_2 = 0.5\ C\ \times \frac{1\ mol\ e^-}{96485\ C} \times \frac{1\ mol\ H_2}{2\ mol\ e^-} \quad (S4)$$

$$Theoretical\ moles\ of\ H_2 = 3.60\ \times\ 10^{-6}\ mol$$

$$\text{y} = 790.35\ ppm/mL \text{ x } (From\ calibration\ curve\ Figure) \quad (S5)$$

$$63.8 \text{ ppm} = 790.35\ ppm/mL \text{ x}$$

$$\text{x} = 0.0807 \ldots mL$$

$$Experimental\ moles\ of\ H_2 = \frac{0.0807 \ldots mL}{24789.57 \ldots\ mL/mol}\ (From\ ideal\ gas\ law\ at\ 25\ °C) \quad (S6)$$

$$Experimental\ moles\ of\ H_2 = 3.26\ \times\ 10^{-6}\ mol$$

$$Faradaic\ Efficiency = \frac{Experimental\ moles\ H_2}{Theoritical\ moles\ H_2} \times 100 \quad (S7)$$

$$Faradaic\ Efficiency = \frac{3.26\ \times\ 10^{-6}\ mol}{3.60\ \times\ 10^{-6}\ mol} \times 100$$

$$Faradaic\ Efficiency = 90.5\%$$

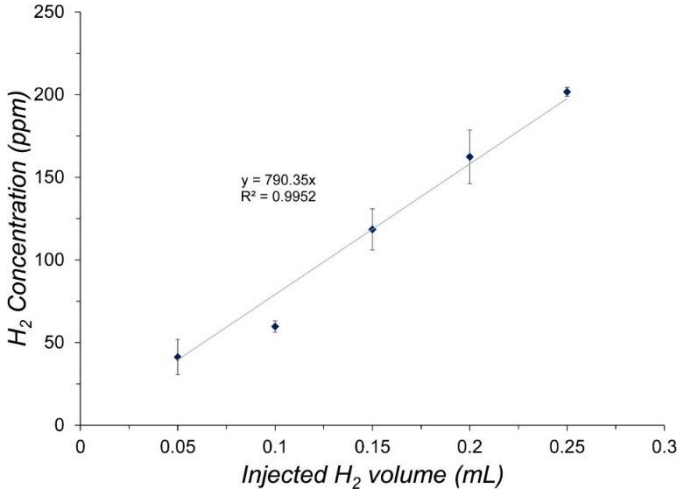

Figure 2.31. Calibration curve used to calculate Faradaic efficiency.

2.5.8. Controlled potential electrolysis

A glassy carbon working electrode was placed into a sealed bulk electrolysis cell filled with a solution of 0.2 M TBAP in THF, 0.25 mM **2** or **3**, 65 mM or 45 mM *p*TSA (for **2** and **3**, respectively), along with a 0.01 M $Ag/AgNO_3$ reference electrode reference electrode (Figure S3). The graphite counter electrode, separated by a porous frit, was submerged in a solution of 0.1M TBAP in THF and 65 mM or 45 mM ferrocene (for **2** and **3**, respectively). Bulk electrolysis experiments were carried out at a controlled potential of -3.0 V vs. Fc/Fc^+ until 0.5 C of charge was passed. The solution in the cell was then stirred for 1 hour to ensure equilibration between the solvent and headspace before sampling.

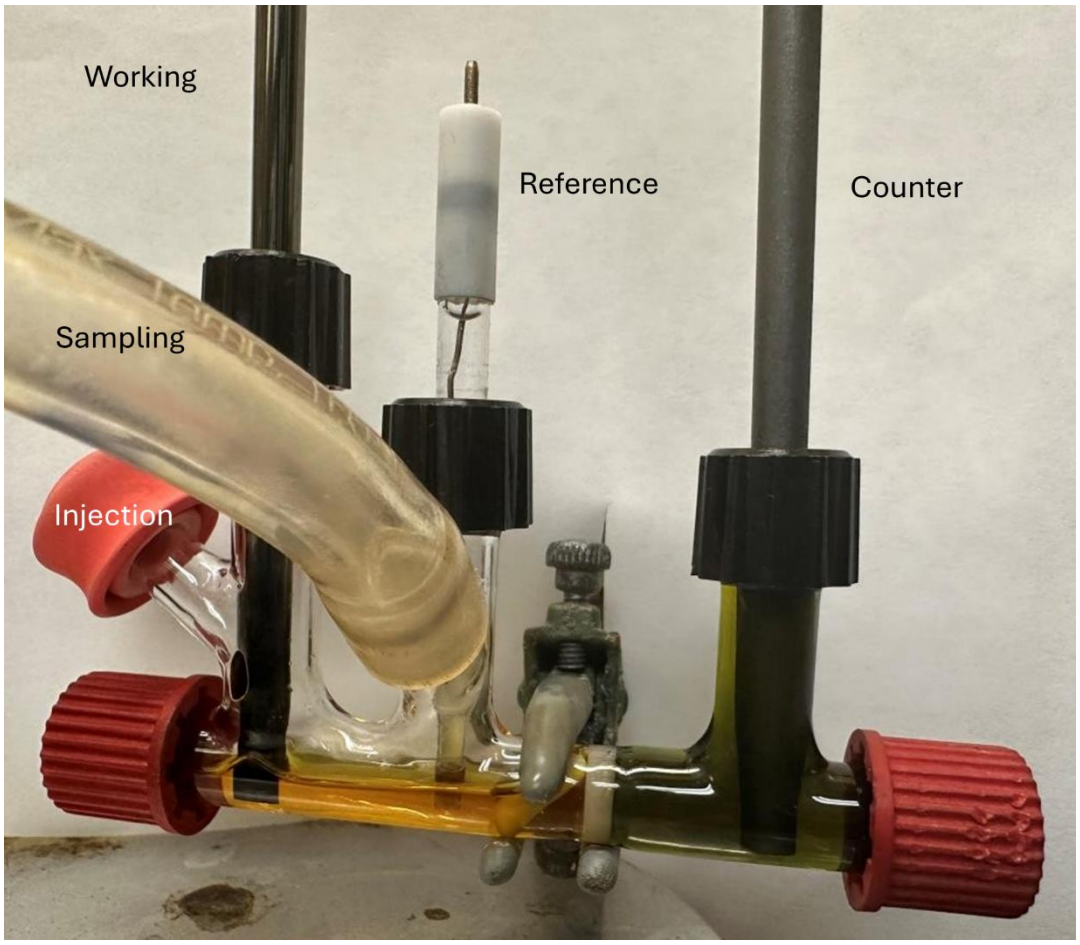

Figure 2.32. Image of the electrolysis cell utilized for controlled potential electrolysis after 0.5 C of charge had been passed.

2.6. References

(1) Somachandra, M. S.; Averkiev, B.; Sues, P. E. Unsymmetric Co-Facial "Salixpyrrole" Hydrogen Evolution Catalysts: Two Metals Are Better than One. *Inorg. Chem.* **2024**, *63* (29), 13346–13357. https://doi.org/10.1021/acs.inorgchem.4c01101.

(2) Stewart, M. P.; Ho, M.-H.; Wiese, S.; Lindstrom, M. L.; Thogerson, C. E.; Raugei, S.; Bullock, R. M.; Helm, M. L. High Catalytic Rates for Hydrogen Production Using Nickel Electrocatalysts with Seven-Membered Cyclic Diphosphine Ligands Containing One Pendant Amine. *J. Am. Chem. Soc.* **2013**, *135* (16), 6033–6046. https://doi.org/10.1021/ja400181a.

(3) McCrory, C. C. L.; Uyeda, C.; Peters, J. C. Electrocatalytic Hydrogen Evolution in Acidic Water with Molecular Cobalt Tetraazamacrocycles. *J. Am. Chem. Soc.* **2012**, *134* (6), 3164–3170. https://doi.org/10.1021/ja210661k.

(4) Lv, H.; Ruberu, T. P. A.; Fleischauer, V. E.; Brennessel, W. W.; Neidig, M. L.; Eisenberg, R. Catalytic Light-Driven Generation of Hydrogen from Water by Iron Dithiolene Complexes. *J. Am. Chem. Soc.* **2016**, *138* (36), 11654–11663. https://doi.org/10.1021/jacs.6b05040.

(5) Vincent, K. A.; Parkin, A.; Armstrong, F. A. Investigating and Exploiting the Electrocatalytic Properties of Hydrogenases. *Chem. Rev.* **2007**, *107* (10), 4366–4413. https://doi.org/10.1021/cr050191u.

(6) Fontecilla-Camps, J. C.; Volbeda, A.; Cavazza, C.; Nicolet, Y. Structure/Function Relationships of [NiFe]- and [FeFe]-Hydrogenases. *Chem. Rev.* **2007**, *107* (10), 4273–4303. https://doi.org/10.1021/cr050195z.

(7) Lubitz, W.; Ogata, H.; Rüdiger, O.; Reijerse, E. Hydrogenases. *Chem. Rev.* **2014**, *114* (8), 4081–4148. https://doi.org/10.1021/cr4005814.

(8) Rauchfuss, T. B. Diiron Azadithiolates as Models for the [FeFe]-Hydrogenase Active Site and Paradigm for the Role of the Second Coordination Sphere. *Acc. Chem. Res.* **2015**, *48* (7), 2107–2116. https://doi.org/10.1021/acs.accounts.5b00177.

(9) Helm, M. L.; Stewart, M. P.; Bullock, R. M.; DuBois, M. R.; DuBois, D. L. A Synthetic Nickel Electrocatalyst with a Turnover Frequency Above 100,000 S−1 for H2 Production. *Science* **2011**, *333* (6044), 863–866. https://doi.org/10.1126/science.1205864.

(10) Brown, H. J. S.; Wiese, S.; Roberts, J. A. S.; Bullock, R. M.; Helm, M. L. Electrocatalytic Hydrogen Production by [Ni(7PPh2NH)2]2+: Removing the Distinction Between Endo- and Exo-Protonation Sites. *ACS Catal.* **2015**, *5* (4), 2116–2123. https://doi.org/10.1021/cs502132y.

(11) Yang, J. Y.; Chen, S.; Dougherty, W. G.; Kassel, W. S.; Bullock, R. M.; DuBois, D. L.; Raugei, S.; Rousseau, R.; Dupuis, M.; DuBois, M. R. Hydrogen Oxidation Catalysis by a Nickel Diphosphine Complex with Pendant Tert-Butyl Amines. *Chem. Commun.* **2010**, *46* (45), 8618–8620. https://doi.org/10.1039/C0CC03246H.

(12) *Multiporphyrinic Cages: Architectures and Functions | Chemical Reviews*. https://pubs.acs.org/doi/10.1021/cr400673y?ref=PDF (accessed 2025-02-03).

(13) *The photophysics and photochemistry of cofacial free base and metallated bisporphyrins held together by covalent architectures - ScienceDirect*.

https://www.sciencedirect.com/science/article/pii/S0010854506001858?via%3Dihub (accessed 2025-02-03).
(14) Lang, P.; Schwalbe, M. Pacman Compounds: From Energy Transfer to Cooperative Catalysis. *Chem. – Eur. J.* **2017**, *23* (69), 17398–17412. https://doi.org/10.1002/chem.201703675.
(15) Collman, J. P.; Tyvoll, D. A.; Chng, L. L.; Fish, H. T. Facile Synthesis of Meso-Tetraaryl Cofacial Diporphyrins. *J. Org. Chem.* **1995**, *60* (7), 1926–1931. https://doi.org/10.1021/jo00112a008.
(16) Collman, J. P.; Fish, H. T.; Wagenknecht, P. S.; Tyvoll, D. A.; Chng, L.-L.; Eberspacher, T. A.; Brauman, J. I.; Bacon, J. W.; Pignolet, L. H. Catalytic Activation of H2 and C−H Bonds by Electron-Deficient Ruthenium(II) Porphyrins. *Inorg. Chem.* **1996**, *35* (23), 6746–6754. https://doi.org/10.1021/ic951495+.
(17) Collman, J. P.; Hutchison, J. E.; Wagenknecht, P. S.; Lewis, N. S.; Lopez, M. A.; Guilard, R. An Unprecedented, Bridged Dihydrogen Complex of a Cofacial Metallodiporphyrin and Its Relevance to the Bimolecular Reductive Elimination of Hydrogen. *J. Am. Chem. Soc.* **1990**, *112* (22), 8206–8208. https://doi.org/10.1021/ja00178a077.
(18) Zhang, W.; Lai, W.; Cao, R. Energy-Related Small Molecule Activation Reactions: Oxygen Reduction and Hydrogen and Oxygen Evolution Reactions Catalyzed by Porphyrin- and Corrole-Based Systems. *Chem. Rev.* **2017**, *117* (4), 3717–3797. https://doi.org/10.1021/acs.chemrev.6b00299.
(19) Liang, Z.; Wang, H.-Y.; Zheng, H.; Zhang, W.; Cao, R. Porphyrin-Based Frameworks for Oxygen Electrocatalysis and Catalytic Reduction of Carbon Dioxide. *Chem. Soc. Rev.* **2021**, *50* (4), 2540–2581. https://doi.org/10.1039/D0CS01482F.
(20) Li, Y.; Wang, N.; Lei, H.; Li, X.; Zheng, H.; Wang, H.; Zhang, W.; Cao, R. Bioinspired N4-Metallomacrocycles for Electrocatalytic Oxygen Reduction Reaction. *Coord. Chem. Rev.* **2021**, *442*, 213996. https://doi.org/10.1016/j.ccr.2021.213996.
(21) Schissler, C.; Schneider, E. K.; Felker, B.; Weis, P.; Nieger, M.; Kappes, M. M.; Bräse, S. A Synthetic Strategy for Cofacial Porphyrin-Based Homo- and Heterobimetallic Complexes. *Chem. – Eur. J.* **2021**, *27* (9), 3047–3054. https://doi.org/10.1002/chem.202002394.
(22) Fletcher, J. T.; Therien, M. J. Transition-Metal-Mediated [2 + 2 + 2] Cycloaddition Reactions with Ethyne-Containing Porphyrin Templates: New Routes to Cofacial Porphyrin Structures and Facially-Functionalized (Porphinato)Metal Species. *J. Am. Chem. Soc.* **2000**, *122* (49), 12393–12394. https://doi.org/10.1021/ja0001557.
(23) Fletcher, J. T.; Therien, M. J. Extreme Electronic Modulation of the Cofacial Porphyrin Structural Motif. *J. Am. Chem. Soc.* **2002**, *124* (16), 4298–4311. https://doi.org/10.1021/ja012489h.
(24) Schwalbe, M.; Metzinger, R.; Teets, T. S.; Nocera, D. G. Terpyridine–Porphyrin Hetero-Pacman Compounds. *Chem. – Eur. J.* **2012**, *18* (48), 15449–15458. https://doi.org/10.1002/chem.201201728.
(25) Schissler, C.; Schneider, E. K.; Rotter, M.; Notter, S.; Geier, C.; Weis, P.; Kappes, M. M.; Bräse, S. Marriage of an N-Fused and a Regular Porphyrin in a Cofacial Ligand System. *Organometallics* **2023**, *42* (15), 1882–1889. https://doi.org/10.1021/acs.organomet.3c00116.
(26) Schissler, C.; Schneider, E. K.; Lebedkin, S.; Weis, P.; Niedner-Schatteburg, G.; Kappes, M. M.; Bräse, S. Novel Cofacial Porphyrin-Based Homo- and Heterotrimetallic Complexes of Transition Metals. *Chem. – Eur. J.* **2021**, *27* (61), 15202–15208. https://doi.org/10.1002/chem.202102376.

(27) Givaja, G.; Blake, A. J.; Wilson, C.; Schröder, M.; Love, J. B. Macrocyclic Diiminodipyrromethane Complexes: Structural Analogues of Pac-Man Porphyrins. *Chem. Commun.* **2003**, No. 19, 2508–2509. https://doi.org/10.1039/B308443D.
(28) Devoille, A. M. J.; Richardson, P.; Bill, N. L.; Sessler, J. L.; Love, J. B. Selective Anion Binding by a Cofacial Binuclear Zinc Complex of a Schiff-Base Pyrrole Macrocycle. *Inorg. Chem.* **2011**, *50* (7), 3116–3126. https://doi.org/10.1021/ic200082r.
(29) Askarizadeh, E.; Devoille, A. M. J.; Boghaei, D. M.; Slawin, A. M. Z.; Love, Jason. B. Ligand Modifications for Tailoring the Binuclear Microenvironments in Schiff-Base Calixpyrrole Pacman Complexes. *Inorg. Chem.* **2009**, *48* (15), 7491–7500. https://doi.org/10.1021/ic900871g.
(30) Love, J. B. A Macrocyclic Approach to Transition Metal and Uranyl Pacman Complexes. *Chem. Commun.* **2009**, No. 22, 3154–3165. https://doi.org/10.1039/B904189C.
(31) Arnold, P. L.; Patel, D.; Wilson, C.; Love, J. B. Reduction and Selective Oxo Group Silylation of the Uranyl Dication. *Nature* **2008**, *451* (7176), 315–317. https://doi.org/10.1038/nature06467.
(32) Arnold, P. L.; Pécharman, A.-F.; Hollis, E.; Yahia, A.; Maron, L.; Parsons, S.; Love, J. B. Uranyl Oxo Activation and Functionalization by Metal Cation Coordination. *Nat. Chem.* **2010**, *2* (12), 1056–1061. https://doi.org/10.1038/nchem.904.
(33) Volpe, M.; Reid, S. D.; Blake, A. J.; Wilson, C.; Love, J. B. Early Transition Metal Complexes of Dinucleating Pacman Ligands: X-Ray Crystal Structures of Mixed-Valence VIII/VIV Complexes. *Inorganica Chim. Acta* **2007**, *360* (1), 273–280. https://doi.org/10.1016/j.ica.2006.07.058.
(34) Arnold, P. L.; Pécharman, A.-F.; Love, J. B. Oxo Group Protonation and Silylation of Pentavalent Uranyl Pacman Complexes. *Angew. Chem. Int. Ed.* **2011**, *50* (40), 9456–9458. https://doi.org/10.1002/anie.201104359.
(35) Arnold, P. L.; Hollis, E.; White, F. J.; Magnani, N.; Caciuffo, R.; Love, J. B. Single-Electron Uranyl Reduction by a Rare-Earth Cation. *Angew. Chem. Int. Ed.* **2011**, *50* (4), 887–890. https://doi.org/10.1002/anie.201005511.
(36) Sessler, J. L.; Cho, W.-S.; Dudek, S. P.; Hicks, L.; Lynch, V. M.; Huggins, M. T. Synthesis and Study of a Calixpyrrole-Texaphyrin Chimera: A New Oligopyrrolic Chloride Anion Receptor. *J. Porphyr. Phthalocyanines* **2003**, *07* (02), 97–104. https://doi.org/10.1142/S1088424603000136.
(37) Devoille, A. M. J.; Love, J. B. Double-Pillared Cobalt Pacman Complexes: Synthesis, Structures and Oxygen Reduction Catalysis. *Dalton Trans.* **2011**, *41* (1), 65–72. https://doi.org/10.1039/C1DT11424G.
(38) Volpe, M.; Hartnett, H.; Leeland, J. W.; Wills, K.; Ogunshun, M.; Duncombe, B. J.; Wilson, C.; Blake, A. J.; McMaster, J.; Love, J. B. Binuclear Cobalt Complexes of Schiff-Base Calixpyrroles and Their Roles in the Catalytic Reduction of Dioxygen. *Inorg. Chem.* **2009**, *48* (12), 5195–5207. https://doi.org/10.1021/ic9001175.
(39) Givaja, G.; Volpe, M.; Edwards, M. A.; Blake, A. J.; Wilson, C.; Schröder, M.; Love, J. B. Dioxygen Reduction at Dicobalt Complexes of a Schiff Base Calixpyrrole Ligand. *Angew. Chem. Int. Ed.* **2007**, *46* (4), 584–586. https://doi.org/10.1002/anie.200603201.
(40) Askarizadeh, E.; Yaghoob, S. B.; Boghaei, D. M.; Slawin, A. M. Z.; Love, J. B. Tailoring Dicobalt Pacman Complexes of Schiff-Base Calixpyrroles towards Dioxygen Reduction Catalysis. *Chem. Commun.* **2010**, *46* (5), 710–712. https://doi.org/10.1039/B923189G.

(41) Nørskov, J. K.; Bligaard, T.; Logadottir, A.; Kitchin, J. R.; Chen, J. G.; Pandelov, S.; Stimming, U. Trends in the Exchange Current for Hydrogen Evolution. *J. Electrochem. Soc.* **2005**, *152* (3), J23. https://doi.org/10.1149/1.1856988.
(42) Greeley, J.; Jaramillo, T. F.; Bonde, J.; Chorkendorff, I.; Nørskov, J. K. Computational High-Throughput Screening of Electrocatalytic Materials for Hydrogen Evolution. *Nat. Mater.* **2006**, *5* (11), 909–913. https://doi.org/10.1038/nmat1752.
(43) Zeng, M.; Li, Y. Recent Advances in Heterogeneous Electrocatalysts for the Hydrogen Evolution Reaction. *J. Mater. Chem. A* **2015**, *3* (29), 14942–14962. https://doi.org/10.1039/C5TA02974K.
(44) Parsons, R. The Rate of Electrolytic Hydrogen Evolution and the Heat of Adsorption of Hydrogen. *Trans. Faraday Soc.* **1958**, *54* (0), 1053–1063. https://doi.org/10.1039/TF9585401053.
(45) Jaksic, M. M. Hypo–Hyper-d-Electronic Interactive Nature of Interionic Synergism in Catalysis and Electrocatalysis for Hydrogen Reactions. *Int. J. Hydrog. Energy* **2001**, *26* (6), 559–578. https://doi.org/10.1016/S0360-3199(00)00120-8.
(46) Sarkar, S.; Peter, S. C. An Overview on Pd-Based Electrocatalysts for the Hydrogen Evolution Reaction. *Inorg. Chem. Front.* **2018**, *5* (9), 2060–2080. https://doi.org/10.1039/C8QI00042E.
(47) Trowbridge, L.; Averkiev, B.; Sues, P. E. Palladium Complexes Bearing Calixpyrrole Ligands with Pendant Hydrogen Bond Donors: Synthesis, Structural Characterization, Electrochemistry and Dihydrogen Evolution. *Polyhedron* **2022**, *225*, 116046. https://doi.org/10.1016/j.poly.2022.116046.
(48) *Organometallics, 3rd, Completely Revised and Extended Edition | Wiley*. Wiley.com. https://www.wiley.com/en-us/Organometallics%2C+3rd%2C+Completely+Revised+and+Extended+Edition-p-9783527293902 (accessed 2025-04-16).
(49) *The Organometallic Chemistry of the Transition Metals - Crabtree, Robert H.: 9780471184232 - AbeBooks*. https://www.abebooks.com/9780471184232/Organometallic-Chemistry-Transition-Metals-Crabtree-0471184233/plp (accessed 2025-04-16).
(50) Morales, S.; Guijarro, F. G.; García Ruano, J. L.; Cid, M. B. A General Aminocatalytic Method for the Synthesis of Aldimines. *J. Am. Chem. Soc.* **2014**, *136* (3), 1082–1089. https://doi.org/10.1021/ja4111418.
(51) Givaja, G.; Volpe, M.; Leeland, J. W.; Edwards, M. A.; Young, T. K.; Darby, S. B.; Reid, S. D.; Blake, A. J.; Wilson, C.; Wolowska, J.; McInnes, E. J. L.; Schröder, M.; Love, J. B. Design and Synthesis of Binucleating Macrocyclic Clefts Derived from Schiff-Base Calixpyrroles. *Chem. – Eur. J.* **2007**, *13* (13), 3707–3723. https://doi.org/10.1002/chem.200600989.
(52) Givaja, G.; Blake, A. J.; Wilson, C.; Schröder, M.; Love, J. B. Macrocyclic Diiminodipyrromethane Complexes: Structural Analogues of Pac-Man Porphyrins. *Chem. Commun.* **2003**, No. 19, 2508–2509. https://doi.org/10.1039/B308443D.
(53) Liu, P.; Feng, X.-J.; He, R. Salen and Half-Salen Palladium(II) Complexes: Synthesis, Characteriztion and Catalytic Activity toward Suzuki–Miyaura Reaction. *Tetrahedron* **2010**, *66* (3), 631–636. https://doi.org/10.1016/j.tet.2009.11.072.
(54) Ulusoy, M.; Birel, Ö.; Şahin, O.; Büyükgüngör, O.; Cetinkaya, B. Structural, Spectral, Electrochemical and Catalytic Reactivity Studies of a Series of N2O2 Chelated Palladium(II) Complexes. *Polyhedron* **2012**, *38* (1), 141–148. https://doi.org/10.1016/j.poly.2012.02.035.

(55) PDF-10-CV-ImpParam.Pdf. https://asdlib.org/onlineArticles/ecourseware/Kelly_Potentiometry/PDF-10-CV-ImpParam.pdf (accessed 2025-02-21).
(56) Rountree, E. S.; Martin, D. J.; McCarthy, B. D.; Dempsey, J. L. Linear Free Energy Relationships in the Hydrogen Evolution Reaction: Kinetic Analysis of a Cobaloxime Catalyst. *ACS Catal.* **2016**, *6* (5), 3326–3335. https://doi.org/10.1021/acscatal.6b00667.
(57) Suliborska, K.; Baranowska, M.; Bartoszek, A.; Chrzanowski, W.; Namieśnik, J. Determination of Antioxidant Activity of Vitamin C by Voltammetric Methods. *Proceedings* **2019**, *11* (1), 23. https://doi.org/10.3390/proceedings2019011023.
(58) Artero, V.; Fontecave, M. Solar Fuels Generation and Molecular Systems: Is It Homogeneous or Heterogeneous Catalysis? *Chem. Soc. Rev.* **2013**, *42* (6), 2338–2356. https://doi.org/10.1039/C2CS35334B.
(59) Rountree, E. S.; McCarthy, B. D.; Eisenhart, T. T.; Dempsey, J. L. Evaluation of Homogeneous Electrocatalysts by Cyclic Voltammetry. *Inorg. Chem.* **2014**, *53* (19), 9983–10002. https://doi.org/10.1021/ic500658x.
(60) Kilgore, U. J.; Roberts, J. A. S.; Pool, D. H.; Appel, A. M.; Stewart, M. P.; DuBois, M. R.; Dougherty, W. G.; Kassel, W. S.; Bullock, R. M.; DuBois, D. L. [Ni(PPh2NC6H4X2)2]2+ Complexes as Electrocatalysts for H2 Production: Effect of Substituents, Acids, and Water on Catalytic Rates. *J. Am. Chem. Soc.* **2011**, *133* (15), 5861–5872. https://doi.org/10.1021/ja109755f.
(61) Kilgore, U. J.; Stewart, M. P.; Helm, M. L.; Dougherty, W. G.; Kassel, W. S.; DuBois, M. R.; DuBois, D. L.; Bullock, R. M. Studies of a Series of [Ni(PR2NPh2)2(CH3CN)]2+ Complexes as Electrocatalysts for H2 Production: Substituent Variation at the Phosphorus Atom of the P2N2 Ligand. *Inorg. Chem.* **2011**, *50* (21), 10908–10918. https://doi.org/10.1021/ic201461a.
(62) Wiese, S.; Kilgore, U. J.; DuBois, D. L.; Bullock, R. M. [Ni(PMe2NPh2)2](BF4)2 as an Electrocatalyst for H2 Production. *ACS Catal.* **2012**, *2* (5), 720–727. https://doi.org/10.1021/cs300019h.
(63) Stewart, M. P.; Ho, M.-H.; Wiese, S.; Lindstrom, M. L.; Thogerson, C. E.; Raugei, S.; Bullock, R. M.; Helm, M. L. High Catalytic Rates for Hydrogen Production Using Nickel Electrocatalysts with Seven-Membered Cyclic Diphosphine Ligands Containing One Pendant Amine. *J. Am. Chem. Soc.* **2013**, *135* (16), 6033–6046. https://doi.org/10.1021/ja400181a.
(64) Hoffert, W. A.; Roberts, J. A. S.; Bullock, R. M.; Helm, M. L. Production of H2 at Fast Rates Using a Nickel Electrocatalyst in Water–Acetonitrile Solutions. *Chem. Commun.* **2013**, *49* (71), 7767–7769. https://doi.org/10.1039/C3CC43203C.
(65) Haddad, A. Z.; Cronin, S. P.; Mashuta, M. S.; Buchanan, R. M.; Grapperhaus, C. A. Metal-Assisted Ligand-Centered Electrocatalytic Hydrogen Evolution upon Reduction of a Bis(Thiosemicarbazonato)Cu(II) Complex. *Inorg. Chem.* **2017**, *56* (18), 11254–11265. https://doi.org/10.1021/acs.inorgchem.7b01608.
(66) Bard, A. J.; Faulkner, L. R.; White, H. S. *Electrochemical Methods: Fundamentals and Applications*; John Wiley & Sons, 2022.
(67) Appel, A. M.; DuBois, D. L.; Rakowski DuBois, M. Molybdenum−Sulfur Dimers as Electrocatalysts for the Production of Hydrogen at Low Overpotentials. *J. Am. Chem. Soc.* **2005**, *127* (36), 12717–12726. https://doi.org/10.1021/ja054034o.

(68) *Interpreting the Electrocatalytic Voltammetry of Homogeneous Catalysts by the Foot of the Wave Analysis and Its Wider Implications | ACS Catalysis*. https://pubs.acs.org/doi/10.1021/acscatal.9b00850 (accessed 2025-03-01).
(69) Costentin, C.; Drouet, S.; Robert, M.; Savéant, J.-M. Turnover Numbers, Turnover Frequencies, and Overpotential in Molecular Catalysis of Electrochemical Reactions. Cyclic Voltammetry and Preparative-Scale Electrolysis. *J. Am. Chem. Soc.* **2012**, *134* (27), 11235–11242. https://doi.org/10.1021/ja303560c.
(70) Costentin, C.; Passard, G.; Savéant, J.-M. Benchmarking of Homogeneous Electrocatalysts: Overpotential, Turnover Frequency, Limiting Turnover Number. *J. Am. Chem. Soc.* **2015**, *137* (16), 5461–5467. https://doi.org/10.1021/jacs.5b00914.
(71) *Toward the rational benchmarking of homogeneous H2-evolving catalysts - Energy & Environmental Science (RSC Publishing)*. https://pubs.rsc.org/en/content/articlelanding/2014/ee/c4ee01709a (accessed 2025-03-01).
(72) Lee, K. J.; Elgrishi, N.; Kandemir, B.; Dempsey, J. L. Electrochemical and Spectroscopic Methods for Evaluating Molecular Electrocatalysts. *Nat. Rev. Chem.* **2017**, *1* (5), 1–14. https://doi.org/10.1038/s41570-017-0039.
(73) Rountree, E. S.; McCarthy, B. D.; Eisenhart, T. T.; Dempsey, J. L. Evaluation of Homogeneous Electrocatalysts by Cyclic Voltammetry. *Inorg. Chem.* **2014**, *53* (19), 9983–10002. https://doi.org/10.1021/ic500658x.
(74) Straistari, T.; Hardré, R.; Fize, J.; Shova, S.; Giorgi, M.; Réglier, M.; Artero, V.; Orio, M. Hydrogen Evolution Reactions Catalyzed by a Bis(Thiosemicarbazone) Cobalt Complex: An Experimental and Theoretical Study. *Chem. – Eur. J.* **2018**, *24* (35), 8779–8786. https://doi.org/10.1002/chem.201801155.
(75) Straistari, T.; Fize, J.; Shova, S.; Réglier, M.; Artero, V.; Orio, M. A Thiosemicarbazone–Nickel(II) Complex as Efficient Electrocatalyst for Hydrogen Evolution. *ChemCatChem* **2017**, *9* (12), 2262–2268. https://doi.org/10.1002/cctc.201600967.
(76) Phipps, C. A.; Hofsommer, D. T.; Toda, M. J.; Nkurunziza, F.; Shah, B.; Spurgeon, J. M.; Kozlowski, P. M.; Buchanan, R. M.; Grapperhaus, C. A. Ligand-Centered Hydrogen Evolution with Ni(II) and Pd(II)DMTH. *Inorg. Chem.* **2022**, *61* (25), 9792–9800. https://doi.org/10.1021/acs.inorgchem.2c01326.
(77) Haddad, A. Z.; Garabato, B. D.; Kozlowski, P. M.; Buchanan, R. M.; Grapperhaus, C. A. Beyond Metal-Hydrides: Non-Transition-Metal and Metal-Free Ligand-Centered Electrocatalytic Hydrogen Evolution and Hydrogen Oxidation. *J. Am. Chem. Soc.* **2016**, *138* (25), 7844–7847. https://doi.org/10.1021/jacs.6b04441.
(78) *Using nature's blueprint to expand catalysis with Earth-abundant metals*. https://doi.org/10.1126/science.abc3183.
(79) Luo, G.-G.; Zhang, H.-L.; Tao, Y.-W.; Wu, Q.-Y.; Tian, D.; Zhang, Q. Recent Progress in Ligand-Centered Homogeneous Electrocatalysts for Hydrogen Evolution Reaction. *Inorg. Chem. Front.* **2019**, *6* (2), 343–354. https://doi.org/10.1039/C8QI01220B.
(80) Simmons, T. R.; Berggren, G.; Bacchi, M.; Fontecave, M.; Artero, V. Mimicking Hydrogenases: From Biomimetics to Artificial Enzymes. *Coord. Chem. Rev.* **2014**, *270–271*, 127–150. https://doi.org/10.1016/j.ccr.2013.12.018.
(81) Orton, G. R. F.; Ghosh, S.; Alker, L.; Sarker, J. C.; Pugh, D.; Richmond, M. G.; Hartl, F.; Hogarth, G. Biomimics of [FeFe]-Hydrogenases Incorporating Redox-Active Ligands: Synthesis, Redox Properties and Spectroelectrochemistry of Diiron-Dithiolate Complexes

with Ferrocenyl-Diphosphines as Fe4S4 Surrogates. *Dalton Trans.* **2022**, *51* (25), 9748–9769. https://doi.org/10.1039/D2DT00419D.
(82) *A guide to secondary coordination sphere editing - Chemical Society Reviews (RSC Publishing)*. https://pubs.rsc.org/en/content/articlelanding/2022/cs/d2cs00022a (accessed 2025-03-01).
(83) Thoi, V. S.; Sun, Y.; Long, J. R.; Chang, C. J. Complexes of Earth-Abundant Metals for Catalytic Electrochemical Hydrogen Generation under Aqueous Conditions. *Chem. Soc. Rev.* **2013**, *42* (6), 2388–2400. https://doi.org/10.1039/C2CS35272A.
(84) Tatematsu, R.; Inomata, T.; Ozawa, T.; Masuda, H. Electrocatalytic Hydrogen Production by a Nickel(II) Complex with a Phosphinopyridyl Ligand. *Angew. Chem. Int. Ed.* **2016**, *55* (17), 5247–5250. https://doi.org/10.1002/anie.201511621.
(85) Wang, J.-W.; Yamauchi, K.; Huang, H.-H.; Sun, J.-K.; Luo, Z.-M.; Zhong, D.-C.; Lu, T.-B.; Sakai, K. A Molecular Cobalt Hydrogen Evolution Catalyst Showing High Activity and Outstanding Tolerance to CO and O2. *Angew. Chem. Int. Ed.* **2019**, *58* (32), 10923–10927. https://doi.org/10.1002/anie.201904578.
(86) *Determining the Overpotential for a Molecular Electrocatalyst | ACS Catalysis*. https://pubs.acs.org/doi/10.1021/cs401013v (accessed 2025-03-01).
(87) Tshepelevitsh, S.; Kütt, A.; Lõkov, M.; Kaljurand, I.; Saame, J.; Heering, A.; Plieger, P. G.; Vianello, R.; Leito, I. On the Basicity of Organic Bases in Different Media. *Eur. J. Org. Chem.* **2019**, *2019* (40), 6735–6748. https://doi.org/10.1002/ejoc.201900956.
(88) *Molecular mechanisms of cobalt-catalyzed hydrogen evolution | PNAS*. https://www.pnas.org/doi/full/10.1073/pnas.1213442109 (accessed 2025-03-02).
(89) *Size- and Shape-Dependent Activity of Metal Nanoparticles as Hydrogen-Evolution Catalysts: Mechanistic Insights into Photocatalytic Hydrogen Evolution - Kotani - 2011 - Chemistry – A European Journal - Wiley Online Library*. https://chemistry-europe.onlinelibrary.wiley.com/doi/10.1002/chem.201002399 (accessed 2025-03-02).
(90) Krishtalik, L. I. Kinetic Isotope Effect in the Hydrogen Evolution Reaction. *Electrochimica Acta* **2001**, *46* (19), 2949–2960. https://doi.org/10.1016/S0013-4686(01)00526-6.
(91) Trowbridge, L.; Averkiev, B.; Sues, P. E. Electrocatalytic Hydrogen Evolution Using a Nickel-based Calixpyrrole Complex: Controlling the Secondary Coordination Sphere on an Electrode Surface. *Chem. – Eur. J.* **2023**, *29* (65), e202301920. https://doi.org/10.1002/chem.202301920.
(92) Stratakes, B. M.; Dempsey, J. L.; Miller, A. J. M. Determining the Overpotential of Electrochemical Fuel Synthesis Mediated by Molecular Catalysts: Recommended Practices, Standard Reduction Potentials, and Challenges. *ChemElectroChem* **2021**, *8* (22), 4161–4180. https://doi.org/10.1002/celc.202100576.

Chapter 3 - Electrocatalytic hydrogen evolution with unsymmetric co-facial "Imixpyrrole": Acid strength governs mechanism and stability

3.1. Abstract

Understanding the challenges and opportunities associated with HER catalysts can help in designing effective electrocatalysts with improved reaction kinetics and stability. Some challenges that are associated with hydrogen evolution reactions (HER) are high overpotential and kinetic limitation requirements in catalysts, as well as the catalyst's dependency on acidic and basic environments. This dependency is leading to differences in reaction mechanisms, kinetics, and adsorption behavior of the reaction intermediates.[1] Based on these principles, a systematic study was carried out in the presence of different acids ($C_6H_8N.BF_4$, $C_3H_5N_2.BF_4$, and $HNEt_3.BF_4$) to understand the impact of acidic environment on the HER catalyst. A monometallic unsymmetric cofacial palladium complex (4) supported by ligands featuring calixpyrrole and imidazole coordination motifs, referred to as "imixpyrrole" ligands, was synthesized and used as a HER catalyst.

The complex was catalytically active for HER in the presence of all three acids. Notably, the catalyst displayed homogeneous behavior in the presence of both anilinium and triethylammonium, whereas it was heterogeneous in nature in the presence of moderate imidazolium acid. The complex showed second-order dependence on acid concentration and first-order dependence on the catalyst concentration in the presence of all three acids, ruling out the bimolecular pathway for HER. Interestingly, the imixpyrrole system was found to be faster (33080 s^{-1} compared to 4160 s^{-1} and 2680 s^{-1} for triethylammonium and imidazolium, respectively) and

more energy efficient with anilinium than with the other two acids. It was found that the catalyst was operating at a much lower overpotential value with anilinium compared to the other two acids (0.53 V compared to 0.99 V and 0.89 V for triethylammonium and imidazole, respectively). KIE values were found to be very distinct, indicating different mechanistic pathways. These findings provide crucial insight into how acid strength can impact on catalyst mechanism and nature.

3.2. Introduction

Relying on non-renewable fossil fuels for our energy needs has been a critical issue that requires immediate attention. As the global population continues to grow, the consumption of fossil fuels and the environmental pollution resulting from fuel combustion have also risen. Consequently, the pursuit of new sustainable and clean energy sources has become a significant focus of scientific research for an extended period. One of the most focused renewable energy sources is hydrogen energy due to its high calorific value (120 $MJkg^{-1}$) and pollution-free combustion.[2,3] Using hydrogen as an alternative energy dates back to 1874, but the interest in hydrogen as a synthetic fuel has increased since the 1970s due to concerns about global warming and the depletion of oil reserves. In the twentieth century, a mixture called "Town gas," which is a combination of carbon monoxide and hydrogen obtained from coal and water, was widely used to heat and light homes and to supply street lighting, but the use was rapidly reduced due to the advent of electricity. [3] In the past 20 years, much research has been done to synthesize a better catalyst to facilitate hydrogen production. Unfortunately, despite all the efforts, the challenges that lie in the way of a hydrogen economy are enormous.

Understanding the challenges and opportunities associated with HER catalysts can help in designing effective electrocatalysts with improved reaction kinetics and stability. Some challenges that are associated with hydrogen evolution reactions are high overpotential and kinetic limitation

requirements in catalysts, which can be improved by optimizing the catalyst structure, the electronic structure of the catalyst, and modifying active sites of the catalyst.[4–8], hereditary adsorption of hydrogen onto the catalyst surface can also be improved by understanding and controlling the adsorption process.[1,9–11] Another major challenge that scientists faced during the development of HER catalysts was the catalyst's dependency on acidic and basic environments. This dependency is leading to differences in reaction mechanisms, kinetics, and adsorption behavior of the reaction intermediates.[1]

Recently, it has been emphasized that optimizing catalyst performance relies not only on tuning the electronic properties of the starting (pre)catalyst but also on manipulating the mechanistic pathways that can affect the nature of the active species.[12] Utilizing a metal complex that exhibits potential bifurcations in its catalytic Pathways because of its ligand system that responds to both protons and redox conditions allows for the comparison of various pathways by adjusting the catalytic parameters, such as pK_a of the acid or applied potential.[13–15] In an acidic environment, the mechanistic pathway for HER primarily includes the discharge of a proton (H^+) from the proton source (electrolyte) onto the catalytic surface, then its reduction to produce hydrogen gas (H_2). The reaction for HER can be represented as: $2H^+ + 2e^- \rightarrow H_2$.[16] Although there are more protons (H^+) readily available in an acidic environment, the overpotential for a specific HER catalyst could be higher compared to alkaline environments, depending on the catalyst's stability in different pH, how protons react with the catalyst surface, and how easily the catalyst can be reduced.[17–20] Under acidic conditions, proton adsorption and desorption steps play a crucial role in determining reaction kinetics, leading to different reaction mechanistic pathways.[13–15,21,22]

Herein, we choose a Schiff-base calixpyrrole complex containing an imidazole moiety in the secondary coordination sphere (Imixpyrrole) for the study to describe how catalytic potential and strength of the proton source affect the HER. Schiff bases are usually synthesized in the presence of acid or base catalysts or with the use of heat[23–27] and some of them are even reactive in the presence of strong acids, resulting in insoluble salts.[28–31] Therefore, finding optimal acidic conditions is very crucial for Schiff-base catalysts. On the other hand, it is expected that the incorporation of the imidazole group, which has both electron-withdrawing and strong proton transfer ability, in the secondary coordination sphere, may improve the electrocatalytic HER activity of metal-calixpyrrole catalysts (**Figure 3.1**).[2,32]

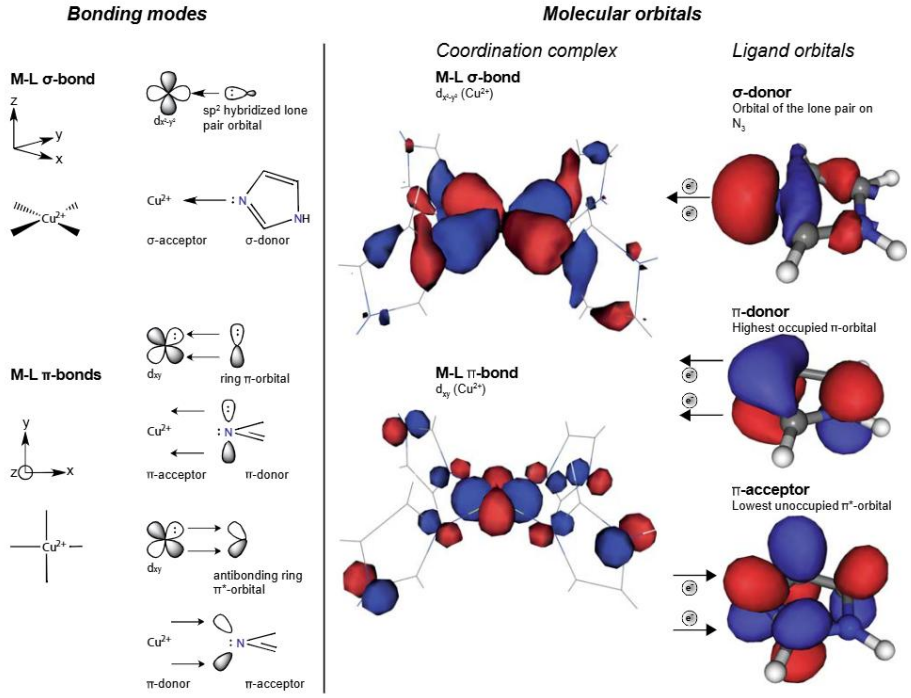

Figure 3.1. Coordination bonding modes (left) and molecular orbitals (right) envisaged for imidazole-Cu(II) in square planer geometry as obtained from DFT calculations. Reproduced with the permission from REF[32].

3.3. Results and discussion

3.3.1. Synthesis and characterization

The palladium imixpyrrole complex was synthesized as shown in **Scheme 3.1** in a similar manner as described in Chapter 2 for the palladium salixpyrrole system.[33] The synthesis was done by using complex 1 and 1-Methyl-2-imidazolecarboxaldehyde as starting materials, and the product was isolated in moderate yields (60%). Pyrrolidine was used as a catalyst to prevent the usage of highly concentrated acidic media during transamination, as well as molecular sieves were used as a water scavenger to increase the reaction rate. The ^{1}H NMR spectra show characteristic peaks for methyl-imidazolecarboxaldehyde incorporation compared to complex 1. The appearance of the 2nd imine peak at 8.16 ppm and the upfield shift of the previous imine peak from 7.75 ppm to 7.43 ppm confirms the imidazole substitution. Also, the appearance of the peak at 3.82 ppm can be attributed to the methyl group in the N1 position on the imidazole ring.

Unfortunately, like the salixpyrrole project, the attempts to synthesize the free imixpyrrole ligand were unsuccessful according to the ^{1}H NMR spectra of the crude reaction mixture. This was also attributed to the hydrolysis of the existing imine bond in the free ligand complex 1 as described in Chapter 2. Therefore, complex 1 was utilized as the starting material, with Pd employed to lock the imine bond within calixpyrrole functionalities.

Scheme 3.1. General Synthesis procedure for Imixpyrrole complex **4**.

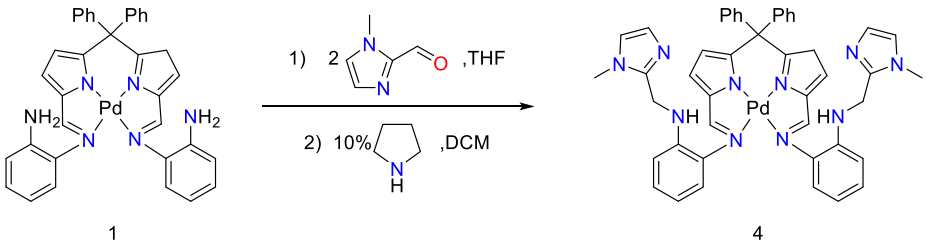

In addition to NMR spectroscopy, complex 4 was characterized in the solid state utilizing single-crystal X-ray diffractometry. The complex adopted a distorted square planar coordination geometry, which resembles the configuration of complex 1 and other reported palladium complexes (**Figure 3.2**).[34,35] Interestingly, unlike the monometallic salixpyrrole complex, the palladium was bound slightly out of the plane of the four nitrogen donors in the calixpyrrole center, similar to complex 1 and the calixpyrrole core of the bimetallic salixpyrrole system.[33,34] Moreover, the palladium center was more tightly bound to the pyrrolidine nitrogen's compared to the imine nitrogen's. It was reflected by having shorter bond lengths between the pyrrolidine nitrogen Pd(1)-N(1) and Pd(1)-N(2) (1.9434 Å and 1.9411 Å, respectively) compared to imine donors where the bond lengths for Pd(1)-N(3) and Pd(1)-N(4) are 2.0825 Å and 2.0825 Å, respectively (**Table 3.1**). These results consisted of complex 1,[34] monometallic and bimetallic salixpyrrole complexes.[33] As well as the results reported by Love *et al*.[35] for bimetallic palladium "pacman" complexes. It was also observed that the angle between N(1)-Pd(1)-N(2) bonds for pyrrolide donors was compressed just below 90° (87.95°), compared to the bond angle between N(1)-Pd(1)-N(3) and N(2)-Pd(1)-N(4) which were more compressed being almost 80° (80.13° and 80.19°, respectively) (**Table 3.1**). That can be attributed to the formation of the five-membered ring between imine and pyrrolidine donors and the palladium metal center upon coordination. In contrast, the bond angle between N(3)-Pd(1)-N(4) for imine donors was expanded beyond 90° (111.67°) to compensate for the compressed angles similar to salixpyrrole systems and complex 1(**Table 3.1**).[33,34]

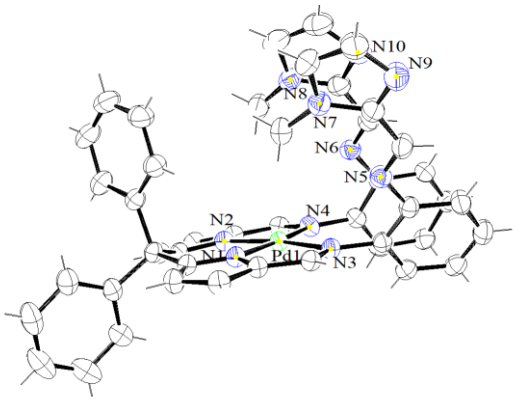

Figure 3.2. ORTEP3 representation (thermal ellipsoids at 50% probability) and atom numbering for complex 4; most of the hydrogen atoms have been omitted for clarity.

Lastly, the calixpyrrole C=N imine bond length (N(3)-C(6) and N(4)-C(11) bond lengths of 1.310 and 1.308 Å, respectively) was slightly longer than the imine bonds seen for free ligand (N(3)-C(6) and N(4)-C(11) bond lengths of 1.28 Å and 1.29 Å, respectively) (**Table 3.1**). As discussed in Chapter 2, those results were comparable to the imine bond lengths seen in the analogous palladium complexes[33–35] and it is believed that this weakening could be due to π back-bonding from the palladium center. The 2nd free imine bond, on the other hand, the imidazole C=N bond length in complex 4 was much similar in length to the free ligand imine bond length.

Interestingly, complex 4 did not display C_2-symmetry like in the monometallic salixpyrrole system. The pendant methyl-imidazole groups can be seen on the same side of the calixpyrrole plane, and no hydrogen bonding is visible with imine nitrogens in the secondary coordination sphere. This phenomenon might be due to having a less bulky methyl group in the imidazole arm compared to the tert-butyl groups in the salen pendant groups in salixpyrrole.

Table 3.1. Selected bond lengths and bond angles for Complex 4.

Bond Lengths (Å)		Bond angles (Deg)	
Pd(1)-N(1)	1.9434(15)	N(1)-Pd(1)-N(2)	87.95(6)
Pd(1)-N(2)	1.9411(15)	N(1)-Pd(1)-N(3)	80.13(6)
Pd(1)-N(3)	2.0825(14)	N(2)-Pd(1)-N(4)	80.19(6)
Pd(1)-N(4)	2.0802(15)	N(3)-Pd(1)-N(4)	111.67(6)
N(3)-C(6)	1.310(2)	N(1)-Pd(1)-N(4)	168.12(6)
N(4)-C(11)	1.308(2)	N(2)-Pd(1)-N(3)	167.72(6)
N(5)-C(24)	1.268(3)	N(3)-C(6)-C(5)	118.42(15)
N(6)-C(28)	1.269(3)	N(4)-C(11)-C(10)	118.24

The straightforward and modular nature of this synthetic route, while incorporating an imidazole moiety into the secondary coordination sphere, makes it attractive for the synthesis of bio-mimicking novel cofacial systems. This synthetic route allowed incorporating amphoteric functionality like imidazole ortho to the imine bond, besides hydroxide functionality on the salicylaldehyde as discussed in Chapter 2. All these modifications suggest the promising nature of this synthesis route for Schiff-base complex formation, even for tuning the binding pockets of the cofacial systems, or with the synthesis advancements of heterobimetallic unsymmetric complexes.

3.3.2. Electrochemical characterization.

The electrochemical properties of imixpyrrole complex 4 were evaluated using cyclic voltammetry (CV) in THF due to the limited solubility in more polar solvents like acetonitrile. Tetrabutylammonium hexafluorophosphate (TBAP) was the supporting electrolyte (**Figure 3.3**). A quasi-reversible redox couple was seen around 0 V vs ferrocene/ferricenium (Fc/Fc^{+}) couple, which corresponds to similar electrochemical characteristics to complex 1 and its free ligand in THF.[34] It can also be seen that these electrochemical features are similar to the salixpyrrole

monometallic system. This hypothesis is further supported by the measured OCP value (-0.88 V vs $Ag/AgNO_3$). Additionally, the OCP of the imixpyrrole system sits closer HER window compared to both monometallic and bimetallic salixpyrrole systems which had a measured OCP of -1.97 V and -1.52 V vs $Ag/AgNO_3$, respectively, suggesting that the imixpyrrole system is more suited for hydrogen evolution reaction.[36–38] It is possible to attribute the two reduction peaks around -1.4 V and -0.15 V vs Fc/Fc^+ in the cyclic voltammogram as ligand-based oxidations according to previous discussions. Also, the two irreversible oxidation peaks around 0.64 V and 0.87 V vs Fc/Fc^+ in CV can be attributed to ligand-based oxidations, possibly from the portion of the ligand containing imidazole.

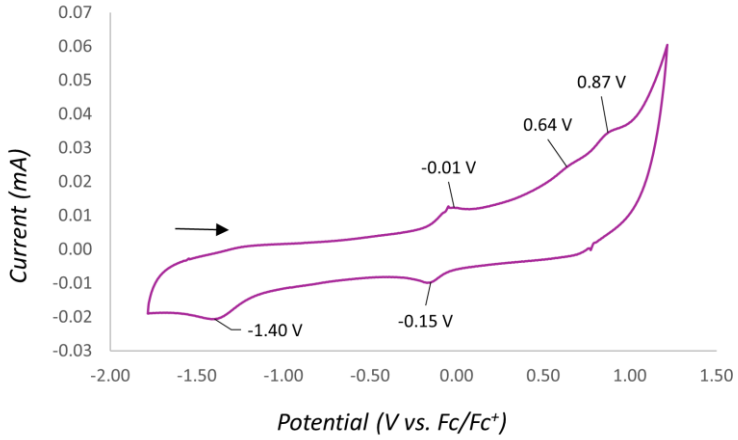

(a)

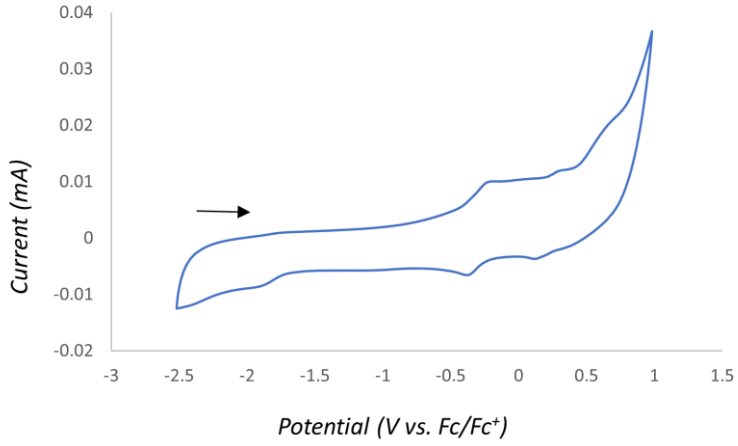

(b)

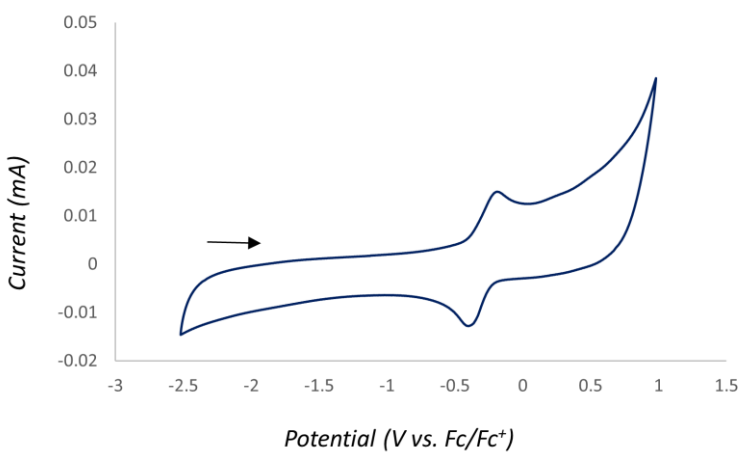

(c)

Figure 3.3. Representative CVs (0.1 M TBAP in THF, 0.25 mM ligand or complex, glassy carbon working electrode, platinum wire counter electrode, 0.01 M $Ag/AgNO_3$ reference electrode, scan rate = 800 mV/s) (a) Complex 4; b) the free ligand of 1; c) complex 1.

3.3.3. Electrocatalytic hydrogen evolution reaction (HER)

As discussed earlier, the catalytic activity and mechanistic pathway for the HER catalyst are highly dependent on the reaction conditions. Therefore, it is important to investigate different experimental conditions for any specific catalytic reaction, such as the hydrogen evolution reaction. Any catalyst can be homogeneous in one set of conditions while it can behave as a heterogeneous catalyst for another set, for the same molecular complex.[39] To examine the above aspect and the potential of the imixpyrrole complex as an HER catalyst, three proton sources with varying pK_a values in THF were selected: anilinium tetrafluoroborate ($C_6H_8N{\bullet}BF_4$, pK_a^{THF} = 5.2), imidazolium tetrafluoroborate ($C_3H_5N_2{\bullet}BF_4$, pK_a^{THF} = 9.4), and triethylammonium tetrafluoroborate ($HNEt_3{\bullet}BF_4$, pK_a^{THF} = 12.5), respectively.[40] Moreover, BF_4^- anion was used as the counterion for all three acids due to its weakly coordinating and electrochemically inert behavior, which makes it a popular choice in nonaqueous electrochemistry for preserving clean, redox behavior.[41–43] A detailed electrochemical analysis was carried out to evaluate the catalytic

efficiency and mechanistic differences of the monometallic imixpyrrole system in the presence of all the above proton sources as the substrate for HER.

At first, cyclic voltammograms were recorded in the presence of both imixpyrrole and the proton source. The voltammograms were compared to see whether the enhancement of current near the onset was due to the presence of the complex or not. Significantly, irreversible reductions accompanied by increased peak current were observed for all three proton sources, suggesting a catalytic proton reduction reaction towards the evolution of H_2 gas (-1.6 V, -1.8 V, and -2.2 V vs Fc/Fc^+ for $C_6H_8N\bullet BF_4$, $C_3H_5N_2\bullet BF_4$, and $HNEt_3\bullet BF_4$, respectively) (**Figure 3.4**). The catalytic wave was shifted cathodically with weaker acid, indicating that more energy is needed to drive HER, as expected. The differential pulse voltammetry (DPV) technique was used to further analyze the complex. Unfortunately, no additional irreversible features were observed in the voltammogram.

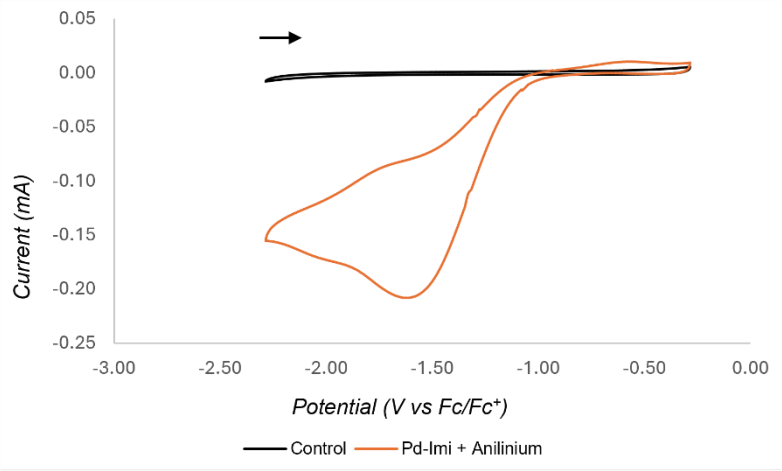

(a)

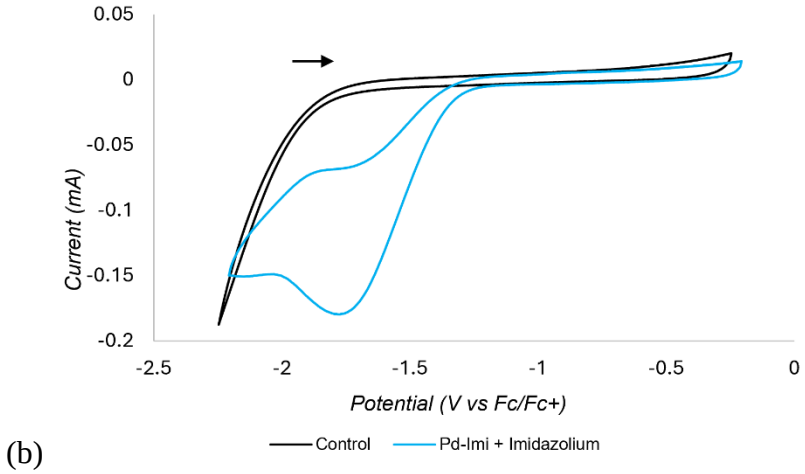

(b)

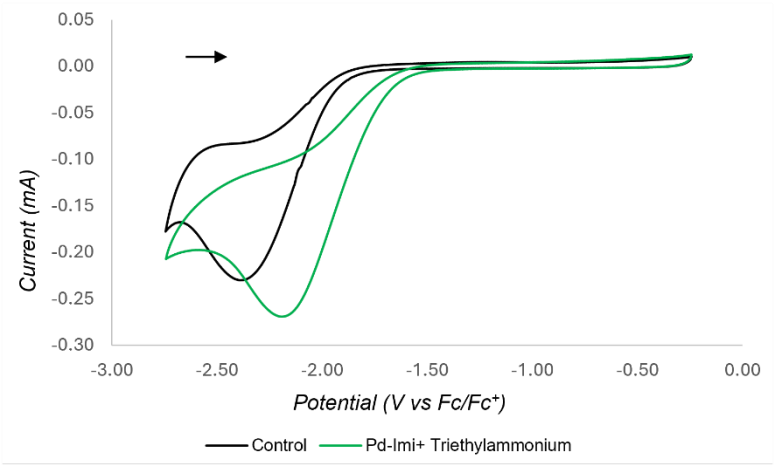

(c)

Figure 3.4. Representative CVs of "Imixpyrrole" showing electrocatalytic HER in THF in the presence of different acids. (0.1 M TBAP, no complex (black) or 0.25 mM complex (colored), 25 mM acid, glassy carbon working electrode, platinum wire counter electrode, 0.01 M $Ag/AgNO_3$ reference electrode, scan rate = 800 mV/s); (a) $C_6H_8N\bullet BF_4$, (b) $C_3H_5N_2\bullet BF_4$, (c) $HNEt_3\bullet BF_4$.

Unlike with the salixpyrrole system, the onset of catalysis correlates with the electrochemical features observed in **Figure 3.3** for all three proton sources. Moreover, the catalyst onset shifts anodically with stronger acid ($C_6H_8N\bullet BF_4$), as anticipated, indicating the need for less driving force for HER. Although, the catalytic onset for HER in the presence of stronger acid was anodic compared to the 2nd reduction peak (-1.4 V vs Fc/Fc^+ in **Figure 3.3**) and cathodic to the first reduction peak (-0.15 V vs Fc/Fc^+), interestingly the onset potential of second reduction of

imixpyrrole matches well with catalytic onset (-1.04 V) observed in **Figure 3.4**. suggesting that the HER catalytic activity depends on the charge state of imixpyrrole complex.[44]

Next, the studies were carried out to determine the current dependence on the scan rate in the presence of all three acids (**Figure 3.5**). For anilinium and imidazolium acids, the peak positions shifted cathodically at higher scan rates and became less well-defined; therefore, the catalytic current i_{cat} was measured at the point where it begins to plateau the most. In contrast, for the weaker acid triethylammonium, the peak shape remained well-defined and S-shaped even at higher scan rates, suggesting the reaction is operating under pure kinetic conditions.[45,46] The scan rate independence point was achieved around 11 V/s for $C_6H_8N{\bullet}BF_4$, 9 V/s for $C_3H_5N_2{\bullet}BF_4$, and 2 V/s for $HNEt_3{\bullet}BF_4$. This suggests that the imixpyrrole complex would experience faster kinetic rates for the hydrogen evolution reaction (HER) in the presence of strong acid. Interestingly, the current response for complex 4, when using anilinium.BF_4 and triethylammonium.BF_4 showed a linear variation with the square root of the scan rate. In contrast, the current response with imidazolium$\bullet BF_4$ displayed a linear relationship with the scan rate itself. This behavior suggests a homogeneous process for the imixpyrrole system in the presence of anilinium$\bullet BF_4$ and triethylammonium$\bullet BF_4$, whereas a heterogeneous process in the presence of imidazolium$\bullet BF_4$.[47] Therefore, several controls were carried out to confirm the catalyst's behavior during the catalytic process for imixpyrrole system in the presence of different acids.[39] As discussed earlier, heterogeneity or homogeneity of a catalyst highly depends on the reaction conditions. Considering that imidazolium acid can promote H-bonding or π–π stacking with pendant uncoordinated imidazole groups in the imixpyrrole system, which may induce pre-organization or extended supramolecular aggregation of complexes at the electrode surface and act as a proton-activated heterogeneous film, leading to heterogeneous

behavior. The authors, Andreas and co-workers, reported the existence of hydrogen bonding between imidazolium and imidazole groups within histidine residues, highlighting their importance in pH sensing mechanisms.[48,49] González et *al*. demonstrated how imidazolium-functionalized polythiophenes aggregated and formed a film on conjugated polyelectrolytes,[50] and Tang et al. investigated how imidazolium cations can form hydrogen bonds with activated carbon electrodes or how imidazole-based molecules can engage in π–π stacking interactions with carbon materials.[51,52] Therefore, it is possible to hypothesize that similar interactions between imidazolium and imidazole lead to such behavior in THF.

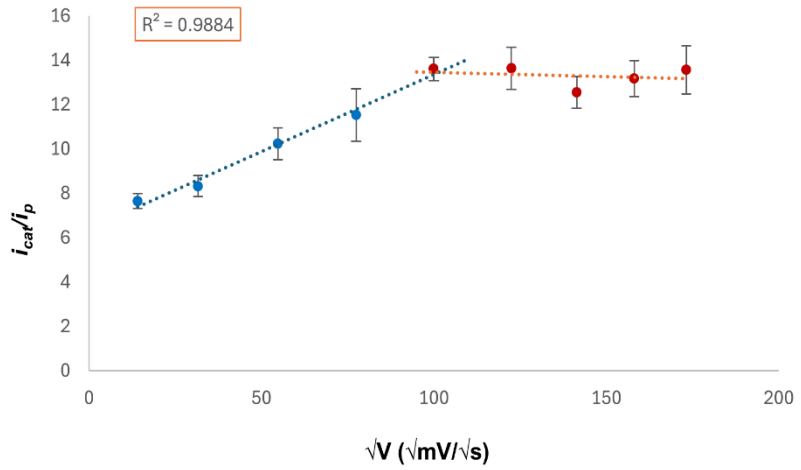

(a)

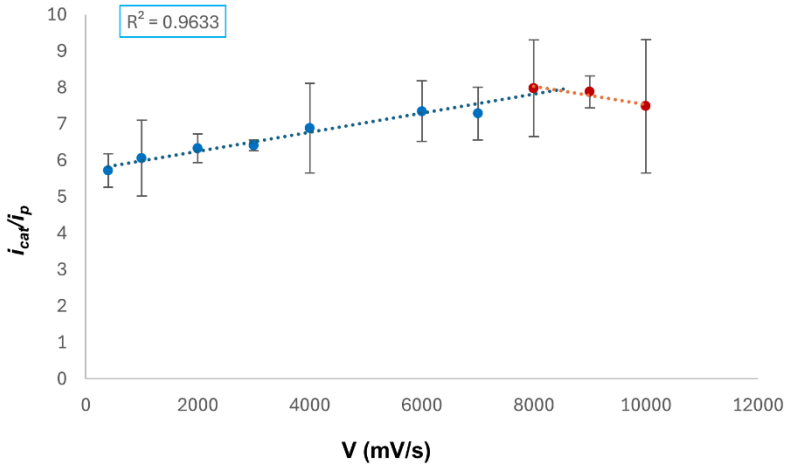

(b)

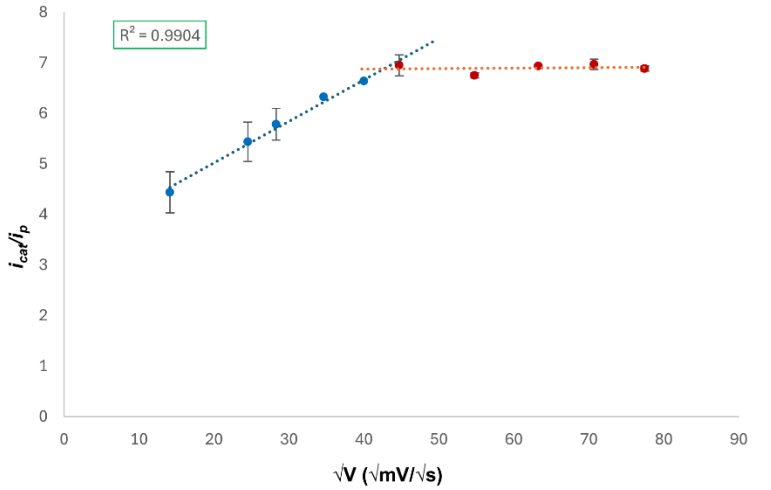
R² = 0.9904
i_{cat}/i_p
√V (√mV/√s)

(c)

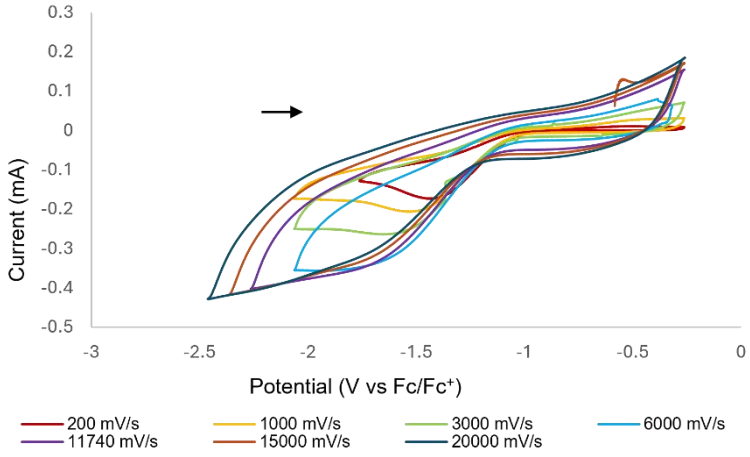
Current (mA)
Potential (V vs Fc/Fc⁺)
200 mV/s
1000 mV/s
3000 mV/s
6000 mV/s
11740 mV/s
15000 mV/s
20000 mV/s

(d)

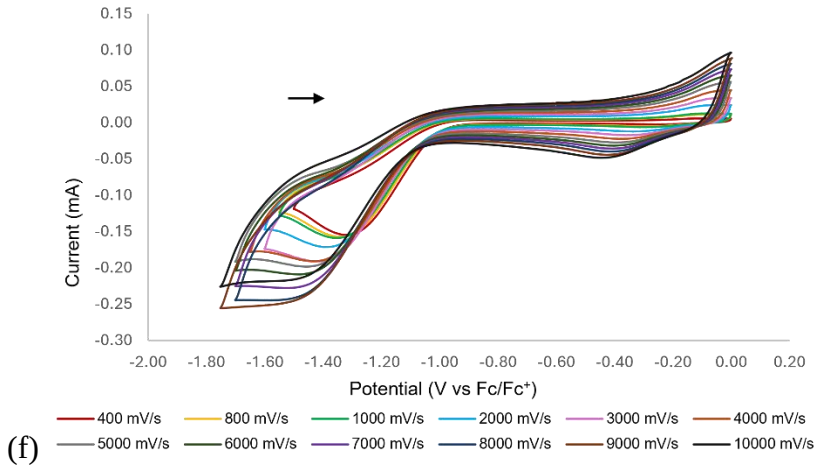

(f)

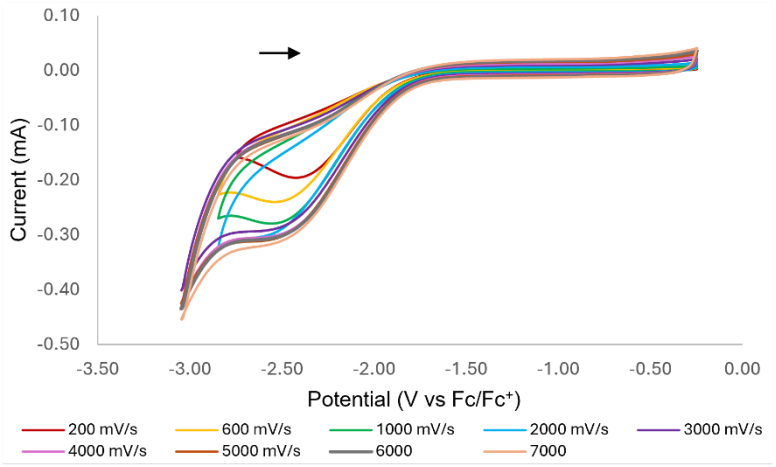

(g)

Figure 3.5. Plot of normalized catalytic current vs. scan rate (a) $C_6H_8N\bullet BF_4$,(b) $C_3H_5N_2\bullet BF_4$, (c) $HNEt_3\bullet BF_4$; Catalytic CVs at different scan rates (0.1 M TBAP in THF, 0.25 mM 4, 25 mM acid, glassy carbon working electrode, platinum wire counter electrode, 0.01 M $AgNO_3$ reference electrode) (d) $C_6H_8N\bullet BF_4$,(scan rate = 200 to 20000 mV/s), (f) $C_3H_5N_2\bullet BF_4$ (scan rate = 400 to 10000 mV/s), (g) $NEt_3\bullet BF_4$ (scan rate = 200 to 7000 mV/s).

Therefore, several controls were carried out to confirm the catalyst's behavior during the catalytic process for imixpyrrole system in the presence of different acids.[39] A simple "rinse" test indicated that the catalytically active species were not adsorbed on the glassy carbon electrode surface in the presence of anilinum and triethylammonium acids, while in the presence of imidazolium acid, it indicated that the active catalytic species were adsorbed on the glassy carbon electrode surface confirming heterogenous process (**Figure 3.18**). Then, a mercury pool

test was carried out to rule out nanoparticle formation (**Figure 3.19**), and a Pt wire test was carried out to confirm that platinum was not leaching from the counter electrode (**Figure 3.20**).

3.3.4. Kinetic investigation

Since the imixpyrrole complex exhibited homogeneous behavior with both anilinium.BF4 and triethylammonium.BF4, the comparison between these acids was conducted first. The background current (the current in the absence of the catalyst) for both acids was negligible therefore, the catalytic peak current was calculated at the peak position (**Figure 3.21**). Kinetic information, such as rate constant (k_{obs}), the maximum turnover frequency (TOF_{max}), can be extracted from cyclic voltammograms when the peaks are S-shaped, the S-shaped catalytic plateau current is independent of the scan rate and acid concentration.[53] Therefore, the acid dependency experiment was carried out for imixpyrrole system in the presence of both $C_6H_8N{\bullet}BF_4$ and $HNEt_3{\bullet}BF_4$ acids. For both systems, the catalytic current was found to increase linearly with acid concentration (**Figure 3.6**). This relationship indicated a second-order dependence on the acid concentration according to Eq. 2,[54] where n where n is the number of electrons transferred in the redox event (2 for HER), *F* is Faraday's constant (96,485 C/mol), A is the electrode surface area in cm^2 (although the electrochemical surface area is preferred it is usually treated as the geometric surface area), D is the diffusion coefficient in cm^2s^{-1}, and x is the order with respect to acid. In the case of $C_6H_8N{\bullet}BF_4$, no visible acid independence point was observed in the graph between i_{cat}^2 vs. $[C_6H_8N{\bullet}BF_4]^2$. Therefore, 94 mM was determined to be the acid independence point based on UV-vis results; beyond that point, the hydrolysis of the free imine functionality (imidazole imine) was possible (**Figure 3.7**). On the other hand, triethylammonium showed a clear acid independence point around 150 mM.

$$i_{cat} = nFA[cat]\sqrt{Dk[H^+]^x} \qquad (1)$$

$$i_{cat}^2 = n^2F^2A^2[cat]^2Dk[H^+]^2 \qquad (2)$$

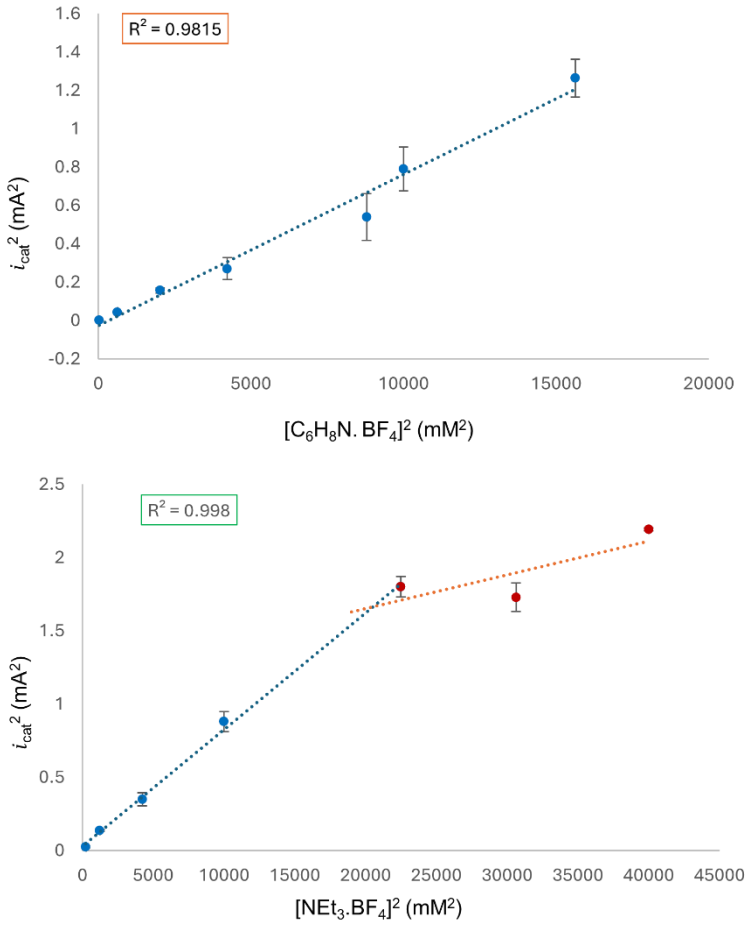

Figure 3.6. Plot of i_{cat}^2 vs acid concentration for: (a) Anilinium•BF_4 (0.1 M TBAP in THF, 0.25 mM 4, 5 to 250 mM C_6H_8N•BF_4, glassy carbon working electrode, platinum wire counter electrode, 0.01 M $AgNO_3$ reference electrode, scan rate = 11 V/s). (b) Triethylammonium•BF_4, 15 to 200 mM $HNEt_3$•BF_4, glassy carbon working electrode, platinum wire counter electrode, 0.01 M $AgNO_3$ reference electrode, scan rate = 2 V/s).

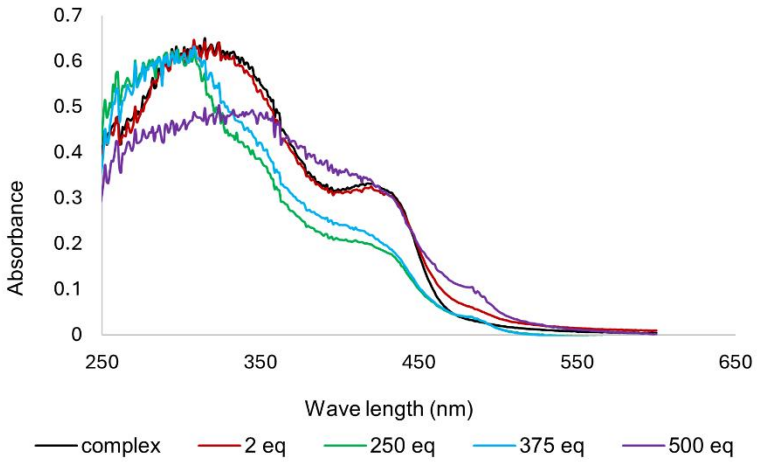

Figure 3.7. UV-vis spectra of 4 with different equivalents of anilinium tetrafluoroborate.

Then, the catalyst dependence of the imixpyrrole system in the presence of both acids for HER was investigated. As mentioned before, the catalytic current was measured at the peak point on the cyclic voltammogram (**Figure 3.22**). For both systems catalytic current was found to increase linearly with catalyst concentration (**Figure 3.8**). This relationship indicated a first-order dependence on the catalyst according to Eq. 1.

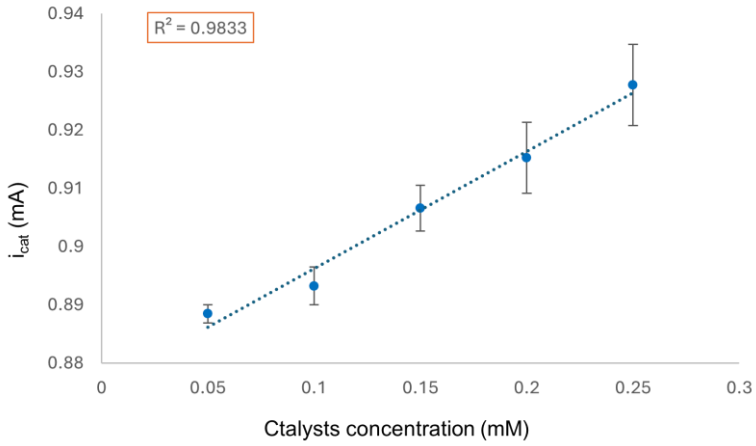

(a)

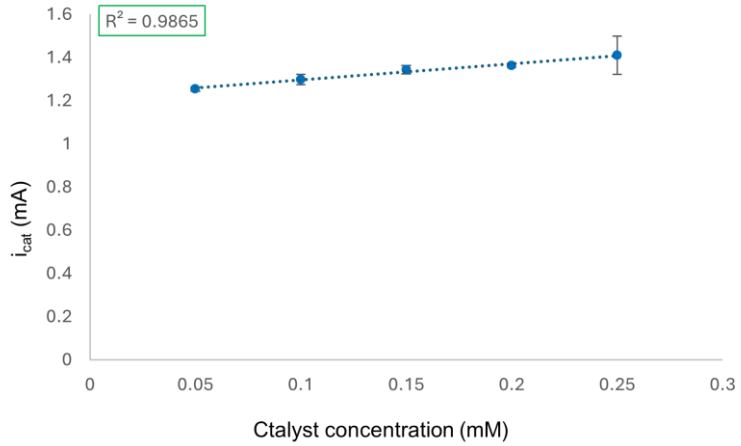

(b)

Figure 3.8. Plot of i_{cat} vs. catalyst concentration for: (a) Anilinium•BF_4 (0.1 M TBAP in THF, 0.05 to 0.25 mM 4, 94 mM C_6H_8N•BF_4, glassy carbon working electrode, platinum wire counter electrode, 0.01 M $AgNO_3$ reference electrode, scan rate = 11 V/s). (b) Triethylammonium•BF_4, 0.05 to 0.25 mM 4, 150 mM $HNEt_3$•BF_4, glassy carbon working electrode, platinum wire counter electrode, 0.01 M $AgNO_3$ reference electrode, scan rate = 2 V/s).

After confirming the heterogeneous nature of the imixpyrrole complex in the presence of imidazolium•BF_4, experiments were carried out to obtain kinetic parameters such as TOF. The background current was negligible, and the voltammogram displayed a S-shaped peak for imixpyrrole complex in the presence of imidazolium•BF_4 acid. Therefore, above mentioned equations (Eq. 1 and Eq. 2) can be used to figure out the reaction order with respect to acid and catalyst concentration. The acid dependency results revealed that the catalytic current linearly increased with acid concentration, indicating a second-order dependence with respect to acid (**Figure 3.9**). The graph between i_{cat}^2 vs. $[H^+]^2$ clearly displayed a plateau, resulting in an acid independence point around 125 mM in the presence of imidazolium•BF_4. The catalyst dependence of supported species in the presence of imidazolium acid was also probed. The catalytic current was found to increase linearly with the catalyst concentration at low catalyst concentration (0.05 to 0.4 mM), confirming first-order dependence on the catalyst according to Eq.1 (**Figure 3.10**). But, upon increasing catalyst concentration beyond 0.4 mM, a plateau was observed as anticipated, indicating a catalyst independence point (**Figure 3.10**) around 0.4 mM for adsorbed species. This

result agreed with the heterogeneous nature of the catalyst in the presence of imidazolium•BF_4, as it would be expected that the electrode surface would become saturated at a certain catalyst concentration, after which, increasing the catalyst concentration would not enhance hydrogen evolution. Interestingly, for all three acids, regardless of their catalytic nature, all of them showed second-order dependence with acid and first-order dependence with catalyst.

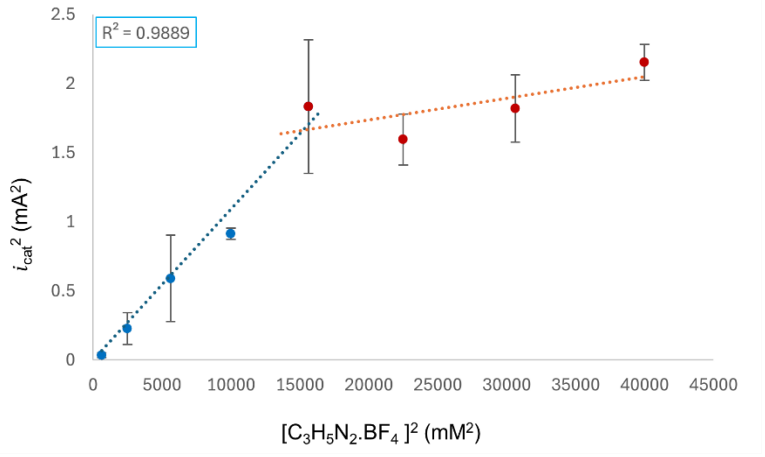

Figure 3.9. Plot of i_{cat}^2 vs acid concentration for imidazolium•BF_4 (0.1 M TBAP in THF, 0.25 mM 4, 5 to 200 mM $C_3H_5N_2$•BF_4, glassy carbon working electrode, platinum wire counter electrode, 0.01 M $AgNO_3$ reference electrode, scan rate = 9 V/s).

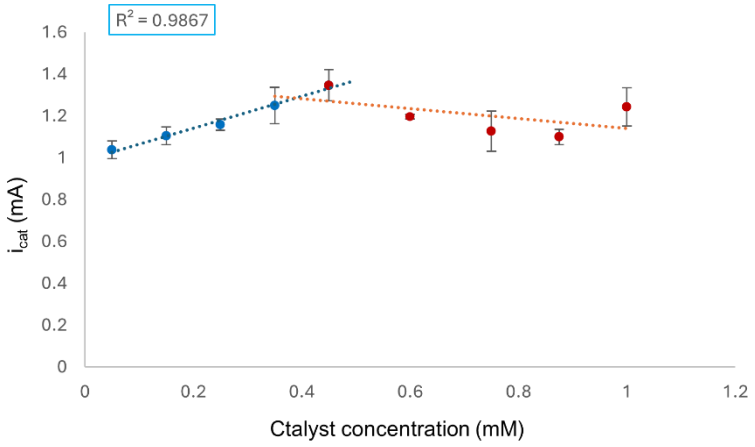

Figure 3.10. Plot of i_{cat} vs. catalyst concentration for Imidazolium•BF_4 (0.1 M TBAP in THF, 0.05 to 1 mM 4, 125 mM $C_3H_5N_2$•BF_4, glassy carbon working electrode, platinum wire counter electrode, 0.01 M $AgNO_3$ reference electrode, scan rate = 9 V/s).

Once the optimized conditions were achieved, other important kinetic parameters like turnover frequency (TOF), overpotential, and faradaic efficiency were calculated. The TOF for the homogeneous catalyst was calculated using Eq. 4, which is a simplified version of the equation below.[55] The Randle-Sevcik equation (Eq. 3) provides the relationship between the peak current i_p and catalytic concentration, where v is the scan rate in the absence of acid, R is the ideal gas constant, T is the temperature in K (298 K), n is the number of electrons transferred in HER (2), the factor of 0.4463 is related to the diffusion equations.[56]

$$\frac{i_{\mathrm{cat}}}{i_{\mathrm{p}}} = \frac{n}{0.4463}\sqrt{\frac{RTk[H^+]^x}{F\nu}} \qquad (3)$$

$$k_{\mathrm{obs}} = TOF_{\mathrm{max}} = (1.94\ V^{-1})\nu\left(\frac{i_{\mathrm{cat}}}{i_{\mathrm{p}}}\right)^2 \qquad (4)$$

As mentioned earlier, the above equations that can be used to calculate TOF are best suited for electrocatalysts under "pure kinetic conditions" where an S-shaped catalytic wave that is scan rate independent is easily observed. Since, S-shaped catalytic wave was observed for imixpyrrole system at optimized conditions in the presence of both acids, it is possible to use above mentioned equation for TOF calculations. The calculated TOFs for $C_6H_8N{\bullet}BF_4$ and $NEt_3{\bullet}BF_4$ were found to be 4190 and 33040 s^{-1}, respectively, as substrates. Although these values are not the highest values that have been reported by using $C_6H_8N{\bullet}BF_4$ and $HNEt_3{\bullet}BF_4$ as proton sources or for a monometallic Schiff base catalyst,[53,57] the imixpyrrole system can be considered quite active and comparatively favorable for HER, like many known HER electrocatalysts from Artero,[58,59] Grapperhaus,[55,60,61] and many others.[62–65] It is also quite impressive that the imixpyrrole system was almost eight times faster with strong acid ($C_6H_8N{\bullet}BF_4$) as a proton source than with weaker $NEt_3{\bullet}BF_4$ acid. Moreover, the monometallic imixpyrrole system in the presence of weaker

triethylammonium•BF_4 as a proton source showed similar activity as the bimetallic salixpyrrole system in the presence of strong *p*TSA•H_2O as a proton source,[33] indicating the promising nature of the imixpyrrole system as a HER catalyst.

The turnover frequency for the imixpyrrole system in the presence of imidazolium.BF_4 was also calculated using stabilized S-shaped peak current. For the calculation of TOF,[66,67] the following equation (Eq. 5) was used initially to figure out the surface coverage of the adsorbed species, where i_p is the peak current of the adsorbed species in the absence of acid, n is the number of electrons transferred (estimated to be 1 for the observed redox couple, **Figure 3.3**), F is the Faraday's constant, R is the ideal gas constant, v is the scan rate T is the temperature in K, Γ^* is the surface coverage area of the working electrode.

$$i_p = \frac{n^2F^2}{4RT} \nu A\Gamma^* \qquad (5)$$

With the calculated value of surface coverage for the adsorbed species, the TOF was then calculated using the equation below (Eq. 6), where j is the catalytic current density and n is the number of electrons transferred during HER. Based on the kinetic data discussed earlier, a first-order dependence on imixpyrrole system surface coverage was expected, and it was also assumed that all the surface-confined species were catalytically active.

$$TOF = \frac{j}{nF\Gamma^*} \qquad (6)$$

The calculated TOF value was 2680 s^{-1} or 37920 s^{-1} cm^{-2} (see experimental for calculations). Although this is not a very high number like other heterogeneous catalysts,[68] it can be considered competitive compared to some of the fastest reported platinum nanoparticles (TOF of 1500 to 9000 s^{-1}.[69] On the other hand, this result is still very impressive considering the molecular origin of the Schiff-base catalyst 4, but exhibits heterogeneous behavior with

imidazolium acid. This kind of hybrid behavior, which combines the molecular design with heterogeneous stability, is rare and notable.

At optimized conditions, the homogeneous catalyst imixpyrrole in the presence of anilinium and triethylammonium acids operates at an overpotential of 0.53 ± 0.07 and 0.99 ± 0.05 V, respectively. Moreover, with anilinium acid, 4 displayed a much lower overpotential than the imixpyrrole with triethylammonium as a proton source. These overpotentials were calculated using established procedures from Appel and Helm (see experimental section for calculations).[70] These overpotential values are comparable to those reported for Pd-based hydrogen production catalysts developed by Bullock *et al*., which had overpotentials of 0.7 V.[71,72] These results confirmed that imixpyrrole complex in the presence of anilinium tetrafluoroborate as a proton source was not only much faster and more active than with triethylammonium tetrafluoroborate as a proton source but also more energetically efficient and required less energy input. When it comes to the imidazolium acid system, the heterogeneous imixpyrrole catalyst is found to operate at an overpotential of 0.89±0.05 V (see experimental for calculations). This value is also comparable to the earlier-mentioned HER catalytic systems.[71,72]

Controlled potential electrolysis (CPE) studies were carried out to figure out the stability and faradaic efficiency of imixpyrrole systems in the presence of both all three acids. For imixpyrrole complex (4) with anilinium•BF_4, the calculated faradaic efficiency was 99.3%, and with imidazolium•BF_4 it was 98.6%, while for the imixpyrrole system with triethylammonium, it was 97.2% (see experimental section for calculations). The imixpyrrole complex displayed a linear increase in charge transfer versus time in the presence of all the acids, resulting in a stable current response for CPE over time. These results indicate that the catalyst was relatively stable under the optimized reaction conditions and did not undergo large structural changes during the catalytic

cycle (**Figure 3.11** and **Figure 3.12**). Once again, the strong acid conditions were proven to be more desirable compared to the weaker acid conditions for the imixpyrrole system, with a larger proportion of the charge productively generating the desired product.

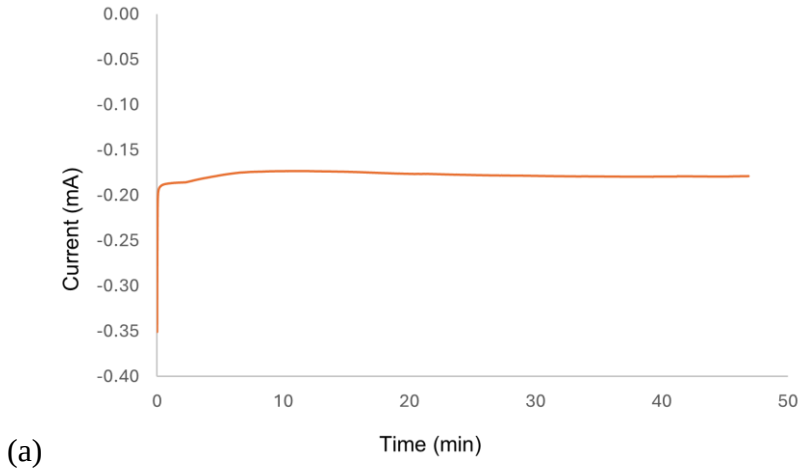

(a)

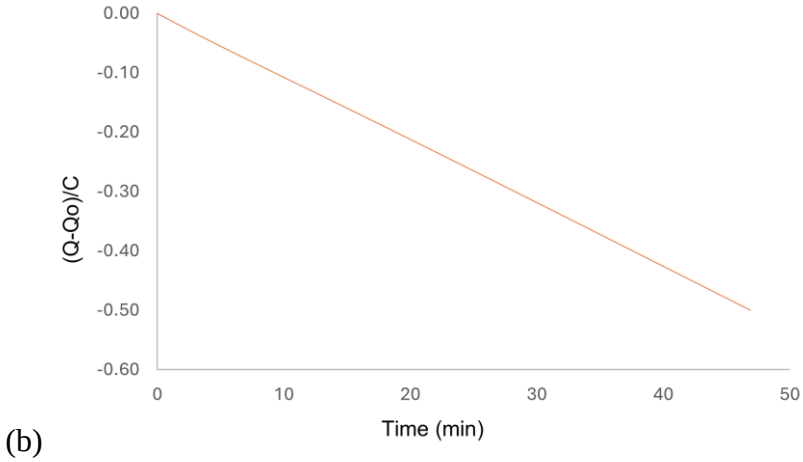

(b)

Figure 3.11. A representative controlled potential electrolysis experiment in THF (0.2 M TBAP, 0.25 mM 4, and 94 mM $C_6H_8N\bullet BF_4$ with a 6 mm glassy carbon rod working electrode, 0.01 M $Ag/AgNO_3$ reference electrode; 0.2 M TBAP, 94 mM ferrocene with a 6 mm graphite counter electrode; 0.5 C of charge passed, potential held at -1.8 V vs. Fc/Fc^+) showing: a) current vs time; b) normalized charge transferred vs. time.

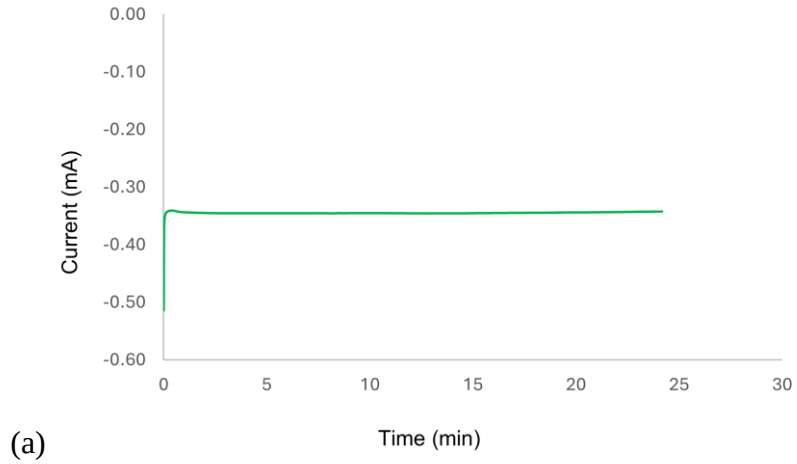

(a)

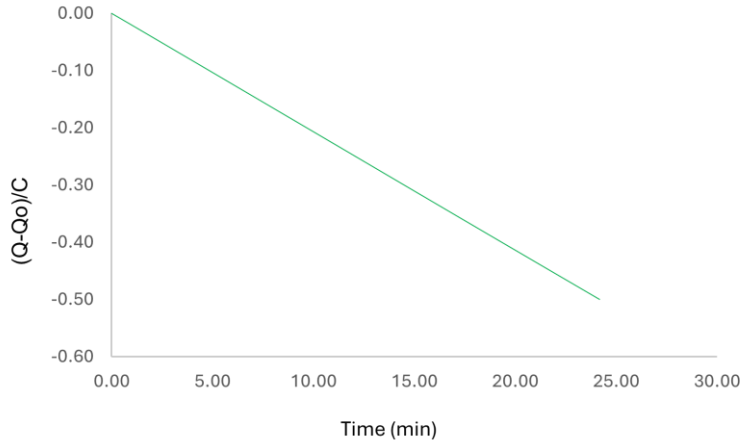

(b)

Figure 3.12. A representative controlled potential electrolysis experiment in THF (0.2 M TBAP, 0.25 mM 4, and 150 mM $HNEt_3 \bullet BF_4$ with a 6 mm glassy carbon rod working electrode, 0.01 M $Ag/AgNO_3$ reference electrode; 0.2 M TBAP, 150 mM ferrocene with a 6 mm graphite counter electrode; 0.5 C of charge passed, potential held at -2.5 V vs. Fc/Fc^+) showing: a) current vs time; b) normalized charge transferred vs. time.

3.3.5. Mechanistic implications

To further understand the homogeneous mechanism of hydrogen evolution using the imixpyrrole system, the kinetic isotope effect (KIE) studies were carried out in the presence of both duretated-anilinium$\bullet BF_4$ (C_6H_5N-$d_3 \bullet BF_4$) and deuterated-triethylammonium$\bullet BF_4$ (NEt_3-$d_1 \bullet BF_4$) acid (**Figure 3.13**). The rate constant derived from Eq. 3 was used to obtain KIE values. Interestingly, in the presence of anilinium$\bullet BF_4$, the obtained H/D KIE value was 1.05 ± 0.031, whereas in the presence of triethylammonium$\bullet BF_4$ it was 6.45 ± 1.09. The imixpyrrole system

with anilinium displayed a smaller KIE value much similar to the salixpyrrole system.[33] As mentioned in Chapter 2, these KIE values are very distinct from inverse KIEs that are associated with electrocatalysts thought to be proceeding through proton shuttling.[73,74] Therefore, it is believed that the imixpyrrole system in the presence of anilinium was displaying secondary KIE values, indicating that H/D bond breaking was not involved in the rate-determining step as reported in the literature.[60,75] In contrast, the imixpyrrole system showed a distinct difference in mechanism in the presence of triethylammonium•BF_4. The obtained KIE value was much bigger than the value obtained in the presence of a stronger acid, anilinium•BF_4 indicating that H/D bond formation was involved in the rate-determining step. Moreover, such larger KIE values are consistent with the proton-coupled electron transfer (PCET) mechanism.[76]

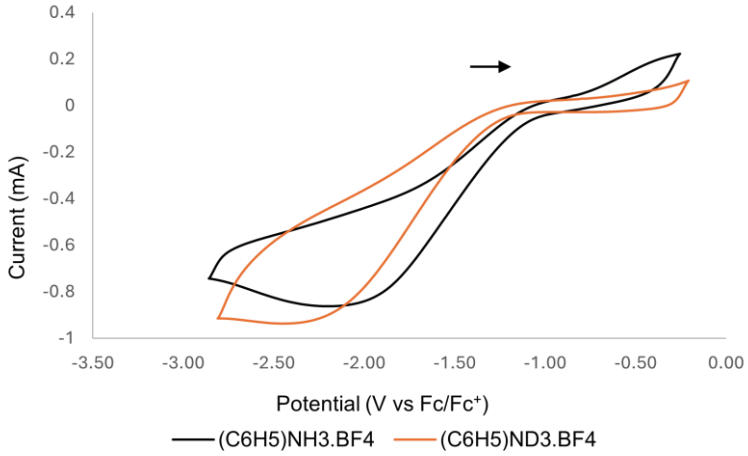

(a)

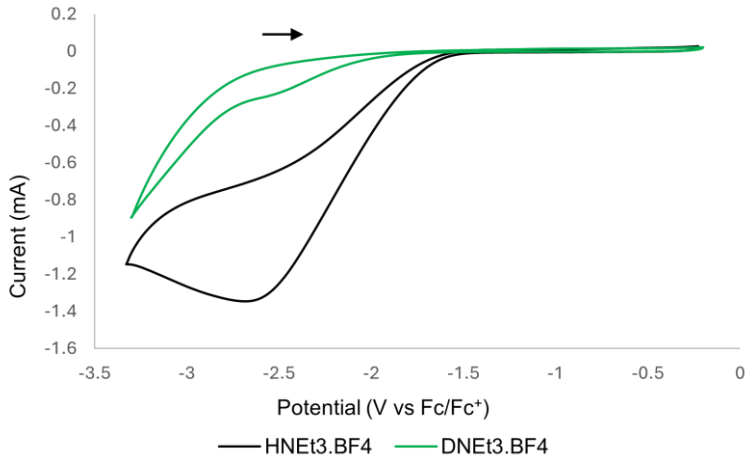

(b)

Figure 3.13. CVs of H/D KIE experiments (0.1 M TBAP in THF, 0.25 mM 4, glassy carbon working electrode, platinum wire counter electrode, 0.01 M $AgNO_3$ reference electrode) for: a) Anilinium•BF_4 (94 mM $(C_6H_5)NH_3$•BF_4 or $(C_6H_5)ND_3$•BF_4, scan rate = 11 V/s); and b) Triethylammonium•BF_4 (150 mM $HNEt_3$•BF_4 or $DNEt_3$•BF_4, scan rate = 2 V/s).

Among all the acids that were used for this study, anilinium•BF_4 was the strongest. Therefore, the protons are readily available in the reaction medium, leading to fast and non-rate-limiting proton transfer. Based on KIE values, the imixpyrrole system is expected to follow a stepwise mechanism, likely adhering to the ECEC mechanism (where E corresponds to an electron transfer step and C to a chemical reaction, here protonation). Initially, it was believed that the uncoordinated, pendant imidazole moieties in 4 can act as internal proton shuttles or relay sites. Although a PCER process after the rate-determining step would still be possible with experimental results for imixpyrrole in the presence of anilinium•BF_4, it is unlikely that it could occur beforehand due to the small KIE value observed. Based on the results obtained from kinetic studies and KIE values, two protonations preceded the rate-determining step, which does not involve bimolecular hydrogen production (first-order dependence with respect to the catalyst was observed for 4 with anilinium). Interestingly, the behaviour of imixpyrrole system in anilinium•BF_4 is quite different compared to its starting material (complex 1), which showed higher KIE values.[34] This can be attributed to the fast proton transfer capability of the imidazole group compared to the

pendant amine group, leading to the mechanistic differences.[77–79] Further mechanistic studies are anticipated to further elucidate the mechanism of action for monometallic system 4 in the presence of anilinium.BF_4, as there is limited literature to support it.

In the case of triethylammonium•BF_4, the KIE results clearly indicate the possibility of PCET mechanism. The imixpyrrole complex with triethylammonium also showed second-order dependency with respect to acid concentration and first-order dependency with respect to catalyst concentration, like when the complex with anilinium•BF_4. Additionally, the hydrolysis of the free imine functionality (imidazole imine) was ruled out for triethylammonium•BF_4 based on CPE results and spectroscopic evidence (UV-vis), it was confirmed that complex 4 is stable in the presence of $HNEt_3$•BF_4 in optimized conditions (**Figure 3.14**). It was reported in several cases that some complexes in the presence of weak acids adopt to undergo a PCET mechanism to overcome the proton transfer barrier.[77,78] It has also been reported that the imidazole group can act as an internal proton shuttle or relay site, indicating support for PCET via the pendant imidazole hypothesis.[73,80] It is believed that the imixpyrrole system also undergoes a similar mechanistic pathway in the presence of triethylammonium•BF_4.

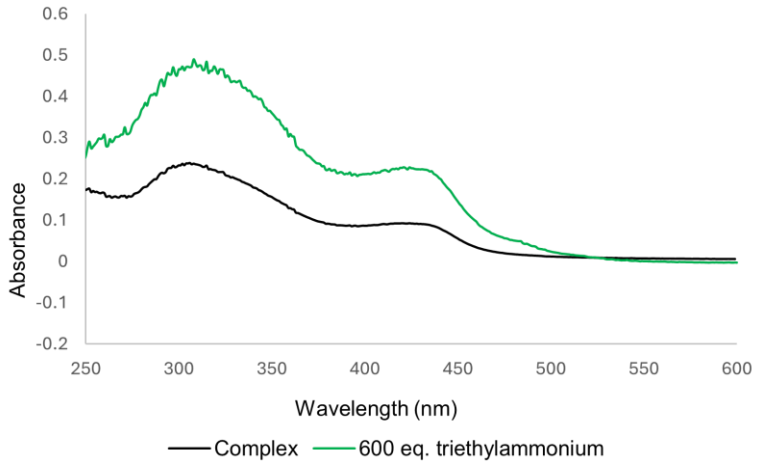

Figure 3.14. UV-vis spectra of 4 with different equivalents of Triethylammonium tetrafluoroborate

The mechanistic investigation in the presence of imidazolium acid is yet to be done. But with the results obtained so far, it is possible to hypothesize some mechanical aspects. The catalyst showed second-order dependency with respect to acid and first-order dependency with respect to catalyst, like both of the anilinium and triethylammonium acids. It is also shown that the hydrolysis of the free imine moiety was not taking place in the presence of optimized imidazolium acid concentration based on CPE and UV-vis evidence (**Figure 3.15**). The anodic shift is displayed with increasing catalyst concentration that can be attributed to the possibility of aggregation, which may stabilize the oxidized form of the catalyst or change its solvation environment.[66,81] making the complex easier to oxidize, or it can indicate the possibility of a PCET mechanism.[77,82]

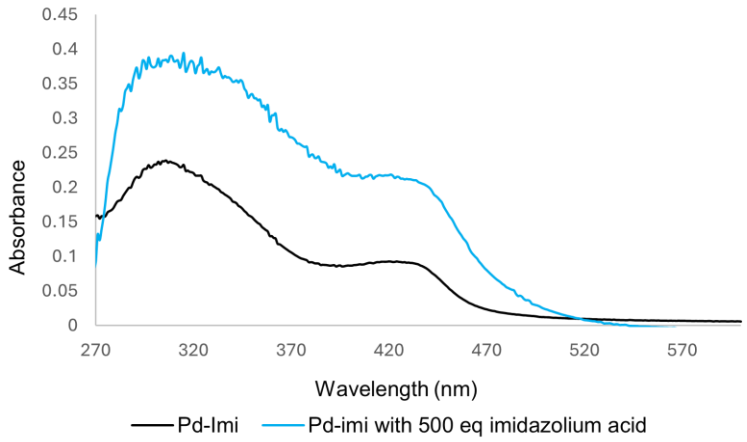

Figure 3.15. UV-vis spectra of 4 with different equivalents of Imidazolium tetrafluoroborate.

3.4. Conclusion

In summary, the monometallic imixpyrrole complex (4) bearing unsymmetric ligands with calixpyrrole and imidazole coordination binding pockets was synthesized, characterized, and its electrochemical properties were studied. Unlike the traditional co-facial "pacman" porphyrin system, the generation of imixpyrrole species was straightforward and relatively high yielding. Synthesis of this novel unsymmetric Schiff base was done using the previously reported palladium calixpyrrole complex 1 as a starting material.

As the catalytic activity, the mechanistic pathway, and the nature of the catalyst for HER are highly dependent on the reaction conditions, this study was carried out to examine the effect of acid on the catalytic HER activity of imixpyrrole complex. Therefore, three proton sources with varying pK_a values in THF were selected: anilinium tetrafluoroborate ($C_6H_8N\bullet BF_4$, $pK_a^{THF} = 5.2$), imidazolium tetrafluoroborate ($C_3H_5N_2\bullet BF_4$, $pK_a^{THF} = 9.4$), and triethylammonium tetrafluoroborate ($HNEt_3\bullet BF_4$, $pK_a^{THF} = 12.5$), respectively.

For imixpyrrole complex (4) in the presence of anilinium$\bullet BF_4$, the catalyst was found to be catalytically active for HER and homogeneous in nature. It also displayed second-order dependence on acid and first-order dependence on catalyst, ruling out a bimolecular pathway for hydrogen production. Additionally, the calculated TOF of 33040 s^{-1} was displayed, with an overpotential of 0.53 ± 0.07 V and a faradaic efficiency of 99.3%. Moreover, a H/D value of 1.06 was measured for the imixpyrrole system in the presence of anilinium$\bullet BF_4$, indicating that H/D bond-breaking was not involved in the rate-determining step.

With triethammonium$\bullet BF_4$, the imixpyrrole catalyst, was catalytically active for HER and homogeneous in nature. The monometallic system was found to be second-order in acid and first-order in catalyst, similar to the previous situation. A lower TOF of 4190 s^{-1} and a higher overpotential of 0.99 ± 0.05 V were indicated as anticipated for a weaker acid environment compared to the strong anilinium$\bullet BF_4$. The faradaic efficiency was found to be 98.6%, which was slightly less than before. Surprisingly, the KIE data indicated a completely different mechanism of action with a calculated KIE value of 6.45, indicating the possibility of PCET mechanism.

Finally, the imixpyrrole complex in the presence of moderate imidazolium acid displayed a completely different behavior. The catalyst was found to be catalytically active for HER but heterogeneous in nature. The imidazolium system also displayed second-order dependency for

acid and first-order dependency for catalyst, ruling out the bimolecular pathway. Surprisingly, the lowest calculated TOF value of 2680 s^{-1} was observed in the presence of imidazolium with a moderate overpotential value of 0.89 V. The faradaic efficiency for the imixpyrrole with imidazolium as the proton source was found to be 97.2%. Further study is needed to understand the mechanistic aspects of this situation.

These results have given a critical insight into ligand/catalyst design and a promising novel pathway for heterobimetallic imixpyrrole synthesis. Moreover, it has provided further insight into the impact of the proton source on catalytic activity. Further studies aimed at elucidating the exact mechanisms of action for 4.

3.5. Experimental Section

3.5.1. General considerations

All procedures and manipulations were performed under an argon or nitrogen atmosphere using standard Schlenk-line and glove box techniques unless stated otherwise. Solvents were dried and deoxygenated under argon using a LC Technology Solutions Inc. SP-1 stand-alone solvent purification system. All alcohols were dried and distilled over activated magnesium (magnesium turnings and a crystal of iodine) under a nitrogen atmosphere. Deuterated solvents were purchased from Cambridge Isotope Laboratories, Sigma Aldrich, Acros Organics, or Alfa Aesar, degassed, and dried over activated molecular sieves prior to use. Imidazolium tetrafluoroborate was purchased from AA Blocks. **1** was synthesized according to a literature procedure with changes as mentioned in chapter 2 (spectroscopic characterization matched reported data).[34] All other reagents were purchased from commercial sources and utilized without further purification unless stated otherwise. NMR spectra were recorded at ambient temperature and pressure using a Bruker 400 MHz spectrometer (400 MHz for ^{1}H and 101 MHz for ^{13}C). The ^{1}H and ^{13}C NMR spectra were

measured relative to partially deuterated solvent peaks, but are reported relative to tetramethylsilane (TMS). Elemental analyses were performed at the University of Rochester, Department of Chemistry, on a PerkinElmer 2400 Series II Analyzer. All crystals were mounted in inert oil and transferred to the cold gas stream of a diffractometer. Single crystal X-ray data were collected using a Rigaku XtaLAB Synergy-S diffractometer equipped with a HyPix-6000HE Hybrid Photon Counting (HPC) detector and dual Mo and Cu microfocus sealed X-ray source (Cu Kα λ = 1.54184 Å). The data collection strategy was calculated using CrysAlisPro to ensure desired data redundancy and percent completeness. Unit cell determination, initial indexing, data collection, frame integration, Lorentz-polarization corrections, and final cell parameter calculations were carried out using CrysAlisPro. An absorption correction was performed using the SCALE3 ABSPACK scaling algorithm embedded within CrysAlisPro. The structures were solved using the ShelXT structure solution program using Intrinsic Phasing and refined by Least Squares using the ShelXL program. All non-hydrogen atoms were refined anisotropically. Hydrogen atom positions were calculated geometrically and refined using the riding model. Olex2 was used for the preparation of the publication materials. Cyclic voltametric measurements were recorded using a Bio-Logic model SP-50 potentiostat. Tetrabutylammonium hexafluorophosphate (TBAP) was used as the supporting electrolyte and was recrystallized prior to use by slow addition of pentane into a THF solution followed by cooling in a freezer (-30 °C). The working electrode was a glassy carbon electrode or a mercury pool electrode; the reference electrode was a $Ag/AgNO_3$ non-aqueous electrode (0.01 M in CH_3CN with 0.1 M TBAP); and a platinum wire or graphite rod was used as the counter electrode. The glassy carbon electrode was polished with 0.05 μm alumina and washed with distilled water prior to each measurement. Electrochemical measurements were conducted at room temperature under an argon or nitrogen atmosphere and

processed using EC-Lab V11.21. Reported half-wave potentials were referenced to the Fc/Fc^+ redox couple by adding high purity ferrocene to the sample solution. Controlled potential electrolysis experiments were also performed with a Biologic SP-50 model potentiostat and processed using EC-Lab V11.21. The working electrode was a 6 mm glassy carbon rod, the counter electrode was a 6 mm graphite rod, and the reference electrode was a 0.01 M $Ag/AgNO_3$ non-aqueous electrode (0.01 M in CH_3CN with 0.1 M TBAP). The amount of hydrogen produced was quantified using an ATO Inc. model ATO-SKY2000-H2 handheld gas detector (0 to 500 ppm) and a calibration curve derived from known volumes of ultra-high purity hydrogen gas (Airgas).

3.5.2. Synthesis of 4[33]

A solution of 0.200 g (0.313 mmol) of **1** in approximately 2 mL of THF was added to a solution of 0.2068 g (1.878 mmol) of 1-methyl-2-imidazolecarboxaldehyde in approximately 1 mL of THF charged with 3Å activated molecular sieves. A catalytic amount of pyrrolidine was added (0.3 mL of 10 mol% pyrrolidine in DCM), and the color of the solution immediately turned from orange to dark red. The reaction mixture was stirred overnight, and then approximately 10 mL of pentane was added. After stirring the suspension for an additional 1 h the solvent was decanted. This step was repeated three times, and the precipitation was isolated by filtration. The orange powder was washed with 2 x 10 mL pentane to remove any unreacted 1-Methyl-2-imidazolecarboxaldehyde. The product was dissolved in approximately 10 mL of DCM and filtered to remove the 3Å activated molecular sieves. The filtrate was dried under reduced pressure to give **2** as an orange solid. Yield: 0.155 g (60%). Crystals suitable for single-crystal X-ray diffraction studies were grown from the slow evaporation of a pentane/dichloromethane solution of **2**. **^{1}H NMR** (400 MHZ, $CDCl_3$) δ: 8.16 (s, 2H, imine-CH), 7.43 (s, 2H, imine-CH), 7.14 (dd, 4H, aromatic-CH, J = 7.13 Hz), 7.09 – 7.02 (m, 4H, aromatic-CH), 6.88 (t, 3H, aromatic-CH), 6.79-6.74 (m, 6H, aromatic-

CH), 6.73 (d, 2H, pyrrole-CH, J = 6.73 Hz), 5.90 (d, 2H, pyrrole-CH, J = 5.89 Hz), and 3.82 (s, 6H, CH_3) ppm.

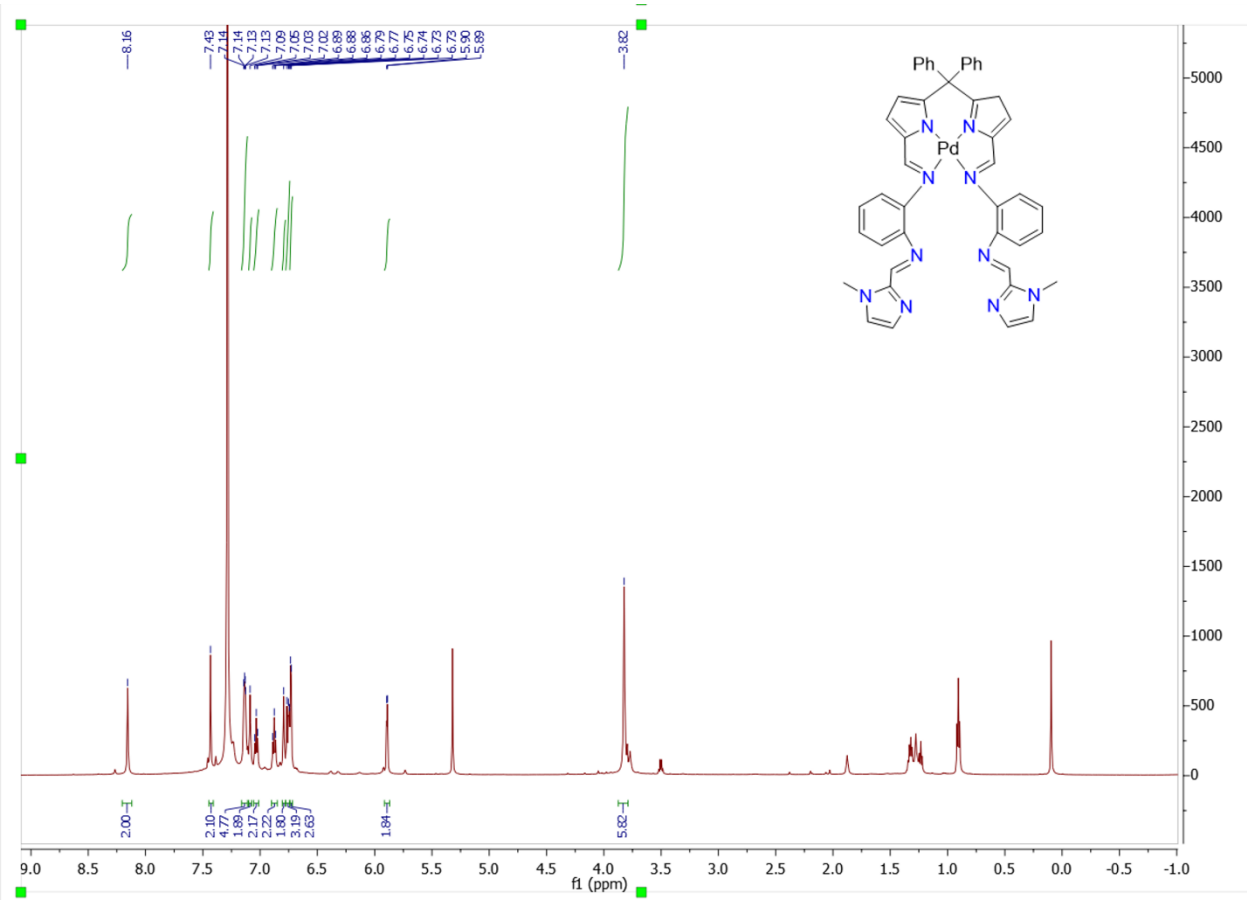

Figure 3.16. ^{1}H NMR spectrum (400 MHz, CDCl3) of 4

3.5.3. Crystal structure data

Table 3.2. Selected Crystal Data, Data Collection, and Refinement Parameters for 4.

	4
empirical formula	$C_{45}H_{36}N_{10}Pd$
FW	823.24
lattice type	triclinic
space group	p-1
T, K	200.0(10)

a, Å	9.48081(7)
b, Å	14.09221(13)
c, Å	14.74721(13)
α, deg	105.8395(8)
β, deg	102.9956(7)
γ, deg	91.3090(6)
V, Å^3	1839.48(3)
Z	2
ρ_{calc}/Mg m^{-3}	1.486
μ/mm^{-1}	4.486
F(000)	844.0
cryst size, mm^3	0.23 x 0.16 x 0.09
range 2θ collected, deg	6.418 to 155.23
reflns collected	42971
abs cor	Semi-empirical from equivalents
Max and min transmn coeff.	1.000 and 0.87625
goodness of fit	1.087
peak and hole, e Å^{-3}	0.41/-0.52

3.5.4. Electrocatalytic H_2 evolution

The electrochemical conditions of the catalytic trials included 0.1 M TBAP electrolyte in THF, 0.05 mM to 0.25 mM of **4** in the presence of anilinium•BF_4 and triethylammonium•BF_4, and 0.05 mM to 1 mM of **4** in the presence of imidazolium•BF_4, 5 to 500 equivalents of anilinium tetrafluoroborate (C_6H_8N•BF_4, 5 to 125 mM), 100 to 800 equivalents of imidazolium

tetrafluoroborate ($C_3H_5N_2 \bullet BF_4$, 25 to 200 mM), and 60 to 1000 equivalents of triethylammonium tetrafluoroborate ($HNEt_3 \bullet BF_4$, 15 to 250 mM), and scan rates between 20 mV/s to 20 V/s. The three-electrode setup consisted of a glassy carbon working electrode, a platinum wire or graphite rod counter electrode, and a 0.01 M $Ag/AgNO_3$ reference electrode. All CVs were referenced versus the Fc/Fc^+ redox couple. All CVs were recorded under an argon or nitrogen atmosphere in dry THF. For the "rinse" test results, the working electrode was removed from the cell following catalysis, rinsed with THF solvent, and then placed in a fresh acidic electrolyte solution without **4** present (0.1 M TBAP, 25 mM of acid). To determine the kinetic isotope effect (KIE), deuterated acids (94 mM for anilinium, 125 mM for imidazolium, and 150 mM for triethylammonium) in THF were utilized.

3.5.5. Controlled potential electrolysis

A glassy carbon working electrode was placed into a sealed bulk electrolysis cell filled with a solution of 0.2 M TBAP in THF, 0.25 mM **4** in the presence of anilinium and triethylammonium, 0.4 mM **4** in the presence of imidazolium, 94 mM anilinium$\bullet BF_4$, or 125 mM imidazolium$\bullet BF_4$, or 150 mM triethylammonium$\bullet BF_4$, along with a 0.01 M $Ag/AgNO_3$ reference electrode (Figure). The graphite counter electrode, separated by a porous frit, was submerged in a solution of 0.2M TBAP in THF and 94 mM or 125 mM, or 150 mM ferrocene (for anilinium, imidazolium, and triethylammonium, respectively). Bulk electrolysis experiments were carried out at a controlled potential of -1.8 V with anilinium, -2.3 V with imidazolium, and -2.5 V with triethylammonium vs. Fc/Fc^+ until 0.5 C of charge was passed. The solution in the cell was then stirred for 1 hour to ensure equilibration between the solvent and headspace before sampling.

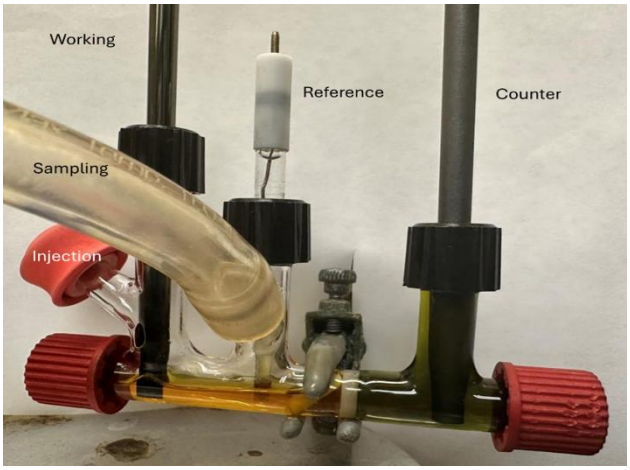

Figure 3.17. Image of the electrolysis cell utilized for controlled potential electrolysis after 0.5 C of charge had been passed.

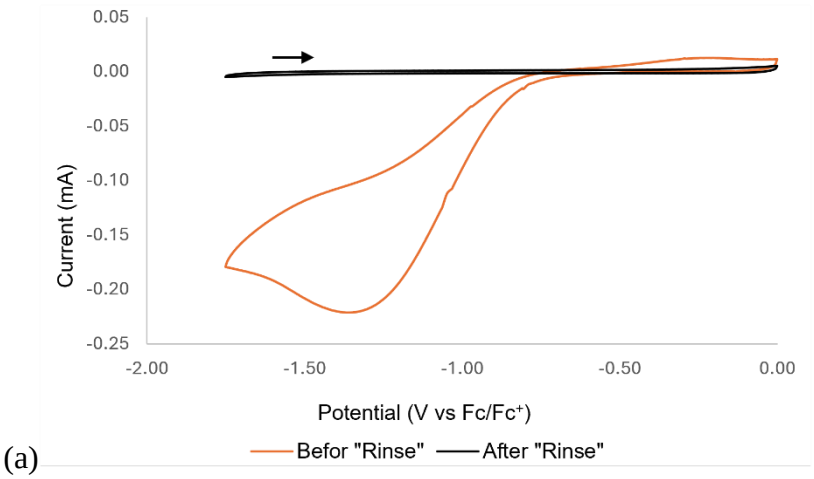

(a)

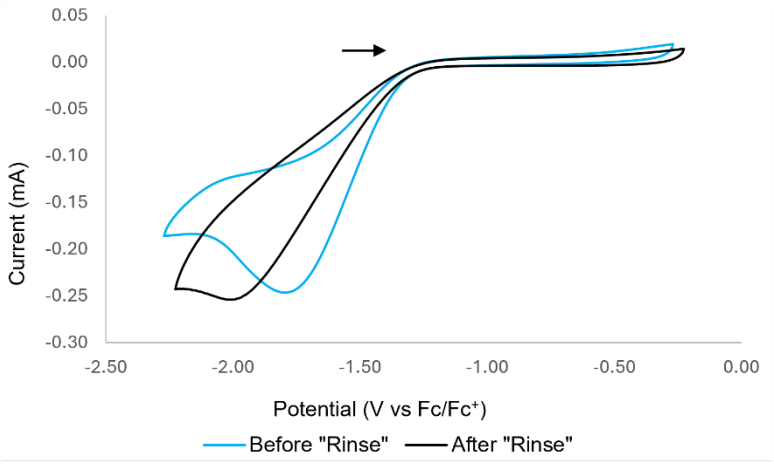

(b)

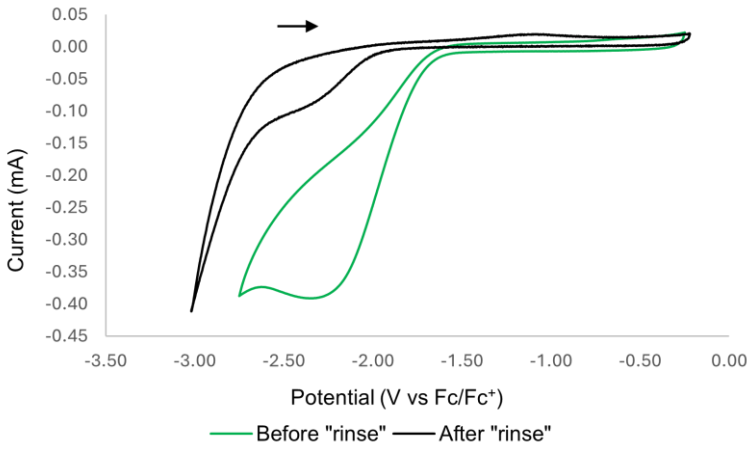

(c)

Figure 3.18. CVs of rinse test results using THF as the rinsing solvent (0.1 M TBAP in THF, 0.25 mM of 4, 25 mM of acid, glassy carbon working electrode, platinum wire counter electrode, 0.01 M $Ag/AgNO_3$ reference electrode, scan rate = 800 V/s) for: a) $C_6H_8N\bullet BF_4$; b) $C_3H_5N_2\bullet BF_4$; and (c) $HNEt_3\bullet BF_4$.

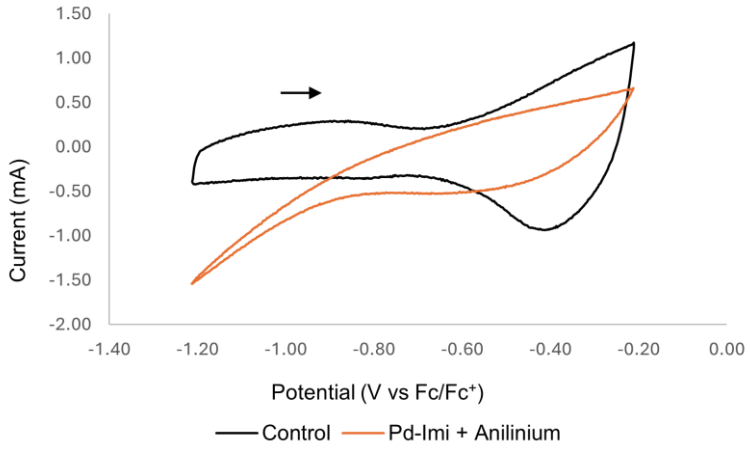

(a)

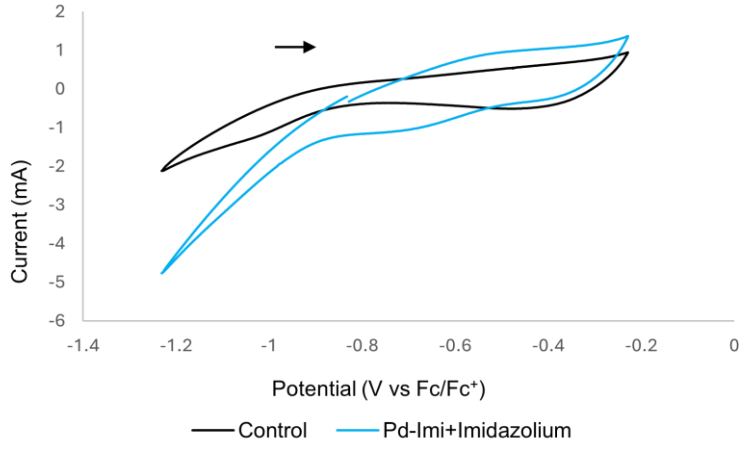

(b)

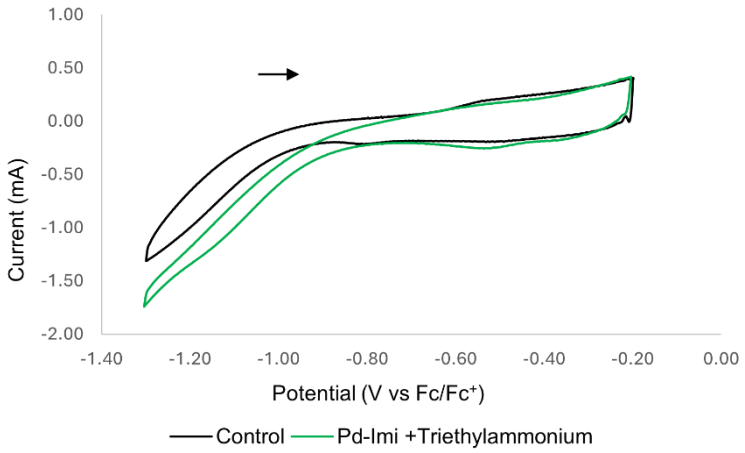

(c)

Figure 3.19. CVs of mercury pool tests for hydrogen evolution (0.1 M TBAP in THF, mercury pool working electrode, platinum wire counter electrode, 0.01 M $Ag/AgNO_3$ reference electrode) for: a) $C_6H_8N\bullet BF_4$ (0.25 mM 4, 94 mM anilinium, scan rate = 11 V); b) $C_3H_5N_2\bullet BF_4$ (0.4 mM 4, 125 Mm imidazolium, scan rate = 9 V); and (c) $HNEt_3\bullet BF_4$ (0.25 mM 4, 150 mM triethylammonium, scan rate = 2 V).

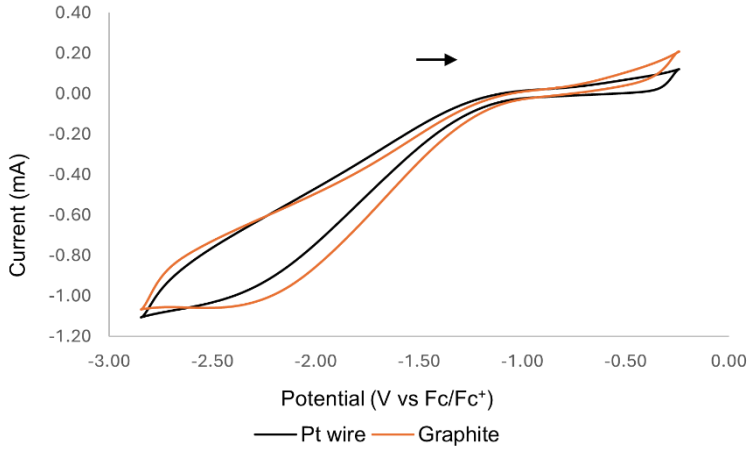

(a)

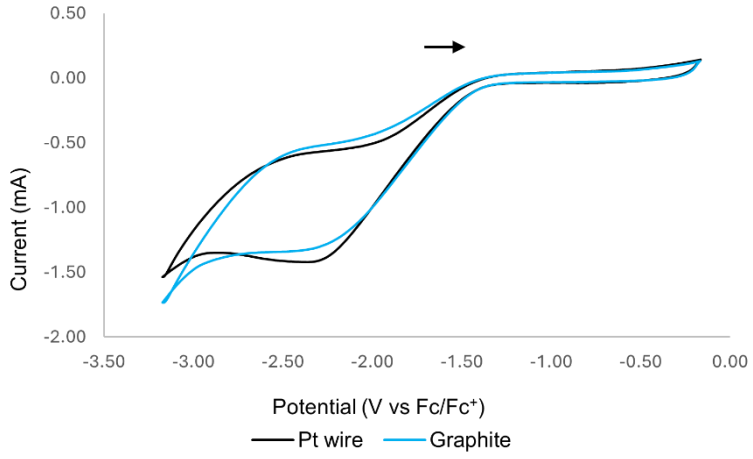

(b)

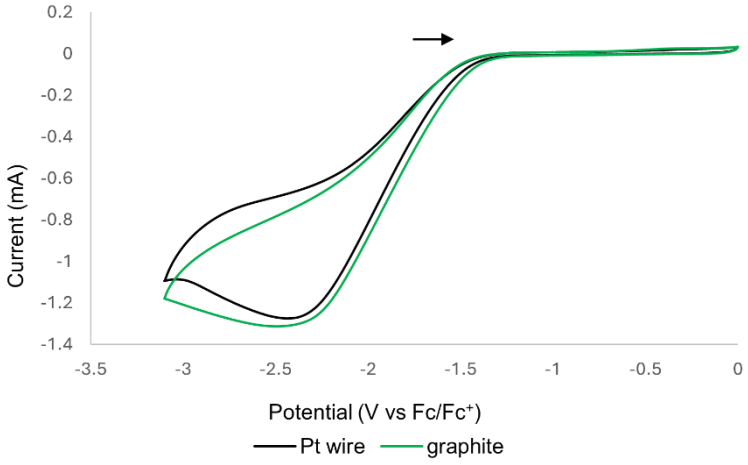

(c)

Figure 3.20. CVs of hydrogen evolution with a graphite rod counter electrode (0.1 M TBAP in THF, glassy carbon working electrode, 0.01 M $Ag/AgNO_3$ reference electrode) for: a) $C_6H_8N\bullet BF_4$ (0.25 mM 4, 94 mM anilinium, scan rate = 11 V); b) $C_3H_5N_2\bullet BF_4$ (0.4 mM 4, 125 Mm imidazolium, scan rate = 9 V); and (c) $HNEt_3\bullet BF_4$ (0.25 mM 4, 150 mM triethylammonium, scan rate = 2 V).

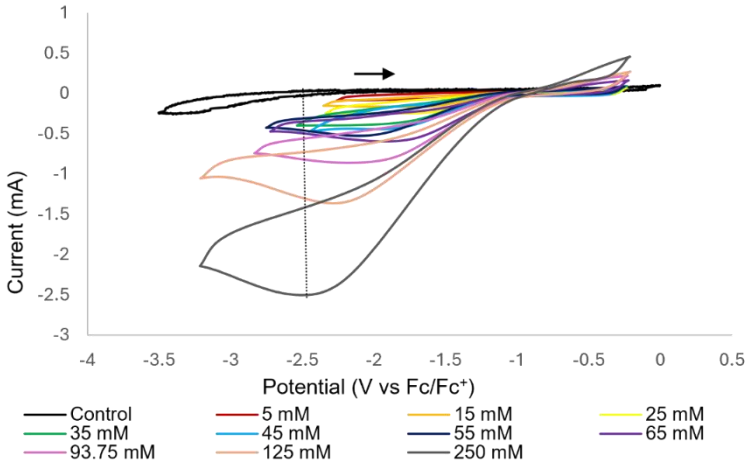

(a)

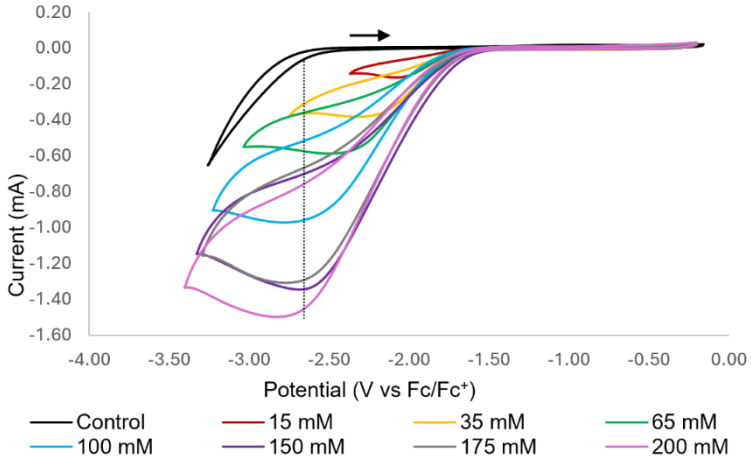

(c)

Figure 3.21. Catalytic CVs with increasing acid concentration (0.1 M TBAP in THF, 0.25 of 4, glassy carbon working electrode, platinum wire counter electrode, 0.01 M $AgNO_3$ reference electrode) for: a) $C_6H_8N\bullet BF_4$ (5 to 250 mM anilinium, scan rate = 11 V); b) $C_3H_5N_2\bullet BF_4$ (25 to 200 Mm imidazolium, scan rate = 9 V); and (c) $HNEt_3\bullet BF_4$ (15 to 200 mM triethylammonium, scan rate = 2 V).

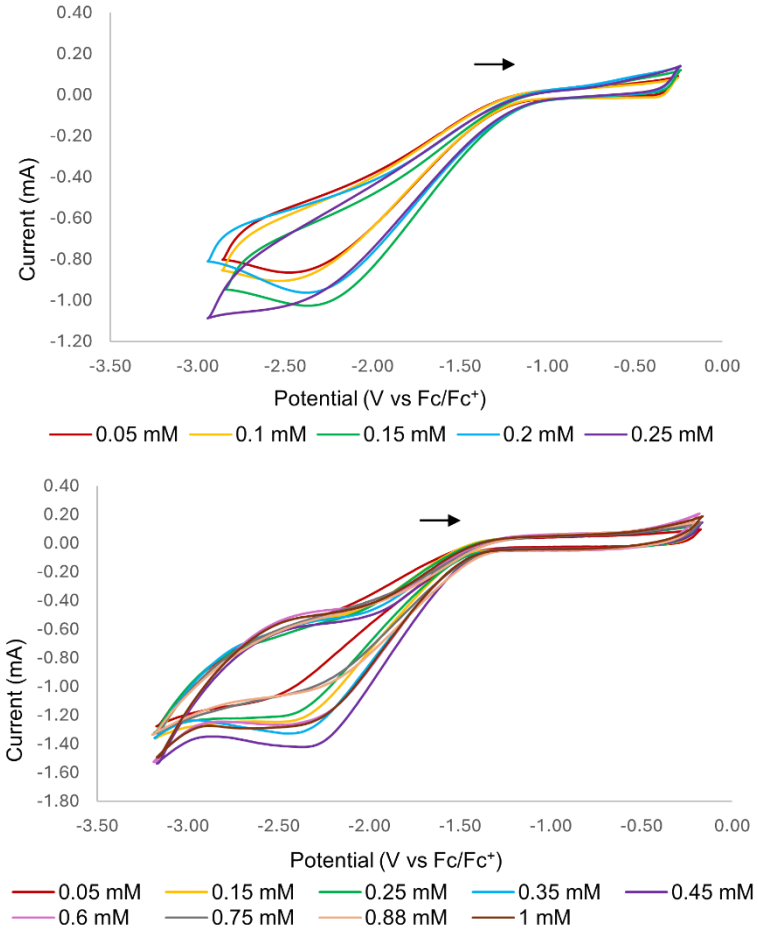

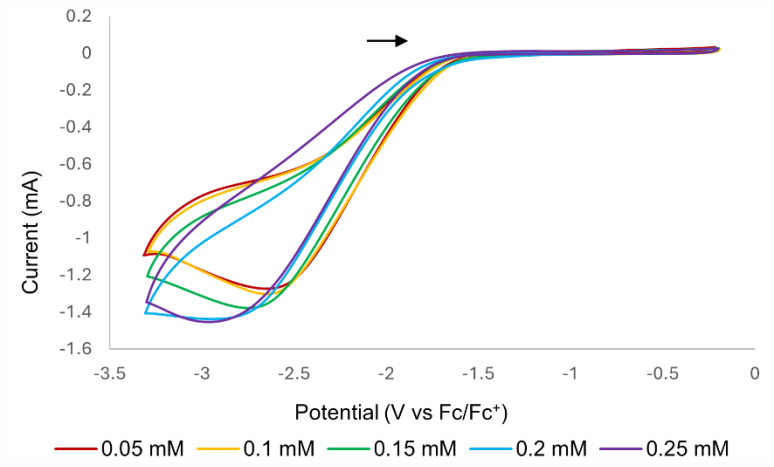

Figure 3.22. Catalytic CVs with increasing catalyst concentration (0.1 M TBAP in THF, glassy carbon working electrode, platinum wire counter electrode, 0.01 M $AgNO_3$ reference electrode) for: a) $C_6H_8N\bullet BF_4$ (0.05 to 0.25 mM 4, 94 mM anilinium, scan rate = 11 V); b) $C_3H_5N_2\bullet BF_4$ (0.05 to 1.00 mM 4, 125 Mm imidazolium, scan rate = 9 V); and (c) $HNEt_3\bullet BF_4$ (0.05 to 0.25 mM 4, 150 mM triethylammonium, scan rate = 2 V).

3.5.6. Sample overpotential calculation with anilinium tetrafluoroborate[40,70,83]

(1) $E_{H^+} = E^{\circ}_{H^+} - 0.05916\ V\ x\ pK_a$

(2) $E_{H^+} = -0.343\ V - 0.05916\ V\ x\ 5.2 = -0.65\ V$

(1) $\eta = \left|E_{H^+} - E_{cat/2}\right|$

(2) $\eta = |-0.65\ V - (-1.16 \pm 0.07\ V)| = 0.51 \pm 0.07\ V$

3.5.7. Sample overpotential calculation with imidazolium tetrafluoroborate[40,70,83]

(1) $E_{H^+} = E^{\circ}_{H^+} - 0.05916\ V\ x\ pK_a$

(2) $E_{H^+} = -0.343\ V - 0.05916\ V\ x\ 9.4 = -0.90\ V$

(1) $\eta = \left|E_{H^+} - E_{cat/2}\right|$

(2) $\eta = |-0.90\ V - (-1.79 \pm 0.05\ V)| = 0.89 \pm 0.05\ V$

3.5.8. Sample overpotential calculation with triethylammonium tetrafluoroborate[40,70,83]

(1) $E_{H^+} = E^{\circ}_{H^+} - 0.05916\ V\ x\ pK_a$

(2) $E_{H^+} = -0.343\ V - 0.05916\ V\ x\ 12.5 = -1.08\ V$

(1) $\eta = \left|E_{H^+} - E_{cat/2}\right|$

(2) $\eta = |-1.08\ V - (-2.05 \pm 0.05\ V)| = 0.97 \pm 0.05\ V$

3.5.9. Sample turnover frequency calculation[54]

(1) $TOF_{max} = (1.94\ V^{-1})v \left(\frac{i_{cat}}{i_p}\right)^2$

(2) $TOF_{max} = 1.94\ V^{-1} \times 11\ V/s \times \left(\frac{0.92776\ mA}{0.022837\ mA}\right)^2$

(3) $TOF_{max} = 33040 \pm 150\ s^{-1}$

3.5.10. Sample turnover frequency calculation with imidazolium tetrafluoroborate[66,84]

$i_p = \frac{n^2F^2}{4RT} vA\Gamma^*$

$0.022015 \pm 0.001966\ mA = \frac{(1\ mole\ e^-)^2(96485\ C/mol)^2}{4(8.314\ J/molK)(298\ K)}(9\ V/s)(0.070686\ cm^2)\Gamma^*$

$\Gamma^* = 3.683913695 \times 10^{-11}\ mol/cm^2$

$TOF = \frac{j}{nF\Gamma^*}$

$TOF = \frac{i_{cat}}{nFA\Gamma^*}$

$TOF = \frac{1.3465\ mA}{2 \times (96485\ C/mol)(0.070686\ cm^2)(4.42 \times 10^{-11}\ mol/cm^2)}$

$TOF = 2680\ s^{-1}\ or\ 37914.15556\ s^{-1}cm^{-2}$

3.5.11. Sample faradaic Efficiency calculation[55,85]

$$Theoretical\ moles\ of\ H_2 = 0.5\ C \times \frac{1\ mol\ e^-}{96485\ C} \times \frac{1\ mol\ H_2}{2\ mol\ e^-} \quad (S4)$$

$$Theoretical\ moles\ of\ H_2 = 3.60 \times 10^{-6}\ mol$$

$$\text{y} = 790.35\ ppm/mL \text{ x } (From\ calibration\ curve\ Figure) \quad (S5)$$

$$63.8 \text{ ppm} = 790.35\ ppm/mL \text{ x}$$

$$\text{x} = 0.08855 \ldots mL$$

$$Experimental\ moles\ of\ H_2 = \frac{0.0807 \ldots mL}{24789.57 \ldots\ mL/mol}\ (From\ ideal\ gas\ law\ at\ 25\ ^\circ\text{C}) \quad (S6)$$

$$Experimental\ moles\ of\ H_2 = 3.57 \times 10^{-6}\ mol$$

$$Faradaic\ Efficiency = \frac{Experimental\ moles\ H_2}{Theoritical\ moles\ H_2} \times 100 \quad (S7)$$

$$Faradaic\ Efficiency = \frac{3.57 \times 10^{-6}\ mol}{3.60 \times 10^{-6}\ mol} \times 100$$

$$Faradaic\ Efficiency = 99.3\%$$

3.6. References

(1) Qadeer, M. A.; Zhang, X.; Farid, M. A.; Tanveer, M.; Yan, Y.; Du, S.; Huang, Z.-F.; Tahir, M.; Zou, J.-J. A Review on Fundamentals for Designing Hydrogen Evolution Electrocatalyst. *Journal of Power Sources* **2024**, *613*, 234856. https://doi.org/10.1016/j.jpowsour.2024.234856.

(2) Wu, L.-W.; Yao, Y.-F.; Xu, S.-Y.; Cao, X.-Y.; Ren, Y.-W.; Si, L.-P.; Liu, H.-Y. Electrocatalytic Hydrogen Evolution of Transition Metal (Fe, Co and Cu)–Corrole Complexes Bearing an Imidazole Group. *Catalysts* **2024**, *14* (1), 5. https://doi.org/10.3390/catal14010005.

(3) Armaroli, N.; Balzani, V. The Hydrogen Issue. *ChemSusChem* **2011**, *4* (1), 21–36. https://doi.org/10.1002/cssc.201000182.

(4) Yuan, S.; Pang, S.-Y.; Hao, J. 2D Transition Metal Dichalcogenides, Carbides, Nitrides, and Their Applications in Supercapacitors and Electrocatalytic Hydrogen Evolution Reaction. *Applied Physics Reviews* **2020**, *7* (2), 021304. https://doi.org/10.1063/5.0005141.

(5) Zhang, H.; Liu, W.; Cao, D.; Cheng, D. Carbon-Based Material-Supported Single-Atom Catalysts for Energy Conversion. *iScience* **2022**, *25* (6). https://doi.org/10.1016/j.isci.2022.104367.

(6) McAllister, J.; Bandeira, N. A. G.; McGlynn, J. C.; Ganin, A. Y.; Song, Y.-F.; Bo, C.; Miras, H. N. Tuning and Mechanistic Insights of Metal Chalcogenide Molecular Catalysts for the Hydrogen-Evolution Reaction. *Nat Commun* **2019**, *10* (1), 370. https://doi.org/10.1038/s41467-018-08208-4.

(7) Chen, D.; Chen, Z.; Zhang, X.; Lu, Z.; Xiao, S.; Xiao, B.; Singh, C. V. Exploring Single Atom Catalysts of Transition-Metal Doped Phosphorus Carbide Monolayer for HER: A First-Principles Study. *Journal of Energy Chemistry* **2021**, *52*, 155–162. https://doi.org/10.1016/j.jechem.2020.03.061.

(8) Pan, S.; Yu, X.; Ling, Y.; Yang, Z. Stable and Efficient Hydrogen Evolution Reaction Catalyzed by NiO-Rh2P Heterostructure Electrocatalyst. *Catalysis Communications* **2022**, *163*, 106404. https://doi.org/10.1016/j.catcom.2022.106404.

(9) Strbac, S. B.; Adzic, R. R. Electrocatalysis, Fundamentals - Electron Transfer Process; Current-Potential Relationship; Volcano Plots. In *Encyclopedia of Applied Electrochemistry*; Kreysa, G., Ota, K., Savinell, R. F., Eds.; Springer: New York, NY, 2014; pp 417–423. https://doi.org/10.1007/978-1-4419-6996-5_485.

(10) Hossain, M. D.; Liu, Z.; Liu, H.; Tyagi, A.; Rehman, F.; Li, J.; Amjadian, M.; Cai, Y.; Goddard, W. A.; Luo, Z. The Kinetics and Potential Dependence of the Hydrogen Evolution Reaction Optimized for the Basal-Plane Te Vacancy Site of MoTe2. *Chem Catalysis* **2023**, *3* (1). https://doi.org/10.1016/j.checat.2022.100489.

(11) Trasatti, S. Work Function, Electronegativity, and Electrochemical Behaviour of Metals: III. Electrolytic Hydrogen Evolution in Acid Solutions. *Journal of Electroanalytical Chemistry and Interfacial Electrochemistry* **1972**, *39* (1), 163–184. https://doi.org/10.1016/S0022-0728(72)80485-6.

(12) Costentin, C.; Savéant, J.-M. Homogeneous Molecular Catalysis of Electrochemical Reactions: Manipulating Intrinsic and Operational Factors for Catalyst Improvement. *J. Am. Chem. Soc.* **2018**, *140* (48), 16669–16675. https://doi.org/10.1021/jacs.8b09154.

(13) Mandal, S. K.; Sunil, C.; Choudhury, J. [Fe]-Hydrogenase-Inspired Proton-Shuttle Installation in a Molecular Cobalt Complex for High-Efficiency H2 Evolution Reaction. *ACS Catal.* **2024**, *14* (3), 2058–2070. https://doi.org/10.1021/acscatal.3c04879.
(14) Tsay, C.; Yang, J. Y. Electrocatalytic Hydrogen Evolution under Acidic Aqueous Conditions and Mechanistic Studies of a Highly Stable Molecular Catalyst. *J. Am. Chem. Soc.* **2016**, *138* (43), 14174–14177. https://doi.org/10.1021/jacs.6b05851.
(15) Queyriaux, N.; Sun, D.; Fize, J.; Pécaut, J.; Field, M. J.; Chavarot-Kerlidou, M.; Artero, V. Electrocatalytic Hydrogen Evolution with a Cobalt Complex Bearing Pendant Proton Relays: Acid Strength and Applied Potential Govern Mechanism and Stability. *J. Am. Chem. Soc.* **2020**, *142* (1), 274–282. https://doi.org/10.1021/jacs.9b10407.
(16) *Water electrolysis | Nature Reviews Methods Primers*. https://www.nature.com/articles/s43586-022-00164-0 (accessed 2025-03-28).
(17) Nørskov, J. K.; Bligaard, T.; Logadottir, A.; Kitchin, J. R.; Chen, J. G.; Pandelov, S.; Stimming, U. Trends in the Exchange Current for Hydrogen Evolution. *J. Electrochem. Soc.* **2005**, *152* (3), J23. https://doi.org/10.1149/1.1856988.
(18) Subbaraman, R.; Tripkovic, D.; Strmcnik, D.; Chang, K.-C.; Uchimura, M.; Paulikas, A. P.; Stamenkovic, V.; Markovic, N. M. Enhancing Hydrogen Evolution Activity in Water Splitting by Tailoring Li+-Ni(OH)2-Pt Interfaces. *Science* **2011**, *334* (6060), 1256–1260. https://doi.org/10.1126/science.1211934.
(19) Trasatti, S. Work Function, Electronegativity, and Electrochemical Behaviour of Metals. *Journal of Electroanalytical Chemistry and Interfacial Electrochemistry* **1972**, *39* (1), 163–184. https://doi.org/10.1016/S0022-0728(72)80485-6.
(20) Zheng, J.; Sheng, W.; Zhuang, Z.; Xu, B.; Yan, Y. Universal Dependence of Hydrogen Oxidation and Evolution Reaction Activity of Platinum-Group Metals on pH and Hydrogen Binding Energy. *Science Advances* **2016**, *2* (3), e1501602. https://doi.org/10.1126/sciadv.1501602.
(21) Sun, J.; Zhang, X.; Jin, M.; Xiong, Q.; Wang, G.; Zhang, H.; Zhao, H. Robust Enhanced Hydrogen Production at Acidic Conditions over Molybdenum Oxides-Stabilized Ultrafine Palladium Electrocatalysts. *Nano Research* **2021**, *14* (1), 268–274. https://doi.org/10.1007/s12274-020-3083-3.
(22) Nguyen, V.-T.; Lee, G.-J.; Ngo, Q.-T.; Omelianovych, O.; Nguyen, N.-A.; Trinh, V.-H.; Choi, H.-S.; Mnoyan, A.; Lee, K.; Larina, L. L.; Chen, G. Robust Carbon-Encapsulated Ni Nanoparticles as High-Performance Electrocatalysts for the Hydrogen Evolution Reaction in Highly Acidic Media. *Electrochimica Acta* **2021**, *398*, 139332. https://doi.org/10.1016/j.electacta.2021.139332.
(23) Ali, M. A. Magnetic and Spectroscopic Studies on Nickel(II) and Copper(II) Complexes of Some Neutral Tridentate ONS Ligands. *Can. J. Chem.* **1980**, *58* (7), 727–732. https://doi.org/10.1139/v80-112.
(24) Patel, N. H.; Parekh, H. M.; Patel, M. N. Synthesis, Characterization and Biological Evaluation of Manganese(II), Cobalt(II), Nickel(II), Copper(II), and Cadmium(II) Complexes with Monobasic (NO) and Neutral (NN) Schiff Bases. *Transition Met Chem* **2005**, *30* (1), 13–17. https://doi.org/10.1007/s11243-004-3226-5.
(25) Tarafder, M. T. H.; Ali, M. A.; Wee, D. J.; Azahari, K.; Silong, S.; Crouse, K. A. Complexes of a Tridentate ONS Schiff Base. Synthesis and Biological Properties. *Transition Metal Chemistry* **2000**, *25* (4), 456–460. https://doi.org/10.1023/A:1007062409973.

(26) Ambike, V.; Adsule, S.; Ahmed, F.; Wang, Z.; Afrasiabi, Z.; Sinn, E.; Sarkar, F.; Padhye, S. Copper Conjugates of Nimesulide Schiff Bases Targeting VEGF, COX and Bcl-2 in Pancreatic Cancer Cells. *Journal of Inorganic Biochemistry* **2007**, *101* (10), 1517–1524. https://doi.org/10.1016/j.jinorgbio.2007.06.028.
(27) More, M. S.; Joshi, P. G.; Mishra, Y. K.; Khanna, P. K. Metal Complexes Driven from Schiff Bases and Semicarbazones for Biomedical and Allied Applications: A Review. *Mater Today Chem* **2019**, *14*, 100195. https://doi.org/10.1016/j.mtchem.2019.100195.
(28) Devi, J.; Yadav, M.; Jindal, D. k.; Kumar, D.; Poornachandra, Y. Synthesis, Spectroscopic Characterization, Biological Screening and in Vitro Cytotoxic Studies of 4-Methyl-3-Thiosemicarbazone Derived Schiff Bases and Their Co (II), Ni (II), Cu (II) and Zn (II) Complexes. *Applied Organometallic Chemistry* **2019**, *33* (10), e5154. https://doi.org/10.1002/aoc.5154.
(29) Omidi, S.; Kakanejadifard, A. A Review on Biological Activities of Schiff Base, Hydrazone, and Oxime Derivatives of Curcumin. *RSC Adv.* **2020**, *10* (50), 30186–30202. https://doi.org/10.1039/D0RA05720G.
(30) Prakash, A.; Adhikari, D. Application of Schiff Bases and Their Metal Complexes-A Review.
(31) Tariqul Islam, M.; Amin Bitu, N.; Mohon Chaki, B.; Jakir Hossain, M.; Ali Asraf, M.; Faruk Hossen, M.; Kudrat-E-Zahan, M.; Abdul Latif, M. Water-Soluble Schiff Base Ligands and Metal Complexes: An Overview Considering Green Solvent. *RSC Advances* **2024**, *14* (35), 25256–25272. https://doi.org/10.1039/D4RA04310C.
(32) Andersson Trojer, M.; Movahedi, A.; Blanck, H.; Nyden, M. Imidazole and Triazole Coordination Chemistry for Antifouling Coatings. *Journal of Chemistry [ISSN:2090-9071]* **2013**. https://doi.org/10.1155/2013/XXXXXX.
(33) Somachandra, M. S.; Averkiev, B.; Sues, P. E. Unsymmetric Co-Facial "Salixpyrrole" Hydrogen Evolution Catalysts: Two Metals Are Better than One. *Inorg. Chem.* **2024**, *63* (29), 13346–13357. https://doi.org/10.1021/acs.inorgchem.4c01101.
(34) Trowbridge, L.; Averkiev, B.; Sues, P. E. Palladium Complexes Bearing Calixpyrrole Ligands with Pendant Hydrogen Bond Donors: Synthesis, Structural Characterization, Electrochemistry and Dihydrogen Evolution. *Polyhedron* **2022**, *225*, 116046. https://doi.org/10.1016/j.poly.2022.116046.
(35) Givaja, G.; Volpe, M.; Leeland, J. W.; Edwards, M. A.; Young, T. K.; Darby, S. B.; Reid, S. D.; Blake, A. J.; Wilson, C.; Wolowska, J.; McInnes, E. J. L.; Schröder, M.; Love, J. B. Design and Synthesis of Binucleating Macrocyclic Clefts Derived from Schiff-Base Calixpyrroles. *Chemistry – A European Journal* **2007**, *13* (13), 3707–3723. https://doi.org/10.1002/chem.200600989.
(36) Wiedner, E. S.; Chambers, M. B.; Pitman, C. L.; Bullock, R. M.; Miller, A. J. M.; Appel, A. M. Thermodynamic Hydricity of Transition Metal Hydrides. *Chem. Rev.* **2016**, *116* (15), 8655–8692. https://doi.org/10.1021/acs.chemrev.6b00168.
(37) Smith, A. M.; Miller, A. J. M. Open Circuit Potential Method for Thermodynamic Hydricity Measurements of Metal Hydrides. *Organometallics* **2024**, *43* (24), 3163–3170. https://doi.org/10.1021/acs.organomet.4c00144.
(38) Roberts, J. A. S.; Bullock, R. M. Direct Determination of Equilibrium Potentials for Hydrogen Oxidation/Production by Open Circuit Potential Measurements in Acetonitrile. *Inorg. Chem.* **2013**, *52* (7), 3823–3835. https://doi.org/10.1021/ic302461q.

(39) Artero, V.; Fontecave, M. Solar Fuels Generation and Molecular Systems: Is It Homogeneous or Heterogeneous Catalysis? *Chem. Soc. Rev.* **2013**, *42* (6), 2338–2356. https://doi.org/10.1039/C2CS35334B.
(40) Tshepelevitsh, S.; Kütt, A.; Lõkov, M.; Kaljurand, I.; Saame, J.; Heering, A.; Plieger, P. G.; Vianello, R.; Leito, I. On the Basicity of Organic Bases in Different Media. *Eur J Org Chem* **2019**, *2019* (40), 6735–6748. https://doi.org/10.1002/ejoc.201900956.
(41) Geiger, W. E.; Barrière, F. Organometallic Electrochemistry Based on Electrolytes Containing Weakly-Coordinating Fluoroarylborate Anions. *Acc. Chem. Res.* **2010**, *43* (7), 1030–1039. https://doi.org/10.1021/ar1000023.
(42) Suryanarayanan, V.; Yoshihara, S.; Shirakashi, T. Electrochemical Behavior of Carbon Electrodes in Organic Liquid Electrolytes Containing Tetrafluoroborate and Hexafluorophosphate Anionic Species in Different Non-Aqueous Solvent Systems. *Electrochimica Acta* **2005**, *51* (5), 991–999. https://doi.org/10.1016/j.electacta.2005.04.064.
(43) Driessen, W. L.; Reedijk, J.; Dunbar, K. R.; Pence, L. E. Solid Solvates: The Use of Weak Ligands in Coordination Chemistry. In *Inorganic Syntheses*; Grimes, R. N., Ed.; Wiley, 1992; Vol. 29, pp 111–118. https://doi.org/10.1002/9780470132609.ch27.
(44) Kwak, K.; Choi, W.; Tang, Q.; Kim, M.; Lee, Y.; Jiang, D.; Lee, D. A Molecule-like PtAu24(SC6H13)18 Nanocluster as an Electrocatalyst for Hydrogen Production. *Nat Commun* **2017**, *8* (1), 14723. https://doi.org/10.1038/ncomms14723.
(45) *Evaluation of Homogeneous Electrocatalysts by Cyclic Voltammetry | Inorganic Chemistry*. https://pubs.acs.org/doi/10.1021/ic500658x (accessed 2025-04-19).
(46) Artero, V.; Saveant, J.-M. Toward the Rational Benchmarking of Homogeneous H2-Evolving Catalysts. *Energy Environ. Sci.* **2014**, *7* (11), 3808–3814. https://doi.org/10.1039/C4EE01709A.
(47) Suliborska, K.; Baranowska, M.; Bartoszek, A.; Chrzanowski, W.; Namieśnik, J. Determination of Antioxidant Activity of Vitamin C by Voltammetric Methods. *Proceedings* **2019**, *11* (1), 23. https://doi.org/10.3390/proceedings2019011023.
(48) Movellan, K. T.; Wegstroth, M.; Overkamp, K.; Leonov, A.; Becker, S.; Andreas, L. B. Imidazole–Imidazole Hydrogen Bonding in the pH-Sensing Histidine Side Chains of Influenza A M2. *J. Am. Chem. Soc.* **2020**, *142* (6), 2704–2708. https://doi.org/10.1021/jacs.9b10984.
(49) Bonsor, D. H.; Borah, B.; Dean, R. L.; Wood, J. L. Complex Hydrogen Bonded Cations. The Imdazole/Imidazolium Complex Cation. *Can. J. Chem.* **1976**, *54* (15), 2458–2464. https://doi.org/10.1139/v76-349.
(50) Domínguez, S. E.; Vuolle, A.; Cangiotti, M.; Fattori, A.; Ääritalo, T.; Damlin, P.; Ottaviani, M. F.; Kvarnström, C. Cationic Imidazolium Polythiophenes: Effects of Imidazolium-Methylation on Solution Concentration-Driven Aggregation and Surface Free Energy of Films Processed from Solvents with Different Polarity. *Langmuir* **2020**, *36* (9), 2278–2290. https://doi.org/10.1021/acs.langmuir.9b03095.
(51) Costa, R.; Pereira, C. M.; Silva, A. F. Charge Storage on Ionic Liquid Electric Double Layer: The Role of the Electrode Material. *Electrochimica Acta* **2015**, *167*, 421–428. https://doi.org/10.1016/j.electacta.2015.02.180.
(52) Ma, S.; Chen, D.; Xu, J.; Ye, Z.; Zhang, J. Glassy Carbon Electrodes Modified with Ru Nanoparticles Loaded in B-Doped Imidazolium Porous Organic Polymers for Hydrogen Evolution Reaction. *Chemistry - An Asian Journal* **2024**, *20*, e202401042. https://doi.org/10.1002/asia.202401042.

(53) Mandal, S. K.; Sunil, C.; Choudhury, J. [Fe]-Hydrogenase-Inspired Proton-Shuttle Installation in a Molecular Cobalt Complex for High-Efficiency H2 Evolution Reaction. *ACS Catal.* **2024**, *14* (3), 2058–2070. https://doi.org/10.1021/acscatal.3c04879.
(54) Rountree, E. S.; McCarthy, B. D.; Eisenhart, T. T.; Dempsey, J. L. Evaluation of Homogeneous Electrocatalysts by Cyclic Voltammetry. *Inorg. Chem.* **2014**, *53* (19), 9983–10002. https://doi.org/10.1021/ic500658x.
(55) Haddad, A. Z.; Cronin, S. P.; Mashuta, M. S.; Buchanan, R. M.; Grapperhaus, C. A. Metal-Assisted Ligand-Centered Electrocatalytic Hydrogen Evolution upon Reduction of a Bis(Thiosemicarbazonato)Cu(II) Complex. *Inorg. Chem.* **2017**, *56* (18), 11254–11265. https://doi.org/10.1021/acs.inorgchem.7b01608.
(56) Bard, A. J.; Faulkner, L. R.; White, H. S. *Electrochemical Methods: Fundamentals and Applications*; John Wiley & Sons, 2022.
(57) Hong, X.-S.; Huo, D.; Jiang, W.-J.; Long, W.-J.; Leng, J.-D.; Tong, L.; Liu, Z.-Q. Electrocatalytic and Photocatalytic Hydrogen Evolution by Ni(II) and Cu(II) Schiff Base Complexes. *ChemElectroChem* **2020**, *7* (24), 4956–4962. https://doi.org/10.1002/celc.202001461.
(58) Straistari, T.; Fize, J.; Shova, S.; Réglier, M.; Artero, V.; Orio, M. A Thiosemicarbazone–Nickel(II) Complex as Efficient Electrocatalyst for Hydrogen Evolution. *ChemCatChem* **2017**, *9* (12), 2262–2268. https://doi.org/10.1002/cctc.201600967.
(59) Straistari, T.; Hardré, R.; Fize, J.; Shova, S.; Giorgi, M.; Réglier, M.; Artero, V.; Orio, M. Hydrogen Evolution Reactions Catalyzed by a Bis(Thiosemicarbazone) Cobalt Complex: An Experimental and Theoretical Study. *Chemistry – A European Journal* **2018**, *24* (35), 8779–8786. https://doi.org/10.1002/chem.201801155.
(60) Haddad, A. Z.; Garabato, B. D.; Kozlowski, P. M.; Buchanan, R. M.; Grapperhaus, C. A. Beyond Metal-Hydrides: Non-Transition-Metal and Metal-Free Ligand-Centered Electrocatalytic Hydrogen Evolution and Hydrogen Oxidation. *J. Am. Chem. Soc.* **2016**, *138* (25), 7844–7847. https://doi.org/10.1021/jacs.6b04441.
(61) Phipps, C. A.; Hofsommer, D. T.; Toda, M. J.; Nkurunziza, F.; Shah, B.; Spurgeon, J. M.; Kozlowski, P. M.; Buchanan, R. M.; Grapperhaus, C. A. Ligand-Centered Hydrogen Evolution with Ni(II) and Pd(II)DMTH. *Inorg. Chem.* **2022**, *61* (25), 9792–9800. https://doi.org/10.1021/acs.inorgchem.2c01326.
(62) *A guide to secondary coordination sphere editing - Chemical Society Reviews (RSC Publishing)*. https://pubs.rsc.org/en/content/articlelanding/2022/cs/d2cs00022a (accessed 2025-03-01).
(63) Orton, G. R. F.; Ghosh, S.; Alker, L.; Sarker, J. C.; Pugh, D.; Richmond, M. G.; Hartl, F.; Hogarth, G. Biomimics of [FeFe]-Hydrogenases Incorporating Redox-Active Ligands: Synthesis, Redox Properties and Spectroelectrochemistry of Diiron-Dithiolate Complexes with Ferrocenyl-Diphosphines as Fe4S4 Surrogates. *Dalton Trans.* **2022**, *51* (25), 9748–9769. https://doi.org/10.1039/D2DT00419D.
(64) Simmons, T. R.; Berggren, G.; Bacchi, M.; Fontecave, M.; Artero, V. Mimicking Hydrogenases: From Biomimetics to Artificial Enzymes. *Coordination Chemistry Reviews* **2014**, *270–271*, 127–150. https://doi.org/10.1016/j.ccr.2013.12.018.
(65) Wang, J.-W.; Yamauchi, K.; Huang, H.-H.; Sun, J.-K.; Luo, Z.-M.; Zhong, D.-C.; Lu, T.-B.; Sakai, K. A Molecular Cobalt Hydrogen Evolution Catalyst Showing High Activity and Outstanding Tolerance to CO and O2. *Angewandte Chemie International Edition* **2019**, *58* (32), 10923–10927. https://doi.org/10.1002/anie.201904578.

(66) *A Practical Beginner's Guide to Cyclic Voltammetry | Journal of Chemical Education*. https://pubs.acs.org/doi/10.1021/acs.jchemed.7b00361 (accessed 2025-04-22).
(67) *Kinetics and Limiting Current Densities of Homogeneous and Heterogeneous Electrocatalysts | The Journal of Physical Chemistry Letters*. https://pubs.acs.org/doi/10.1021/jz2008227 (accessed 2025-04-22).
(68) Trowbridge, L.; Averkiev, B.; Sues, P. E. Electrocatalytic Hydrogen Evolution Using a Nickel-based Calixpyrrole Complex: Controlling the Secondary Coordination Sphere on an Electrode Surface. *Chemistry A European J* **2023**, *29* (65), e202301920. https://doi.org/10.1002/chem.202301920.
(69) Artero, V.; Fontecave, M. Some General Principles for Designing Electrocatalysts with Hydrogenase Activity. *Coordination Chemistry Reviews* **2005**, *249* (15), 1518–1535. https://doi.org/10.1016/j.ccr.2005.01.014.
(70) *Determining the Overpotential for a Molecular Electrocatalyst | ACS Catalysis*. https://pubs.acs.org/doi/10.1021/cs401013v (accessed 2025-03-01).
(71) Stewart, M. P.; Ho, M.-H.; Wiese, S.; Lindstrom, M. L.; Thogerson, C. E.; Raugei, S.; Bullock, R. M.; Helm, M. L. High Catalytic Rates for Hydrogen Production Using Nickel Electrocatalysts with Seven-Membered Cyclic Diphosphine Ligands Containing One Pendant Amine. *J. Am. Chem. Soc.* **2013**, *135* (16), 6033–6046. https://doi.org/10.1021/ja400181a.
(72) Hoffert, W. A.; Roberts, J. A. S.; Bullock, R. M.; Helm, M. L. Production of H2 at Fast Rates Using a Nickel Electrocatalyst in Water–Acetonitrile Solutions. *Chem. Commun.* **2013**, *49* (71), 7767–7769. https://doi.org/10.1039/C3CC43203C.
(73) *Molecular mechanisms of cobalt-catalyzed hydrogen evolution | PNAS*. https://www.pnas.org/doi/full/10.1073/pnas.1213442109 (accessed 2025-03-02).
(74) *Size- and Shape-Dependent Activity of Metal Nanoparticles as Hydrogen-Evolution Catalysts: Mechanistic Insights into Photocatalytic Hydrogen Evolution - Kotani - 2011 - Chemistry – A European Journal - Wiley Online Library*. https://chemistry-europe.onlinelibrary.wiley.com/doi/10.1002/chem.201002399 (accessed 2025-03-02).
(75) Krishtalik, L. I. Kinetic Isotope Effect in the Hydrogen Evolution Reaction. *Electrochimica Acta* **2001**, *46* (19), 2949–2960. https://doi.org/10.1016/S0013-4686(01)00526-6.
(76) Tyburski, R.; Liu, T.; Glover, S. D.; Hammarström, L. Proton-Coupled Electron Transfer Guidelines, Fair and Square. *J. Am. Chem. Soc.* **2021**, *143* (2), 560–576. https://doi.org/10.1021/jacs.0c09106.
(77) Costentin, C.; Savéant, J.-M. Multielectron, Multistep Molecular Catalysis of Electrochemical Reactions: Benchmarking of Homogeneous Catalysts. *ChemElectroChem* **2014**, *1* (7), 1226–1236. https://doi.org/10.1002/celc.201300263.
(78) Warren, J. J.; Tronic, T. A.; Mayer, J. M. Thermochemistry of Proton-Coupled Electron Transfer Reagents and Its Implications. *Chem. Rev.* **2010**, *110* (12), 6961–7001. https://doi.org/10.1021/cr100085k.
(79) Wilson, A. D.; Newell, R. H.; McNevin, M. J.; Muckerman, J. T.; Rakowski DuBois, M.; DuBois, D. L. Hydrogen Oxidation and Production Using Nickel-Based Molecular Catalysts with Positioned Proton Relays. *J. Am. Chem. Soc.* **2006**, *128* (1), 358–366. https://doi.org/10.1021/ja056442y.
(80) Gotico, P.; Herrero, C.; Protti, S.; Quaranta, A.; Sheth, S.; Fallahpour, R.; Farran, R.; Halime, Z.; Sircoglou, M.; Aukauloo, A.; Leibl, W. Proton-Controlled Action of an Imidazole as

Electron Relay in a Photoredox Triad. *Photochem Photobiol Sci* **2022**, *21* (2), 247–259. https://doi.org/10.1007/s43630-021-00163-2.
(81) Aoki, K. J.; Chen, J.; Liu, Y.; Jia, B. Peak Potential Shift of Fast Cyclic Voltammograms Owing to Capacitance of Redox Reactions. *Journal of Electroanalytical Chemistry* **2020**, *856*, 113609. https://doi.org/10.1016/j.jelechem.2019.113609.
(82) Montgomery, C. L.; Lee, J.; Donley, C. L.; Jackson, M. N.; Tereniak, S. J.; Dempsey, J. L. Kinetic Analysis of Proton-Coupled Electron Transfer at an Electrode-Immobilized Complex. *ACS Electrochem.* **2025**, *1* (3), 303–314. https://doi.org/10.1021/acselectrochem.4c00099.
(83) Stratakes, B. M.; Dempsey, J. L.; Miller, A. J. M. Determining the Overpotential of Electrochemical Fuel Synthesis Mediated by Molecular Catalysts: Recommended Practices, Standard Reduction Potentials, and Challenges. *ChemElectroChem* **2021**, *8* (22), 4161–4180. https://doi.org/10.1002/celc.202100576.
(84) Sathrum, A. J.; Kubiak, C. P. Kinetics and Limiting Current Densities of Homogeneous and Heterogeneous Electrocatalysts. *J. Phys. Chem. Lett.* **2011**, *2* (18), 2372–2379. https://doi.org/10.1021/jz2008227.
(85) Haddad, A. Z.; Garabato, B. D.; Kozlowski, P. M.; Buchanan, R. M.; Grapperhaus, C. A. Beyond Metal-Hydrides: Non-Transition-Metal and Metal-Free Ligand-Centered Electrocatalytic Hydrogen Evolution and Hydrogen Oxidation. *J. Am. Chem. Soc.* **2016**, *138* (25), 7844–7847. https://doi.org/10.1021/jacs.6b04441.

Chapter 4 - Synthesizing heterobimetallic complexes as promising catalysts for small molecule activation.

4.1. Abstract

Heterobimetallic complexes have attracted interest for decades due to their resemblance to metalloenzyme active sites. But only recently have chemists started to have an interest in developing ligand scaffolds that are specifically designed to support multinuclear transition metal cores. Those ligand systems were designed not only to hold multiple metal centers in close proximity but also allow for fine-tuning of their electronic structures and surrounding steric environments. This specific project highlights a synthetic route that allows the formation of heterobimetallic complexes based on an unsymmetric Schiff-base ligand scaffold through stepwise metalation. The monometallic complexes from Chapters 2 (Pd-salixpyrrole) and 3 (Pd-imixpyrrole) were used as the starting material. Although heterobimetallic complex formation with the "Salixpyrrole" system turned out to be rather unsuccessful to this date, the "imixpyrrole" system resulted in two promising heterobimetallic complexes, PdZn-Imixpyrrole and PdCu-Salixpyrrole. The cyclic voltammetry features suggest the possibility of cooperative small molecule activation specifically for the hydrogen evolution reaction.

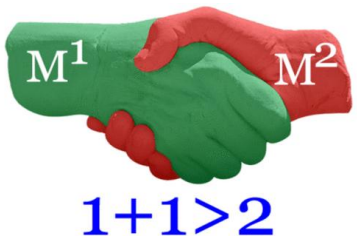

4.2. Introduction

Cooperation between multiple metal atoms to obtain catalytic properties that are "greater than the sum of their parts" is drawing the attention of the inorganic community.[1] Mononuclear metal complexes and homodinuclear metal complexes have received much attention over the past years, but when it comes to hererodinuclear/heterobimetallic complexes, their advanced activity has been unexplored unlike their mono- or homodinuclear counterparts.[2] When metal centers are in close proximity in the ligand system or a direct metal-metal bond, they can enhance the catalytic activity via synergistic and cooperative effects that could result from the simultaneous or consecutive action of different metals present in a homogenous or heterogenous medium.[1] Therefore, heterobimetallic complexes gain special interest due to generating highly active species, even if the exact active species is often unknown. Selecting metal centers wisely can influence the overall performance of the complex, allowing the complex to achieve chemical transformations otherwise inaccessible.[3] By tuning parameters like ligand steric and electronics, bond polarity, and bond order, provides a wide area of research for inorganic chemists to explore.[4]

Recent publications have emphasized the advantages of bimetallic complexes and their applications in many areas like biology, medicine, catalysis, nanoscience, redox and photoactive materials, etc.[5,6] This attraction is mainly due to the unique reactivity and/or selectivity patterns that multimetallic systems offer compared to their monometallic analogue and due to the tunable characteristics of their chemical reactivity in terms of both kinetics (rate of ligand exchange) and thermodynamics (strength of metal-ligand, redox potentials, etc.).[7–9] So far, most of these heterobimetallic catalysts have been studied for organic transformations such as olefin metathesis reactions, and various cross-coupling catalysts, catalyzing asymmetric nitro-Mannich-type reactions, nitroaldol reactions, etc.[1,10,11] However, when it comes to small molecule activation, the

majority of work has been done to develop mononuclear catalysts and fine-tune the steric and electronic parameters of the supporting ligand environment.[12–17]

The growing interest in discovering new complexes with multiple metal centers is inspired by biocatalytic systems. Protein crystallography data revealed the active site of most enzymes, such as [NiFe]-, [FeFe]-hydrogenases, CO-dehydrogenases, and acetyl-CoA synthase (ACS), which emphasizes the need for more than one metal center in their active site to achieve organometallic-like functions.[18,19] Specifically, when it comes to hydrogenases, their active site contains at least two first-row transition metals which are connected by sulfides or thiolates along with Lewis acid/base sites (**Figure 4.1**).[19–21] [FeFe]-hydrogenase is known for H_2 production where each Fe center contains a distinct ligand environment and proton-shuttling groups enhancing catalysis. On the other hand, [NiFe]-hydrogenase is particularly efficient at H_2 oxidation which features a heterobimetallic structure in its active site with complex coordination and redox-sensitive clusters.[19,21] Therefore, when it comes to designing model catalysts for hydrogen evolution reaction (HER) or any other catalysis processes, few structural features are considered such as; 1) the availability of low-valent metals. 2) homo or hetero metallic structure with a unique coordination environment around each metal, 3) structural flexibility for the substrate to access the active site of the catalyst, 4) the availability of "in-built" functional groups that can participate in proton shuttle or the groups that are rich in electrons to supply electrons rapidly during catalysis.

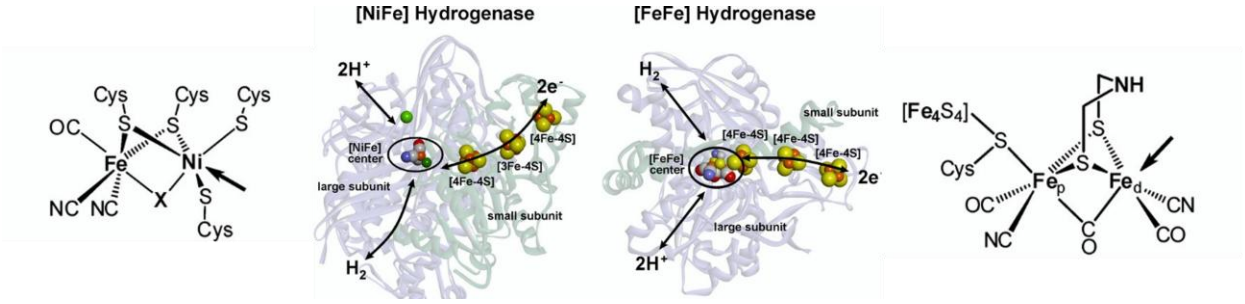

Figure 4.1. Structures of the [NiFe] hydrogenase from DvMF18 and the [FeFe] hydrogenase from *Dd*.[22] Schematically indicated are the ET chain (via iron-sulfur centers) and pathways for

the dihydrogen and the H^+ transfer. At the bottom, the chemical structures of the active sites of the two types of hydrogenases are given; the arrows indicate the open metal coordination site. Adopted from REF[19].

The origin of this field is considered Muetterties' study of the cluster surface analogy,[23] where the cluster compound often contains low-valent late-metals, then bimetallic compounds that are usually surrounded by simple carbonyl, hydride, and phosphine ligands were studied.[24–27] Since then, a number of metal complexes containing σ-donating and π-accepting ligands such as Bergman's sulfur-atom abstraction reactions by a heterobimetallic $Cp_2Zr(\mu\text{-}N^tBu)IrCp^*$ complex (Cp* = pentamethylcyclopentadienyl),[28] Mankad's bimetallic (^{Dipp}NHC)Cu–$FeCp(CO)_2$ complexes (^{Dipp}NHC = *N*,*N*′-bis(2,6-diisopropylphenyl)imidazol-2-ylidene) that perform catalytic photochemical C–H borylation reactions,[29] etc. were studied for small molecule activation.[3] Interestingly, all of these multinuclear complexes can be seen using the ligands that are commonly used in mononuclear transition metal complexes to achieve unique reactivities. Therefore, the recent interest has shifted towards cofacial porphyrins and dinuclear Schiff base complexes since those ligand systems are much more popular as small molecular activation catalysts.[10,30,31]

The main criteria to consider when it comes to synthesizing heterobimetallic complexes, designing the ligand architecture to facilitate the coordination of multiple metals within close proximity of one another. Steric and electronic parameters play a crucial role in metal coordination and substrate accessibility.[32,33] There are two main primary classes of ligand design strategies according to Tomson and co-workers,[3] one involves designing a ligand system to support the coordination of an ancillary metal (M_A) as a ligand on the catalytically active metal (M_B) (Class 1) and the other class involves designing ligand systems that provide access for multiple metals to coordinate and activate small molecules (Class 2) (**Figure 4.2**).[34–37] For the class 1 situation to

work, the coordination environment around M_A needs to be saturated, and the coordination environment around M_B should have a vacant spot so the substrate of interest can access the metal complex and the catalytic activity can take place at M_B. Class 2 can be subdivided into systems that have metal-metal (M-M) separation greater than the bonding range (Class 2A) and those that support M-M bonding (Class 2B).

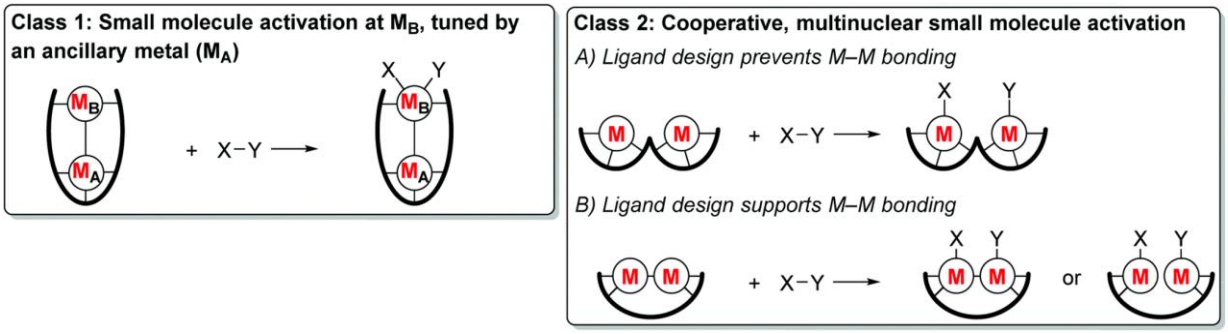

Figure 4.2. Categories of ligand design classes aimed at generating multinuclear complexes capable of undergoing small molecule activation chemistry. Adopted from REF[3].

Besides ligand designing, metal coordination can be achieved through a few methods. One method is stepwise metalation, where synthesis of the monometallic complex is done first, followed by the introduction of the second metal. In this case, the ligand system can be designed to bind selectively to the first metal, then the second metal will bind to the remaining donor atoms, or the synthesis of the monometallic complex can be done first, followed by a post-synthetic modification to build up donor sites for the second metal.[10,31,38,39] The second method can be considered as one-pot synthesis or simultaneous metalation where the mixing of the ligand with both metal salts takes place at the same time in a single pot under a stoichiometrically controlled environment.[40,41] Metalation also can be done through the templating method, where a metal ion is used as a template to promote the formation of the ligand followed by the second metalation.[42–45]

This Chapter is an attempt towards the synthesis of new unsymmetric heterobimetallic complexes using previously discussed "Salixpyrolle" systems (Chapter 2) and the "Imixpyrrole" system (Chapter 3). Herein, the synthesis attempts of a series of heterobimetallic complexes containing Pd(II) with various other transition metals (Ni(II), Zn(II), Cu(I), Co(II), etc.) based on novel unsymmetric ligands is discussed. In addition, the spectroscopic characterization and electrochemical characterization with catalytic activities of some compounds are addressed.

4.3. Results and discussion

4.3.1. Synthesis of heterobimetallic complexes from the "Salixpyrrole" system.

The initial work for this project was inspired by Stefan Bräse and his group, who employed a stepwise metalation strategy to coordinate the second cation, resulting in a heterobimetallic "Pacman" porphyrin system. [31] The monometallic salixpyrrole complex (2) was used as a starting material, and its synthesis was carried out as discussed in Chapter 2.[46] Complex 2 was used as a starting material and reacted with a base to deprotonate phenol OH groups in the salen moiety, followed by metalation with a metal salt, as illustrated in **Scheme 4.1**.

Scheme 4.1. General Synthetic procedure for heterobimetallic complexes utilizing the monometallic Salixpyrrole complex **2** as a starting material.

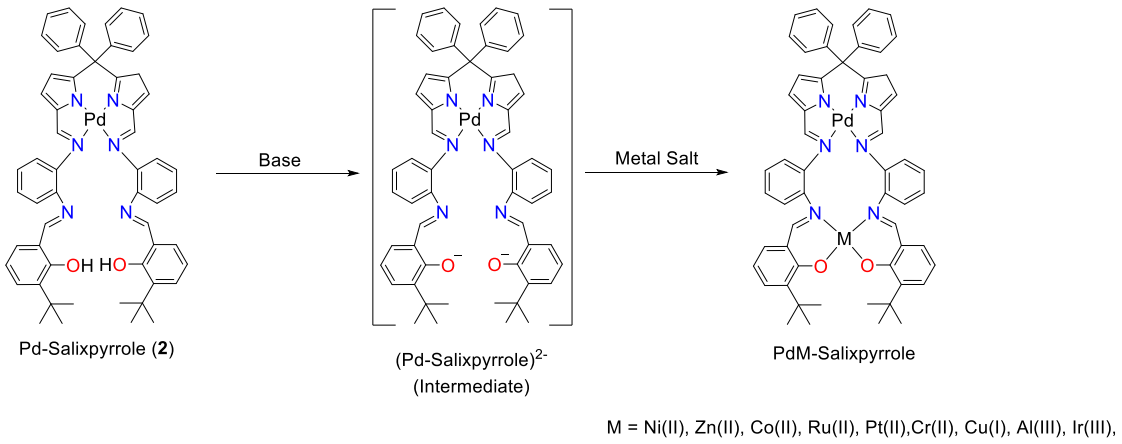

The completion of the reactions was assessed by the appearance of only two distinct imine peaks in the ^{1}H NMR spectra. Successful coordination with the second metal was indicated by a

pronounced chemical shift of the imine proton associated with the salen imine moiety, along with a moderate peak shift for the calixpyrrole imine proton. When stoichiometric amounts of base and metal salts (4:1) were used, the ^{1}H NMR spectra showed no significant changes for Co(II), Cr(II), Ru(II), Cu(I), Al(III), Ir(III) metal salts, suggesting unsuccessful metal coordination (Table 4.3.1). In contrast, reactions with Zn(II), Ni(II), Pt(II) metal salts resulted in the appearance of more than two imine peaks in the ^{1}H NMR spectra, indicating the possibility of multiple side reactions or suboptimal reaction conditions in the reaction medium (**Table 4.1**).

Table 4.1. The initial reaction conditions were used for heterobimetallic complex synthesis with the Salixpyrrole system. (all the reaction was carried out at room temperature in an inert atmosphere, the ratio between base: metal = 2:1).

Metal ion	**Solvent**	**Metal source**	**Base**	**Results**
Cu(I)	THF	$[(CH_3CN)_4Cu]PF_6$	NEt_3	No significant change
Cr(II)	THF	$CrCl_3$	NEt_3	No significant change
Ru(II)	THF/CH_3CN	$[Ru(PPh_3)_3]Cl_2$	NEt_3	No significant change
Co(II)	THF	$Co(acac)_2$	NEt_3	No significant change
Ni(II)	DCM	$[Ni(CH_3CN)_6][BF_4]_2$	NEt_3	Multiple Imine peaks
Zn(II)	DCM	$Zn(OTf)_2$	NEt_3	Multiple Imine peaks
Pt(II)	THF/CH_3CN	K_2PtCl_4	NEt_3	Multiple Imine peaks
Al(III)	THF	$AlCl_3$	NEt_3	No significant change
Ir(III)	THF	$IrCl_3$	NEt_3	No significant change

Since reaction conditions such as the type of the base, the type of the metal salt, the stoichiometric ratio between the base and the metal salt, temperature, and the type of the solvent can significantly influence the outcome of metal coordination, a systematic optimization study was carried out by varying one parameter at a time. This study was initially focused on Zn(II), Ni(II), Pt(II) metals, as these metals showed positive responses upon metal addition. In earlier observations with the bimetallic salixpyrrole complex (3), the appearance of multiple imine peaks

in the ^{1}H NMR spectrum was attributed to the incomplete deprotonation of the phenolic OH groups of the salen moiety. Therefore, the Initial case study was carried out by changing the choice of base aiming to identify one capable of achieving complete deprotonation under the provided reaction conditions. For Zn(II) coordination, strong bases such as KH and $KOC(CH_3)_3$ were tested under the hypothesis that stronger bases would more effectively deprotonate the phenolic groups without decomposing the ligand system (**Table 4.2**). The experiment with KH at room temperature yielded promising results. Specifically, the ^{1}H NMR spectrum revealed the presence of only four distinct imine peaks alongside a clear indication of the remaining monometallic starting material, complex 2 (**Figure 4.3**). The appearance of four imine peaks may suggest either bivalent coordination of Zn(II) metal, deviating from a distorted square planar geometry, or a loss of molecular symmetry due to bulky substituents, such as the *tert*-Butyl groups. On the other hand, with $KOC(CH_3)_3$, the NMR showed the appearance of aldehyde peaks around 10 ppm, indicating a possible decomposition of the system in the presence of a strong base, $KOC(CH_3)_3$.

Table 4.2. The study for the effect of base type with Zn(II) coordination for the Salixpyrrole system. (all the reaction was carried out at room temperature in an inert atmosphere, the ratio between base: metal = 2:1).

Metal ion	**Solvent**	**Metal source**	**Base**	**Results**
Zn(II)	DCM	$Zn(OTf)_2$	NEt_3	Multiple Imine peaks
			KH	Only four imine peaks
			$KOC(CH_3)_3$	Possible decompositions.

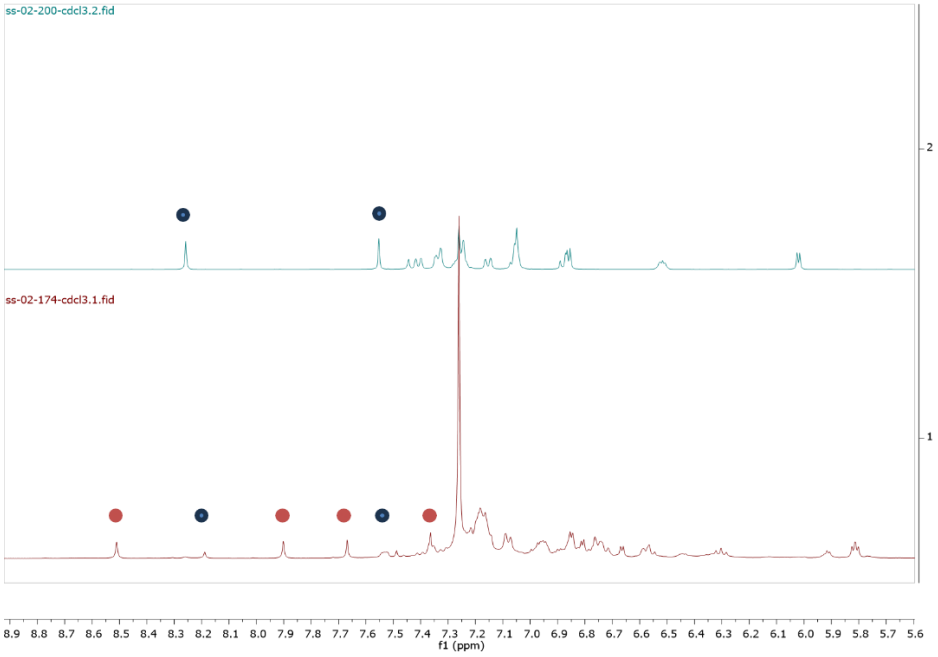

Figure 4.3. Comparison between ^{1}H NMRs with marked imine peak shifts - Pd-Salixpyrrole NMR (top) and PdZn-Salixpyrrole NMR (bottom) (400 MHz, $CDCl_3$).

Also, for Ni(II) coordination, strong bases such as KH, $LiOC(CH_3)_3$, and KOC(CH3)3 were evaluated (**Table 4.3**). Interestingly, in contrast to Zn(II) coordination, $KOC(CH_3)_3$ did not lead to the decomposition of the system. Instead, the reaction yielded a significantly cleaner ^{1}H NMR spectrum, indicative of potential Ni(II) coordination along with the unreacted starting material as the predominant species. These findings suggest that further optimization, particularly through adjustments in the stoichiometric ratio of the base to the metal salt, may enhance the efficiency of the coordination process. When it comes to Pt(II) coordination, strong bases like KH and $LiOC(CH_3)_3$ were tested (**Table 4.3**). Surprisingly, with both KH similar to Ni(II) coordination, the reaction yielded a significantly cleaner ^{1}H NMR spectrum, indicative of potential Pt(II) coordination along with the unreacted starting material as the predominant species. $LiOC(CH_3)_3$ did not show any significant changes in the NMR.

Table 4.3. The study for the effect of base type with Ni(II) and Pt(II) coordination for the Salixpyrrole system. (all the reaction was carried out at room temperature in an inert atmosphere, the ratio between base: metal = 2:1).

Metal ion	Solvent	Metal source	Base	Results
Ni(II)	DCM	$[Ni(CH_3CN)_6][BF_4]_2$	NEt_3	Worse
			KH	Better
			$LiOC(CH_3)_3$	Better
			$KOC(CH_3)_3$	Best
Pt(II)	THF/CH_3CN	K_2PtCl_4	NEt_3	Worse
			KH	Better
			$LiOC(CH_3)_3$	worse

Further investigations were conducted to optimize the conditions to achieve the expected ^{1}H NMR profile upon Zn(II) coordination. Increasing the stoichiometric ratio of KH base to metal salt up to 4:1 resulted in a notable reduction in the presence of the starting material, as observed in the ^{1}H NMR spectrum (**Figure 4.3**). However, further increasing the amount of base beyond this ratio led to the decomposition of complex 2, indicating a narrow window for optimal base concentration. Efforts are currently ongoing to obtain single crystals suitable for X-ray diffraction to confirm the structure of the resulting Zn-containing complex. Despite multiple attempts, crystallization has thus far been unsuccessful.

Similar to Zn(II) coordination, increasing the stoichiometric ratio of $KOC(CH_3)_3$ base to metal salt up to 4:1 resulted in the completion of the reaction, indicating the disappearance of starting material chemical shifts in the ^{1}H NMR spectrum (**Figure 4.4**). Efforts are currently ongoing to obtain single crystals suitable for X-ray diffraction to confirm the structure of the resulting Ni-containing complex.

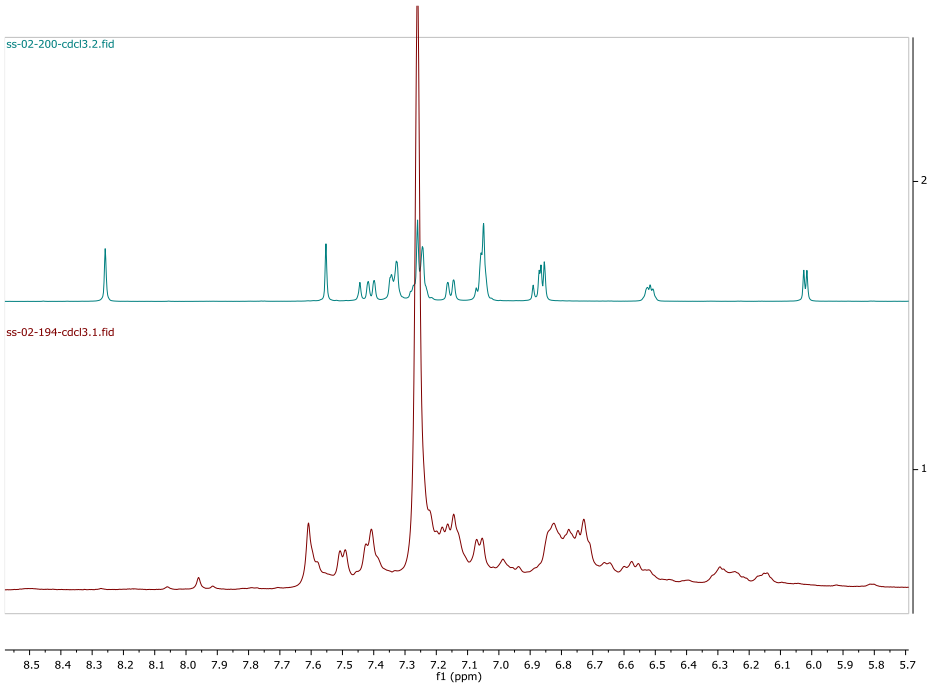

Figure 4.4. Comparison between ^{1}H NMRs - Pd-Salixpyrrole NMR (top) and PdNi-Salixpyrrole NMR (bottom) (400 MHz, $CDCl_3$).

Further investigations into Pt(II) coordination, involving an increased molar ratio of KH base, revealed the possibility of forming Pt-salen rather than the intended bimetallic PdPt-salix pyrrole. ^{1}H NMR indicated the appearance of only one significant imine peak along with the disappearance of characteristic pyrrole doublets. This observation supports the dissociation of imine bonds within the salen moiety, leading to the formation of a monometallic Pt-salen complex (**Figure 4.5**).[47–49]

Despite the aforementioned challenges associated with the synthesis of heterobimetallic complexes, this approach remains a promising strategy due to the presence of a selective coordination site for the second metal cation. With the appropriate choice of metal precursors and bases, or through structural modifications of the ligand to reduce steric hindrance, successful coordination of a second metal center may be achieved. Continued optimization and ligand design could thus enhance the efficiency and scope of this synthetic methodology.

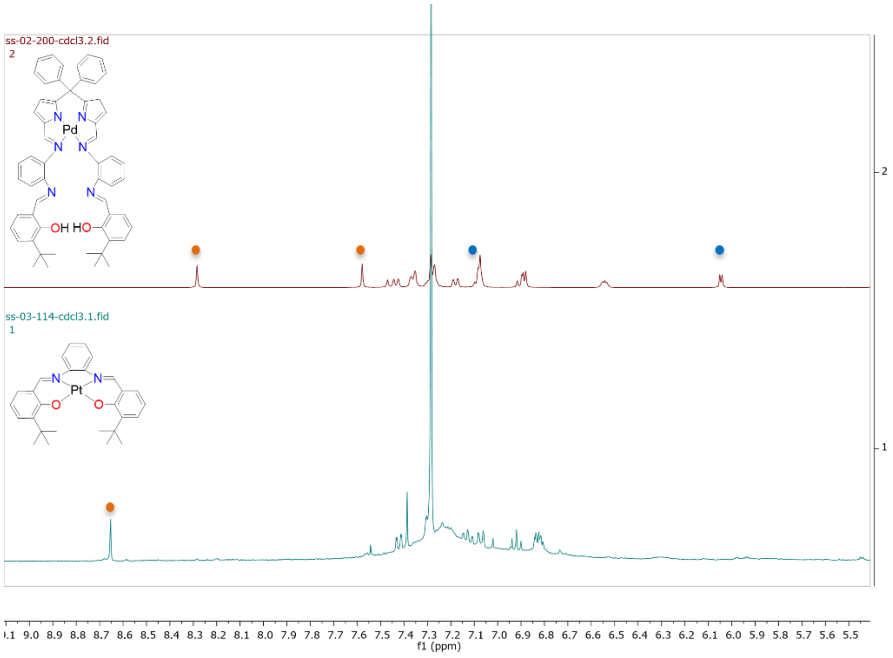

Figure 4.5. Comparison between ^{1}H NMRs - Pd-Salixpyrrole NMR (top) and suspected monometallic Pt-salen complex NMR (bottom) (400 MHz, $CDCl_3$).

4.3.2. Synthesis and characterization of heterobimetallic complexes from the "Imixpyrrole" system.

The synthetic approach employed in this project aimed to establish a new and facile route for the synthesis of heterobimetallic Schiff base complexes, inspired by Stefan Bräse and his group's work.[31] This approach was primarily developed as a proof-of-concept to demonstrate the feasibility of producing unsymmetric Schiff-based ligand systems bearing two distinct transition-metal centers. Similar to their work, a stepwise metalation strategy was utilized, where the monometallic complex (**4**) was synthesized as discussed in Chapter 3 to use as a starting material and subsequently reacted with an appropriate metal salt to produce the desired heterobimetallic complex (**Scheme 4.2**). The complexation of the second metal cations can be effectively monitored by ^{1}H NMR spectroscopy in the case of diamagnetic complexes; however, if the complexes are paramagnetic, ^{1}H NMR becomes less informative due to the broadening and shifting of the signals.

4.2. Synthesis of unsymmetric double-Schiff-base ligands starting from the monometallic "Imixpyrrole system.

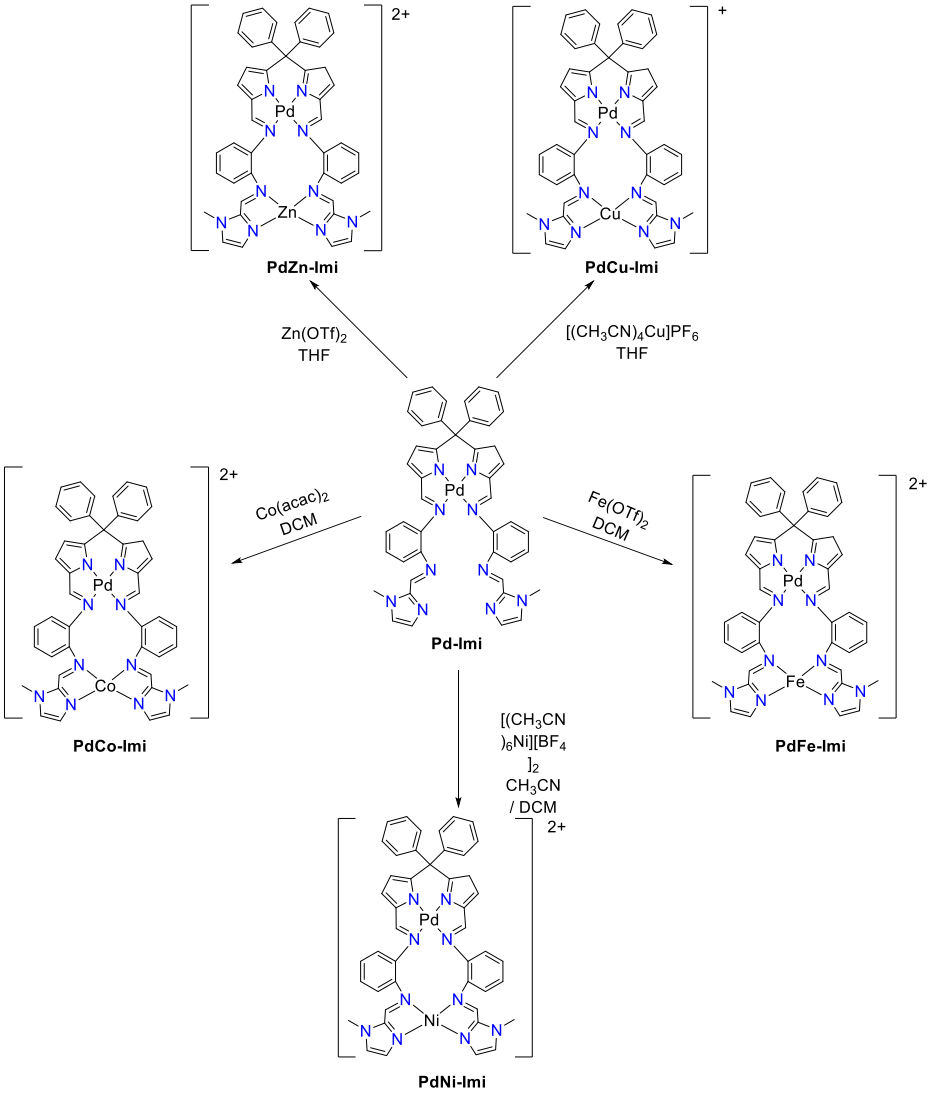

Zinc coordination to the secondary coordination sphere in the monometallic Imixpyrrole system was carried out by using $Zn(OTf)_2$ as the metal salt in THF, resulting in the formation of a diamagnetic PdZn-Imixpyrrole complex (Complex 5) (**Figure 4.6**). The product was isolated in fair yields (38%), and the ^{1}H NMR spectrum provided strong evidence of successful metal coordination. A characteristic downfield shift of the salen imine peak from 8.15 ppm to 8.68 ppm was observed, along with a slight downfield shift of the pyrrole imine proton from 7.43 ppm to

7.77 ppm (**Figure 4.6**). the latter shift is consistent with its position being more distal from the metal coordination site. Typically, when a metal is coordinated to the imine nitrogen, it withdraws electron density from the imine bond, which deshields the adjacent carbon atom and, consequently, the attached proton. This leads to a downfield shift in the imine proton in the ^{1}H NMR.[50,51] Despite multiple attempts, single crystals suitable for X-ray diffraction could not be obtained. This may be attributed to crystallization conditions favoring the formation of the monometallic form over the bimetallic complex due to superior crystal packing as reported in the literature for some complexes.[52] Alternatively, the absence or weakness of the metal-metal interaction, which can occur with close-shell metals or sterically crowded metal centers, may result in metal leaching upon crystallization.[53,54] To further support the existence of the bimetallic structure, elemental analysis (EA) was conducted, and the results confirmed the coordination of the second metal.

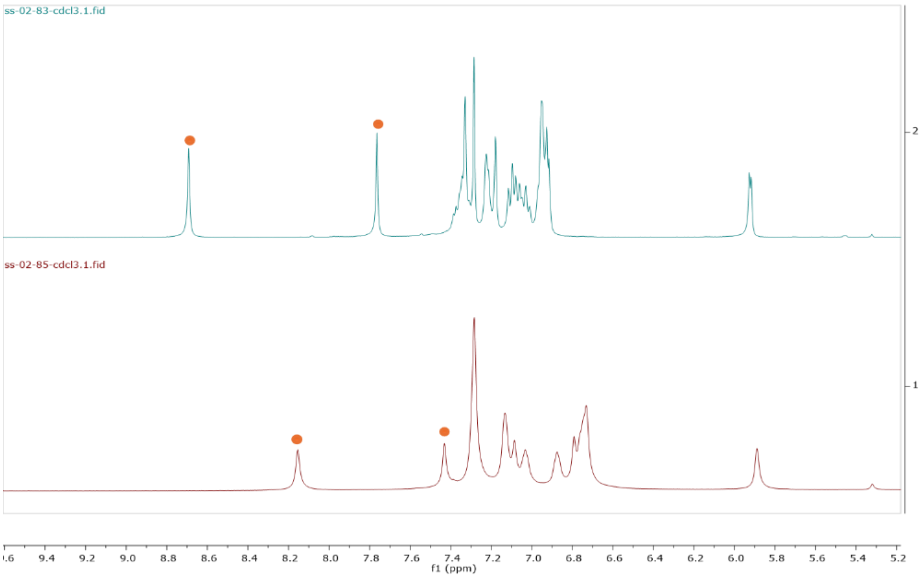

Figure 4.6. Comparison between ^{1}H NMRs with marked imine peak shifts - PdZn-Imixpyrrole NMR (top) and Pd-Imixpyrrole NMR (bottom) (400 MHz, $CDCl_3$).

The monometallic imixpyrrole complex was further reacted with $[(CH_3CN)_4Cu]PF_6$ in THF at room temperature to incorporate the Cu(I) ion as the second cation into the secondary

coordination sphere of the imixpyrrole system. This reaction yielded a diamagnetic heterobimetallic complex, PdCu-Imixpyrrole (complex 6), with a 30% yield. Due to its diamagnetic nature, ^{1}H NMR spectroscopy was employed to confirm the successful coordination of the Cu(I) (**Figure 4.7**). As observed with Zn metal coordination, the imine proton signal in the imidazole moiety exhibited a notable downfield shift from 8.15 ppm to 8.51 ppm. Additionally, the pyrrole imine proton displayed a slight downfield shift from 7.43 ppm to 7.48 ppm. These imine chemical shifts serve as reliable indicators of the second metal coordination in diamagnetic complexes. As with the PdZn-Imixpyrrole complex scenario, attempts to obtain a single crystal for X-ray crystallographic analysis of the PdCu-Imixpyrrole complex were unsuccessful. Nevertheless, the coordination of Cu(I) was further corroborated by EA results, which confirmed the incorporation of the second metal ion into the complex.

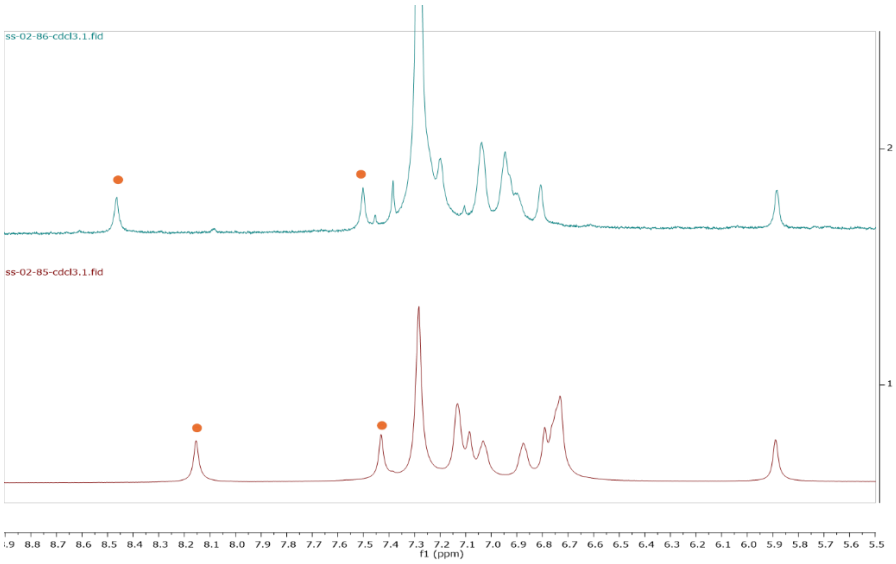

Figure 4.7. Comparison between ^{1}H NMRs with marked imine peak shifts – PdCu-Imixpyrrole NMR (top) and Pd-Imixpyrrole NMR (bottom) (400 MHz, $CDCl_3$).

Both of the above complexes are charged species, incorporating triflate ions and PF_6 counterions for PdZn-Imixpyrrole and PdCu-Imipyrrole, respectively. The challenges encountered during crystallization may, in part, stem from the formation of these charged bimetallic complexes

with differing counterions. As noted in the literature, charged complexes often present unique obstacles in crystallization.[55–57] One key difficulty that arises during crystallization is the requirement for charge balance, which can significantly influence crystal packing depending on the nature of the counterions, thereby complicating the co-crystalization process. Moreover, the ionic nature of these complexes often leads to high solubility in a wide range of solvents, increasing the likelihood of reaching supersaturation without nucleation and crystal growth. Additionally, the presence of solvent-filled voids within the crystal lattice may contribute to structural disorder, twinning, or poor diffraction quality, further hindering the successful acquisition of high-quality single crystals suitable for X-ray crystallographic analysis.

Attempts were made to coordinate the secondary coordination sphere with Fe(II), Co(II), and Ni(II) cations. The ^{1}H NMR spectra of the resulting complexes exhibited broad, shifted signals characteristic of paramagnetic species, which is consistent with the expected distorted square planar geometries commonly adopted by d^6, d^7, and d^8 metal centers such as Fe(II), Co(II), and Ni(II), respectively (**Figure 4.8**). Due to their paramagnetic nature, ^{1}H NMR spectroscopy is unsuitable for detecting specific chemical shifts associated with second metal coordination. However, it remains a useful tool for confirming the formation of paramagnetic complexes.[58–60] Similar to previous bimetallic complexes, attempts at crystallization were unsuccessful. Furthermore, elemental analysis of these complexes has not yet been conducted.

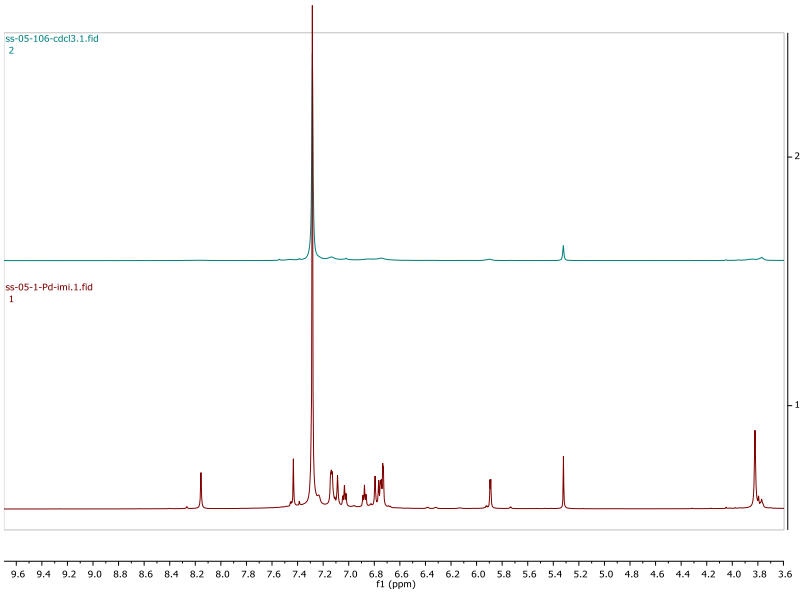
ss-05-106-cdcl3.1.fid
2
ss-05-1-Pd-imi.1.fid
1
2
1
9.6 9.4 9.2 9.0 8.8 8.6 8.4 8.2 8.0 7.8 7.6 7.4 7.2 7.0 6.8 6.6 6.4 6.2 6.0 5.8 5.6 5.4 5.2 5.0 4.8 4.6 4.4 4.2 4.0 3.8 3.6
f1 (ppm)

(a)

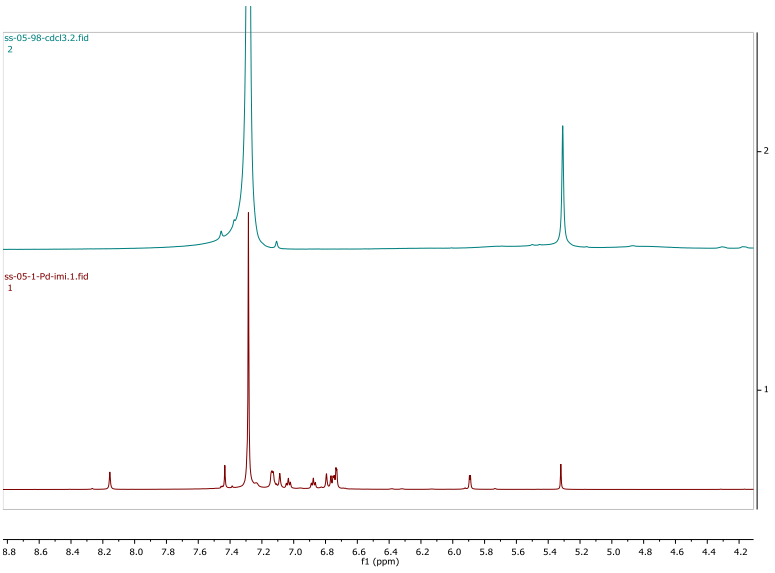
ss-05-98-cdcl3.2.fid
2
ss-05-1-Pd-imi.1.fid
1
2
1
8.8 8.6 8.4 8.2 8.0 7.8 7.6 7.4 7.2 7.0 6.8 6.6 6.4 6.2 6.0 5.8 5.6 5.4 5.2 5.0 4.8 4.6 4.4 4.2
f1 (ppm)

(b)

(c)

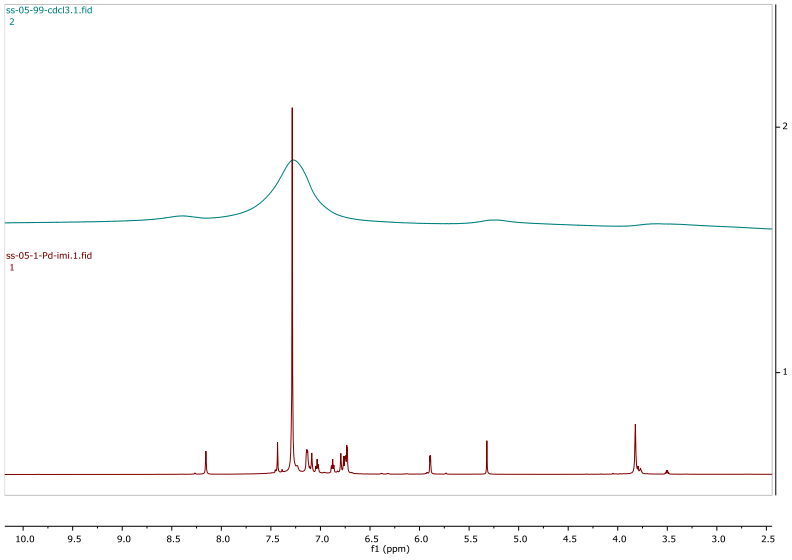

Figure 4.8. ^{1}H NMR comparisons between Pd-Imixpyrrole (bottom) and paramagnetic bimetallic complexes (top) (400 MHz, $CDCl_3$) (a) PdFe-Imixpyrrole, (b) PdCo-Imixpyrrole, (c) PdNi-Imixpyrrole.

4.3.3. Electrochemical characterization for PdZn-Imixpyrrole (5) and PdCu-Imixpyrrole (6).

The electrochemical properties of Imixpyrrole complexes 5 and 6 were investigated using cyclic voltammetry (CV) in tetrahydrofuran (THF), with comparisons made to the monometallic precursor complex (4) (**Figure 4.9**). As in previous experiments, tetrabutylammonium hexafluorophosphate (TBAP) was employed as the supporting electrolyte. In the anodic region, the bimetallic complex 5 exhibited electrochemical behavior comparable to that of complex 4. A quasi-reversible redox couple centered around –0.17 V vs Fc/Fc^{+} was observed, which is attributed to a calixpyrrole ligand-based oxidation process, as discussed earlier. Additionally, two irreversible oxidation events were recorded at approximately 0.73 V and 1.06 V vs Fc/Fc^{+}, likely corresponding to strong ligand-based oxidations (**Figure 4.9a**). Although the Zn(II) center is typically redox-inactive, the observed anodic shifts in oxidation potentials upon metal coordination

suggest a decrease in electron density on the ligand framework and possible modulation of the Pd center.[61–63] In the cathodic region, irreversible reduction peaks appeared at –0.78 V and –1.56 V vs Fc/Fc^{+}, which are tentatively assigned to ligand-based reduction processes (**Figure 4.9a**). Notably, compared to the monometallic complex (4), the bimetallic system displayed more cathodic reduction potentials, indicating a lower overpotential requirement for proton reduction. This shift suggests enhanced potential for catalytic HER activity in the bimetallic complex.

(a)

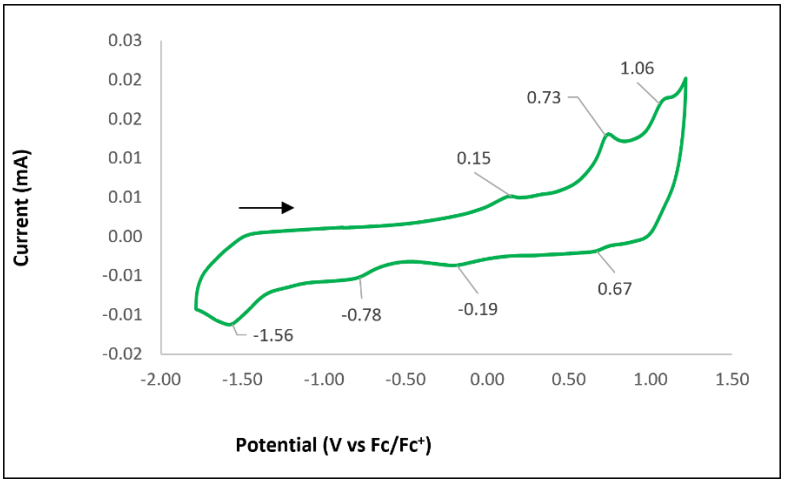

(b)

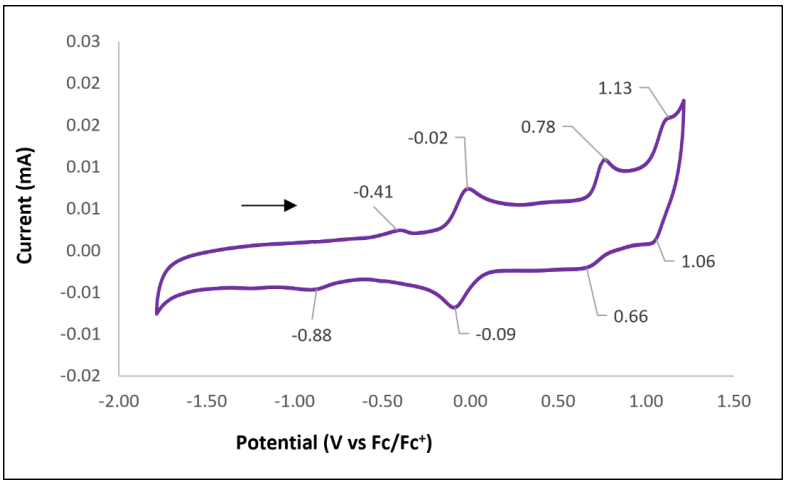

(c)

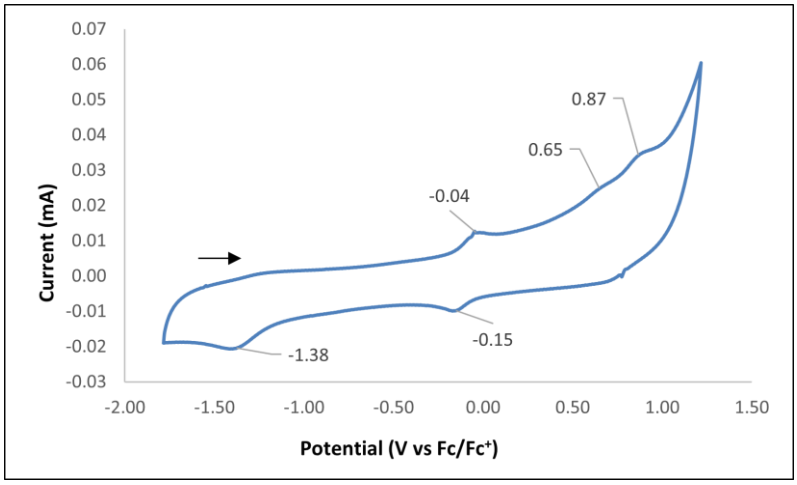

Figure 4.9. Representative CVs (0.1 M TBAP in THF, 0.25 mM complex, glassy carbon working electrode, platinum wire counter electrode, 0.01 M $Ag/AgNO_3$ reference electrode, scan rate = 800 mV/s) of: a) complex 5; b) complex 6; c) complex 4.

The bimetallic complex 6 exhibited notably distinct electrochemical behavior compared to its monometallic analogue, complex 4 (**Figure 4.9 a and c**). As discussed in previous chapters, a quasi-reversible redox couple observed around –0.06 V vs Fc/Fc^+ is attributed to a calixpyrrole ligand-based oxidation process. An additional oxidation feature, absent in the monometallic system, appears at approximately –0.41 V vs Fc/Fc^+. This new oxidation event may correspond to a Cu(I)/Cu(II) redox process, as reported in the literature.[64] Two further irreversible oxidation peaks, located at 0.78 V and 1.13 V vs Fc/Fc^+, are likely associated with ligand-based oxidation processes (**Figure 4.9b**). However, it is also plausible that the irreversible peak at 0.78 V corresponds to a Cu(II)/Cu(III) oxidation event, in line with previously documented redox behavior of copper complexes.[64] The less prominent reduction peak around -0.88 V vs Fc/Fc^+ was indicative of a very unstable or transient redox event. Compared to the voltammogram of complex 4, all redox features for complex 6 were shifted anodically, suggesting an electron-deficient ligand environment resulting from Cu(I) coordination. This observation is consistent with ^1H NMR data, which also indicated a decrease in electron density upon the formation of the bimetallic complex.

The presence of a potentially redox-active Cu(I) center further supports the hypothesis of cooperative behavior between the metal centers in the bimetallic system. These electrochemical findings suggest that complex 6 may possess enhanced catalytic activity relative to complex 4. Its cationic nature, combined with the possibility of Cu(I) serving as an electron reservoir, could facilitate proton reduction during hydrogen evolution reaction (HER) catalysis.

4.4. Conclusion and future work.

4.4.1. Conclusion

In summary, a novel synthetic route was established as a proof-of-principle reaction to produce Schiff-based transition-metal-containing heterobimetallic complexes. Unfortunately, all the attempts to synthesize bimetallic complexes using monometallic Slixpyrrole complex as a starting material were unsuccessful to this date regardless of the numerous methods that were used.

Interestingly, a stepwise metalation strategy was successfully developed to synthesize heterobimetallic Schiff base complexes from the imixpyrrole system. This synthetic route provides a straightforward novel synthetic route to access unsymmetric bimetallic complexes based on Schiff-based ligand structure using a pre-formed monometallic Pd-Imixpyrrole precursor as a starting material. Coordination of a second metal, either a redox-inactive Zn(II) ion or redox-active Cu(I) was successfully achieved under mild reaction conditions in a inert environment with fairly good yields, resulting in two diamagnetic heterobimetallic complexes PdZn-Imixpyrrole (5) and PdCu-Imixpyrrole (6). The metal coordination was confirmed by a characteristic downfield shift in the free-imine peak at the secondary coordination sphere in the ^{1}H NMR spectra which was supported by EA analysis.

Unfortunately, the crystallization of these complexes was unsuccessful despite the numerous attempts. It is possible that this scenario is a result of forming a charged, multimetallic

species. Additionally, further attempts to coordinate other metals such as Fe(II), Co(II), and Ni(II) into the secondary coordination sphere were carried out and ^{1}H NMRs were evident for the formation of paramagnetic complexes with ongoing verification with EA.

Electrochemical studies revealed that coordination of Zn(II) slightly altered the redox potentials of the ligand framework without introducing metal-centered redox activity, while Cu(I) coordination led to more pronounced changes in the voltammogram, including the appearance of a low-potential oxidation feature potentially corresponding to a Cu(I)/Cu(II) redox process. These findings support the hypothesis that redox-inactive Zn(II) subtly tunes the electronic environment of the complex, whereas redox-active Cu(I) introduces new redox processes and possibly enables metal–metal cooperativity. The anodic shift in voltammetric peaks, along with lower cathodic overpotentials, suggests that the bimetallic Cu(I)-containing system (6) could be a more efficient catalyst for the hydrogen evolution reaction (HER), potentially due to the synergistic interaction between Pd and Cu centers.

Altogether, this work provides a platform for constructing electronically tunable heterobimetallic Schiff base complexes with promising applications in small molecule activation and electrocatalysis, while also highlighting the structural and electrochemical challenges inherent to charged, multimetallic species.

4.4.2. Future work

As for future work, further attempts to obtain the crystal structures, specifically for the heterobimetallic complexes from the imixpyrrole system, need to be made. Since crystallinity can be affected by multiple factors such as the solubility of the interested complex in the solvent mixture used for crystallization, the availability of multiple forms, or structural flexibility of the metal complex, counterion effect, possible decomposition or hydrolyzation over time in the solvent

mixture used for crystallization, etc. a proper study needs to be carried out by changing these parameters.

The investigations of PdZn-Imixpyrrole and PdCu-Imixpyrrole for catalytic activities toward small molecule activation can be considered as another future direction of this project. Both complexes need to be evaluated for the hydrogen evolution reaction (HER) to obtain a better comparison of the catalytic activities of bimetallic complexes compared to their monometallic analogues. It is also possible to evaluate these systems for other small molecule activation processes, such as the oxygen evolution reaction (OER) and nitrogen evolution reaction.

Finally, for the salixpyrrole system, further investigations need to be conducted to synthesize heterobimetallic complexes. The investigation of other methods such as temptation, transmetalation, etc. needs to be carried out.

4.5. References

(1) Buchwalter, P.; Rosé, J.; Braunstein, P. Multimetallic Catalysis Based on Heterometallic Complexes and Clusters. *Chem. Rev.* **2015**, *115* (1), 28–126. https://doi.org/10.1021/cr500208k.

(2) Cooper, B. G.; Napoline ,J. Wesley; and Thomas, C. M. Catalytic Applications of Early/Late Heterobimetallic Complexes. *Catalysis Reviews* **2012**, *54* (1), 1–40. https://doi.org/10.1080/01614940.2012.619931.

(3) Wang, Q.; Brooks, S. H.; Liu, T.; Tomson, N. C. Tuning Metal–Metal Interactions for Cooperative Small Molecule Activation. *Chem. Commun.* **2021**, *57* (23), 2839–2853. https://doi.org/10.1039/D0CC07721F.

(4) Neumann, T.; C. Thompson, B.; Hebron, D.; M. Graycon, D.; Collauto, A.; M. Roessler, M.; N. Wilson, D. W.; A. Musgrave, R. Heterobimetallic 3d–4f Complexes Supported by a Schiff-Base Tripodal Ligand. *Dalton Transactions* **2024**, *53* (23), 9921–9932. https://doi.org/10.1039/D3DT03760F.

(5) Venkatesh, G.; Vennila, P.; Kaya, S.; Ahmed, S. B.; Sumathi, P.; Siva, V.; Rajendran, P.; Kamal, C. Synthesis and Spectroscopic Characterization of Schiff Base Metal Complexes, Biological Activity, and Molecular Docking Studies. *ACS Omega* **2024**, *9* (7), 8123–8138. https://doi.org/10.1021/acsomega.3c08526.

(6) Boulechfar, C.; Ferkous, H.; Delimi, A.; Djedouani, A.; Kahlouche, A.; Boublia, A.; Darwish, A. S.; Lemaoui, T.; Verma, R.; Benguerba, Y. Schiff Bases and Their Metal Complexes: A Review on the History, Synthesis, and Applications. *Inorganic Chemistry Communications* **2023**, *150*, 110451. https://doi.org/10.1016/j.inoche.2023.110451.

(7) Chaudhary, A.; Singh, A.; Kamboj, R. C. Heterobimetallic Complexes as Promising Catalysts. **2016**.

(8) Thompson, K. H.; Orvig, C. Metal Complexes in Medicinal Chemistry: New Vistas and Challenges in Drug Design. *Dalton Trans.* **2006**, No. 6, 761–764. https://doi.org/10.1039/B513476E.

(9) Cohen, S. M. New Approaches for Medicinal Applications of Bioinorganic Chemistry. *Current Opinion in Chemical Biology* **2007**, *11* (2), 115–120. https://doi.org/10.1016/j.cbpa.2007.01.012.

(10) Shibasaki, M.; Matsunaga, S. Bifunctional Asymmetric Catalysis Based on Dinuclear Schiff Base Complexes. *J. Synth. Org. Chem. Jpn.* **2010**, *68* (11), 1142–1149. https://doi.org/10.5059/yukigoseikyokaishi.68.1142.

(11) Handa, S.; Gnanadesikan, V.; Matsunaga, S.; Shibasaki, M. Heterobimetallic Transition Metal/Rare Earth Metal Bifunctional Catalysis: A Cu/Sm/Schiff Base Complex for Syn-Selective Catalytic Asymmetric Nitro-Mannich Reaction. *J. Am. Chem. Soc.* **2010**, *132* (13), 4925–4934. https://doi.org/10.1021/ja100514y.

(12) Drozdzak, R.; Allaert, B.; Ledoux, N.; Dragutan, I.; Dragutan, V.; Verpoort, F. Ruthenium Complexes Bearing Bidentate Schiff Base Ligands as Efficient Catalysts for Organic and Polymer Syntheses. *Coordination Chemistry Reviews* **2005**, *249* (24), 3055–3074. https://doi.org/10.1016/j.ccr.2005.05.003.

(13) Nam, W.; Lee, Y.-M.; Fukuzumi, S. Tuning Reactivity and Mechanism in Oxidation Reactions by Mononuclear Nonheme Iron(IV)-Oxo Complexes. *Acc. Chem. Res.* **2014**, *47* (4), 1146–1154. https://doi.org/10.1021/ar400258p.

(14) Hetterscheid, D. G. H.; Reek, J. N. H. Mononuclear Water Oxidation Catalysts. *Angewandte Chemie International Edition* **2012**, *51* (39), 9740–9747. https://doi.org/10.1002/anie.201202948.
(15) Itoh, S. Developing Mononuclear Copper–Active-Oxygen Complexes Relevant to Reactive Intermediates of Biological Oxidation Reactions. *Acc. Chem. Res.* **2015**, *48* (7), 2066–2074. https://doi.org/10.1021/acs.accounts.5b00140.
(16) Zeng, Q.; Lewis, F. W.; Harwood, L. M.; Hartl, F. Role of Ligands in Catalytic Water Oxidation by Mononuclear Ruthenium Complexes. *Coordination Chemistry Reviews* **2015**, *304–305*, 88–101. https://doi.org/10.1016/j.ccr.2015.03.003.
(17) Stucke, N.; Flöser, B. M.; Weyrich, T.; Tuczek, F. Nitrogen Fixation Catalyzed by Transition Metal Complexes: Recent Developments. *European Journal of Inorganic Chemistry* **2018**, *2018* (12), 1337–1355. https://doi.org/10.1002/ejic.201701326.
(18) Can, M.; Armstrong, F. A.; Ragsdale, S. W. Structure, Function, and Mechanism of the Nickel Metalloenzymes, CO Dehydrogenase, and Acetyl-CoA Synthase. *Chem. Rev.* **2014**, *114* (8), 4149–4174. https://doi.org/10.1021/cr400461p.
(19) *Hydrogenases | Chemical Reviews*. https://pubs.acs.org/doi/10.1021/cr4005814 (accessed 2025-04-11).
(20) Lubitz, W.; Tumas, W. Hydrogen: An Overview. *Chem. Rev.* **2007**, *107* (10), 3900–3903. https://doi.org/10.1021/cr050200z.
(21) Vashi, P. Hydrogenases – Achievements and Expectations (Eur. J. Inorg. Chem. 7/2011). *European Journal of Inorganic Chemistry* **2011**, *2011* (7), 915–916. https://doi.org/10.1002/ejic.201190016.
(22) Nicolet, Y.; Piras, C.; Legrand, P.; Hatchikian, C. E.; Fontecilla-Camps, J. C. *Desulfovibrio Desulfuricans* Iron Hydrogenase: The Structure Shows Unusual Coordination to an Active Site Fe Binuclear Center. *Structure* **1999**, *7* (1), 13–23. https://doi.org/10.1016/S0969-2126(99)80005-7.
(23) Muetterties, E. L.; Rhodin, T. N.; Band, Elliot.; Brucker, C. F.; Pretzer, W. R. Clusters and Surfaces. *Chem. Rev.* **1979**, *79* (2), 91–137. https://doi.org/10.1021/cr60318a001.
(24) Dyson, P. J. Catalysis by Low Oxidation State Transition Metal (Carbonyl) Clusters. *Coordination Chemistry Reviews* **2004**, *248* (21), 2443–2458. https://doi.org/10.1016/j.ccr.2004.04.002.
(25) Zwart, J.; Snel, R. Metal Carbonyl Clusters in the Catalytic Hydrogenation of Carbon Monoxide. *Journal of Molecular Catalysis* **1985**, *30* (3), 305–352. https://doi.org/10.1016/0304-5102(85)85044-6.
(26) Pakkanen, T. A.; Pursiainen, J.; Venäläinen, T.; Pakkanen, T. T. Mixed Metal Clusters: Structural and Reactivity Trends. *Journal of Organometallic Chemistry* **1989**, *372* (1), 129–139. https://doi.org/10.1016/0022-328X(89)87083-4.
(27) Ghosh, P.; Ding, S.; Chupik, R. B.; Quiroz, M.; Hsieh, C.-H.; Bhuvanesh, N.; Hall, M. B.; Darensbourg, M. Y. A Matrix of Heterobimetallic Complexes for Interrogation of Hydrogen Evolution Reaction Electrocatalysts †Electronic Supplementary Information (ESI) Available: Experimental, Spectroscopic, Additional Electrochemical and Computational Details, X-Ray Crystallographic Data (CIF) from the Structure of the Complexes [Ni–Fe]0, [Ni2–Fe2]2+, [Ni2–Fe]+, and Computational Coordinates Are Available. CCDC Crystallographic Data for the Complexes [Ni–Fe]0, [Ni2–Fe2]2+ and [Ni2–Fe]+ Were Deposited in the Cambridge Crystallographic Data Centre. CCDC [Ni–Fe]0 (CCDC 1045461), [Ni2–Fe2]2+ (CCDC 1045460) and [Ni2–Fe]+ (CCDC 1565539). For ESI and

Crystallographic Data in CIF or Other Electronic Format See DOI: 10.1039/C7sc03378h. *Chem Sci* **2017**, *8* (12), 8291–8300. https://doi.org/10.1039/c7sc03378h.
(28) Baranger, A. M.; Hanna, T. A.; Bergman, R. G. Transfer of Oxygen and Sulfur from Organic Molecules to a Zr-Ir Bond. Evidence for an Unusually Rapid Atom Abstraction Reaction. *J. Am. Chem. Soc.* **1995**, *117* (40), 10041–10046. https://doi.org/10.1021/ja00145a015.
(29) Mazzacano, T. J.; Mankad, N. P. Base Metal Catalysts for Photochemical C–H Borylation That Utilize Metal–Metal Cooperativity. *J. Am. Chem. Soc.* **2013**, *135* (46), 17258–17261. https://doi.org/10.1021/ja408861p.
(30) Lang, P.; Pfrunder, M.; Quach, G.; Cula, B.; Moore, E.; Schwalbe, M. Sensitized Photochemical CO2 Reduction by Hetero-Pacman Compounds Linking a Re Tricarbonyl with a Porphyrin Unit. *Chemistry - A European Journal* **2019**, *25*. https://doi.org/10.1002/chem.201806347.
(31) Schissler, C.; Schneider, E. K.; Felker, B.; Weis, P.; Nieger, M.; Kappes, M. M.; Bräse, S. A Synthetic Strategy for Cofacial Porphyrin-Based Homo- and Heterobimetallic Complexes. *Chemistry – A European Journal* **2021**, *27* (9), 3047–3054. https://doi.org/10.1002/chem.202002394.
(32) Liu, G.; Chauhan, V.; Aydt, A. P.; Ciborowski, S. M.; Pinkard, A.; Zhu, Z.; Roy, X.; Khanna, S. N.; Bowen, K. H. Ligand Effect on the Electronic Structure of Cobalt Sulfide Clusters: A Combined Experimental and Theoretical Study. *J. Phys. Chem. C* **2019**, *123* (41), 25121–25127. https://doi.org/10.1021/acs.jpcc.9b04153.
(33) Cirri, A.; Morales Hernández, H.; Kmiotek, C.; Johnson, C. J. Systematically Tuning the Electronic Structure of Gold Nanoclusters through Ligand Derivatization. *Angewandte Chemie International Edition* **2019**, *58* (39), 13818–13822. https://doi.org/10.1002/anie.201907586.
(34) Cammarota, R. C.; Clouston, L. J.; Lu, C. C. Leveraging Molecular Metal–Support Interactions for H2 and N2 Activation. *Coordination Chemistry Reviews* **2017**, *334*, 100–111. https://doi.org/10.1016/j.ccr.2016.06.014.
(35) Zhang, H.; Hatzis, G. P.; Moore, C. E.; Dickie, D. A.; Bezpalko, M. W.; Foxman, B. M.; Thomas, C. M. O2 Activation by a Heterobimetallic Zr/Co Complex. *J. Am. Chem. Soc.* **2019**, *141* (24), 9516–9520. https://doi.org/10.1021/jacs.9b04215.
(36) Krogman, J. P.; Thomas, C. M. Metal–Metal Multiple Bonding in C3-Symmetric Bimetallic Complexes of the First Row Transition Metals. *Chem. Commun.* **2014**, *50* (40), 5115–5127. https://doi.org/10.1039/C3CC47537A.
(37) Moore, J. T.; Lu, C. C. Catalytic Hydrogenolysis of Aryl C–F Bonds Using a Bimetallic Rhodium–Indium Complex. *J. Am. Chem. Soc.* **2020**, *142* (27), 11641–11646. https://doi.org/10.1021/jacs.0c04937.
(38) Prakash, S.; Gupta, A. K.; Prakash, S.; Singh, K. R. R. P.; Prakash, D. SYNTHESIS AND SPECTRAL STUDIES OF HETEROBIMETALLIC SCHIFF BASE COMPLEXES. *RJC* **2022**, *15* (01), 628–632. https://doi.org/10.31788/RJC.2022.1516604.
(39) Odhiambo, R.; Muthakia, G. K.; Kagwanja, S. M. **Synthesis, Characterization and Electrochemistry of Heterobimetallic Complexes Containing Molybdenum(II) Nitrosyl and Manganese(II)-Schiff Base Centers**. *Bull. Chem. Soc. Eth.* **2010**, *24* (1). https://doi.org/10.4314/bcse.v24i1.52960.
(40) Roth, A.; Buchholz, A.; Rudolph, M.; Schütze, E.; Kothe, E.; Plass, W. Directed Synthesis of a Heterobimetallic Complex Based on a Novel Unsymmetric Double-Schiff-Base Ligand: Preparation, Characterization, Reactivity and Structures of Hetero- and Homobimetallic

Nickel(II) and Zinc(II) Complexes. *Chemistry – A European Journal* **2008**, *14* (5), 1571–1583. https://doi.org/10.1002/chem.200701124.
(41) Majumdar, D.; Das, D.; Nag, S.; Bhattacharyya, M.; Singh, D. K.; Parai, D.; Bankura, K.; Mishra, D. A Rare Hetero-Bimetallic Zn(II)/Ca(II) Schiff Base Complex: Synthesis, Crystal Structure, DFT, Molecular Docking and Unveiling Antimicrobial Activity. *Journal of Molecular Structure* **2020**, *1222*, 128951. https://doi.org/10.1016/j.molstruc.2020.128951.
(42) Revenco, M. D.; Palamarciuc, O. V.; Bourosh, P. N.; Lipkowski, J.; Gdaniec, M.; Simonov, Y. A.; Clérac, R. New Template Reactions of Salicylaldehyde S-Methyl-Isothiosemicarbazone with 2-Formylpyridine Promoted by Ni(II) or Cu(II) Metal Ions. *Inorganica Chimica Acta* **2011**, *368* (1), 157–164. https://doi.org/10.1016/j.ica.2010.12.068.
(43) Katovic, V.; Taylor, L. T.; Busch, D. H. Application of the Coordination Template Effect to Prepare Five-Coordinate Nickel(II) and Copper(II) Complexes Containing a "Basket-like" Polycyclic Ligand. *J. Am. Chem. Soc.* **1969**, *91* (8), 2122–2123. https://doi.org/10.1021/ja01036a050.
(44) Ilhan, S.; Temel, H. Synthesis and Spectral Studies of Macrocyclic Cu(II), Ni(II) and Co(II) Complexes by Template Reaction of 1,4-Bis(3-Aminopropoxy)Butane with Metal(II) Nitrate and Salicylaldehyde Derivatives. *Journal of Molecular Structure* **2008**, *891* (1), 157–166. https://doi.org/10.1016/j.molstruc.2008.03.016.
(45) Mahapatra, P.; Ghosh, S.; Giri, S.; Ghosh, A. The Unusual Intermediate Species in the Formation of Ni(II) Complexes of Unsymmetrical Schiff Bases by Elder's Method: Structural, Electrochemical and Magnetic Characterizations. *Polyhedron* **2016**, *117*, 427–436. https://doi.org/10.1016/j.poly.2016.06.020.
(46) Somachandra, M. S.; Averkiev, B.; Sues, P. E. Unsymmetric Co-Facial "Salixpyrrole" Hydrogen Evolution Catalysts: Two Metals Are Better than One. *Inorg. Chem.* **2024**, *63* (29), 13346–13357. https://doi.org/10.1021/acs.inorgchem.4c01101.
(47) Azam, M.; Al-Resayes, S. I.; Soliman, S. M.; Trzesowska-Kruszynska, A.; Kruszynski, R.; Khan, Z. A (Salicylaldiminato)Pt(II) Complex with Dimethylpropylene Linkage: Synthesis, Structural Characterization and Antineoplastic Activity. *Journal of Photochemistry and Photobiology B: Biology* **2017**, *176*, 150–156. https://doi.org/10.1016/j.jphotobiol.2017.10.005.
(48) Qu, L.; Li, C.; Shen, G.; Gou, F.; Song, J.; Wang, M.; Xu, X.; Zhou, X.; Xiang, H. Syntheses, Crystal Structures, Chirality and Aggregation-Induced Phosphorescence of Stacked Binuclear Platinum(II) Complexes with Bridging Salen Ligands. *Mater. Chem. Front.* **2019**, *3* (6), 1199–1208. https://doi.org/10.1039/C9QM00105K.
(49) Houjou, H.; Hoga, Y.; Ma, Y.-L.; Achira, H.; Yoshikawa, I.; Mutai, T.; Matsumura, K. Dinuclear Fused Salen Complexes of Group-10 Metals: Peculiarity of the Crystal Structure and near-Infrared Luminescence of a Bis(Pt-Salen) Complex. *Inorganica Chimica Acta* **2017**, *461*, 27–34. https://doi.org/10.1016/j.ica.2017.01.031.
(50) Khalaji, A. D.; Grivani, G.; Akerdi, S. J.; Stoeckli-Evans, H.; Das, D. Synthesis, Spectroscopic and Thermal Studies of Zinc(II) Complexes with the Symmetrical Bidentate Schiff-Base Ligand (2,3-MeO-Ba)2en: Crystal Structure of Zn((2,3-MeO-Ba)2en)I2. *J Chem Crystallogr* **2012**, *42* (1), 83–88. https://doi.org/10.1007/s10870-011-0207-3.
(51) Sumrra, S. H.; Ibrahim, M.; Ambreen, S.; Imran, M.; Danish, M.; Rehmani, F. S. Synthesis, Spectral Characterization, and Biological Evaluation of Transition Metal Complexes of Bidentate N, O Donor Schiff Bases. *Bioinorg Chem Appl* **2014**, *2014*, 812924. https://doi.org/10.1155/2014/812924.

(52) Tanui, H. *REVIEW Bimetallic Complexes; A Mini Review of Their Synthesis, and Potential Antitumor Activities*; 2019. https://doi.org/10.13140/RG.2.2.19269.50400.
(53) Wei, X.; Xing, J.; Wang, Y.; Wu, Y.; Qian, J.; Shi, F. Co-Ln (Ln = Ce ∼ Yb) Bimetal Complexes: Syntheses, Structures and Their Applications as Supercapacitor Anode Materials. *Inorganica Chimica Acta* **2024**, *570*, 122159. https://doi.org/10.1016/j.ica.2024.122159.
(54) Incarvito, C.; Rheingold, A. L.; Gavrilova, A. L.; Qin, C. J.; Bosnich, B. Bimetallic Reactivity. One-Site Addition Two-Metal Oxidation Reactions Using a Di-Co(II) Complex of a Binucleating Ligand with 5- and 6-Coordinate Sites. *Inorg. Chem.* **2001**, *40* (17), 4101–4108. https://doi.org/10.1021/ic010235r.
(55) Chernyshev, A. V.; Tkachev, V. V.; Rostovtseva, I. A.; Lazarenko, V. A.; Guda, A. A.; Shilov, G. V.; Utenyshev, A. N.; Solov'eva, E. V.; Gaeva, E. B.; Voloshin, N. A.; Aldoshin, S. M.; Metelitsa, A. V. Anion Effect on Crystal Structure of Zn-Complexes of Spironaphthopyran and Their Chromogenic Properties in Solution. *Polyhedron* **2023**, *239*, 116409. https://doi.org/10.1016/j.poly.2023.116409.
(56) Trang, C. D. M.; Mora Perez, C.; Ran, J.; Prezhdo, O. V.; Inkpen, M. S. Counterion Loss from Charged Surface-Bound Complexes Drives the Formation of Loosely Packed Monolayers. *J. Am. Chem. Soc.* **2024**, *146* (37), 25625–25639. https://doi.org/10.1021/jacs.4c07327.
(57) Cong, Y.; Zhou, Y.; Bao, J.; Zhang, X. Crystallization, Recrystallization and Melting Behaviors in Supramolecular Poly(l-Lactic Acid) Bonded by Metal-Ligand Coordination. *Polymer* **2024**, *294*, 126702. https://doi.org/10.1016/j.polymer.2024.126702.
(58) *Paramagnetic Nuclear Magnetic Resonance: The Toolkit*. https://www.mdpi.com/2304-6740/12/1/15 (accessed 2025-04-14).
(59) Belle, C.; Bougault, C.; Averbuch, M.-T.; Durif, A.; Pierre, J.-L.; Latour, J.-M.; Pape, L. Paramagnetic NMR Investigations of High-Spin Nickel(II) Complexes. Controlled Synthesis, Structural, Electronic, and Magnetic Properties of Dinuclear vs Mononuclear Species. *Journal of the American Chemical Society* **2001**, *123*, 8053–8066. https://doi.org/10.1021/ja010342k.
(60) 200602-Ni(II)+Schiff+Base+Complexes-App-Note-W.Pdf. https://static1.squarespace.com/static/5707ede0d210b8708e037a1e/t/5ed67177e24722090cfe9a1e/1591112057146/200602-Ni%28II%29%2BSchiff%2BBase%2BComplexes-App-Note-W.pdf?utm_source=chatgpt.com (accessed 2025-04-14).
(61) Kelsey, S. R.; Kumar, A.; Oliver, A. G.; Day, V. W.; Blakemore, J. D. Promotion and Tuning of the Electrochemical Reduction of Hetero- and Homobimetallic Zinc Complexes. *ChemElectroChem* **2021**, *8* (15), 2792–2802. https://doi.org/10.1002/celc.202100358.
(62) Franks, M.; Gadzhieva, A.; Ghandhi, L.; Murrell, D.; Blake, A. J.; Davies, E. S.; Lewis, W.; Moro, F.; McMaster, J.; Schröder, M. Five Coordinate M(II)-Diphenolate [M = Zn(II), Ni(II), and Cu(II)] Schiff Base Complexes Exhibiting Metal- and Ligand-Based Redox Chemistry. **2013**. https://doi.org/10.1021/ic301731w.s001.
(63) *Redox Activity of Noninnocent 2,2′-Bipyridine in Zinc Complexes: An Experimental and Theoretical Study | ACS Omega*. https://pubs.acs.org/doi/10.1021/acsomega.1c02201?utm_source=chatgpt.com (accessed 2025-04-15).
(64) Kargar, H.; Fallah-Mehrjardi, M.; Moghadam, M.; Yarahmadi, S.; Omidvar, A.; Zare-Mehrjardi, H. R.; Dege, N.; Ashfaq, M.; Munawar, K. S.; Tahir, M. N.; Shahsavari, H. R.

Structural and Electrochemical Properties of a Cu(I) Schiff-Base Complex: Catalytic Application to the Synthesis of Tetrahydropyrimidine Derivatives. *Inorganica Chimica Acta* **2024**, *570*, 122160. https://doi.org/10.1016/j.ica.2024.122160.

Chapter 5 - Conclusions and future directions

5.1. Conclusions

Broadly, considerable advancements have been achieved in developing new molecular electrocatalysts for the production of hydrogen, such as understanding their mechanism, factors that are affecting to the catalyst reaction, etc. Hydrogen presents itself as a potential fuel substitute due to being a renewable energy source with zero carbon emissions, having a maximum gravimetric energy density to replace petroleum and other petroleum products. The HER is heavily dependent on the efficiency of the catalyst that facilitates the forward reaction.

This work demonstrates the successful design, formulation, and electrochemical H_2 evaluation of a novel mono- and bimetallic Schiff-base complexes bearing unsymmetric ligands derived from a calixpyrrole framework. The introduction of chemically distinct coordination binding pockets, such as salen or imidazole, has enabled a straightforward pathway to coordinate various transition metals into the secondary coordination sphere, hence the development of structurally versatile and catalytically competent systems for the hydrogen evolution reaction (HER).

In Chapter 2, the mono- and bimetallic salixpyrrole complexes (2 and 3, respectively) established the utility of co-facial, unsymmetric ligand architecture in HER catalysis. The monometallic complex 2 displayed moderate activity with TOF 1680 s^{-1} with an overpotential of 0.69 V and a faradaic efficiency of 90.5%. The complex can be seen to follow a mechanism that excludes H/D bond cleavage in the rate-determining step with second-order dependence on acid and first-order dependence on the catalyst. In contrast, the bimetallic complex 3 showcases significantly improved performance with TOF 4640 s^{-1} operating at a lower overpotential of 0.39 V(**Table 5.1**). Complex 3 was found to be first-order in both acid and catalyst, with a similar KIE

value to the monometallic system. The mechanistic pathway is suggestive of possible bimetallic synergy, emphasizing the power of cooperative metal centers in catalysis.

Chapter 3 introduced a new Schiff-base complex, abbreviated as “imixpyrrole” (complex 4), which further expanded the scope of unsymmetric calixpyrrole-based systems. The tunability of the complex in the presence of different proton sources was studied, and strikingly different catalytic behaviors were observed under varying acid strengths. In the presence of a strong acid, anilinium•BF_4, the complex, displayed homogeneous behavior with exceptional performance. The complex was operating at an overpotential of 0.53 V with TOF of 33040 s^{-1} and a faradaic efficiency of 99.3%, following a mechanism that excludes proton transfer in the rate-determining step. in contrast, the weaker acid (Triethylammonium•BF_4) showcased lower catalytic activity and unveiled a potential proton-coupled electron transfer (PCET) mechanism with a KIE of 6.45. Interestingly, the intermediate acid (Imidazolium•BF_4) produces a heterogeneous system, suggesting that the catalyst behavior and speciation can change depending on the acid source used (**Table 5.1**). This study underscores the profound impact of external conditions on HER activity and the mechanistic pathways.

Building on this framework, Chapter 4 revealed a novel synthetic strategy for constructing heterobimetallic Schiff-base complexes. Through a stepwise metalation approach, a successful incorporation of redox-inactive Zn (II) and redox-active Cu(I) ions into the secondary coordination sphere of the imixpyrrole system resulted in two diamagnetic heterobimetallic complexes (5 and 6). Electrochemical characterization revealed that Zn(II) subtly modulated the ligand’s redox properties, while Cu(I) introduced additional redox activity. Although crystallographic characterization remains elusive due to challenges in crystalizing charged multimetallic

complexes, spectroscopic and analytical evidence confirms the formation of the expected complexes.

Table 5.1. Comparison of relevant catalysis parameters.

Complex	Proton source	Nature	TOF	Over potential	KIE	Faradaic efficiency
(a)	[(DMF)H]OTf	Homogeneous	33000 s^{-1}	625 mV	N/A	N/A
(b)	TFA (DCM)	Homogeneous	> 2000000 s^{-1}	570 mV	N/A	~100%
Pd-Sal	pTSA.H_2O (11.8)/THF	Homogeneous	1680 s^{-1}	690 mV	1.33	90.5%
PdPd-Sal	pTSA.H_2O (11.8)/THF	Homogeneous	4640 s^{-1}	390 mV	1.13	91.7%
Pd-Imi	Anilinium (5.2)/THF	Homogeneous	33040 s^{-1}	530 mV	1.05	99.3%
	Imidazolium (9.4)/THF	Heterogeneous	2680 s^{-1}	890 mV	N/A	98.6%
	Triethylammonium (12.5)/THF	Homogeneous	4190 s^{-1}	990 mV	6.45	97.2%

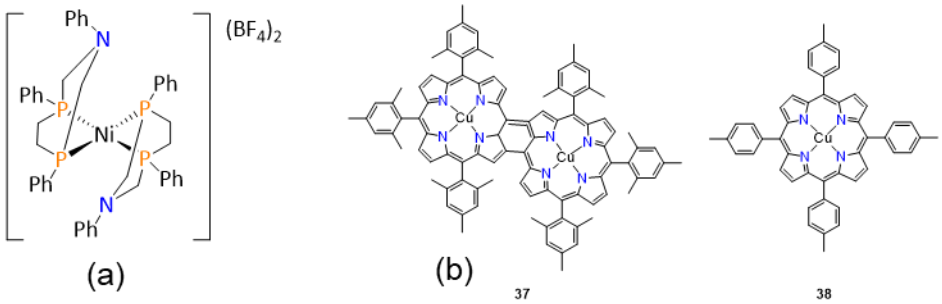

5.2. Future directions

The reactivity of both homogenous and heterogeneous HER catalysts is overviewed by focusing on reaction mechanisms. There are three main reaction mechanisms that can be seen for homogenous systems such as dimer formation of one-electron reducible complexes, bimolecular reaction of hydride complexes, and disproportionation reactions of one-electron reduced metal complexes to form two-electron reduced complexes.[3] When it comes to heterogenous systems, the

HER mechanism mainly consists of three distinct steps, the electrochemical hydrogen adsorption reaction (Volmer reaction), the electrochemical desorption reaction (Heyrovsky reaction), and the chemical desorption reaction (Tafel reaction) which can be described with below reaction elementary steps (* = active site on electrode surface, H* = hydrogen atom adsorbed on the active site).[4] Therefore, enhancing the catalytic performances of electrocatalysts would pave the pathway toward cost-effective and energy-efficient catalysis. Catalyst structure modifications can be considered one of the main strategies to improve the catalyst's performance.

$$H^+ + e^- \rightarrow H^* \, (Volmer)$$

$$H^* + H^+ + e \rightarrow H_2 \, (Heyrovsky)$$

$$H^* + H^* \rightarrow H_2 \, (Tafel)$$

5.2.1. Elucidating reaction mechanism for HER

With cyclic voltammetry results in hand, it is possible to perform a computational study on salixpyrrole and imixpyrrole systems to elucidate possible mechanistic pathways to HER. Density Functional Theory (DFT) is one common method that is used to model reaction pathways, intermediate structures, and activation energies of the catalysts which helps to rationalize experimental data and predict the catalytic pathways.[5,6]

Another method that can help to elucidate mechanistic pathways is stoichiometric reaction studies. The catalyst can be reacted with a chemical reductant and a proton donor under chemical conditions to synthesize intermediates and isolate them. This method would allow the possibility of understanding mechanistic pathways under non-electrochemical conditions and comparing the data to CV to confirm the reaction mechanisms.[7–9]

5.2.2. Optimizing metal-metal separation

According to the research, spatial arrangement and electronic interactions between metal centers are highly influential for catalytic activity. The optimal distance between metals for any catalyst (monometallic or bimetallic) always depends on the mechanism, the ligand environment, the proton delivery method, etc. Specifically for bimetallic cofacial systems, the effect of metal-metal distance for HER depends on the mechanism of H-H bond formation.[3] According to the literature, having a lower metal-metal distance is often more advantageous in HER when the catalysts are operating through a homolytic pathway where two M-H species combine to release H_2 gas.[3,10–13] When two M-H compartments are in close proximity or optimal distance, it can facilitate the direct coupling of the hydrides to release H_2. It was reported the distance between Ni-Fe in a synthetic mimic for hydrogenase was measured at 3.001 Å and such distances facilitate the electronic communication and cooperative interactions essential for HER which often lead to faster H_2 evolution.[14] For monometallic mechanisms or stepwise or in proton relays, higher metal-metal separation in cofacial geometry could be more advantageous due to reducing interference or crowing/steric hindrance, or providing easier access for substate (proton source) to the active site, or preventing unwanted side reactions or lead to metal aggregation.[3,10,11]

Recently, a study has been done to investigate more rigid macrocyclic porphyrins due to their redox properties and catalytic potential.[15,16] During that study, they used different porphyrinylene nano hoops to change the distance between two ligand compartments. When it comes to macrocyclic Schiff-base calixpyrrole, using different spacers or substituting the 3rd and 4th positions of *o*-aryl spacer between two compartments showed a significant impact on overall molecular chape including metal-metal separation.[17,18]

Another way to change the distance between two compartments in a cofacial structure is by having different substituents at the *meso*-carbon atom. It was reported that changing meso-phenyl groups to meso-methyl groups can increase the metal-metal separation due to increased flexibility within the macrocycle and lack of electronic conjugation.[17,18] Therefore, it is expected to apply similar changes to unsymmetric cofacial systems to figure out the optimal distance between two coordination spheres and to study the effect of that for HER reaction (**Figure 5.1**).

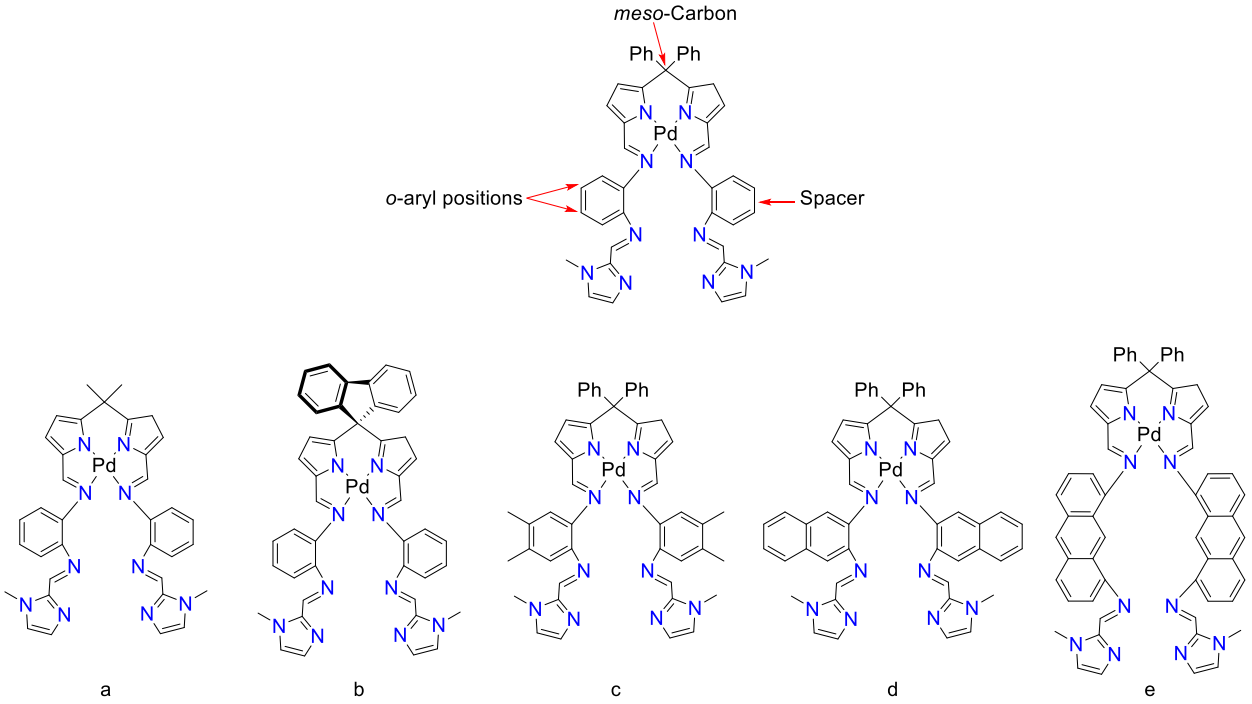

Figure 5.1. Proposed structures for the "Imixpyrrole" system with substitutions at meso-carbon, 3rd and 4th position on o-aryl group, and spacers.

5.2.3. Introducing different hetero atoms

Schiff-base ligand architecture typically contains a C=N functional group which enhances the coordination ability of catalysts to various metals. Therefore, incorporating more heteroatoms such as N, O, S, or P into the Schiff-base ligand structure would allow alterations of electron density around the metal center and fine-tune the metal-ligand interactions, which would affect the redox properties and the catalytic activity of the complexes.[7,19,20] As discussed earlier, hydrogenase

enzyme active sites also contain thiolate groups, which are considered to play a vital role in catalyzing HER.[14] It is also reported that axial coordination of O or S in Co-Schiff base Complexes can promote a facile H^+ binding/release mechanism which in turn improves the HER kinetics.[10,21] Having more heteroatoms such as O and N in the ligand structure showed enhanced chelation, making the complex more robust and less likely to decompose.[5,22,23] At the same time, incorporating polar heteroatoms like N and O can make the catalyst more hydrophilic which is crucial for HER in aqueous solutions.[23]

One way to incorporate heteroatoms into the ligand structure is by synthesizing unsymmetric Schiff-base ligands. As we discussed earlier, the incorporation of N and O into the secondary coordination sphere can be seen in the "Salixpyrrole" system.[1] Also, in Chapter 3, more N atoms were incorporated into the secondary coordination sphere of the "Imixpyrrole" system. Similarly, it is possible to incorporate P and S heteroatoms into the secondary coordination sphere of calixpyrrole Pd Complex and study its catalytic activity (**Figure 5.2**).[10,21]

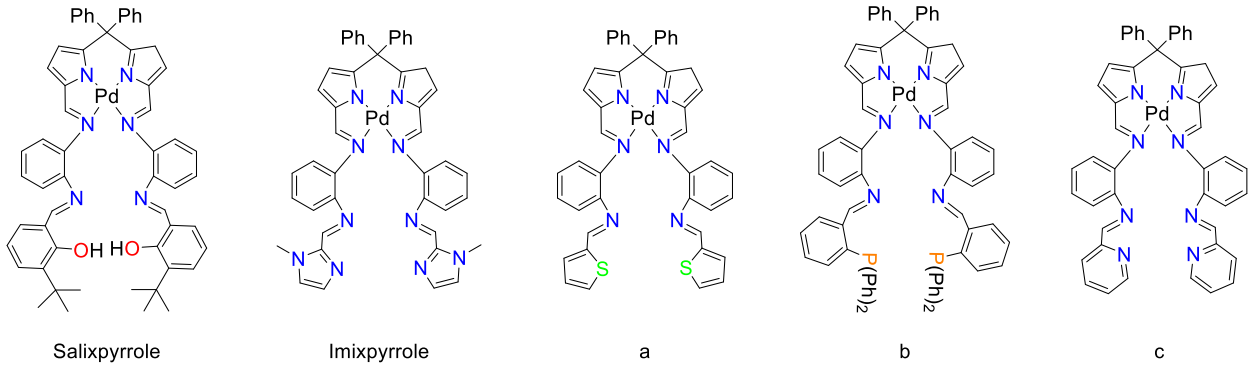

Figure 5.2. Proposed Structures of unsymmetric cofacial complexes.

Another way to incorporate heteroatoms into the ligand structure is by substituting a spacer that already has a heteroatom (**Figure 5.3**). As discussed earlier, this modification would change the

distance between the two coordination spheres, as well as it can promote a facile H^+ binding/release mechanism, which in turn improves the HER kinetics.[24]

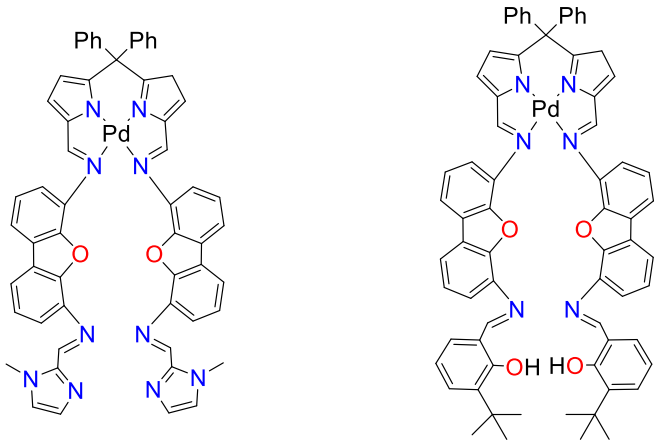

Figure 5.3. Proposed structures with spacers containing heteroatoms.

5.2.4. Cation inclusion

The inclusion of cationic ions into ligand architecture would be a way to tune the reduction potential of the complexes. According to previous studies, the inclusion of cationic ions into the metal complexes has shown an anodic shift in redox potentials.[25,26] One way to achieve this requirement is by encapsulating a metal ion within a crown ether moiety (**Figure 5.4**). The addition of crown ether to the secondary coordination sphere will enhance the complexation of monovalent (1+) and divalent (2+) cations, which in turn may promote the reduction of the complex.[27,28]

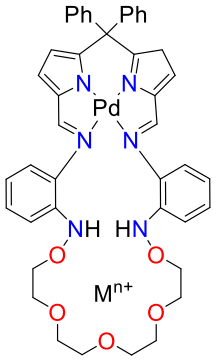

Figure 5.4. Proposed structure of crown ether calixpyrrole complex.

5.3. References

(1) Somachandra, M. S.; Averkiev, B.; Sues, P. E. Unsymmetric Co-Facial "Salixpyrrole" Hydrogen Evolution Catalysts: Two Metals Are Better than One. *Inorg. Chem.* **2024**, *63* (29), 13346–13357. https://doi.org/10.1021/acs.inorgchem.4c01101.

(2) Krishtalik, L. I. Kinetic Isotope Effect in the Hydrogen Evolution Reaction. *Electrochimica Acta* **2001**, *46* (19), 2949–2960. https://doi.org/10.1016/S0013-4686(01)00526-6.

(3) Fukuzumi, S.; Yamada, Y.; Suenobu, T.; Ohkubo, K.; Kotani, H. Catalytic Mechanisms of Hydrogen Evolution with Homogeneous and Heterogeneous Catalysts. *Energy Environ. Sci.* **2011**, *4* (8), 2754–2766. https://doi.org/10.1039/C1EE01551F.

(4) Shi, J.; Bao, Y.; Ye, R.; Zhong, J.; Zhou, L.; Zhao, Z.; Kang, W.; Aidarova, S. B. Recent Progress and Perspective of Electrocatalysts for the Hydrogen Evolution Reaction. *Catal. Sci. Technol.* **2025**, *15* (7), 2104–2131. https://doi.org/10.1039/D4CY01449A.

(5) 10459058.Pdf. https://par.nsf.gov/servlets/purl/10459058?utm_source=chatgpt.com (accessed 2025-04-09).

(6) Keszei, S.; Wang, Y.; Zhou, H.; Ollár, T.; Kováts, É.; Frey, K.; Tapasztó, L.; Shen, S.; Pap, J. S. Hydrogen Evolution Driven by Heteroatoms of Bidentate N-Heterocyclic Ligands in Iron(II) Complexes. *Dalton Trans.* **2024**, *53* (35), 14817–14829. https://doi.org/10.1039/D4DT02081B.

(7) Chukwu, C. D. Transition Metal Schiff Base Complexes as Potential Non-Platinum Catalysts for Hydrogen Evolution Reaction: A Comparative Study of Co (II) and Ni (II). ChemRxiv January 3, 2025. https://doi.org/10.26434/chemrxiv-2025-v53df.

(8) Upadhyay, A.; V. Saurav, K.; Lilly Varghese, E.; S. Hodage, A.; Paul, A.; Kumar Awasthi, M.; Kumar Singh, S.; Kumar, S. Proton Reduction by a Bimetallic Zinc Selenolate Electrocatalyst. *RSC Advances* **2022**, *12* (7), 3801–3808. https://doi.org/10.1039/D1RA08614F.

(9) Wu, L.-W.; Yao, Y.-F.; Xu, S.-Y.; Cao, X.-Y.; Ren, Y.-W.; Si, L.-P.; Liu, H.-Y. Electrocatalytic Hydrogen Evolution of Transition Metal (Fe, Co and Cu)–Corrole Complexes Bearing an Imidazole Group. *Catalysts* **2024**, *14* (1), 5. https://doi.org/10.3390/catal14010005.

(10) Marinescu, S. C.; Winkler, J. R.; Gray, H. B. Molecular Mechanisms of Cobalt-Catalyzed Hydrogen Evolution. *Proceedings of the National Academy of Sciences* **2012**, *109* (38), 15127–15131. https://doi.org/10.1073/pnas.1213442109.

(11) Huang, D.; He, B.; Zhao, Y.; Liu, M.; Wang, L. Homogeneous Electrocatalytic Hydrogen Evolution by a N2P2Fe(II) Complex: Structural Characterization of Iron-Hydride Intermediate. *Journal of Molecular Structure* **2025**, *1325*, 141021. https://doi.org/10.1016/j.molstruc.2024.141021.

(12) Jiang, B.; Gil-Sepulcre, M.; Garrido-Barros, P.; Gimbert-Suriñach, C.; Wang, J.-W.; Garcia-Anton, J.; Nolis, P.; Benet-Buchholz, J.; Romero, N.; Sala, X.; Llobet, A. Unravelling the Mechanistic Pathway of the Hydrogen Evolution Reaction Driven by a Cobalt Catalyst. *Angewandte Chemie International Edition* **2022**, *61* (40), e202209075. https://doi.org/10.1002/anie.202209075.

(13) Artero, V.; Fontecave, M. Solar Fuels Generation and Molecular Systems: Is It Homogeneous or Heterogeneous Catalysis? *Chem. Soc. Rev.* **2013**, *42* (6), 2338–2356. https://doi.org/10.1039/C2CS35334B.

(14) Ghosh, P.; Ding, S.; Chupik, R. B.; Quiroz, M.; Hsieh, C.-H.; Bhuvanesh, N.; Hall, M. B.; Darensbourg, M. Y. A Matrix of Heterobimetallic Complexes for Interrogation of Hydrogen Evolution Reaction Electrocatalysts †Electronic Supplementary Information (ESI) Available: Experimental, Spectroscopic, Additional Electrochemical and Computational Details, X-Ray Crystallographic Data (CIF) from the Structure of the Complexes [Ni–Fe]0, [Ni2–Fe2]2+, [Ni2–Fe]+, and Computational Coordinates Are Available. CCDC Crystallographic Data for the Complexes [Ni–Fe]0, [Ni2–Fe2]2+ and [Ni2–Fe]+ Were Deposited in the Cambridge Crystallographic Data Centre. CCDC [Ni–Fe]0 (CCDC 1045461), [Ni2–Fe2]2+ (CCDC 1045460) and [Ni2–Fe]+ (CCDC 1565539). For ESI and Crystallographic Data in CIF or Other Electronic Format See DOI: 10.1039/C7sc03378h. *Chem Sci* **2017**, *8* (12), 8291–8300. https://doi.org/10.1039/c7sc03378h.

(15) Jökel, J.; Schwer, F.; Delius, M. von; Apfel, U.-P. A Dinuclear Porphyrin-Macrocycle as Efficient Catalyst for the Hydrogen Evolution Reaction. *Chemical Communications* **2020**, *56* (91), 14179–14182. https://doi.org/10.1039/D0CC05229A.

(16) Xu, Y.; Gsänger, S.; Minameyer, M. B.; Imaz, I.; Maspoch, D.; Shyshov, O.; Schwer, F.; Ribas, X.; Drewello, T.; Meyer, B.; von Delius, M. Highly Strained, Radially π-Conjugated Porphyrinylene Nanohoops. *J. Am. Chem. Soc.* **2019**, *141* (46), 18500–18507. https://doi.org/10.1021/jacs.9b08584.

(17) Askarizadeh, E.; Devoille, A. M. J.; Boghaei, D. M.; Slawin, A. M. Z.; Love, Jason. B. Ligand Modifications for Tailoring the Binuclear Microenvironments in Schiff-Base Calixpyrrole Pacman Complexes. *Inorg. Chem.* **2009**, *48* (15), 7491–7500. https://doi.org/10.1021/ic900871g.

(18) Givaja, G.; Volpe, M.; Leeland, J. W.; Edwards, M. A.; Young, T. K.; Darby, S. B.; Reid, S. D.; Blake, A. J.; Wilson, C.; Wolowska, J.; McInnes, E. J. L.; Schröder, M.; Love, J. B. Design and Synthesis of Binucleating Macrocyclic Clefts Derived from Schiff-Base Calixpyrroles. *Chemistry – A European Journal* **2007**, *13* (13), 3707–3723. https://doi.org/10.1002/chem.200600989.

(19) Shi, J.; Bao, Y.; Ye, R.; Zhong, J.; Zhou, L.; Zhao, Z.; Kang, W.; B. Aidarova, S. Recent Progress and Perspective of Electrocatalysts for the Hydrogen Evolution Reaction. *Catalysis Science & Technology* **2025**, *15* (7), 2104–2131. https://doi.org/10.1039/D4CY01449A.

(20) Keszei, S.; Wang, Y.; Zhou, H.; Ollár, T.; Kováts, É.; Frey, K.; Tapasztó, L.; Shen, S.; Pap, J. S. Hydrogen Evolution Driven by Heteroatoms of Bidentate N-Heterocyclic Ligands in Iron(II) Complexes. *Dalton Trans.* **2024**, *53* (35), 14817–14829. https://doi.org/10.1039/D4DT02081B.

(21) Drosou, M.; Kamatsos, F.; A. Mitsopoulou, C. Recent Advances in the Mechanisms of the Hydrogen Evolution Reaction by Non-Innocent Sulfur-Coordinating Metal Complexes. *Inorganic Chemistry Frontiers* **2020**, *7* (1), 37–71. https://doi.org/10.1039/C9QI01113G.

(22) Shamskhou, K.; Awada, H.; Yari, F.; Aljabour, A.; Schöfberger, W. A Molecular Binuclear Nickel (II) Schiff Base Complex for Efficient HER Electrocatalysis. *Catalysts* **2023**, *13* (10), 1348. https://doi.org/10.3390/catal13101348.

(23) Cropley, J. D.; Mitchell, A. C.; Fritsch, N. A.; Ho, M.; Wells, T. D.; Reynolds, T. M.; Brennessel, W. W.; McNamara, W. R. Mononuclear Fe(III) Schiff Base Antipyrine Complexes for Catalytic Hydrogen Generation. *Dalton Trans.* **2024**, *53* (37), 15421–15426. https://doi.org/10.1039/D4DT01876A.

(24) Volpe, M.; Hartnett, H.; Leeland, J. W.; Wills, K.; Ogunshun, M.; Duncombe, B. J.; Wilson, C.; Blake, A. J.; McMaster, J.; Love, J. B. Binuclear Cobalt Complexes of Schiff-Base

Calixpyrroles and Their Roles in the Catalytic Reduction of Dioxygen. *Inorg. Chem.* **2009**, *48* (12), 5195–5207. https://doi.org/10.1021/ic9001175.
(25) Chantarojsiri, T.; Reath, A. H.; Yang, J. Y. Cationic Charges Leading to an Inverse Free-Energy Relationship for N−N Bond Formation by MnVI Nitrides. *Angewandte Chemie International Edition* **2018**, *57* (43), 14037–14042. https://doi.org/10.1002/anie.201805832.
(26) Drover, M. W. A Guide to Secondary Coordination Sphere Editing. *Chem. Soc. Rev.* **2022**, *51* (6), 1861–1880. https://doi.org/10.1039/D2CS00022A.
(27) Van Staveren, C. J.; Van Eerden, Johan.; Van Veggel, F. C. J. M.; Harkema, Sybolt.; Reinhoudt, D. N. Cocomplexation of Neutral Guests and Electrophilic Metal Cations in Synthetic Macrocyclic Hosts. *J. Am. Chem. Soc.* **1988**, *110* (15), 4994–5008. https://doi.org/10.1021/ja00223a017.
(28) Jee, J.-E.; Chai Chang, M.; Kwak, C.-H. Binding Property and Redox Behaviour of Nickel(II) Macrocyclic Complex Containing Crown Ether toward Alkaline Earth Metal Ions. *Inorganic Chemistry Communications* **2004**, *7* (5), 614–617. https://doi.org/10.1016/j.inoche.2004.02.030.